

Space Research Center of the Polish Academy of Sciences

Acceleration and heating of electrons
in the Earth's magnetosphere
during substorm development:
Interball-Tail observations

Piotr Koperski

Thesis submitted for the degree of
Doctor of Physics

Supervisor Dr. hab. Barbara Popielawska

Warszawa, 8th May 2005

*I dedicate this work, with Love:
D.O.M.,
to liberation of all sentient beings,
(and to/including) The ButterFish ;)*

Introduction

The magnetospheric substorm is, in brief, the process of abrupt reconfiguration of the magnetic field in the night-side magnetosphere, accompanied by the release of energy stored in the magnetic field due to interaction with the solar wind. The substorm activity in the magnetosphere and in the ionosphere is well documented, but our understanding of the global nature of this phenomenon is still insufficient. On the one hand, there are the hot plasma injections, the magnetic field dipolarizations, and the cross-tail current disruptions in the near geostationary region of the magnetosphere as well as the fast, localized plasma flows and signatures of magnetic reconnection at more distant tail regions. On the other hand, there are the horizontal- and magnetic field-aligned currents in the ionosphere and above, where the particle accelerations take place and the auroras brighten with their complex time- and space characteristics. However, many details concerning the ionosphere-magnetosphere coupling as well as the time sequence and localization of some important features are not clear. For instance, the mechanisms of substorm initiation and the question of how-and-where the auroral particles are accelerated are still the subjects of vigorous debate.

One of the reasons for the controversy is the lack of observations covering simultaneously both the magnetospheric and the ionospheric regions of interest. In particular, until very recently there were only a few reports on the active auroral region observed at low altitudes simultaneously with the closely conjugate high altitude magnetospheric source (and the keywords are *simultaneously* and *conjugated*).

One of the poorly understood topics is the role of low energy (a few hundreds eV to about 1 keV) electrons in the magnetosphere-ionosphere coupling during active times. There are reports (Klumpar et al. 1988, [89]; Johnstone et al. 1994, [80]) on the bursts of magnetic field-aligned 100 to 1000 eV electron fluxes which were observed beyond and near the geosynchronous region. The details and the relationship to the substorm were not reported directly, though. Another case study (Roux et al. 1991, [160]) reported, in turn, the drop in similar electron fluxes accompanied by the cross-tail current disruption at substorm onset in the geostationary region. The bursts of field aligned electron fluxes at energies of a few hundreds eV and below are the feature frequently observed in the auroral regions at different levels of substorm activity (e.g. Meng et al. 1978, [120]; Lotko et al. 1998, [103]; Miyake et al. 2001, [124]). Their relation to similar magnetospheric features and the possible relevance for substorm onset are however not well established; due to the lack of simultaneous multi-point observations this remains an open question.

The initial studies of hot plasma injections observed by the Interball Tail satellite had revealed sporadic occurrence of similar low-energy electron fluxes and allowed me to identify the specific event relevant to the onset of substorm: The streaming electron population of a few hundreds eV which was observed during the substorm growth phase in the near- Earth plasma sheet had

disappeared at the burst of the Ultra Low Frequency (ULF) magnetic turbulence coincident with the onset of substorm.

Following up this finding, next steps of research were undertaken:

- To identify the similar “macroscopic” events in the database of the ELECTRON experiment observations from the Interball-Tail satellite.
- To perform the comparative analysis of the events found and to specify their relation to the geomagnetic activity.
- To analyze the microscopic properties of electron population for the geomagnetically “active” events found and to obtain the representative characteristics.
- Based on the observed large scale magnetospheric dynamics and on the microscopic properties of the electron population, to try to identify both the physical mechanisms related to the observed events as well as their role in the magnetospheric dynamics.
- In particular, to find the relationship between the observed features on the one hand, and the auroral acceleration mechanisms, the substorm currents, and the substorm initiation on the other hand.

This work consists of 6 chapters. In Chapter 1, I draw the context for the ongoing considerations. It presents the structure of the Earth magnetosphere, the topics related to its dynamics, the auroral acceleration of charged particles, and the geomagnetic substorm activity.

In Chapter 2, I describe the experiments and the data used and briefly summarize the routines applied to generate and to explore the data.

The proper identification of the events on Interball in the context of substorm activity was the key step to understand the observations. The significant part of this work has been then devoted to the time-consuming search for- and the analysis of the satellite- and the ground-based observations from several sources. The detailed case study of the events of 13 January, 1996, which had inspired me to pursue this work, is presented in Chapter 3. The large-scale oriented, multi-point analysis allowed to identify the important aspects of substorm expansion phase (the repetitive character, the time- and location of initialization and the expansion rates). It also points out the typical features of magnetospheric electron population to be studied in the following chapters.

The details of the selection process and the procedures of the large-scale data analysis, applied to identify the rest of the events, are included in Chapter 4. For 178 “active” ground events identified, the search has been made for the specific features in the Interball data. 40 events, for which the satellite was located in the near/middle magnetosphere were initially chosen, and 9 cases were selected for the final detailed analysis. They are reviewed in Chapter 4, the last section of which summarizes the observed large-scale features.

In Chapter 5, I perform the quantitative analysis of the data for the “positively verified” cases. The electron distribution function and its moments are explored first. The simple model function is then proposed to represent the observed distributions and to model the data. Both approaches are used to analyze the observations.

I discuss the findings in Chapter 6, in the context of substorm initiation and auroral acceleration processes. The observed features agree with the model of the near-Earth cross-tail current disruption via the joined action of the current-driven Alfvén waves and the ballooning-mode instability (e.g. Roux et al. 1991, [160]; Perraut et al. 2000, [143]). This scenario, supported by the observations, also fits into the “O-shaped” model of auroral electron acceleration (Janhunen and Olsson, 2000, [77]). The low energy electrons, being able to carry the field-aligned currents of low intensity, are shown to participate in the Pc5 plasma oscillations in the near- Earth plasma sheet before and after the onset of substorm.

Contents

Introduction	i
1 Earth's magnetosphere.	1
1.1 Structure of the near-Earth space environment	1
1.1.1 Solar wind	1
1.1.2 Magnetospheric boundaries	3
1.1.3 Magnetospheric interior	5
1.1.4 Ionosphere- the low altitude boundary	6
1.2 Convection, currents and connection with the solar wind and ionosphere	7
1.2.1 Solar wind and magnetospheric convection	7
1.2.2 Currents in the system	9
1.2.3 Coupling between the magnetosphere and the ionosphere	12
1.3 Acceleration and heating of auroral electrons	14
1.3.1 Microscopic description	14
1.3.2 Single particle motion	16
1.3.3 Auroral particle acceleration	19
1.3.4 Adiabatic- and non-adiabatic effects in the nightside plasma sheet	24
1.4 Elements of dynamics of the Earth's magnetosphere	25
1.4.1 Magnetospheric activity	26
1.4.2 Magnetospheric substorm	30
1.4.3 Driving by the solar wind	32
1.4.4 Phenomenological models of substorm	32
2 Data sources and the instruments.	36
2.1 Interball mission and instruments	36
2.1.1 ELECTRON experiment	37
2.1.2 MIF-M magnetometer	38
2.1.3 Other Interball Tail data used	39
2.2 Other spacecraft data	39
2.2.1 Geostationary and low-altitude satellite data	39
2.2.2 Other satellite data	40
2.3 Electron pitch-angle data	40
2.3.1 The concept	40
2.3.2 Database	41
2.3.3 Restrictions	41
2.4 Ground-based data	42
2.4.1 Activity indices and the 1-minute geomagnetic data	42
2.4.2 High-resolution magnetic data	42
2.4.3 Other ground-based data	44
2.4.4 Software	47

3	Large-scale multi-point study of 13/January/1996 substorm expansion.	48
3.1	Introduction	48
3.2	Instruments and data used	48
3.3	Observations	49
3.3.1	Ground based observations	49
3.3.2	Satellite observations	58
3.4	Summary and discussion	65
3.4.1	Multiple intensifications	65
3.4.2	Expansion rates of the disturbed region	68
3.4.3	The 03:30 UT substorm intensification	72
3.5	Conclusions	76
4	Changes of the electron distribution function in the plasma sheet related to the onset of substorm/pseudobreakup.	78
4.1	Introduction	78
4.2	Data selection	79
4.3	Review of selected events	82
4.3.1	06/October/1995- an “unclear” case	82
4.3.2	21/October/1995	89
4.3.3	02/December/1995	96
4.3.4	09/December/1995	100
4.3.5	25/December/1995	106
4.3.6	28/December/1995	115
4.3.7	13/January/1996	117
4.3.8	16/January/1996	125
4.4	Summary of large scale observations	136
5	Properties of electron distribution and signatures of acceleration.	140
5.1	Introduction	140
5.2	Quantitative characteristics of electron distributions	141
5.2.1	Moments of the distribution function	141
5.2.2	Microscopic details	148
5.3	Data modeling	153
5.3.1	Model of the distribution function	153
5.3.2	Quality of the method	154
5.3.3	Results of modeling	154
5.4	Summary of observations	163
6	Discussion and summary.	167
6.1	Interpretation of observed electron phenomena	167
6.2	Consequences for auroral acceleration	170
6.3	Consequences for substorm onset	172
6.4	Summary	175
	Appendix	176
A.1	Modeling the electron distribution function	177
A.1.1	The distribution function	177
A.1.2	Assumptions	178
A.1.3	Method and its quality	178
A.2	Current-Voltage relationship	179

References	180
Acknowledgments	193
Podsumowanie wyników	194

Chapter 1

Earth's magnetosphere.

After over four decades of investigations of the near space environment of the Earth, the understanding of its structure and the physical processes taking place there have significantly increased. It is impossible to give a survey of the subject in a short chapter. Here, I will review in brief some aspects of current state of knowledge of the morphology and the dynamics of the (Earth's) magnetosphere. First of all, I will consider the facts most important to understanding the rest of this work.

The magnetosphere can be regarded as an element of the larger system, composed of the solar wind, the ionosphere, the radiation belts and the magnetosphere itself. From this point of view, the solar wind is the energy- and the plasma source as well as the forcing factor for the rest of the system. The ionosphere is the source of the cold plasma and, together with the radiation belts, is the place of storage and the main part where the energy is dissipated. The magnetosphere is the component where the energy is stored, transformed and transferred into the radiation belts and the ionosphere, as well as partially released back to the solar wind. The storage takes the form of an enhanced magnetic flux in the magnetotail and the higher thermal energy in the Plasma Sheet. The energy is then transformed, through the various plasma flow-, heating- and acceleration processes and transferred to other parts of the system. The internal dynamics of the magnetosphere and its coupling with the ionosphere and the solar wind has the complex, multi-scale- and multi-factor character. Although a huge volume of observations has already been collected, which are related to this subject and the various physical models are commonly used to describe them, some of the most principal mechanisms have not reach yet the satisfactory explanation.

1.1 Structure of the near-Earth space environment

The Earth's magnetosphere is the region near the Earth (above the ionosphere) where the magnetic field essentially influences the behavior of charged particles of the space environment. When the streaming, electrically charged particles (the plasma) of the solar wind encounter the obstacle of the Earth's magnetic field, the shock wave forms (the bow shock), the field itself is modified and the "magnetic cavity" of the magnetosphere is formed. The braked solar wind, heated and turbulent after crossing the bow shock, forms a narrow region around the magnetosphere called the magnetosheath (thick on average about $3 R_E$, at the sub-solar point). The configuration of the near space environment of the Earth is schematically shown in Figure 1.1.

1.1.1 Solar wind

The outermost part of the Sun, the solar corona, is the source of the intense outflow of electrically charged particles. These particles form the electrically neutral medium that also contains the

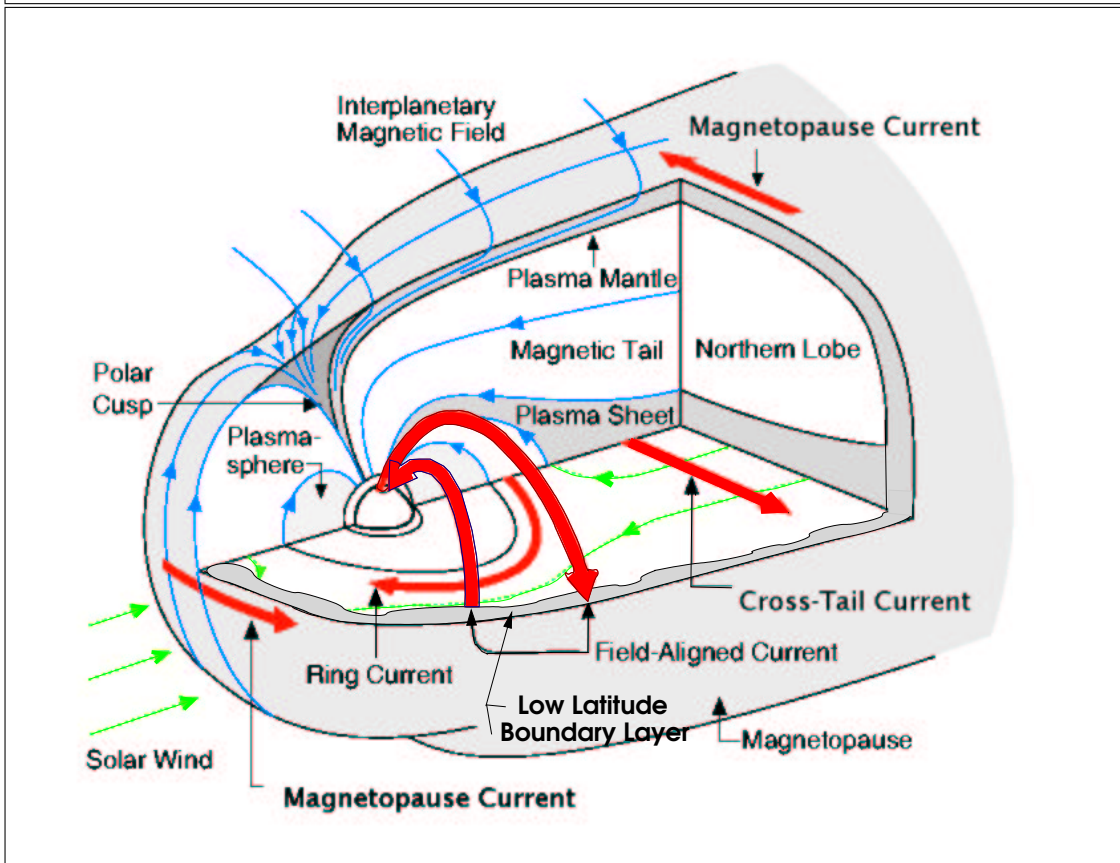
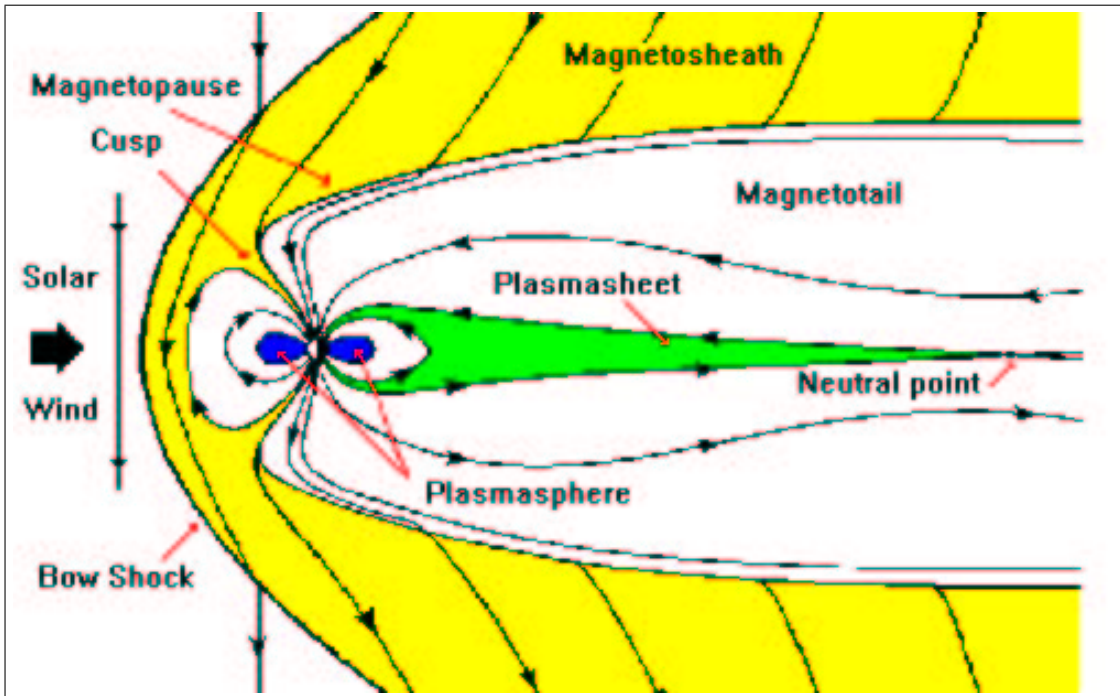


Figure 1.1: (Upper) noon-midnight meridian cross-section illustrating the formation of the magnetosphere; (lower) 3D internal structure of the Earth's magnetosphere.

remnants of the solar magnetic field and is called the Solar Wind. The composition, the energies and the densities of the particles allow for treatment of the solar wind as a collisionless, magnetized plasma. It is mainly composed of protons, of alpha particles (He^{2+} ions, between 4 and 25 percent) and of electrons. The properties of the solar wind vary significantly with the distance from the Sun as well as with time and the space location. Near the Earth's orbit (1 astronomical unit, AU), the Solar Wind bulk flow velocities vary between 200 and 1000 km per second (about 450 km/s on average) which is much above both the sound- and the Alfvén- velocities (the characteristic velocities in the magnetized plasma, typically, 60 km/s and 40 km/s respectively, near 1AU). Typical values of the density and of the temperature of protons are 6.6 cm^{-3} and $1.2 \times 10^5 \text{ K}$ (10.3 eV) respectively while for electrons they are 7.1 cm^{-3} and $1.4 \times 10^5 \text{ K}$ (12.1 eV). The magnetic field (induction) value is $7 \times 10^{-9} \text{ T}$ on average. Due to plasma outflow and the rotation of the Sun, the magnetic field lines have a spiraling structure. AT 1 AU it is nearly 45 deg. inclined to the Sun- Earth line. The above “static” image of Solar Wind has to be corrected by taking into account the temporal effects. Broadly speaking, they result from: (i) the rotation of the Sun (the 27 day period) (ii) the tilt angle of the Sun's dipole axis to its rotation axis, (iii) the inhomogeneous structure of the corona (coronal holes and streamers- the sources of plasma expanding with different velocities, densities and magnetic field strengths and orientations), (iv) the changing solar activity (mainly of the 11- and 22 years period). The superposed effects of these factors are further complicated by the turbulent character of the solar wind flow. The observations near the Earth's orbit routinely show dynamic changes, over many time- and space scales, of direction and strength of the magnetic field, as well as of the velocity, the density and the composition of the medium. All such variability significant influence the dynamics of the magnetosphere.

1.1.2 Magnetospheric boundaries

Magnetopause

The magnetopause is a current layer separating the magnetosphere from the turbulent solar wind of the magnetosheath, heated after crossing the shock wave in front of the Earth. It is sketched on top of Figure 1.2. As a zero order approximation, the magnetopause can be thought of as a surface where the balance between the magnetic pressure on the inner side- and the dynamic pressure of the solar wind from the outside takes place. The current on this surface renders the magnetic field discontinuous there.

More detailed investigations reveal complex, multi-scale processes taking place here, leading to a transfer of mass, momentum and energy to- and from the solar wind. As we know it now, this transfer is mainly realized by (more or less localized in space and in time) merging and reconnecting of the magnetic field of the magnetosphere and of the solar wind, though other mechanisms (as e.g. surface waves) also play a role. The magnetopause approaches the distances to the Earth of $10 R_E$ on average at the subsolar point, about $16 R_E$ at the terminator line and delimits the magnetotail from the solar wind to the distances of above hundreds of R_E on the night side. The size of the magnetopause and the physical processes taking place there are highly influenced by the solar wind parameters: the dynamic pressure, the density and the velocity, the strength and the direction of the interplanetary magnetic field.

Low Latitude Boundary Layer (LLBL)

Adjacent to the magnetopause from the inner side, this region extends from the dayside to the flanks of the magnetosphere around the equator plane. The LLBL is schematically shown at the bottom of Figure 1.2. Dominated by the mixture of interchanging hot- and cold plasma regions and the large scale flows, this region is an important place of transport and of mixing of the

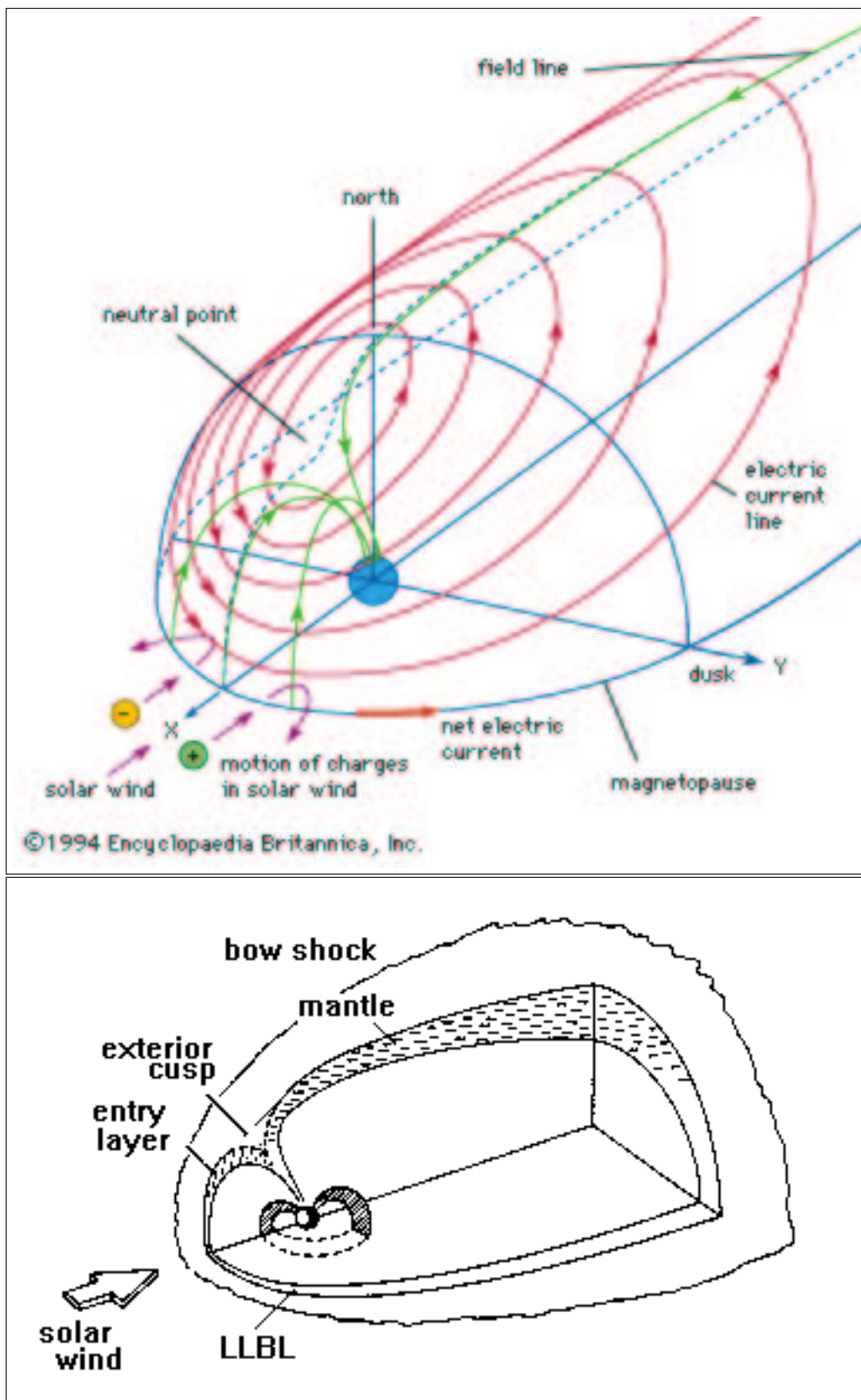


Figure 1.2: The magnetospheric boundaries: (top) The magnetopause current layer (the Chapman-Ferraro current) separating the magnetosphere from the solar wind. (bottom) The Low Latitude- and the High Latitude- Boundary Layers (LLBL and Mantle).

magnetospheric- and the external (i.e. of solar wind origin) plasma.

Plasma mantle

The high latitude extension of the boundary layer is called the (plasma) mantle. It is also schematically shown at the bottom of Figure 1.2. The topology of the magnetic field (the direction of which nears the flow direction) distinguishes this region, and the processes taking place within it, from the LLBL.

Magnetospheric cusps

Magnetospheric cusps are located not far from the magnetic poles, and form a special region because of the topology and the localization. The converging magnetic field lines allow for the transmission of the waves and streaming particles from waste region near the magnetopause. Its highly variable flows, currents and waves reflect the dynamics of the whole magnetospheric boundary and the near environment. Moreover, the orientation of the magnetic field allows the charged particles an easy access towards the Earth, along the field lines. This access is much easier here than at lower latitudes, due to the very weak magnetic field. The exact localization and the size of this region depends on the conditions of the solar wind (the density, the velocity, the strength and the orientation of the magnetic field).

1.1.3 Magnetospheric interior

Plasma sheet and current layer

The plasma sheet extends, generally speaking, tailward from the near geostationary region ($\sim 6.6R_E$) up to even $1000 R_E$ on the nightside, in the central part of the magnetotail. It is separated from the magnetopause by the LLBL near the equatorial plane and by the magnetotail lobes from above and below. It is the reservoir of hot plasma in the nightside magnetosphere. Its average density is $0.3 - 3$ particles in a cubic cm and its thermal energy is 0.5 to 5.0 keV. The plasma thermal pressure balances the tension of highly stretched magnetic field in the lobes. In the central part of the plasma sheet, there is the region where the magnetic field weakens and changes direction (earthward above-, anti-earthward below it). It is called the cross-tail current sheet, because of the intense currents flowing there, induced by the solar wind influence (see the following section). Such configuration can be relatively easily destabilized, so the physics of the current sheet plays the central role in the dynamics of the magnetosphere.

Magnetotail lobes

Magnetotail lobes constitute the (relatively) empty region out of the plasma sheet, dominated by the enhanced magnetic field of stretched geometry. They extend to the farthest end of the magnetosphere, where they connect to the interplanetary medium. Their typical density falls below 0.1 cm^{-3} and the temperature below ~ 0.3 keV.

Radiation belts

The region near the Earth between 2 and $6 R_E$ (a variation depending on the “disturbances” in magnetosphere, see below) is dominated by the energetic particles (mainly electrons and protons of energies from few keV up to hundreds MeV) and the increased magnetic field of the (nearly) dipolar configuration. The charged particles can be trapped in the magnetic field in consequence of processes commonly related to the geomagnetic activity (see the final section of this chapter). They form the intense currents around the Earth, known as the Ring Current. The trapped particles are subsequently lost by the various processes of charge exchange, diffusion and precipitation

to the ionosphere and the upper atmosphere, all of which are rather slow mechanisms. This region then acts as the accumulator and the sink for the accelerated particles and the energy formerly transferred from the solar wind and then transformed/released by the internal dynamics of the magnetosphere.

1.1.4 Ionosphere- the low altitude boundary

Although very small when compared to the magnetosphere, the ionosphere plays the essential role in the dynamics of the whole system. It is the principal source of the cold plasma and provides the feedback for the magnetospheric influences. The ionosphere is the ionized region of the upper atmosphere, at heights of about 80 to few hundreds km, which develops under the combined influence of the photoionization (mainly by the solar UV photons) and the impact ionization (by various kinds of the energetic particles, mainly the galactic cosmic rays, the magnetospheric- and the ionospheric particles). Its structure and dynamics depend on several factors, such as the intensity of the ionizing fluxes, the composition of the neutral atmosphere, the local time and the geographic position. It is too complex to be comprehensively described in a short chapter.

The most important here is the ionosphere of the auroral region (between about 60 deg and 75 deg geomagnetic latitude). It is where, mostly at altitudes between ~ 90 and 200 km, the phenomenon of Northern Lights or Aurora occurs. They are permanently observed from space in the sub-polar latitudes in the UV range or at the nighttime in the visual range (Figure 1.7 below), forming unstructured and slowly changing, so called diffuse auroral oval. Superimposed onto it are the discrete aurora, more dynamic and directly related to the geomagnetic activity (see Section 1.4). Listed below are some important facts concerning the auroral ionosphere:

- The region is connected, through the magnetic field lines, to the magnetospheric plasma sheet. (as sketched in Figure 1.1).
- The horizontal current exists, called the auroral electrojet, with the intensity high enough ($\sim 10^6$ A or more on the nightside), to modify the magnetic field observed on the ground. It is usually described as being composed of two parts: the convection- and the substorm electrojet (see middle panel of Figure 1.3) though there is no consensus about it.
- The field-aligned currents also exist, providing the connection to the more distant regions in the magnetosphere. The typical densities of the ionospheric field-aligned currents are below- or near $1 \mu A/m^2$, but increase up to $10 \mu A/m^2$ for the substorm-related, localized events (see Section 1.4).
- The magnetospheric particles of field-aligned currents (with the energies ~ 10 eV to hundreds keV, compared to ≤ 1 eV of ionospheric particles) excite and ionize the ionospheric medium, inducing the aurora. They are the source of the diffuse auroral oval during the magnetically quiet periods or the substorm's growth phase (see Section 1.4). During the magnetically active periods, the nightside aurora becomes more structured, intensive and dynamic. The most active (bright) part of the expanding auroral oval is called the Westward Traveling Surge (WTS; see bottom of Figure 1.3). The structure of the active auroral oval is very complex,
- The precipitating magnetospheric particles also modify the conductivity of the medium, especially during the active periods, when the fluxes are strong. Such modification influences the currents and the electric field in the ionosphere, giving feedback to the magnetospheric processes.

1.2 Convection, currents and connection with the solar wind and ionosphere

1.2.1 Solar wind and magnetospheric convection

The first satellite observations showed that the early idea of closed “magnetospheric cavity” by Chapmann and Ferraro was not appropriate and that the magnetosphere was indeed connected to the solar wind. Theoretical predictions of the open magnetosphere of Dungey, [40] offered the explanation of such connection. Sketched in upper panel of Figure 1.1 is the mechanism where three kinds of magnetic field lines can be found- those of the solar wind, with the two edges “free”, the closed field lines with two edges connected to the Earth and the “open” field lines with one edge on the Earth and a “free” one, connected to solar wind. The, previously closed, open field lines have merged to the Interplanetary Magnetic Field (IMF). The merging process favors the configurations where the fields of both media are initially nearly anti-parallel. This condition is easily met on the dayside when the B_Z component of IMF is negative (southward oriented), and near the cusps (when the IMF B_Z is positive).

The magnetic field of the solar wind can be seen as frozen in the medium (the “ideal MHD” condition) except for the merging process itself, which takes place locally. The open field lines are then dragged by the solar wind flowing tailward with the velocity \vec{V}_{SW} . Such dragging, with the magnetic field \vec{B}_N normal to the magnetopause, is seen in the magnetospheric frame of reference as the dynamo process. It generates potential difference between the two flank sides of the magnetosphere, with the magnitude typically of a few keV. The resulting electric field is called the cross-tail- or the convection electric field.

The merged and dragged field lines become very elongated and at a certain point (the distant reconnection line, situated at as high as even few hundreds R_E downtail) they re- connect to become closed again. After that, the magnetic tension acts to contract them earthward. This mechanism transports the magnetic flux to the nightside (an important way of the energy transfer to the magnetosphere), induces the plasma convection in the tail and is mostly anticipated during the southward oriented IMF. The momentum from the solar wind is also transferred this way, while the fluxes of particles along the open field lines contribute to interchange of mass and of energy.

For the positive (northward) IMF B_Z , the magnetic field merging is favored near the cusp, but it is less important in the energy- and the mass exchange with the solar wind. Other mechanisms (e.g. the “generic” hydrodynamic viscous interactions, the Kelvin-Helmholz instability etc.) near the cusp and the LLBL become important in such case (e.g. Axford 1964, [7]; Stasiewicz 1991, [190]).

Resulting from the coupling with the solar wind, the large scale plasma flows exist in the magnetosphere. The movement of a plasma particle depends in general on the electric- and the magnetic fields via the Lorentz force, $q(\vec{\mathcal{E}} + \vec{v} \times \vec{B})$, and on the “external” (non- electromagnetic) forces, \vec{F}_{ext} . The fields are nonuniform, non-stationary and depend on plasma properties, which are in turn modified by the fields. The nonlinear, non-stationary system then develops, with the various kinds of large- and small scale waves, currents, transient flows and magnetic field configurations (see the following section). The proper, full description of such system is nowadays far from being complete and feasible.

It is possible nonetheless to identify the principal factors that the movement of a particle depends on. The large scale inhomogeneity of the magnetic field is important in the plasma sheet (due to the high curvature of the field lines) and near the Earth (due to both gradient- and curvature- effects). The electric field has two main sources: the Earth’s rotation and the influence of the solar wind. The first follows from dragging of the near-earth’s plasma in the geomagnetic field by the Earth, rotating with the angular velocity $\vec{\Omega}$. Assuming the axial symmetry at a

geocentric distance r , this “electric field of corotation” equals $\vec{\mathcal{E}}_\Omega = -(\vec{\Omega} \times \vec{r}) \times \vec{B}_N$. In the equatorial plane, it decreases as r^{-2} and dominates other influences at geocentric distances below $\sim 4R_E$. The second component is the “convection electric field” mentioned above, $\vec{\mathcal{E}}_C = -\vec{V}_{SW} \times \vec{B}_N$, oriented from East to West (“dawn-to-dusk”) and penetrating the magnetotail. In the inner magnetosphere, this field is shielded due to effect of polarization. This effect develops due to the opposite drift velocities of electrons and of positive ions in the nonuniform magnetic field (the “gradient-” and the “curvature” drifts).

If the time- (space-) scale of changes are much longer than a particle’s gyroperiod (gyroradius), the “guiding-center drift” approach (see Section 1.3) approximates the particle’s dynamics. In the quasi-stationary case ($\partial/\partial t \simeq 0$):

$$\vec{V}_D = \frac{W_\perp \vec{B} \times \nabla B}{q B^3} + \frac{2W_\parallel \vec{R}_c \times \vec{B}}{q R_c^2 B^2} + \frac{\vec{F}_{ext} \times \vec{B}}{q B^2} + \frac{\vec{\mathcal{E}} \times \vec{B}}{B^2} \quad (1.1)$$

\vec{V}_D is the velocity of the gyrocenter, q is the particle’s charge and other terms describe (left- to right): the gradient- and the curvature drifts in the nonuniform magnetic field, the “external” force drift and the $\vec{\mathcal{E}} \times \vec{B}$ drift. W_\perp and W_\parallel are kinetic energies of the movements- perpendicular and parallel to \vec{B} and \vec{R}_c is the curvature vector of the magnetic field line, directed from the center of curvature. The electric field has two components (“convection”, and “corotation”) and the external force is in practice important only for the ions close to the Earth, as the gravity force.

This approach does not include changes in the magnetosphere (see below) nor in the Solar Wind. Neither is it self-consistent, describing the particles as a passive agent only, which does not influence the fields. Also, the guiding-center approximation imposes constraints on the time- and the space scales of interest and is not appropriate in many situations met in the magnetosphere, when the processes going on are both, faster and localized (see Section 1.3). Even with such simplifications, the proper description of the magnetospheric convection is a difficult task, since the fields have to be described realistically. It has been, nevertheless, successfully used in modeling e.g. the substorm- related injections of energetic particles close to the earth (see e.g. the review of Ebihara and Ejiri 2003, [41] and further references in Section 3.4.1).

A simple MHD model allows for a self-consistent description of plasma and fields. Convection, in terms of the bulk plasma velocity \vec{v} , is governed by the momentum equation:

$$\rho \frac{d\vec{v}}{dt} = -\vec{\nabla} \hat{p} + \vec{j} \times \vec{B} \quad (1.2)$$

where: ρ is mass density, \vec{j} is current and \hat{p} is pressure tensor (in general- anisotropic), and the viscosity has been neglected. To complete the model, the usual set of fluid equations has to be formed (by adding the mass continuity equation and e.g. a relation between ρ and p). Also the relevant form of the Ohm’s law relating the current and the electric field has to be included and so has the Maxwell equations. In particular, Ampere and Faraday laws yield:

$$\nabla \times \vec{B} = \mu_0 \vec{j} + \frac{1}{c^2} \frac{\partial \vec{\mathcal{E}}}{\partial t} \quad (1.3)$$

$$\frac{\partial \vec{B}}{\partial t} = -\nabla \times \vec{\mathcal{E}} \quad (1.4)$$

The appropriate form of the Ohm’s Law to be used depends on the time- and the space- scales of interest as well as on the properties of the medium. A quite effective approach for the (magneto- spheric) plasma, is to consider the momentum equations of different plasma components treated separately (the “multi-fluid approach”). One has to subtract them, accounting for their charges and leaving only the most significant components in the equation (see e.g. Song and Lysak 2001

[187] and references therein). Neglecting the small terms of the order electron-to-ion mass ratio ($m_e/m_i \ll 1$) and the space charge, one gets the approximate form of the generalized Ohm's Law:

$$\vec{\mathcal{E}} + \vec{v} \times \vec{B} = \eta \vec{j} - \frac{\nabla \cdot \hat{p}_e}{qn_e} - \frac{\vec{j} \times \vec{B}}{qn_e} + \frac{m_e}{nq^2} \left[\frac{\partial \vec{j}}{\partial t} + \nabla \cdot (\vec{v} \vec{j} + \vec{j} \vec{v}) \right] \quad (1.5)$$

where η in the first term on the right hand side is the resistivity (mainly the ‘‘anomalous’’ effects due to wave-particle interactions are important in magnetospheric plasma) and \hat{p}_e in the second term is the electron pressure. The third- (or ‘‘Hall’’) term accounts for the ion inertia and the fourth- for the electron inertia.

Considering the large scale- (above $\sim 1R_E$) and slowly changing (above a few minutes) processes in magnetosphere, the right hand terms are often very small, leading to:

$$\vec{\mathcal{E}} + \vec{v} \times \vec{B} = \vec{0} \quad (1.6)$$

This equation is the basis for the ‘‘ideal MHD’’ approximation (the magnetic field ‘‘frozen’’ into the mass flow). Its consequence is nonexistence of the parallel electric field.

Another approach has been used for the general quasi-static, electromagnetic perturbations in the near- earth plasma sheet region by LeContel et al. 2000, [31] and [32] (see also e.g. Cheng et al. 2004, [27] and references therein). They had applied the full Vlasov- Maxwell set of equations in the ‘‘magnetic mirror’’ geometry, with the quasi- neutrality condition added. The considered time scale of changes had to exceed the particle bounce period in the converging magnetic field and the period of an Alfvén wave (respectively: $T > \tau_b, V_A/k_{\parallel}$; see Section 1.3). This self consistent, bounce period-averaged model allowed to describe the transport of plasma and the possible mechanisms of current disruption at substorms (Perraut et al. 2000, [143]; LeContel et al. 2001, [33]. see also Section 1.4).

In order for a smaller scale effects to be accounted properly, as e.g. for the time- dependent magnetosphere- ionosphere coupling or for the fast/localized processes during the substorm (see below), the parallel electric field is important and some of the right-hand terms of Equation 1.5 have to be non-vanishing. Such situations can often be described in various ‘‘non-ideal’’ and multi- fluid models (e.g. Birn and Hesse 1996, [12]; Birn et al. 1999, [14]; Song and Lysak 2001, [187] and references therein). In some situations, neither approach is adequate, e.g. for the multicomponent-, non-maxwellian distribution function of particles, evidenced even in some ‘‘steady state’’ situations or for the field line merging. These limitations can often be removed, at least partially, in the full kinetic particle simulations, (e.g. Walker et al., 1995, [205]; Schriver et al. 1998, [173]; Pritchett and Coroniti 2000, [151]; Hoshino et al. 2001, [65]; Nishikawa 2001, [131] and references therein).

1.2.2 Currents in the system

The magnetic field in the near-Earth space is significantly deviated from the natural dipolar shape observed closer to the surface. This deviation is related to the existence of the electric currents, sketched at the bottom of Figure 1.1, in top of Figure 1.2 and in Figure 1.3. The following large scale currents can be identified:

- The **ring current** composed of charged particles drifting in the nonuniform, nearly dipolar magnetic field close to the Earth. The current arises due to oppositely directed drift of positively- and negatively- charged particles.
- The **magnetopause current** (called also the Chapman-Ferraro current), which sustains the separation between the magnetosphere and the solar wind (see Figure 1.2).
- The field-aligned **cusp currents**, related to the dayside reconnection.

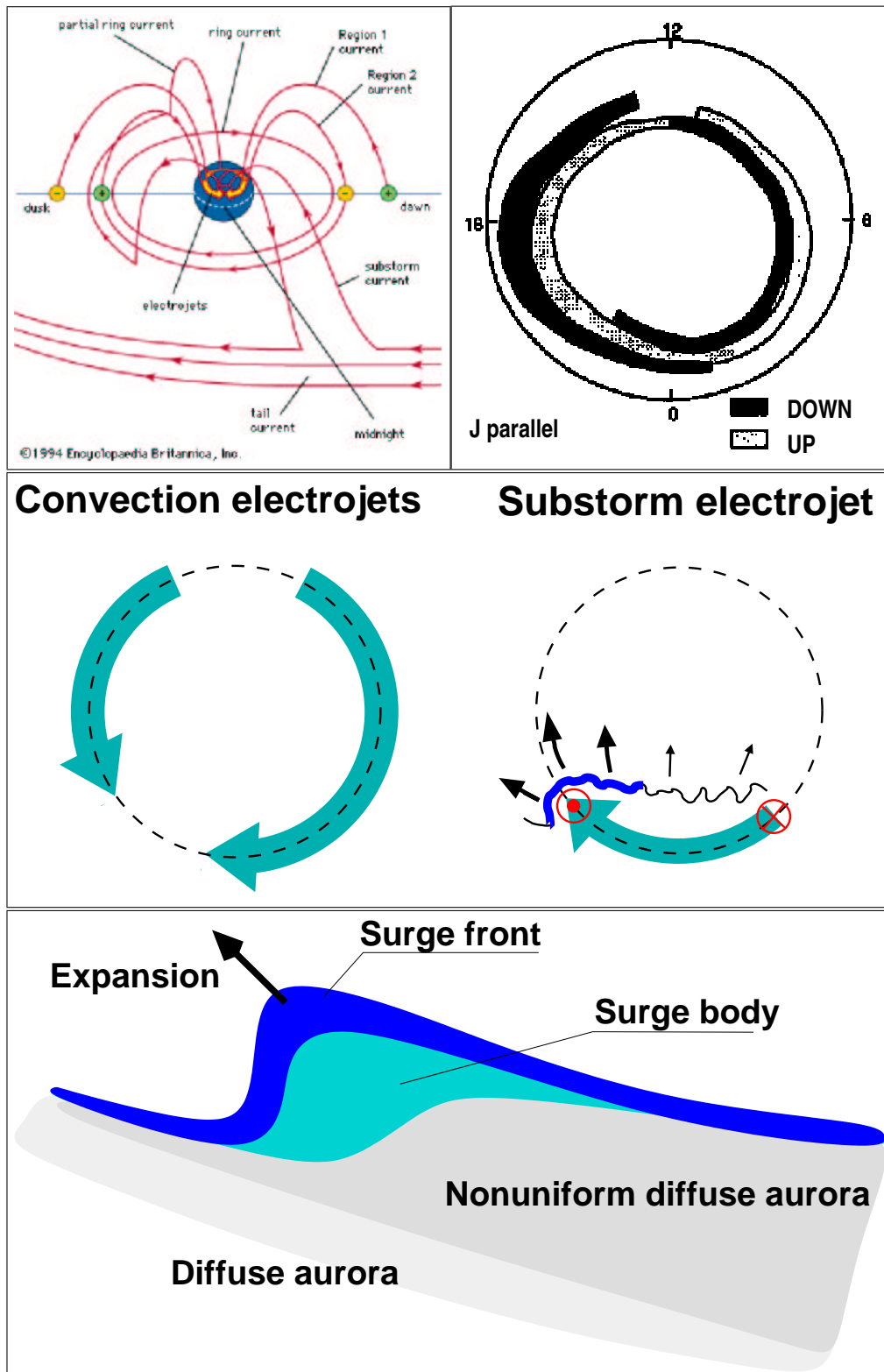


Figure 1.3: The magnetospheric and the ionospheric currents. (Upper left) Principal currents in the magnetosphere; (Upper right) Statistical picture of the upward and downward field-aligned currents in the ionosphere (after Ijima and Potemra, 1978 [69]); (Middle) Horizontal currents in the auroral ionosphere: (right) the substorm electrojet and the field-aligned currents (red) of the current wedge superposing on the (left) convection electrojets; (Lower) Eastward traveling surge (WTS, marked also in the middle right as the blue line around the upward current).

- The **cross-tail current** flowing near the equatorial plane across the magnetotail. Directed westward (“dawn-to-dusk“), it supports the stretched configuration of the nightside magnetic field and closes partially the magnetopause current.
- The small part (about 5%) of the above current system is diverted into the ionosphere through the **field-aligned- currents** (FAC, called also the “Birkeland currents”) at high latitudes. Sketched in Figure 1.3 are so called “Region 1-” and “Region 2” currents (after “the first-” and “the second-” when counted from the pole), connected to regions of tailward- and sunward convection in the equatorial plane.
- The **auroral convection electrojets**, which are the ionospheric horizontal currents, connected to the regions of the magnetospheric convection through the field-aligned currents of Region- 1 and 2 (see Figure 1.3).

This “static” picture has to be appended by the dynamics related to the “magnetospheric activity” (see the following section), as e.g. build-up of the ring current, transient effects related to the, so called, “bursty bulk flows”/convection jets in the tail or disruption of the cross-tail current. The last process, is related to development of two, closely related elements:

- the intense, temporary current system, called the “**current wedge**”, where the partially disrupted cross-tail current is redirected along the field lines to- and from the ionosphere, connecting to the additional “**substorm electrojet**” (also shown in Figure 1.3).
- the **Westward Traveling Surge** which is the western terminal part of the substorm electrojet and where the intense upward field- aligned current goes out from the ionosphere. This is the most dynamic and structured region of the auroral zone, where the 3-dimensional pattern of the electric field and current develop and where the intense fluxes of the magnetospheric electrons significantly modify the ionospheric conductivity. The same electrons are responsible for the spectacular substorm auroral forms.

The cross-tail current, in the slowly changing- large scale situation, is obtained from the perpendicular component of the momentum equation (Equation 1.2):

$$\vec{j}_{tail} = \frac{\vec{B}}{B^2} \times \left[\nabla p_{\perp} + \frac{p_{\parallel} - p_{\perp}}{B^2} (\vec{B} \cdot \nabla) \vec{B} + \rho \frac{d\vec{v}}{dt} \right] \quad (1.7)$$

The formula illustrates the influence of the field- and the pressure inhomogeneities, of the pressure anisotropy and of the inertial effects.

The field-aligned currents follow from the current closure condition. Neglecting the displacement current in Ampere’s law, Equation 1.3 (reasonable in a slowly changing situation) implies:

$$0 = B \frac{\partial}{\partial s} \left(\frac{j_{\parallel}}{B} \right) + \nabla_{\perp} \cdot \vec{j}_{\perp} \quad (1.8)$$

where s is the arc length of the field line and the current is split into parallel- (to \vec{B}) and perpendicular components. From this and from the momentum equation 1.2 with isotropic pressure, one gets the well known “Vasyliunas equation” for $\vec{j}_{\parallel,I}$, the parallel current in the ionosphere (e.g. Vasyliunas, 1970, [202] and 1984, [203]; here in corrected form of Sato and Ijima, 1979, [162]; see also e.g. Song and Lysak 2001, [187] and references therein for the discussion):

$$\vec{j}_{\parallel,I} = B_I \int_S^I \left[\frac{2\vec{j}_{\perp} \cdot \nabla B}{B^2} + \frac{\rho}{B} \frac{d}{dt} \left(\frac{\Omega}{B} \right) - \nabla \rho \cdot \frac{\vec{B}}{B^3} \times \frac{d\vec{v}}{dt} \right] ds \quad (1.9)$$

The integral is taken along the magnetic field line between the source region (S) in the equatorial magnetosphere and the ionosphere (I), $\vec{b} = \vec{B}/B$ and $\Omega = \vec{b} \cdot \nabla \times \vec{v}$ is the parallel vorticity of the convection flow.

Equation 1.9 relates the parallel current at the ionospheric level to the, field line- integrated: pressure gradients, the “grad B” / “curvature” drifts, the inertial- and the shear effects. Details of this relation had been investigated by several authors. E.g. Vasyliunas 1970, [202] or 1984, [203] and Sato and Ijima, 1979, [162] discussed the origins of source components and connection to the ionosphere in the quasi stationary case. The influence of anisotropic pressure was analyzed by Birmingham, 1992, [11] and the analytical formula was obtained, at the price of the purely magneto-static and more complex description. Relative meaning of components of equation 1.9 for the substorm current wedge (see next section) were estimated numerically (e.g. Birn and Hesse 1996, [12]; Birn et al. 1999, [14]) and compared with observations (e.g. Shiokawa 1997, [182]).

A more general, time dependent description can also be obtained, at the price of further assumption on the time/space scales and the structure of the medium. In particular, Southwood and Kivelson 1991, [188] directly showed that the field-aligned currents in the magnetosphere are related to two major types of forcing- the alfvénic structures (both standing or traveling waves) and the transient, pressure driven disturbances. The role of Alfvén waves is explained below.

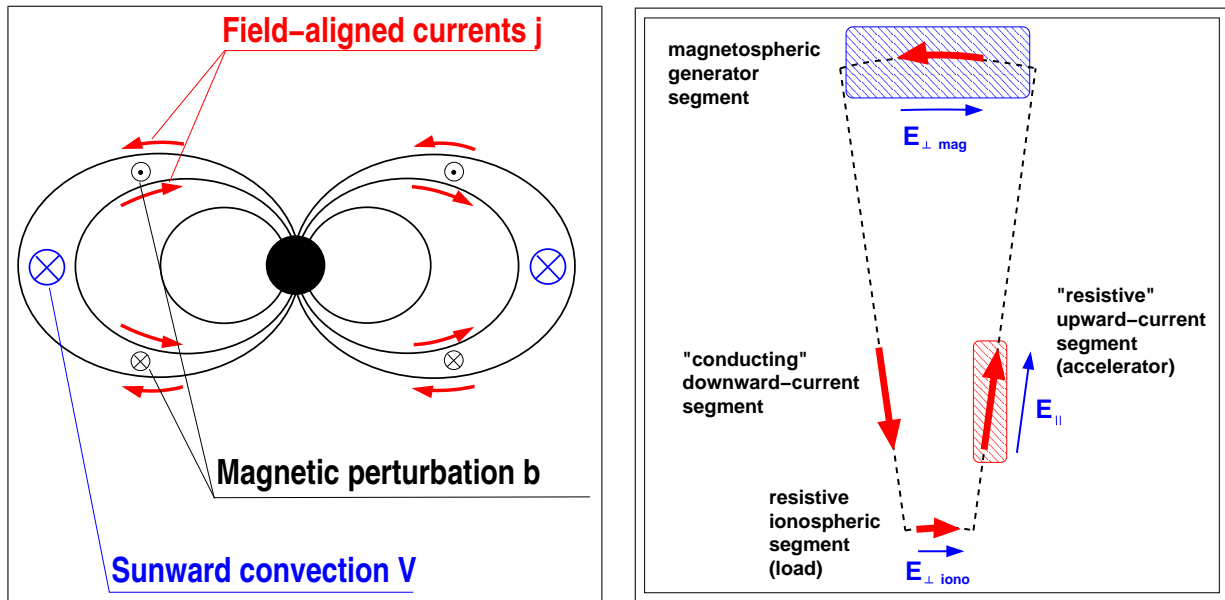


Figure 1.4: (Left) Convection and field-aligned current generation (viewed earthward from the tail); (Right) The auroral current circuit, with the magnetospheric generator-, the upward- current accelerator and the ionospheric load.

1.2.3 Coupling between the magnetosphere and the ionosphere

The magnetic field- aligned magnetospheric currents (FAC) flow towards- and from the ionospheric regions where aurora occur (see e.g. Kamide and Baumjohann 1993, [81]; Chun and Russell 1997, [34]; Ijima and Potemra, 1976 [69] and references therein). They transport the transverse momentum along the magnetic field lines, providing the coupling between the magnetosphere and the ionosphere (e.g. Vasyliunas 1970, [202]; Sato and Ijima 1979, [162]; Lysak, 1990, [114]; Birn and Hesse 1996, [12]; Song and Lysak 2001; Vogt 2002, [204]). The mechanism relating the convection and the field-aligned currents is sketched in the left panel of Figure 1.4 .

The coupling follows from the magnetospheric generation of currents (Equation 1.9) and from the continuity requirement (Equation 1.8), applied to the ionospheric medium (which is collisional with the anisotropic conductivity). The integration along the ionospheric height (assuming it is

a thin slab perpendicular to \vec{B}), yields for the ionospheric current:

$$\vec{j}_{\parallel,I} = \nabla_{\perp} \cdot \left(\begin{bmatrix} \Sigma_P & -\Sigma_H \\ \Sigma_H & \Sigma_P \end{bmatrix} \cdot \vec{\mathcal{E}}_{\perp} \right) \quad (1.10)$$

where Σ_P and Σ_H are so called ‘‘Pedersen’’- and ‘‘Hall’’ (height-integrated) conductivities and $\vec{\mathcal{E}}_{\perp}$ is the ionospheric horizontal electric field. Equations 1.9 and 1.10 are the starting point for modeling the magnetospheric- ionospheric connections (e.g. Kamide and Baumjohann 1993, [81]; Vogt 2002, [204]; and references therein). In this context, the picture of the auroral current circuit is often used, sketched in right panel of Figure 1.4. The magnetospheric convection driven by the solar wind is the current generator. The ionosphere, with the dissipation of currents in the collisional medium and the precipitating charged particles in the auroral zone, is the load for such current circuit. The ionospheric conductivity, modified by precipitating particles, is also able, to some extent, to control the currents- and thus the state of the plasma sheet.

Under the quasi-stationary, ideal MHD conditions (Equation 1.6) the magnetic field-lines are equipotential. The plasma sheet convection is in turn dominated by the $\vec{\mathcal{E}} \times \vec{B}$ drift so the flow remains equipotential when projected down-to the ionosphere along the field lines. Consequently the Hall component of the ionospheric current (perpendicular to $\vec{\mathcal{E}}$, Equation 1.10) corresponds to the magnetospheric convection, while the Pedersen component (parallel to $\vec{\mathcal{E}}$) is responsible for the Joule dissipation of the magnetospherically generated current, $Q_J = \Sigma_P \mathcal{E}_{\perp}^2$.

As pointed out by several authors (see e.g. Song and Lysak 2001, [187]; Vogt 2002, [204]; and references therein), this steady-state, ‘‘perfect coupling’’ scheme has several limitations. It is, in reality influenced by the existing parallel electric fields (see the following section). It does not include the full dynamics of the generator (the pressure distribution and the flow pattern has to be treated separately), nor does the rest of the current system- the ionosphere and the acceleration region. Finally, it allows for the quasi-steady description only. This last limitation is especially important during the ‘‘geomagnetically active periods’’ (see Section 1.4), when the time scale of changes becomes very short (of minute or less).

The Alfvén waves provide a way to add the dynamics to the system. Considering, in the framework of the ideal MHD, a weak disturbance propagating along the homogeneous, background magnetic field \vec{B}_0 (in z direction), yields (as one of the solutions) the ‘‘shear Alfvén’’ wave. It is governed by the equation:

$$\frac{\partial^2 \vec{\mathcal{E}}_{\perp}}{\partial t^2} = V_A^2 \frac{\partial^2 \vec{\mathcal{E}}_{\perp}}{\partial z^2} \quad (1.11)$$

where $V_A = B_0/\sqrt{\mu_0\rho_0}$ is the ‘‘Alfvén velocity’’, ρ_0 is the mass density, and the electric field $\vec{\mathcal{E}}_{\perp}$ is the small disturbance perpendicular to \vec{B}_0 , related to the magnetic disturbance \vec{B} through the relation:

$$\vec{\mathcal{E}}_{\perp} = \pm V_A \vec{B} \times \vec{B}_0 / B_0 \quad (1.12)$$

Two other kinds of wave existing in this situation are the ‘‘fast-mode’’ and the ‘‘slow-mode’’ waves. Contrary to shear Alfvén, they include compressional effects, going on in phase (for the fast-mode) or in anti-phase (for the slow-mode) to the wave magnetic oscillations. Only the fast-mode waves can propagate transverse to magnetic field.

The meaning of Alfvén waves is that they carry the parallel current. Considering the polarization current related to the disturbance (e.g. Vogt 2000, [204]), $\vec{j}_p = 1/\mu_0 V_A^2 d\vec{\mathcal{E}}_{\perp}/dt$ and applying to it the current closure requirement 1.8, one gets :

$$j_{\parallel} = \Sigma_A \nabla \cdot \vec{\mathcal{E}}_{\perp} \quad (1.13)$$

where $\Sigma_A = 1/\mu_0 V_A$ is called the ‘‘Alfvén conductance’’.

The wave reaching the ionosphere will be in general partially reflected. Considering its contribution to the ionospheric current (equations 1.10 and 1.13) with the uniform ionospheric conductance ($\Sigma_P = \Sigma_H$), the current continuity leads to relation between the inciding- and the reflected parallel currents: $j_{\parallel}^{ref} = -R_I j_{\parallel}^{inc}$, with the reflection coefficient (see e.g. Lysak 1990, [114]; Vogt 2002, [204]; for discussion and references):

$$R_I = \frac{\Sigma_A - \Sigma_P}{\Sigma_A + \Sigma_P} \quad (1.14)$$

In the ionosphere, the Alfvén conductivity is usually less than 0.5 S. The Pedersen conductivity in turn is variable- typically 1 – 10S, but it can drop below 0.1S in the nightside zone, in the absence of particle precipitation. In general, the mismatch between the two conductivities leads to partial bouncing of the incoming wave until it is dissipated. In particular case, when $\Sigma_A = \Sigma_P$, the incoming wave is totally absorbed in the ionosphere.

The most important limitation of the above model is that it is based on the cold fluid approximation (Equations 1.11 - 1.13), ignoring the kinetic effects, important for the short wavelengths. The observed parallel electric fields (see subsection 1.3.3) make necessary the use of the non-ideal Ohm's Law. Several more advanced models have been used to remove this and other limitations (see e.g. Birn and Hesse 1996, [12]; Song and Lysak, 2001, [187]; Vogt 2002, [204] and references therein).

The explanation of the magnetosphere- ionosphere coupling details at substorm remains one of the key, unsolved problems of the magnetospheric physics.

1.3 Acceleration and heating of auroral electrons

A comprehensive presentation of the mechanisms of heating and acceleration of electrons in the auroral zone and in the conjugated magnetosphere can be the subject of a voluminous monograph. This work is focused on the observations and, regarding the specific data set under study and the experimental conditions (see the following chapter), I address only the small part of the subject, related to the slow processes. More precisely, the time scales of changes above a few seconds (i.e. longer than both electron- and proton gyro-period) are of main interest.

1.3.1 Microscopic description

The most general way to describe a plasma is to use the N- particle distribution function in the $6N$ - dimensional phase space (where N is the- very large- number of particles). This function gives simultaneously the positions and the momentum of all the particles, and allows (formally) to follow the dynamics of the whole system, knowing all the forces acting (including those between the particles). This exact description is the starting point for the reduced models, usually statistical ensemble- averaged and approximating the correlations (of different orders) in a relevant way. The basic approach for the magnetosphere and the ionosphere is to apply the single- particle description. It represents the system as the point in the 6- dimensional phase space of position and velocity (or momentum, more generally), $F(\vec{r}, \vec{V})$, and can be interpreted as the number of particles in an infinitesimally small phase space volume around the point $[\vec{r}, \vec{V}]$. Its evolution is described by the kinetic equation:

$$\frac{\partial f}{\partial t} + \vec{V} \cdot \nabla_r f + \frac{q}{m} (\vec{\mathcal{E}} + \vec{V} \times \vec{B}) \cdot \nabla_V f = \left(\frac{\partial f}{\partial t} \right)_c \quad (1.15)$$

where ∇_r and ∇_V are the gradient operators in configuration- and velocity spaces and the right hand term is responsible for the collisional changes. It has to be completed by the usual set of Maxwell equations. The approximation of a self- consistent fields is typically used in plasma to

account for the multi- particle interactions and to neglect the right hand term. The charge- and the current density are then obtained from the zero- and first order moments of 1.15 (without the collisional term). This leads to the “Vlasov equation”, broadly used for kinetic description of the magnetospheric plasma. In the ionosphere however, where the binary collisions are important with both the charged- and neutral particles, the collisional term has to remain, to account for this.

The macroscopic quantities (the number density, the current, the pressure tensor etc.) are obtained from the moments of f in the velocity space. However, as follows from Equation 1.15, the expression for the moment of a given order depends on the higher order moment. Various approximations are then used to get the closed set of equations, relevant to a physical situation considered. In particular, assuming the local thermodynamic equilibrium for the plasma component α , the distribution is the maxwellian function:

$$f_{\alpha}(\vec{V}) = n_{\alpha} \frac{m_{\alpha}}{2\pi k_B T_{\alpha}} \exp \left[-\frac{m_{\alpha}(\vec{V} - \vec{V}_0)^2}{k_B T_{\alpha}} \right] \quad (1.16)$$

where n and \vec{V}_0 (i.e. density and bulk velocity) are the moments of the 0- th and 1- st order, respectively and T (temperature) is proportional to the 2- nd order moment. Only in the case of the maxwellian function, the distribution is fully represented by its moments (up to 2-nd order, as above).

Usually, the observed electron distributions are regular enough to be well approximated by some simple analytical functions, which allow to significantly reduce the description (e.g. the bi-maxwellian, with the different parallel- and perpendicular temperatures, or the loss-cone type distribution). In some situation however, some of the velocity moments may even lose their physical meaning. E.g. for the mixture of two counter-streaming maxwellian populations, the temperature or the average velocity have in general nothing to do with the real values and do not properly represent the real physical process (as an example, see Parks et al. 1999, [140] and references therein).

The non-maxwellian distributions of particles of the power- law type at higher energies are routinely observed in the magnetosphere. They can be often approximated by the so called “generalized Lorentzian-” or the “kappa” type function (first proposed in 1968 by Olbert [136] and by Vasyliunas, [201]). In the simplest, isotropic case it has the form:

$$f(V) = \frac{n}{(\pi W^2 \kappa)^{3/2}} \frac{\Gamma(\kappa + 1)}{\kappa(\kappa - 1/2)} \left(1 + \frac{V^2}{\kappa W^2} \right)^{-(\kappa+1)} \quad (1.17)$$

where V is the velocity, n - the number density, Γ is the Euler gamma function, and κ is called the “spectral index”. (see also Summers and Thorne, 1991, [192] for the extensions of this definition). The characteristic velocity W is related to the temperature T (the “true” thermodynamic temperature, see Treumann 1999, [197]) through:

$$T = \frac{mW^2}{2} \frac{\kappa}{\kappa - 3/2} \quad (1.18)$$

where m is the particle’s mass and $\kappa > 3/2$. The important properties of the kappa functions are that (i) for $V \gg W$ the function decreases as $v^{-(2\kappa + 1)}$, and (ii) that they approach the maxwellian with the same n and T for $\kappa \rightarrow \infty$.

Statistical studies performed in the plasma sheet by Christon et al. 1989, [29] and 1991, [30] provided the satisfactory approximations (by the kappa functions) of electron- and ion distributions, during the geomagnetically quiet- and disturbed periods. This kind of distribution was also found in several case studies at the boundaries of plasma sheet, in the magnetotail lobes (e.g.

Popielawska et al. 1993, [148]) or near the high- altitude cusp (e.g. Koperski et al. 2002, [95]) as well as in other astrophysical situations (see e.g Maksimovic et al. 1997 for the solar wind- /solar corona).

The physical mechanisms proposed, leading to development of the kappa distributions are generally related to the quasi-linear diffusion in a turbulent wave field (of a power law- type). It was first proposed by Hasegawa et al. 1985, [60] in a general form and further developed by others (e.g Miller and Steinacker 1992, [121], who considered the velocity- space diffusion due to the Alfvén- and the whistler mode turbulence). The results were applied in several domains: e.g. Schlickeiser 1997, [172] applied the formulas of Miller and Steinacker, [121], for the cosmic rays, Dendy et al. 1995, [38] used them for the auroral acceleration and Summers and Ma, 1999, [193] for the whistler- wave energization of magnetospheric electrons. In particular, the lower-hybrid- and the Alfvén wave turbulence were shown to be an effective mechanism of the electron energization compared to other diffusion processes. The dependence of the κ on the plasma- and the wave parameters has also been obtained in the simple cases.

These approaches though, gave no self- consistent explanation, because no feedback mechanisms were considered acting upon the waves. Only recently Treumann 1999 ([197] and [198]) provided the general, kinetic theory- based approach to explain such kind of distributions in case of the fully developed turbulence. In particular, he showed that the T parameter in Equation 1.18 is the proper “thermodynamic” temperature. In a slightly different way, based on non conservation of the entropy, Milovanov and Zelenyi 2000, [122] also obtained the similar results. Treumann 1999, [198] has also showed how the usual thermodynamic parameters have to be changed by including the κ (which still remains the “free parameter” to be set externally).

The conclusion is that the observed electron spectra of type of the generalized Lorentzian function can be thought of as the signature of the turbulent processes. In general, the more intensive turbulence, the lower value of the κ will be (“more non-maxwellian” distribution function).

1.3.2 Single particle motion

A convenient approach to investigate some aspects of the magnetospheric dynamics and configuration is to follow the movement of an individual, charged particle in a representative configuration of plasma and fields. This task can be often significantly simplified by applying the concept of adiabatic invariants (e.g. Kivelson and Russell 1995, [86] and references therein). Two adiabatic invariants of practical use are most frequently used: the magnetic moment μ , (called the “first adiabatic invariant” in context of dynamics of a charged particle) and the “longitudinal” invariant I (also called the “second”- or the “bounce” invariant), related to the movement between the mirror points in a converging magnetic field geometry. They are sketched in Figure 1.5. Accompanied by conservation of energy, E , this gives a useful set of equations:

$$E = \Pi + W_{\perp} + W_{\parallel} = \text{const.} \quad (1.19)$$

$$\mu \equiv \frac{W_{\perp}}{B} = \text{const.} \quad (1.20)$$

$$I \equiv \oint_{m1}^{m2} p_{\parallel} dl = \oint_{m1}^{m2} \sqrt{2 m W_{\parallel}} dl = \text{const.} \quad (1.21)$$

Here $\Pi = q\Delta\Phi$ is the energy in the electrostatic potential Φ (it can be generalized to an arbitrary potential energy), $W_{\perp} = mv_{\perp}^2/2$ and $W_{\parallel} = mv_{\parallel}^2/2 = p_{\parallel}/2m$ are the kinetic energies of the, respectively, perpendicular- and parallel (to \vec{B}) motions and $m1, m2$ are the mirror points.

The condition of applicability is a sufficient time- and space scale separation of the bounce- and the gyro motions from the larger scale processes under investigation. In particular, when μ is conserved, one can approximate the full particle’s motion by the motion of its gyrocenter i.e.

apply the “gyro-kinetic” approximation (Equation 1.1). In some situations, these conditions are not fulfilled simultaneously- e.g. they only hold on for one of plasma components and/or for one of invariants. There are also situations (e.g. in thin current sheets), where the two motions are not well separated one from another, and the above approach also breaks down.

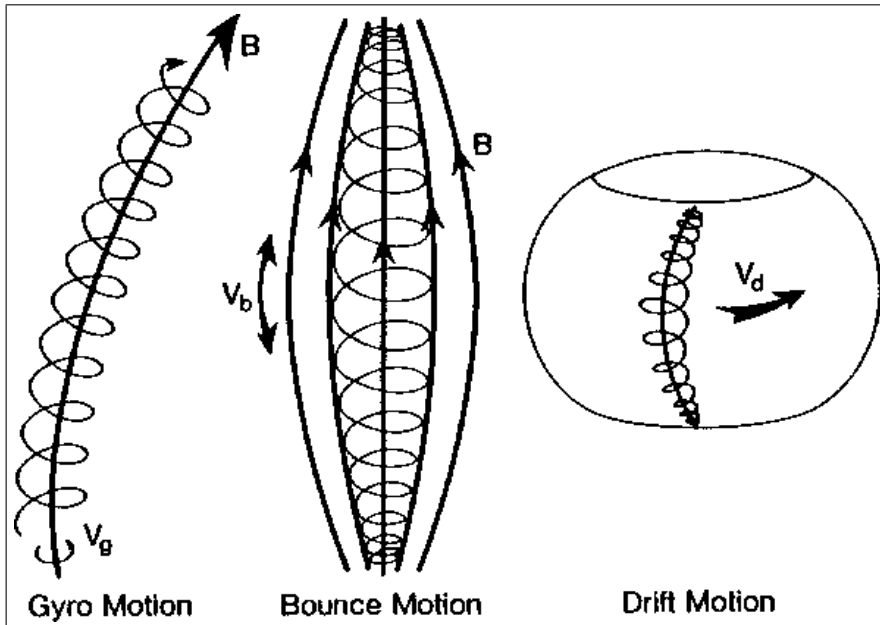


Figure 1.5: Sketch illustrating (not in scale) three types of periodic motion in the near- Earth magnetosphere, well separated in the time- and in the space scales: gyration around the field line, mirroring in the convergent magnetic field and drift around the Earth.

Two regions of applicability of this approach are referred below. The first concerns the converging geometry of the magnetic field in the auroral zone, with a field-aligned electric potential Φ . As follows from equations 1.19 and 1.20, a charged particle have the “effective” parallel potential energy: $\Pi + \mu B$. As it moves along \vec{B} between points S_1 and S_2 , the change of W_{\parallel} depends on the potential difference $\Delta\Phi$ and of ratio B_1/B_2 while W_{\perp} is proportional to B . This puts constraints on accessibility from S_1 to S_2 , if $B_1 < B_2$ - only a part of the source particle population would have enough amount of W_{\parallel} relative to W_{\perp} to reach the point S_2 . In terms of the pitch angle,

$$\Theta = \arctan(v_{\perp}/v_{\parallel}) \quad (1.22)$$

the accessibility condition for a particle (taking for simplicity $\Pi = 0$) is to have a velocity inside the cone limited by the pitch angle:

$$\Theta_{1,2} \leq \arcsin \sqrt{\frac{B_1}{B_2}} \quad (1.23)$$

In particular, the ratio B_1/B_2 between the equatorial plasma sheet and the ionospheric top is below 10^{-3} , yielding the limit below 1.8 deg. The appropriate region in the velocity space of the source population is called the “source cone”. In case of particles reaching the atmosphere (so lost from the system) it is called the (atmospheric) “loss cone”. In the absence of accelerating potential, only the very small part of the magnetospheric particles would reach the ionosphere (below 1/4000-th part in the case of an isotropic distribution). The following subsection summarizes some of the auroral acceleration processes, also invoking the role of the dispersive Alfvén waves for the time-dependent magnetospheric- ionospheric connection.

Bounce half period [s] (dipol, L=8 R_E)				
protons	1.0 keV	7.0 keV	30.0 keV	
$\Theta_{eq} = 2$ deg	600	227	109	
$\Theta_{eq} = 30$ deg	472	178	86	
electrons	0.1 keV	1.0 keV	10 keV	
$\Theta_{eq} = 2$ deg	44.2	14.0	4.4	
$\Theta_{eq} = 30$ deg	34.8	11.0	3.5	

protons: Gyroradius [km]				Gyroperiod [s]
B	1.0 keV	7.0 keV	30.0 keV	
5 nT	920	2434	5039	13.2
30 nT	153	405	840	2.2
electrons: Gyroradius [km]				Gyroperiod [s]
B	0.1 keV	1.0 keV	10.0 keV	
5 nT	6.8	21.4	67.7	$7.2 \cdot 10^{-3}$
30 nT	1.1	3.6	11.3	$1.2 \cdot 10^{-3}$

Table 1.1: Characteristic time- and length scales of gyro- and bounce motions (i.e. related to the first- and the second adiabatic invariants), for typical particles in the near-Earth magnetotail. (**Top**) Bounce half-periods (between two mirror points on opposite hemispheres) for the protons and the electrons in the model dipolar magnetic field, and two different values of the equatorial pitch angle Θ_{eq} . The energy values are the full kinetic energies. Note that: (i) a magnetic field line (so the bounce time) may be significantly longer than the dipolar in the real situation at distances above $\sim 8R_E$. (ii) for an energetic particle in a thin current sheet, the trajectory no longer follows the field line (non-adiabaticity) and the concept of the bounce period is meaningless; (**Bottom**) Gyroradii and gyroperiods in the neutral sheet and in the outer plasma sheet ($B = 5$ nT and 30 nT respectively). The energy values correspond to a strictly perpendicular movement.

Another application of gyro-kinetic approximation concerns the near-Earth plasma sheet (Subsection 1.3.4). For the typical particles in the near-Earth magnetotail, the characteristic time- and length scales are listed in Table 1.1. The “bounce period” of protons (in the upper part of the table) is comparable to- or longer than a typical substorm- related dipolarization (a few minutes- Section 1.4). This evidences the meaning of the non-adiabatic ion acceleration at a substorm onset. Significant parallel electric fields that can develop then, will easily influence the electrons. Another length scale is the thickness of the neutral sheet, where the magnetic field weakens and where the cross-tail current concentrates. This thickness is often small enough to destroy the first adiabatic invariant of energetic particles. The similar conditions are met close to the reconnection X line, expected in the magnetotail at the substorm onset (see Section 1.4).

A useful quantity to organize the adiabatic/non-adiabatic dynamics of a particle in the tail-like magnetic field is the parameter χ (Büchner and Zelenyi in 1989, [20]). It is broadly known as the “kappa”, κ , but this name is used here for the power law index of generalized Lorentzian function). It is defined as the square root of the minimum curvature radius of a field line to the particle’s maximum gyro-radius, or:

$$\chi = \sqrt{\frac{qLB_n^2}{mvB_{lobe}}} \quad (1.24)$$

where q , m , v are the particle’s charge, mass and velocity, B_n and B_{lobe} are magnetic field in the current sheet and in the lobe, and L is the length scale of changes of tangential component of \vec{B} across the current sheet (see lower panel of Figure 1.9). It was introduced to consider the chaotic orbits of charged particles (but was also used earlier by e.g. Sergeev et al. 1983 [174]). For $\chi > \sim 3$ the particle motion is saving the magnetic moment, but the dynamics becomes more complex when this condition does not hold (see below).

In the rest of this section, regarding the broadly used terminology and wishing to avoid confusion, I will use the term “adiabatic” only to denote the conservation of the magnetic moment.

1.3.3 Auroral particle acceleration

Summary of observations

There is the evidence of acceleration of charged auroral particles along the field lines. The keV range, precipitating electrons are routinely observed at low altitudes in the auroral region, in structures called “inverted-V events” and in collimated beams (McIlwain 1960, [70]; Frank and Ackerson, 1971, [50]) Their spectral characteristics suggest parallel (to \vec{B}) acceleration in the U-shaped potential structures. The satellite- observed parallel currents, stronger than expected, yielded further indication of the parallel acceleration (e.g. Zmuda et al. 1966, [210]). Finally, direct measurements confirmed the existence of the parallel electric field in the auroral zone (Mozer et al. 1980, [125]). These results evidenced the existence and meaning of the parallel electric field (not allowed in the ideal MHD model, see Equation 1.6) in auroral and magnetospheric processes.

More recent observations from the satellites DMSP, Viking, Freja, Astrid-2 and FAST have added many important informations on the fine scale structures and FAC below- and in the acceleration regions, at altitudes up to $2 R_E$ (see e.g. Lundin and Eliasson 1991, [112]; McFadden et al. 1999, [45]; Marklund and Karlsson 2001, [117]). The observations of the POLAR satellite, in turn, allowed to sketch the field-aligned current- and the potential structures up to 3 to 4 R_E (e.g. Janhunen and Olsson 2000, [77]; Mozer and Hull 2001, [126]; Hull et al. 2003, [67]) (see right panel of Figure 1.4).

The picture arising is very rich in details, mostly out of scope of this work. Some most important facts are listed below:

- The ionospheric auroral forms (including parallel electric fields and currents, as well as discrete aurora) are observed in very structured regions- the length scales span the range

of 1000 - 0.1 km. Bright, discrete auroral forms are located in regions of upward directed FAC (carried by the precipitating electrons). The up- and down-going FAC regions are interchanged, with the downward FAC coinciding with the dark auroral regions ;

- The acceleration seems to occur at altitudes of $\sim 0.5 - 3.0 R_E$, and is the most intensive at 1 - 2 R_E . In large scales ($\sim 10^3$ km length), and in the lower part ($\sim 4 - 11 \cdot 10^3$ km altitude) it corresponds to the field aligned electrostatic potential drop of 1-10 kV (see e.g. McFadden et al. 1999, [45] and references therein);
- At small scales, the acceleration region is organized in localized pulses of type of electrostatic solitary waves and double layers (Mozer et al. 1980, [125]; Temerin et al. 1982, [195]; Ergun et al. 1998, [43]; McFadden et al. 1999, [45]; Catell et al. 2001, [21]; Hull et al. 2003 [67]). These small scale potential structures can be of weak- ($q\Delta\Phi < kT_e$) as well as of strong type ($q\Delta\Phi \sim kT_e$; T_e being the electron temperature). The corresponding electric field amplitudes are of a few mV/m , up to hundreds mV/m and the parallel length of structure may be as small as 1 km at low altitudes;
- No significant, wave-induced pitch-angle scattering is observed between the magnetospheric source and the acceleration region, that would isotropize the electron distributions and populate the loss cone (Kletzing and Scudder 1999, [87]). Dynamics of electrons is dominated by adiabatic behavior (i.e. the gyro-kinetic approximation holds) on large scales. There are however observations of smaller scale ULF- and faster wave processes (e.g. the Auroral Kilometric Radiation, AKR), highly structured and closely related to localized current- and precipitating particle features;
- Electron distribution functions have a non-thermal character and various types of energy- and pitch angle distributions. In particular, the “horseshoe” distributions are observed at low altitudes in association with the AKR bursts (Strangeway et al. 2001, [191]), two-component, field-line accelerated distributions (“inverted-V”) are typical in the upward FAC regions while more narrowly field-aligned and the less energetic “Supra-Thermal Electron Bursts” often accompany the small-scale dispersive Alfvén waves. Finally, the up-going electron conics, beams and other features are detected in the downward FAC regions (see e.g. Lundin and Eliasson 1991, [112] and references therein). The accelerated electrons can carry significant energy flux towards- and from the ionosphere (comparable to the wave Poynting energy flux, Chaston et al. 2002, [23]);
- Although the structure of the lower part of auroral field lines (below $\sim 11 \cdot 10^3$ km altitude) is relatively well known, the region above is not. In particular, it is still not sure if and how far towards the equatorial plane extends the acceleration region and if it is U-shaped or O-shaped (see e.g. Janhunen and Olsson 1998 [76] and compare two panels of Figure 1.6). Similarly, it is not sure what kind of processes in the magnetospheric “generator” are exactly responsible for the substorm-related auroral phenomena.

There is the long lasting and still active debate on details of the auroral particle acceleration, and many models has been proposed. E.g. Borovsky 1993, [17], discussed 22 different theoretical mechanisms to explain fine structures (below ~ 1 km) of auroral arcs (which appeared to be the main discriminating criterion).

The FAC in the absence of an external accelerating potential can emerge due to e.g. a thermal spread of velocities of ionospheric and magnetospheric plasma (the thermoelectric current) or as the effect of the pitch angle scattering by waves. In particular, the whistler mode noise has been shown to provide the loss-cone filling in the near-Earth region (Kennel and Putsches 1996, [83]; Johnstone et al. 1993, [79]). Simple estimates for the representative plasma parameters give a current of a few $0.1 \mu A/m^2$. Such values are comparable to those observed on the quiet time,

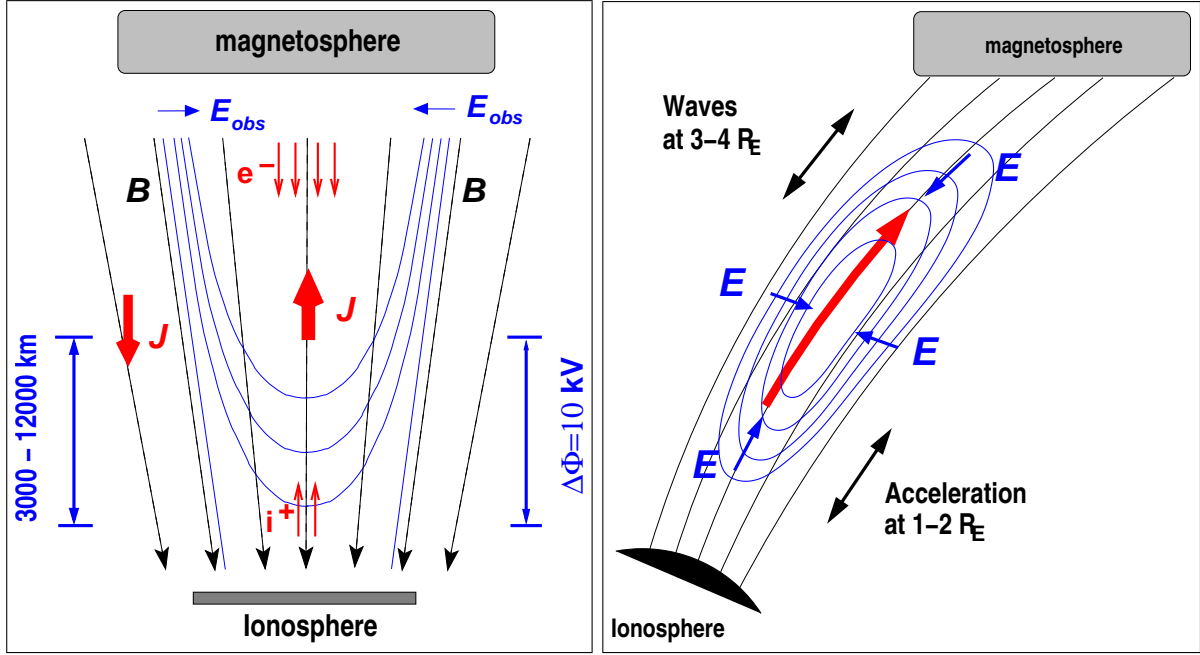


Figure 1.6: (Left) The auroral U-shaped acceleration region, based on low- altitude satellites observations. (Right) The “cooperative model” of the O-shaped potential- and the wave acceleration.

diffuse auroral arc, but typically are an order of magnitude too low for the discrete aurora in the upper FAC regions.

“Kinetic orbit” model of parallel auroral current

The role of the large scale, parallel electric field was recognized in the approach referred to as the adiabatic- or the kinetic orbit description (Knight 1973 [90]; Chiu and Schultz 1978, [28]). It was to treat the acceleration region as the quasi-stationary potential structure and has led to development of the so called “current-voltage” and “energy flux- voltage” relations for the auroral field lines (see below). The dynamics of a charged particle is governed by adiabatic equations 1.19 and 1.20. Including the electric potential and introducing the “mirror-ratio”, $\zeta = B_I/B_M \geq 1$, where B_I and B_M is the magnetic field strength in the ionosphere and the magnetosphere, one can express the condition of accessibility of a particle from the magnetospheric source to the ionosphere, as (e.g. Böstrom 2003, [18]):

$$W_{\parallel M} > \max \begin{cases} (\frac{\zeta_M}{\zeta} - 1) W_{\perp M} + \Pi_M - \Pi(\zeta) \\ 0 \end{cases} \quad (1.25)$$

for: $1 < \zeta < \zeta_M$

As pointed out by Böstrom 2003, the role of the mirror force is essential for creation of a potential drop associated with the field-aligned current, but is not properly included into the fluid description. Taking the distribution functions of the involved plasma populations α , $f_\alpha(E, \mu)$ depending on the above constants of motion, one gets the net current through the acceleration region as the sum of the 1-st moments of the distribution functions:

$$j_{\parallel} = \sum_{\alpha} q_{\alpha} \iint_{A_{\alpha}} v_{\parallel} f_{\alpha}(E, \mu) \quad (1.26)$$

The integration is over the regions A_{α} in the phase space, allowed by the accessibility conditions of type of 1.25. By Liouville theorem, only the boundary distributions (ionospheric and

magnetospheric) are involved in the formula, i.e. the particles passing through both edges of the acceleration region (the electric potential well or hill, in the upward- or the downward FAC region, respectively).

Knight 1973, [90], used this approach for the ionospheric- and the magnetospheric particles of maxwellian distributions. The result was the relationship between the potential drop- and the current flowing along the field line. Lundin and Sandahl 1978 [111], calculated in the similar way the energy flux of precipitating electrons. These current-voltage and energy flux-voltage relations was then used by Lyons 1980 [113], to model the large scale, steady state inverted-V structures in two dimensions. Pierrard 1996, [141], considered so called “kappa”-type distribution function. This model was then corrected and extended for energy flux by Janhunen and Olsson 1998 [76] and independently by Dors and Kletzing 1999, [39], who also applied it in the model of Lyons ([113]), using the finite values of the mirror ratio, ζ . Finally, Böstrom 2003, [18] and 2004, [19] pointed out the importance of the proper choice of the potential- and the space charge structure along B (discussed also to a lesser extend by Chiu and Schultz 1978, [28], and Khazanov et al. 1998, [85]). Böstrom also pointed out the importance of an adequate mirror ratio and provided the current-voltage formulas for different model distribution functions, f_α .

Applying equation 1.26 to the upward FAC one can, as the first step, neglect the ionospheric ions (as heavy and difficult to accelerate upward) as well as the ionospheric electrons and the magnetospheric ions (due to the potential barrier). Then for the maxwellian magnetospheric electrons:

$$j_{\parallel}(\Phi) = -qn_M \left(\frac{T}{2\pi m_e} \right)^{1/2} \zeta_M \left[1 - (1 - 1/\zeta_M) \exp \left\{ -\frac{q\Phi}{T(\zeta - 1)} \right\} \right] \quad (1.27)$$

where n_M and T are the density and the temperature of the magnetospheric population and Φ is taken as zero in the magnetosphere. In this formula, called the “Knight relation”, the dependence on the magnetic field enters only through ζ and the electric potential- only through the difference Φ between the ionosphere and magnetosphere. It is in general the nonlinear formula for j and Φ , which saturates at high- and low values of Φ . Under the often met condition that

$$1 \ll \frac{q\Phi}{k_B T} \ll \zeta_M \quad (1.28)$$

it reduces to a large-scale “kinetic Ohm’s law”

$$j_{\parallel, I} = K \Phi \quad (1.29)$$

where

$$K = \frac{q^2 n_M}{\sqrt{2\pi m_e k_B T}} \quad (1.30)$$

As analyzed by Chiu and Schultz 1978, [28], Khazanov et al. 1998, [85] and Böstrom, 2003 [18] and 2004 [19], the above approach essentially depends on the distribution of Φ along the field line. Earlier analyzes usually took assumption of a simple distribution of $\Phi(\zeta)$, mostly monotonic, which allowed to neglect the particles trapped between the potential barrier and the mirror point. As shown in these works, the inclusion of a non-monotonic potential or a quasi-neutrality condition leads in general to one or several discontinuities of potential along the field line and to the nonanalytic formulas for current-voltage and energy flux-voltage relationships.

Influence of the Alfvén waves on parallel currents

Another common approach to describe parallel currents points out the role of Alfvén waves . In the framework of the current circuit- model, the acceleration and/or the generation regions are modified by, or follow from, the Ultra Low Frequency (ULF) wave influence (e.g. Lysak 1990, [114]; Vogt 2002, [204]).

The key point is that the Alfvén waves carry the parallel electric field when the short perpendicular wavelengths are included. This field is time changing and disappears in the steady state. The ideal MHD approach is inappropriate here and, e.g., the two fluid model can be applied instead. Leaving in the generalized Ohm’s Law 1.5 respectively the polarization term (proportional to $\partial \vec{j}/\partial t$) or the pressure terms ($\propto -\nabla p_e$) one gets, for the isotropic electrons, two limits of practical importance (see e.g. Lysak 1990, [114]; Vogt 2002, [204]; for the discussion and further references). The “inertial regime”, where the wavelengths are comparable to the electron “skin depth” $\lambda_e = c/\omega_{pe}$, corresponds to a cold plasma (where the thermal velocity of electrons v_{Te} is much below V_A), as e.g. in the ionosphere. Here:

$$\mathcal{E}_{\parallel} = \frac{k_{\parallel} k_{\perp} \lambda_e^2}{1 + k_{\perp}^2 \lambda_e^2} \mathcal{E}_{\perp} \quad (1.31)$$

where ω_{pe} is the electron plasma frequency. In the “kinetic regime”, the effects of finite ion gyroradius and of the electron pressure become important ($v_{Te} \gg V_A$ as e.g. in the case of magnetosphere):

$$\mathcal{E}_{\parallel} = -\frac{k_{\parallel} k_{\perp} \rho_s^2}{1 + k_{\perp}^2 \rho_i^2} \mathcal{E}_{\perp} \quad (1.32)$$

where $\rho_s = \rho_i \sqrt{T_e/T_i}$, ρ_i is ion gyroradius, T_e and T_i are electron- and ion temperatures (see e.g. Lysak 1990, [114]).

The single- (i.e. the electron-) fluid model of acceleration was applied by Ronmark [156], who obtained the parabolic dependence of current on voltage (instead of linear in 1.29). Similar result followed from the, basically kinetic, model of Wright 2003 ([206] and references therein), who considered, due to large mirror ratio, only strictly parallel moving electrons. Acceleration of electrons by Alfvén waves propagating downward from the magnetosphere was also confirmed by the numerical simulations for the realistic conditions below the acceleration region (e.g. Kletzing and Hu 2001, [88]; and Chaston et al. 2002, [23] for the observations of FAST and Andersson et al. 2002, [5] for Freja). This kind of acceleration was shown to be able to generate the so called “Supra Thermal Electron Bursts” (STEB) of a few hundred eV observed on borders of the Upward FAC region.

The above “Alfvén wave-” and the “quasi-stationary” models of parallel auroral currents and acceleration need not necessary exclude one another. The bounce period of $\sim 1 keV$, parallel streaming electron on an auroral field line is a few seconds while a typical wave period- few dozens of seconds or more, so the wave electric field can be seen by the electrons as a quasi-steady structure. The model of Janhunen and Olsson 2000, [77], of an O-shaped field-aligned potential structure, based on the Polar satellite observations, also tries to connect the two approaches. In this model, the potential barrier, localized below about 3 - 4 R_E and closing the “O shape” at the magnetospheric end, is accompanied by waves, which can accelerate the particles and allow them to access the acceleration region below.

Recent observations show also the importance of even faster processes, as the lower hybrid- or the electron cyclotron waves, in forming the localized potential structures (e.g. Ergun et al, 1998; McFadden et al. 1999, [45]; Cattell et al. 2001) or in the AKR generation (Strangeway et al. 2001, [191]; deFeraudy et al. 2001, [48]). These processes, when considered in large scale, all have the predominantly electrostatic character.

Whatever model of the auroral acceleration applied, the proper recognition of the magnetospheric source plasma is of great importance for further analysis. There is however almost no observations providing the appropriate information. Shiokawa 2000, [183] compared low altitude inverted-V particle spectra with the representative AMPTE- mission data from the plasma sheet. He fitted the DMSP data by streaming maxwellian and used the typical moments of distribution function routinely collected by AMPTE. The results showed that the magnetospheric source population is not that from the equatorial plane and that acceleration is accompanied by heating.

However the plasma sheet data were not directly related to low altitude data observed and the moments of distribution function provided too poor information on the plasma. Recently, at the final stage of data analysis in the large scale, done in this work, Vaivads et al. 2003, [200] reported the conjugated Cluster/DMSP, high- and low altitude crossing of outer edge of the plasma sheet. Their results gave the first possibility to check consistency of high altitude measurements with the (linearized) Knight relation. Observed plasma- and electric field properties were in accord with the quasi-stationary, U-shaped potential in the acceleration region (but not the O-shaped, of Janhunen and Olsson [77]). This potential could, for the reported crossing, be related to an Alfvén wave of ULF frequencies and wavelength of $\sim 100R_E$, the energy of which was mainly converted into acceleration of electrons.

The Interball Tail observations presented in this work, of electrons at the moment of substorm onset from the near-Earth plasma sheet (so in the region different than in case study of Vaivads et al. 2003, cited above), are an important new input for the above considerations.

1.3.4 Adiabatic- and non-adiabatic effects in the nightside plasma sheet

As discussed above, the observed auroral particle precipitation requires the energization and/or the pitch angle diffusion to occur on magnetic field lines. Several mechanisms have been proposed to fill the loss cone and to ensure such precipitation. E.g., whistler mode noise has been shown to provide the loss-cone filling in the near-Earth region (Kennel and Petschek 1966, [83]; Johnstone et al. 1993, [79]). This mechanism, proposed as being responsible for the diffuse aurora, is however not sufficient for the localized and non-stationary aurora during substorm.

As the time of the magnetic field dipolarization at substorm onset is very short (a few minutes), Mauk proposed the convection surge mechanism to bounce- and to field-line accelerate the ions, through the violation of the second adiabatic invariant (see Mauk 1989, [119] and references therein). He showed that the field-aligned potential drops of few keV can be generated. Considering the non-adiabatic effects (in the sense of the magnetic moment) of a particle movement in the cross-tail current sheet, Delcourt et al. 1990, [35] demonstrated even larger energization rates. Non-adiabatic effects have also been considered an efficient mechanism scattering the pitch angles and filling the loss cone (Sergeev et al. 1983, [174]; Chen and Palmadesso 1986, [25]; Büchner and Zelenyi 1989, [20]; Delcourt et al. 1990, [35] and 1996, [36]).

The low energy particles in the magnetotail current, and the energetic particles in the nearly dipolar magnetic field close to the Earth, fall into regime $\chi > 3$ (see Equation 1.24). This is where the guiding center approximation can be used (Equation 1.1 above). Two another regimes exist and were intensively analyzed: the chaotic ($\sim 3 > \chi > \sim 1$; see e.g. Büchner and Zelenyi 1989, [20]; Delcourt et al. 1996, [36]; and references therein) and the “current sheet” (also called the quasi-adiabatic or the “Speiser-type”: $\chi \ll 1$, see e.g. Speiser 1965, [189]; Sergeev 1983, [174]; Chen and Palmadesso 1986, [25]). In this case, depending on initial parameters, a strong energization- and/or magnetic moment scattering may occur.

Although these works concerned the positively charged ions, the general considerations apply to the electrons as well. Because of much smaller gyro-radii of electrons, however, the conditions for the electrons to behave non-adiabatically are less easily met. Simple estimation of thickness of a model current sheet (defined as in Büchner and Zelenyi 1989, [20]) necessary for a 10 keV electrons to behave chaotically passing through it ($\chi = 2$) gives the value below $0.2R_E$ (note also that χ scales as the fourth root of energy, so the condition weakly depends on it). In particular, the adiabatic description allowed to successfully model the observations of energetic electrons near- and inside the geostationary region, for both quiet conditions and substorm injections (see the references in Section 3.4.1). Also the features of the electron distribution functions observed in the plasma sheet boundary in the magnetotail were successfully modeled using the adiabatic description (e.g. Onsager et al. 1990, [138]). On the other hand, studying the satellite data,

Pulkkinen et al. 1992 ([152]) showed that in some cases in the distant magnetotail the field line curvature is so high, that the adiabatic approximation is violated even for the electrons.

Several studies were dedicated to analyze the particle's motion in a two dimensional magnetic field geometry, such as formed near the reconnection X line (e.g. the review paper of Chen 1992, [24]). In particular, Martin and Speiser 1988, [118] found the non-adiabatic effects near the X line resulting in a characteristic “ridge” structure in the ion distribution function. Smets et al, 1996, [184] repeated the analysis of Martin and Speiser 1988, [118] for the electrons, finding the similar feature near the reconnection line. Calculations by Schriver et al. 1998, [173], Smets et al. 1998, [185] and more recent simulations of Hoshino et al. 2001, [65] showed that the non-adiabatic effects near the reconnection line in the magnetotail influence the ion- and the electron spectra.

Smets et al. 1999, [186] modeled the electron dynamics following the magnetic field dipolarization during substorm in the near magnetotail, away from the reconnection region. Their results successfully reproduced the pitch-angle distribution changes of 10 keV electrons observed by Interball Tail. The observed features followed from the adiabatic evolution of both, betatron- and Fermi- type (i.e. saving the first- and the second invariant respectively). Sergeev et al. 2001, [181] studied bi-directional electron distributions observed by APMTE/IRM in the plasma sheet, between 10 and 15 R_E . The observed flux anisotropy was interpreted in terms of the plasma bubbles of limited extent related to impulsive reconnection in the tail and convecting earthward. Their observations were consistent with the adiabatic transport modeled by Smets et al. 1999, [186].

The conclusions from the above is that in the near magnetotail ($|X| < \sim 15R_E$), away from a reconnection site, the electrons of energies up to above 10 - 15 keV behave in general adiabatically, i.e., saving their magnetic moment. Moreover the longitudinal invariant is also conserved, except for the fast magnetic field reconfiguration, e.g., near a substorm. This conclusion is true as long as the influence of waves is negligible, but the observations show that this is often the case except for the substorm onset and similar events.

In the near-equatorial plasma sheet, between 6.6 and 8.8 R_E (i.e. on auroral field lines) Klumpar et al. 1988, [89] found two events of field-aligned, counter-streaming electron fluxes. They were observed at low energies (about 0.1 to 2.0 keV) and have a short duration (a few minutes). Johnstone et al. 1994, [80], reported similar features at 0.1 to 1.0 keV, observed inside the geostationary orbit on CRRES. They noticed the similarity to Supra-Thermal Electron Bursts (STEB) at low altitudes and suggested the field-alignment to result from the $\partial B/\partial t$ acceleration at the substorm onset. They showed however no details of electron spectra nor the relation of their observations to substorm activity. Roux et al. 1991, [160] observed the field-aligned low-energy electron fluxes in geostationary orbit during the growth phase of the substorm, abruptly disappearing at the onset. The observations supported the cross- tail current being disrupted at the substorm onset by a ballooning-type instability.

Perraut et al. 2000, [143] and [144] gave further interpretation of this and similar events in terms of the current- driven Alfvén waves. It was closely related to the shielding field-aligned electric field fed by the electrons below ~ 500 eV, as shown by LeContel et al. 2000, [32].

These observations are important regarding the electron dynamics presented in this section. Such field aligned anisotropy in the near plasma sheet can appear due to some short-scale acceleration processes and not as a “quiet time” effect. The existence - and the possible role of such processes in the near magnetosphere is essential to understand the magnetospheric dynamics and for the substorm models (see Section 1.4 below).

1.4 Elements of dynamics of the Earth's magnetosphere

I review below the selected phenomenological aspects of the large- scale magnetospheric dynamics.

1.4.1 Magnetospheric activity

The observations evidence changes of the magnetosphere and the ionosphere in the broad range of time- and space scales. These changes can often be interpreted as the elements of the sequence: loading- transformation- dissipation of energy, driven by both the solar wind- and the internal mechanisms. The most important features, commonly related to the magnetospheric activity are:

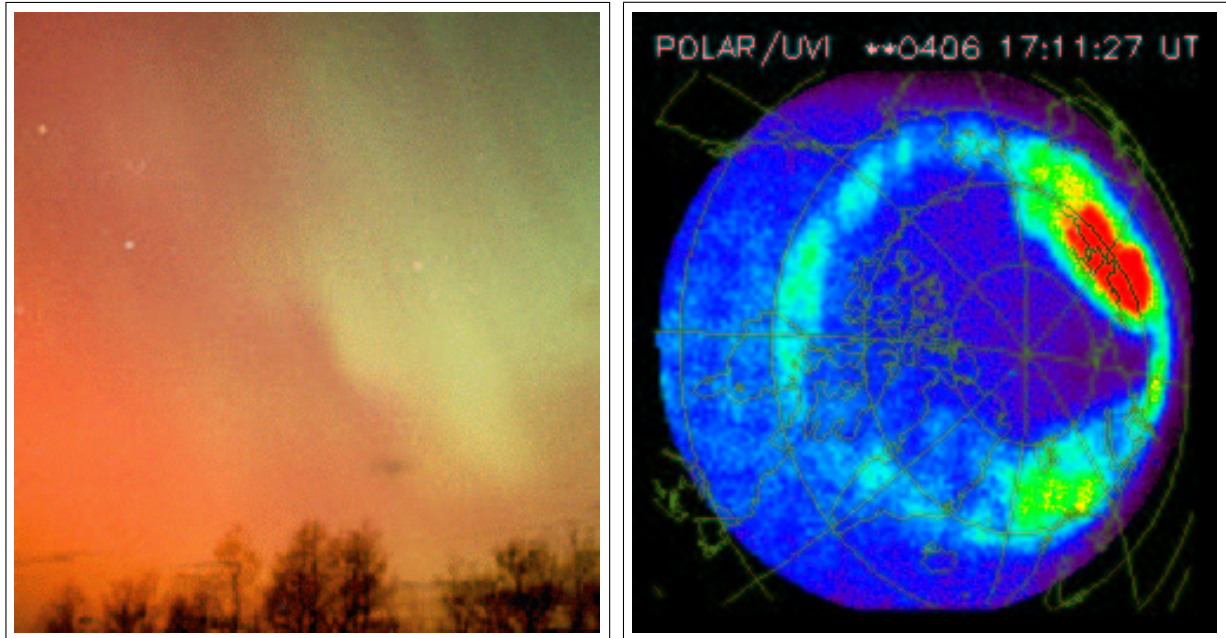


Figure 1.7: Two examples of aurora on 06 April 2000. (Left) observed on the ground, in the visible range. Three colors are seen- light- and dark- red and green, depending on the altitude (i.e. on different atmospheric components being excited, which dominate at different altitudes); (right) observed by the Polar satellite in the ultraviolet range (the colors are false).

- Intense and structured optical phenomena (Aurora) in the sub-polar region, called the auroral oval and located around the magnetic poles in the ionosphere, at heights 80 - 250 km. They result from excitation of atmospheric atoms and molecules by (mainly) electrons moving along the magnetic field lines. The auroral oval is located on the closed field lines and is the geomagnetic projection of the plasma sheet down to the ionosphere. Aurora of the regular, diffuse form are permanently observed, but become structured and intensive during the “disturbed” conditions, mainly in the night sector (see Figure 1.7). The features are actually observed not only in the visual- but also in the UV-, infrared-, radio- and soft X ranges of electromagnetic spectrum.
- Changes of the magnetic field observed on Earth (the most intensive in the auroral zone). They are related to dynamics of the auroral electrojets, the field-aligned currents and the ring current. There is a rich collection of the magnetic features, observed as e.g. the “magnetic bays” and the different classes of “pulsations” (1 - 1000 mHz).
- The injections of the hot plasma and the energetic particles observed in the geosynchronous region or closer (see the upper panel of Figure 1.8).
- The magnetic field dipolarizations in the geosynchronous region, occurring on time scales of a few minutes (see lower panel of Figure 1.8).

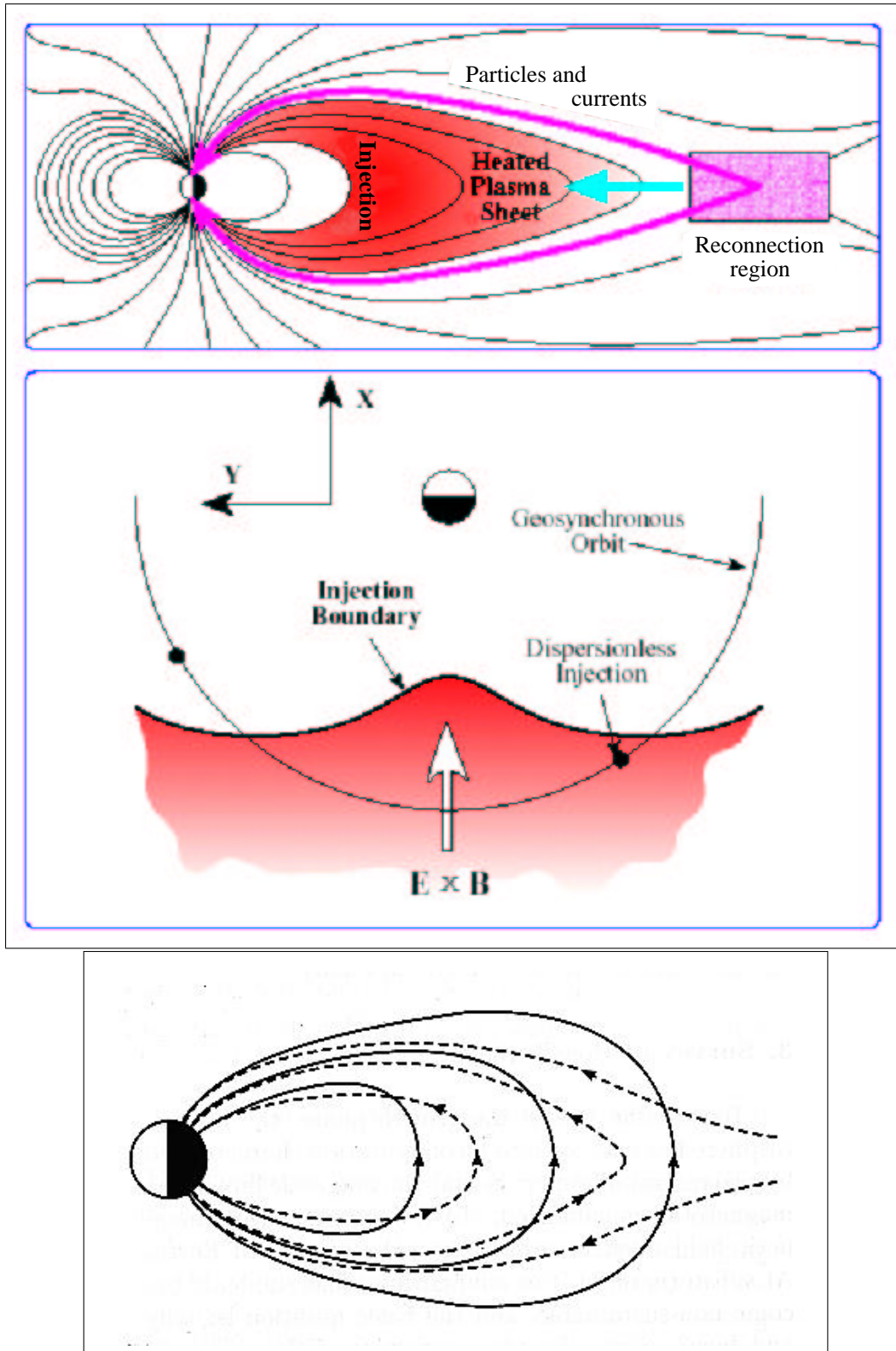


Figure 1.8: Illustration of the dynamics of the magnetosphere: (Upper) Acceleration in the close vicinity of the reconnection line in the near magnetotail results in the intense field-aligned particle fluxes towards the Earth (at the boundary of the Plasma Sheet). Further from it, the relaxing magnetic field lines and the induced electric field result in the earthward injection and heating of plasma. It is seen, near the geostationary orbit, as the nearly dispersionless convection front. (after: Reeves 1998 [155]), (Lower) Stretched- and dipolarized (dashed and solid respectively) magnetic field lines in the near Earth- and the middle magnetotail- the meridional cut.

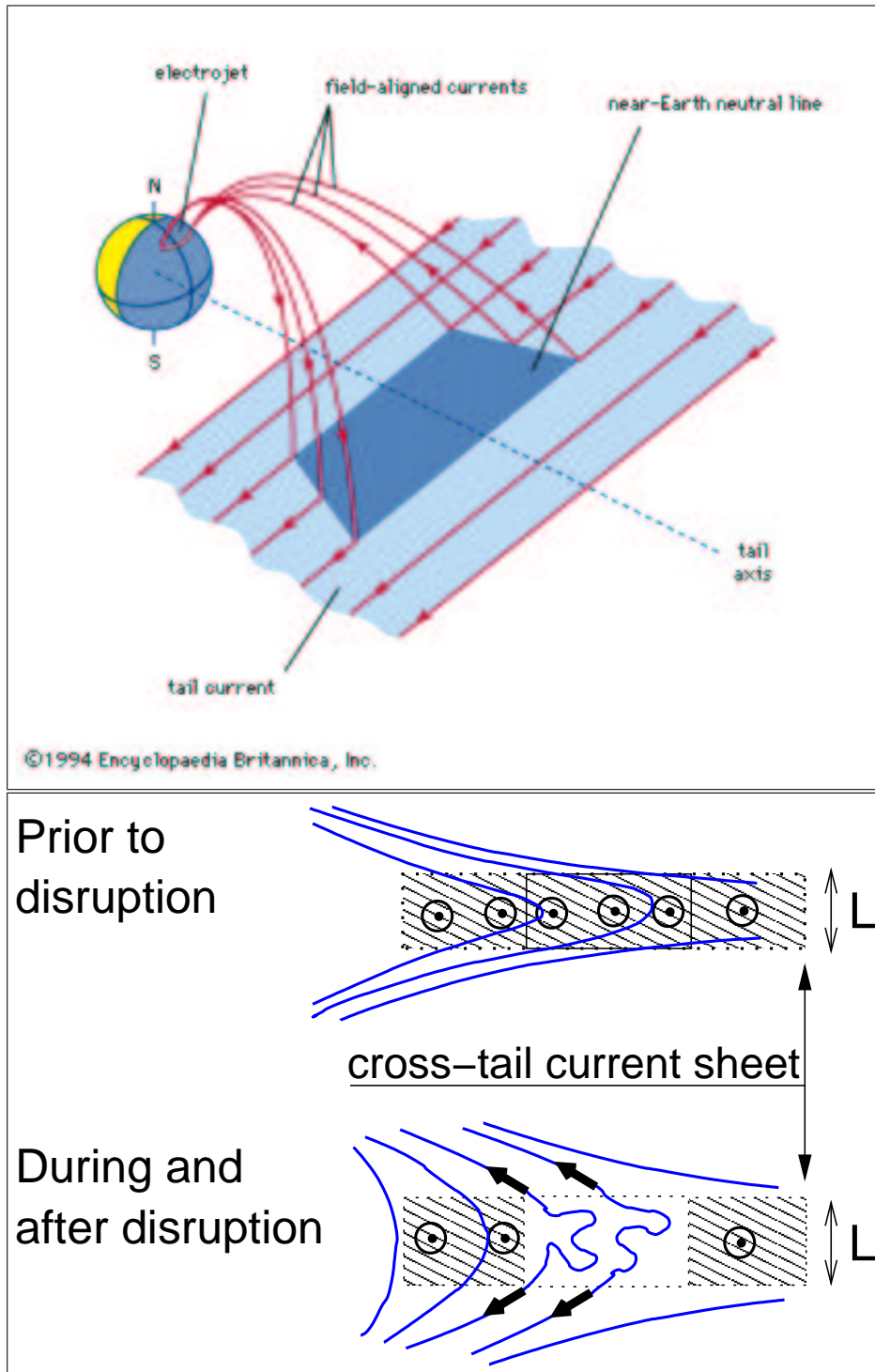


Figure 1.9: Sketch illustrating the substorm-related current disruption: (Upper) The field aligned currents, the cross-tail current and the current wedge in the magnetosphere; (Lower) The cross-tail current is partially disrupted and diverted towards the ionosphere through the field-aligned currents (black arrows). The current system is closed by the substorm electrojet in the ionosphere and the upward, field-aligned current in the pre-midnight sector (not shown).

- Short scale (~ 10 min), intense flow enhancements in the nightside magnetosphere (called the Bursty Bulk Flows, BBF's) at distances above 10 - 15 R_E . Antisunward- directed tailward of $\sim 30R_E$, they are more often earthward-directed at closer distances (see the references related to the NENL model of substorm in Subsection 1.4.4 below).
- The plasmoid formation, i.e. fast, tailward plasma flows (few hundreds km/s) in the plasma sheet, with the specific magnetic signatures (north-to-south turning) and total pressure enhancements (e.g. Hones et al, 1984 [64]; Ieda et al. 1998, [68]). Originating at 20-30 R_E , they are observed up to more than 200 R_E in the tail, in correlation with (and delayed to) the onset of a substorm (see below).

Geomagnetic indices

Several signatures has been selected to routinely monitor the level of geomagnetic activity. Because of the global nature of the involved phenomena, they can express the dynamics of the magnetosphere, even if obtained only from the ground-based data. On the other hand, different physical processes involved result in time delay between different signatures used to monitor the same global phenomena. The indices used in this work, are listed below and the motivation for the use is given in Chapter 2.

- The AU, AL, AE, called the “auroral electrojet indices” are obtained from a number (usually above 10) of stations distributed in local time in the latitudes typical for the northern auroral zone. For each station, the northern (H) component of the magnetic perturbation is recorded. The superposition of all the data allows to determine the lower- and the upper envelopes of the H disturbances. The former, called the AL gives the measure of individual strength of westward flowing electrojet, while the second, AU (after the “upper”) - the measure of eastward electrojet. The difference, AU-AL, called the AE, provides a measure of the overall horizontal current strength (compare Figure 1.3).
- The Kp index is obtained from the magnetometer stations at mid-latitudes. When the auroral zone expands equatorward, these stations can record the effects of the auroral electrojet current system as well as of the ring current and field-aligned currents that can connect it to the ionosphere. This describes so-called magnetically disturbed periods. The Kp index utilizes both northward (H) and eastward (D) component perturbations. It equals the logarithm of the largest excursion in H or D over a 3-h period, placed on a scale from 0 to 9.
- The Dst index is obtained hourly from magnetometer stations at low latitudes away from the equator. At such latitudes the H (northward) component of the magnetic perturbation is dominated by the intensity of the ring current. The Dst is the direct value of the hourly average of this perturbation. Large negative perturbations indicates increased intensity of the ring current and typically appear on the time scales of about an hour. The decrease of intensity may take much longer, on the order of tens of hours. The entire such period is called a magnetic storm (see below).
- Ground-based Pi2 pulsations are not strictly speaking an index, but the quasi global occurrence of their bursts near the substorm onset or intensification made them a useful tool (even though it should be used with care- e.g. Olson 1999; [137]; Liou et al. 2000, [100]; Kepko and Kivelson 2001, [84]). Related to field-aligned currents and field line resonances excited by transient flows in the near magnetosphere, they are confined to a narrow local time range at middle- and at high latitudes and may help to localize the westward traveling surge. On low latitudes in turn, they are not localized, and were used as a global indicator

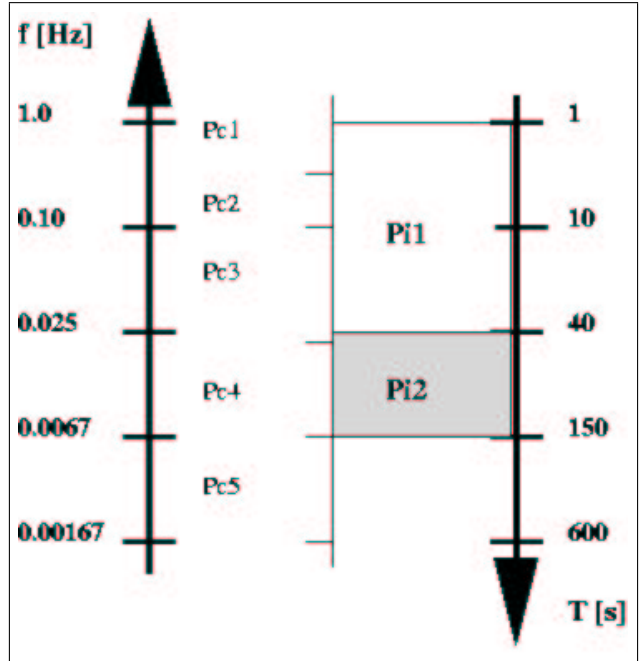


Figure 1.10: Frequency range (left axis) and time range (right axis) of the most frequently used geomagnetic pulsations of regular type (Pc) and of impulsive type (Pi). The magnetic field data used throughout this work allow for the analysis in the Pc5, Pi2 and (for the Interball observations) Pc3 range (see Chapter 2).

of the magnetic activity. To give the reference for the ongoing use, Figure 1.10 shows the time and frequency range of some of geomagnetic pulsations.

Based on observations, two kinds of disturbances from the average conditions are usually identified: first, called the magnetic- (or magnetospheric-) storm and another, the magnetospheric substorm.

Magnetic storms are the most intensive events and have the longest duration (up to several days). There are related to energy transfer from the solar wind/IMF during a period of enhanced convection or a sudden, abrupt change of the solar wind dynamic pressure, e.g. related to the solar coronal mass ejection. The essential is that, visibly driven by the solar wind conditions, the energy input leads to intense and long lasting intensification of the ring current. Three phases of a magnetic storm can be identified: (i) the initial phase, lasting from minutes to hours, when the ring current weakens (the Dst index positively increases) and the dayside magnetosphere is compressed, (ii) the main phase, continuing up to several hours, during which the ring current intensifies (the Dst become more negative) and the enhanced cross-tail current moves earthward, (iii) the recovery phase, which can last up to a week, during which the energetic particles trapped in the ring current are slowly lost due to various processes and the ring current weakens (the Dst index become less negative).

There are controversies about the relationship between storm and substorm (which was thought of as the “elementary disturbance” of the magnetosphere- see below). In the “classical” picture, a storm builds up of sequence of substorms, according to usual observations (and this is the former source of the term “substorm”). According to some other, recent works, the substorm expansion phase (see below) contradicts the storm development, and the global energy flow in the system (solar wind- magnetosphere- ring current) may differ in the case of a substorm and of a storm (see e.g. Gonzales et al.1984, [58]; Iyemori and Rao, 1996, [73]).

1.4.2 Magnetospheric substorm

This phenomenon is usually thought of as the “elementary disturbance” of the magnetosphere. Three phases of such disturbance were identified.

Substorm phases

- **The Growth Phase** starts the substorm. When the IMF turns southward, it enhances the magnetospheric convection and input of the energy from the solar wind through the merging and reconnection of the magnetic field. The field strength in the tail increases (e.g. McPherron, 1972; [146]) as well as the cross- tail current (Kaufman, 1987 [82]). The field lines near the Earth become more stretched and the plasma sheet become compressed (e.g. Fairfield et al., 1981 [46]; Nagai et al., 1997 [127]). In the ionosphere, the quiet auroral arcs drift equatorward and the polar cap region expands, according to increased tail diameter (e.g. Rostoker 1980, [157]). The increased convection usually corresponds to intensive auroral convection- electrojets. This phase lasts about one hour.
- **The Expansion phase** of a single, separate substorm lasts about 30 min., but the fine structures and the multiple intensifications (see below) can prolong it up to above 1 hour. It starts with the so called onset or breakup, when the aurora suddenly brightens and starts expand poleward from the most equatorward located, diffuse arc. Ground magnetometers show magnetic bays related to intensive substorm electrojet and the bursts of Pi2 type pulsations. Field-aligned currents and precipitating charged electrons, generating the discrete auroral forms, also produce bursts of auroral kilometric radiation (AKR) and soft-X radiation in auroral region. The features in the near-geostationary region are injections of hot plasma and magnetic field dipolarizations, as sketched in Figure 1.8. Further downtail, fast flows (BBF) are observed and release of the plasmoid takes place (see below).
- **The Recovery phase** is when the magnetosphere is slowly returning to its pre-substorm state. Plasma sheet recovers and the substorm electrojet starts to fade. The auroral forms stop their poleward expansion and, after stagnation of 10 to 20 minutes, retract and / or degenerate. This phase lasts of one to two hours.

Fine structures

Both the storm and the substorm are global phenomena, where the whole system (magnetosphere, ring current and ionosphere) is involved. The observations evidence also, that the substorms are in turn composed of the shorter events, possibly not of the global nature, but more localized.

The class of “microsubstorms” or “intensifications” has been identified with a duration of 5 to 10 minutes and a recurrence of 10 to 20 minutes (see e.g. Rostoker et al. 1980, [157]; Sauvaud et al. 1987, [167]; Sergeev et al. 1986, [175], 1998, [178] and 1999, [179]), as step like and localized intensifications of the auroral bulge and of the electrojet. Spatially localized plasma jets with an azimuthal extent of 1-2 h were observed inside the auroral plasma sheet during enhanced convection periods and during substorm expansion phases (e.g. Sauvaud et al. 1999, [171]; Sergeev et al. 2000, [180]).

A typical, localized feature is a “pseudobreakup”, often observed before the expansion phase onset. It has some characteristics similar to that of the substorm, except that is weaker, it does not start on the equatorward edge of the aurora neither expand poleward, but first of all it does not develop into a global scale feature (e.g. Rostoker, 1998, [158], Aikio et al. 1999, [1]). Indeed, more detailed analysis have shown (e.g. Rostoker, 1998, [158]; Aikio et al. 1999, [1] and references therein) that there is no typical low scale delimiting a substorm from the pseudobreakup.

Another class of even shorter structures has been found for the substorm, called “injectionlets” or “Impulsive Dissipation Events”. Typically with a duration of 1 minute and 1 - 3 min. recurrence, they were identified both in the auroral arc and in the geosynchronous injections- fine structure (Belian et al. 1984 [10]; Sergeev et al. 1998, [178]).

Observations of multi-scale magnetospheric activity have led to the first multi-scale model of substorm (e.g. Sergeev et al. 1996, [177] ; Lui 2001a, [108] and references therein) and to apply

the ideas of Self Organized Criticality (SOC) to the magnetospheric dynamics (see e.g. Chapman and Watkins 2001, [22] and references therein). These fascinating and promising ideas still need some amount of development and more better observational support.

1.4.3 Driving by the solar wind

The main driving factor in the ionosphere- magnetosphere- solar wind system, is the variability of the solar wind parameters: density, velocity, strength and direction of the magnetic field (IMF), fluxes of energy etc.

Contrary to early, long term observations, it has been found (Akasofu and Chapman 1963, [2]) that there is no correlation between the kinetic energy flux available in the solar wind, ρV^3 , and the energy dissipation rate in the magnetosphere, U . (The measure of such dissipation rate is the summary effect of intensities of the ring current, of the particle precipitation in the auroral region and of the auroral currents of the electrojets.)

Considering the electromagnetic energy flux in the solar wind and taking into account the orientation of the IMF controlling the efficiency of the reconnection, the simple models of the energy transmission rate to the magnetosphere can be constructed. Based on the observations, Perraut and Akasofu (see Akasofu 1980, [4] and references therein) have shown that the dissipation rate, U , correlates well with the parameter

$$\epsilon = \frac{1}{\mu_0} V B^2 L_0 \sin^4 \frac{\Theta}{2} \quad (1.33)$$

, where Θ is the polar angle of IMF projected on the plane perpendicular to the Sun-Earth line and L_0^2 represents the effective cross-section of the magnetosphere ($\sim 50R_E^2$). This correlation holds for ϵ above $\sim 10^{19} \text{erg}/\text{sec.}$, the minimal level of influence. Several other, systematic attempts have been performed to determine the degree at which the solar wind parameters control magnetospheric activity as well as the principal parameters playing the role (see e.g. the introductory review in Chapter 13.4 of Kivelson and Russell [86] and references therein). The conclusion is that the magnetosphere- solar wind coupling is, first of all, of the electromagnetic nature. Large volume of observations and of theoretical works support the basic role of magnetic field line merging and reconnection between the solar wind and the magnetosphere for such coupling.

The magnetosphere, driven by the external source and by its own internal dynamics, can reach the steady state with no substorm observed (the “steady magnetospheric convection”). It follows from observations for long lasting solar wind conditions with steady southward oriented IMF (Yahnin et al. 1994, [208]). This would suggest that the state of the magnetosphere is driven externally. The solar wind, however, does not fully control the magnetospheric dynamics. E.g. applying the solar-wind data- based linear prediction models to analyze the magnetospheric activity works well for the D_{st} index but can explain less than half the variance in the AL index (McPherron et al. 1988, [147]). The onset of the substorm expansion phase is the most unpredictable event in such analysis.

1.4.4 Phenomenological models of substorm

While the overall features of substorm are rather well recognized, there are still considerable controversies about their sequence and the cause-effect relationships. Substorm models that try to organize the huge amount of observations and related physical mechanisms are usually divided into two or three main branches, referred below.

Near-Earth Neutral Line model

This model (abbreviated as NENL) invokes magnetic reconnection in the middle magnetotail, at 10 - 20 R_E (so is used also the Mid-Tail Initiation model, MTI), to form the neutral line and

inject plasma earthward and tailward. It was proposed initially by Coppi et al. in 1966, adapted by E. W. Hones Jr. in 1973, [62], and more recently refined by Baker et al. 1996, [8]. The inflow of magnetic flux into the magnetotail, after the southward turning of the interplanetary magnetic field (IMF), results in the intensification of the cross-tail current and the thinning of the tail current sheet (at the growth phase). At the final stage of the growth phase, the current sheet becomes so thin that the ion movement become non-adiabatic (the curvature radius of the magnetic field lines become comparable to ion Larmor radius). The ions no longer carry the cross tail current (the “resistivity” of the medium increases), which helps the reconnection process to develop along the X-type neutral line in the tail (at the onset of the expansion phase). Tailward from the X-line, the region of hot plasma and closed, O-shaped magnetic field lines appears, disconnected from the Earth (the plasmoid). The magnetic tension and the plasma pressure pushes it out in the anti-solar direction, where it is lost. On the Earth’s side, strong acceleration of particles near the magnetic X- line and the magnetic tension lead to injection of hot plasma in the geostationary region (see Figure 1.8), dipolarization of the magnetic field and to precipitation of particles into the atmosphere in the auroral latitudes.

Analyzes of GEOTAIL observations (Nagai et al. 1998, [128]; Machida et al. 1999, [115]; Miyashita et al. 2000, [123]) recently provided new support for this model. Around the onset, fast tailward convection flows (Bursty Bulk Flows, BBF, after Angelopoulos 1994, [6] are observed in the tail mostly outside $15 R_E$, while fast, earthward convection flows are observed exclusively inside $30 R_E$ from the Earth. This suggest that the neutral line forms between $15 R_E$ and $30 R_E$. Furthermore, cross-analyzes of low latitude Pi2 bursts and of BBF showed that bursty fast flows often precede Pi2 (e.g. Shiokawa 1997, [182]; Machida et al. 1999, [115]; Miyashita et al. 2000, [123]). BBF also precede the auroral AKR intensifications (Fairfield et al. 1999, [47] as well as the UV auroral activations and the geosynchronous dispersionless energetic particle injections events (Nakamura et al., 2001, [129] and [130]; Liou et al., 2001, [101]). It has also been shown, that the onset of low latitude Pi2 often follows the UV signatures of auroral breakups (Liou et al., 2000, [100]). Moreover, for localized auroral activations, the occurrence of flow bursts before auroral activations is uncertain (Nakamura et al. 2001, [129]). Difficulties in establishing the relation between the above features and the substorm onset come from the fact that the impulsive midtail flows and the near-Earth current disruptions occupy different locations of the magnetotail. This has been explained for certain cases by the “flow-braking” (or “pile-up”) variant of the NENL model (see below).

Tail Current Disruption model

Here, the cross-tail current disruption in the near-Earth region coincides with the substorm expansion (because of this localization, it is also called the Near Geostationary Onset model, NGO, or the Near Earth Initiation model). The main difference to the NENL model is the order and the generation mechanism of the sequence: current disruption-neutral line formation-hot plasma injection and dipolarization. The expansion phase starts because of development of the thin current sheet in the near- Earth plasma sheet (between 15 and $7 R_E$ or even closer). An instability leads to the cross-tail current disruption and redirection of the current system through the ionosphere, along the field lines.

The TCD model was initially proposed by McPherron et al. 1972, [146] and further developed by e.g. Lui (e.g. Lui 1990 and 1996, [104] and [106]). Auroral breakups, initiated at the most equatorward auroral arc (e.g. Akasofu 1968, [3], Rostoker et al. 1980, [157]; Friedrich et al. 2001, [56]) and observations of field line resonances (Samson et al. 1992, [164]) suggested the near-Earth initiation of auroral processes. Energetic particle- and magnetic field observations (e.g. Takahashi 1987, [194]; Sauvaud and Winckler 1980, [165]; Lopez et al. 1990, [102]; Lui et al. 1990, [104]; Roux et al 1991, [160]; Ohtani et al. 1992, [133]) have shown a sudden decrease in the cross-field current. Accompanied by strong low frequency magnetic turbulence bursts, it

coincides with the expansion phase onset, observed in situ at distances as close as $7 R_E$. These bursts were interpreted as the signatures of the cross tail current disruption in the near plasma sheet. The region of the current diverted to/from the ionosphere along the field lines, was observed to propagate tailward (Jacquey et al. 1991, [74] and 1993, [75]; Ohtani et al 1992, [133]) and to induce the formation of a neutral line further downtail (e.g. Sauvaud et al. 1996, [169]). Also more recent multi-point observations with the CRRES and POLAR data (e.g. Erickson et al. 2000, [44]; Frank et al. 2000, [52] and 2001, [53]) are consistent with the TCD model. The scenario proposed is based on instabilities of the thinned cross-tail current sheet and several specific mechanisms were considered (see e.g. the recent review of Lui 2004, [110]). The localized current disruption can destabilize the current in adjacent locations by momentary thinning of the plasma sheet. This can in turn lead to further local current intensification and disruption. The model thus explains the global character of phenomenon by the domino effect.

Flow- Braking model

This model was recently proposed by Shiokawa on the basis of the multi-point observations of the AMPTE and ground based data (Shiokawa et al. 1997, [182] as well as on numerical simulations (e.g. Birn and Hesse 1996, [12]. It aimed to explain the difficulties of the NENL model in establishing the relationship between the BBF and the near-Earth signatures of a current disruption at substorm onset. According to this model, the earthward flowing plasma jets (resulted from neutral line/lines located at 20-30 R_E) reach the near-Earth region separating the tail-like elongated field lines from dipole-like lines. Increased pressure gradient in this region accompanied with magnetic field configuration leads to flow diversion towards the flanks and increase of magnetic field. The diverted and slowed-down flow induces the field-aligned current system (substorm current wedge) and compression impulse propagating earthward. The inertial current generated by this mechanism last only as long as the flow burst, i.e., a few minutes, so strictly speaking, concerns only the initial phase of the substorm development (e.g. Birn et al. 1999, [14]). There are observations where such explanation does not hold even for the initial substorm development, which is the consequence of the non-MHD processes (e.g. Lui et al. 1999, [107]; Ohtani et al. 2002, [135]).

Ballooning instability and related mechanisms

Several substorm-initiation models were developed, which propose different mechanisms of instability, not always well fitting into the above classification scheme (NGO vs. MTI). Just to mention, these are, the Magnetospheric-Ionospheric Coupling, the tearing mode instability and others- further details, references and more comprehensive comparison can be found elsewhere (see e.g. the reviews in the June 1996 issue of *Journal of Geophysical Research*, dedicated to substorm models: of Baker et al., [8]; Lui, [106] and others; Ohtani 2001, [134]; Lui 2001b, [109]; or more recent reviews of Lui 2004, [110] and Cheng 2004, [27]).

One of quite general mechanisms is the ballooning instability, sketched in Figure 1.11. It was identified in substorm studies in the near-geostationary region (e.g. Roux et al. 1991, [160]; Cheng and Lui 1998, [26]; and Erickson et al 2000, [44]). The conditions of its generation were then analyzed several times (e.g. Horton et al. 1999, [66]; see also recent review of Cheng 2004, [27] and references therein). It arises as quasi-electrostatic drift waves, in the high β plasma (β is the ratio of thermal-to-magnetic energy) in the presence of density- and magnetic field gradient. Such conditions arise in the near-Earth edge of the current sheet during the growth phase of substorm. The drift waves develop in association with the gradients and the cross-tail current (see Figure 1.11): the azimuthal drift of particles in the more dipolar region is faster than further tailward and the differential drift polarize the medium. The polarization electric field $\delta\vec{E}$, resulting in $\delta\vec{E} \times \vec{B}$, tends to further destabilize the wave (as sketched in the right panel of Figure 1.11). The

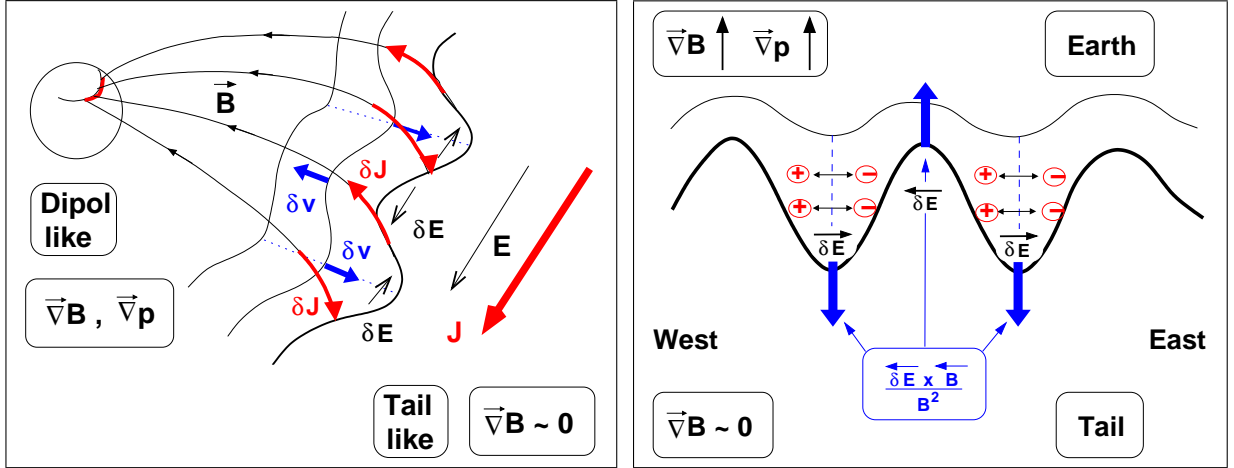


Figure 1.11: Sketch illustrating the development of the ballooning mode instability. The disturbances in the cross-tail current generate the wave in the near-Earth neutral sheet. The cross-tail drift of particles in the density- and magnetic field gradients there, is stronger than in the tail-like configuration further down-tail. This results in the disturbed electric field δE , destabilizing the wave (see the right panel). The magnetic field-aligned currents (left panel, red) can support the charge neutrality, acting against the growth of instability.

important elements are the field-aligned currents (left panel of Figure 1.11)- providing the charge neutrality, they shield electric field δE , acting against the wave growth.

Stability of this mechanism depends crucially on the structure of the equilibrium magnetic field and compressibility of plasma, as well as on the frequency range considered. In particular, Roux et al. 1991, [160] considered $\beta \sim 1$ and the Pi2 frequency range and Holter et al. 1995, [61] identified them as the ballooning mode in the thin current sheet. Higher frequencies were considered by Horton et al. 1999, [66] and Cheng and Lui 1998, [26] considering in addition the high beta situation ($\beta > \sim 10$). The detailed quantitative discussion of these mechanisms exceeds the scope of this work. One clue issue, as pointed out by Cheng 2004, [27] is that to properly consider stability of the ballooning mode, it is necessary to take account for the kinetic and nonlocal effects, such as the dynamics of trapped particles and the bounce-averaged properties of the medium, the parallel electric fields, the wave-particle resonances etc.

The related mechanism concerns the self consistent description of the electric field in the near-Earth plasma sheet. Assuming the quasi-static situation ($\omega < k_{parallel} V_A$, where $k_{parallel}$ is the parallel component of the wave vector and V_A is the Alfvén velocity) and requiring the quasi-neutrality, LeContel et al. 2000a, [31] and 2000b, [32] found the large scale electrostatic potential, that can significantly influence perpendicular (to \vec{B}) transport of plasma in the near-Earth plasma sheet. They also found (LeContel et al. 2000b, [32]) the field aligned potential that develops for the small, nonzero electron-to-ion temperature ratio, typical for the plasma sheet ($\sim 0.1 - 0.2$). Not stronger than a few hundreds eV, this parallel potential difference was proposed to accelerate the electrons and support the field-aligned currents due to differential electron-ion drift. The effect is essentially nonlocal, including the large-scale, bounce-averaged response of plasma to external forcing (e.g. from the solar wind). Perraut et al. 2000a, [143] and 2000b [144] discussed the possibility to destabilize such parallel currents by the current-driven Alfvén waves near the Pc1 frequency range. The influence of this mechanism on the plasma transport in the near-Earth plasma sheet was then discussed by LeContel et al. 2001, [33]. In particular, it can influence the ballooning-mode waves, as concluded also by Erickson et al. 2000, [44] for the set of observation on CRRES satellite.

Chapter 2

Data sources and the instruments.

This work would not be born without the Interball mission in general, and without the MIF-M - and the ELECTRON experiments on-board the Interball Tail satellite in particular. Throughout this work, I'm also using the data from many ground-based magnetic observatories as well as the data from several other satellites. In this chapter I briefly describe the Interball mission, the instruments and the data used. The electron pitch-angle data were not routinely available, so I developed the method to obtain them from the MIF-M data and to include them to the existing ELECTRON database. Similarly, the use of multiple ground based magnetic data required the small database to be developed and implemented.

2.1 Interball mission and instruments

The objective of the mission was to investigate the details of the energy-, the momentum- and the mass transfer in the critical regions of the solar wind- magnetosphere system with the use of multiple satellites. The mission fleet consisted of four spacecrafts- two closely spaced pairs on different high-altitude orbits. Each pair was the main satellite and the smaller, less equipped sub-satellite.

The Interball mission was initially planned to be launched in early 80's as the former INTER-COSMOS agency project. It was already a relatively old project during its operation phase (since August 1995). The more distant pair of satellites, the Interball Tail, was launched on 3 August 1995 on the elliptical orbit inclined 62.8 degrees to the ecliptic plane with the (initial) perigee of 776 km and the (initial) apogee of 192000 km ($30.1 R_E$). The second pair of satellites, the Interball Auroral, has been launched on 29 August 1996. Its orbit, with the apogee of $3R_E$, was inclined (62.8°) and passed over the auroral region.

The main satellites were the Prognoz type spacecraft, relatively slowly spinning (nearly 2 minutes rotation period) with the spin axis directed towards the Sun (within 10 degrees). The sub-satellites, MAGION-4 and MAGION-5 were less equipped and followed the main spacecraft trajectory, separated by hundreds- to several thousands of kilometers in the case of the Tail pair. Schematic view of the Interball Tail main satellite, with its scientific payload is sketched in Figure 2.1.

This work is based on the data provided by some instruments of the main Interball Tail satellite. The data were registered before the Interball Auroral has been launched and I am not using the sub-satellite data neither. In the following, I will be using the term "Interball", "Interball Tail" or "IT" having in mind the main spacecraft of the Interball Tail pair. The principal informations on the instruments used are given below. More information about the mission can be found in: *INTERBALL Mission and Payload* (see [168] or [92]) and in the dedicated issue of *Annales Geophysicae* of May 1997 (see [170] or [93]).

Despite its several limitations, mainly the low telemetry rate and the slightly out of date

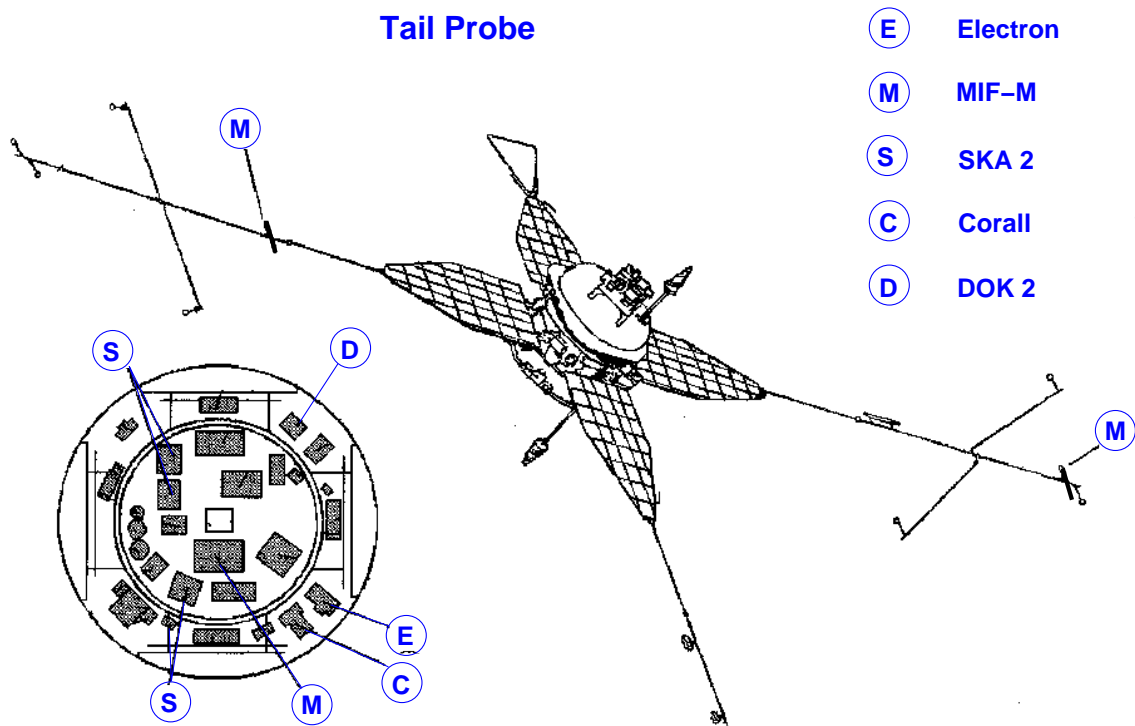


Figure 2.1: Schematic view of The Interball Tail main satellite and its scientific payload. Only some of the instruments are marked.

instrumentation in some cases, the Interball mission was still able to provide many new and important observations. Some can be found in, e.g., the issues of *Annales Geophysicae* (May 1997), *Czechoslovak Journal of Physics* (April 1999, [161]) or *Advances in Space Research* (2002, [16]) dedicated to the results of the Interball mission.

2.1.1 ELECTRON experiment

The low energy electron spectra from the Interball-Tail satellite has been obtained with the ELECTRON experiment (the P.I. was Dr. Jean-André Sauvaud from the CESR in Toulouse, France). The experiment provided the 3D measurements of the electron distribution function in the energy range 10–26000 eV. The instrument used, the top-hat electrostatic analyzer, consisted of 8 detectors (of 6 by 22.5 deg. field of view) covering together 180 deg., sunward- to- anti-sunward angle of view along the satellite spin axis.

The analyzer was principally the same as, e.g., the one successfully used on-board the AMPTE/IRM spacecraft, i.e. allowing for 360 deg. field of view, but the satellite's geometry forced the use of half of its field of view. This is sketched in Figure 2.2

As the result, the 3D (4π solid angle) spectrum could be obtained only after the full, 120-seconds satellite rotation. However, the analyzer gives one full energy spectrum from 8 detectors spanned over a half- plane with much better resolution. This allowed for the fast registration of the electron spectra in the reduced range of pitch angles. Details on pitch-angle calculations are explained below in Section 2.3.

In the mostly used working-mode, the above energy range was sampled in 32 logarithmically spaced steps, simultaneously for all 8 detectors in nearly 3.75 s (32 times during one satellite spin period). In other working modes also used here, the 16 energy levels and/or 16 measurements per

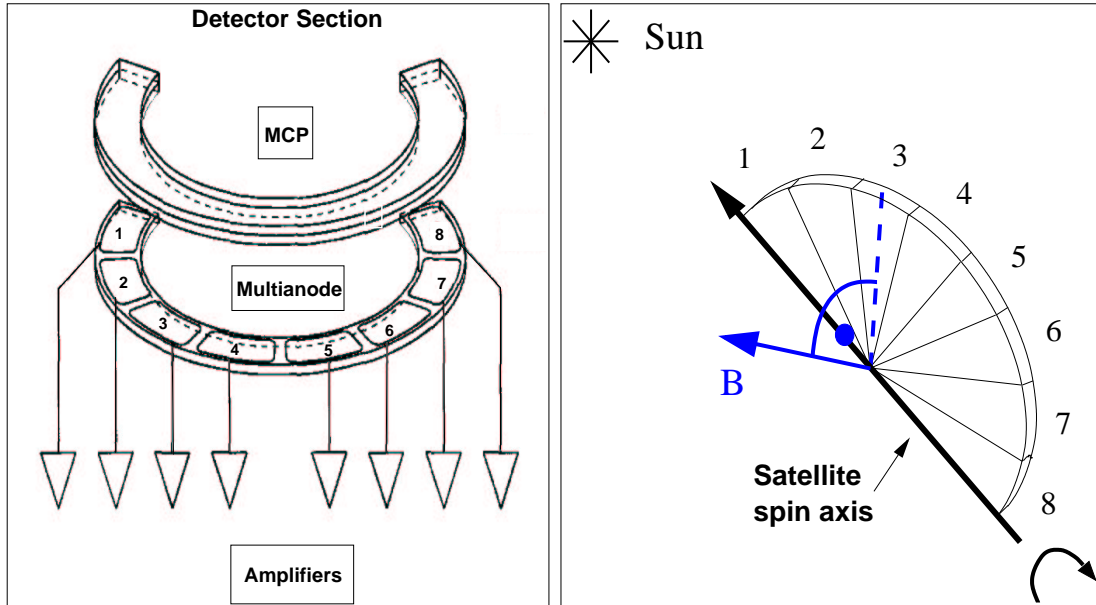


Figure 2.2: . (Left) Schematic view of detector part of the ELECTRON instrument, with the microchannel plate, the multi-anode and 8 amplifiers. (Right) The instrument mounted on the satellite can be effectively represented by the sectorized half-plane with the detectors. The satellite's axis of rotation (black line) points towards the Sun. The instantaneous magnetic field is marked in solid blue, and the in-plane direction perpendicular to B (dashed blue) falls into the field of view of the 3-rd detector. No detector is looking at this moment along/opposite to B . Under condition of gyrotropy, other detectors observe the electrons differing only by the pitch angles.

spin was also been performed.

Finally, the spectrometer could scan, depending on the working mode, three slightly different energy ranges. Other informations on the ELECTRON instrument can be found in Sauvaud et al. 1997, [168], and (together with the first results of observations in the low latitude boundary layer) in Sauvaud et al. 1997, [170].

2.1.2 MIF-M magnetometer

The magnetic field data were provided by the MIF-M magnetometer, a part of the ASPI (Analysis of Spectra of Plasma waves and Instabilities) experiment on-board the main IT satellite. It consisted of the fluxgate- (BD-3 instrument) and the search coil sensors (performing one component AC measurements), the block of analogue electronics with filters, the filter bank, the A/D converter and the DC/DC converters. See Klimov et al. 1997, [92] and Klimov et al. 1997, [93] for more details on the MIF-M instrument and the ASPI experiment. (The P.I. of the instrument was Dr. S. Romanov from SRI in Moscow, Russia).

The MIF-M DC data have been used throughout this work in two ways- as the main source of the magnetic field and to calculate the instantaneous pitch angle distributions of electrons. Especially for the second aim, the MIF-M data replaced the another magnetometer, the FGM-I, that the ELECTRON instrument was developed to work closely with but which suffered from some working problems and was not being used to this aim. Mainly the 1 or 4 second. resolution data has been used to get the pitch angle distributions (see below for more details) and the 0.25 sampling rate data has been used only (if they existed) to get the ULF magnetic spectra.

2.1.3 Other Interball Tail data used

At the initial stage of data analysis, the Key Parameters (the data with reduced amount of information and low time resolution, prepared without the indepth error analysis) have been used to better identify the substorm-related plasma injection events. Also in the case study of the substorm of 13 January 1996 (see Chapter 3, Figure 3.9), the Key Parameters from two IT experiments has been used . The use of these data was not crucial for the results presented in two last chapters.

The Key Parameters from the following experiments were used, accessed from the Interball KP web page (for more informations see *INTERBALL Mission and Payload*, e.g. [168] and dedicated issue of *Annales Geophysicae*, May 1997, e.g. [209]):

- DOK2: energetic electron- and proton spectrometer in the energy range 20 keV to 1 MeV;
- SKA-2: the energetic particle-, mass and composition spectrometer in a wide energy range 50 keV to 150 MeV;
- CORALL: the ion- 3D, energy-per-charge analyzer in the energy range 0.03 to 24.2 keV.

2.2 Other spacecraft data

One of main difficulties in the magnetospheric research is the necessity to perform the observations in different locations simultaneously, to get the necessary global information on the plasma medium. To get the necessary information and to make the relevant analysis possible, in many cases, I used the data from several other satellites.

2.2.1 Geostationary and low-altitude satellite data

The satellites in the geosynchronous region provided the important information on the substorm related processes in the magnetosphere, Data accessibility and continuous time coverage allowed to easier identify the substorms.

Los Alamos geostationary satellites

The SOPA instrument data were used here in some cases to trace the injections of the energetic particles in the geostationary region. The injections of energetic particles were also routinely used as signatures of a possible substorm at the initial stage of the data selection. The data in the first 7 energy channels (50 to 750 keV for the electrons, 50 to 1200 keV for protons) were being mainly used. The location of the satellites is fixed in the Local Time. For the events considered in this work, the data from three LANL satellites were used, namely 1990-095, 1991-080 and 1994-084. Unfortunately, the spacecraft are not equipped with the magnetometer.

NOAA GOES geostationary satellites

For purposes of this work, the GOES-7 and GOES-8 satellites provided the 1-minute resolution magnetic field, the 5-minute averaged, differential fluxes of high energy electrons and protons and the 1-minute X ray fluxes. The data were accessed through the NGDC Space Physics Interactive Data Resource (SPIDR) Internet site at <http://spidr.ngdc.noaa.gov/spidr/>.

DMSP satellites

The low orbiting satellites of the Defense Meteorological Satellite Program provides a useful, information on the precipitating particles in the auroral zone (the instruments J4, IES) as well as the visual- and the infrared range images of the Earth (the OLS instruments). Each DMSP satellite has a 101 minute, sun-synchronous, near-polar orbit at the altitude of 830 km and the polar regions are covered at least twice per day. The available data set was searched for the information related to the observed Interball features. In this work, the visual-range images were used as an important, additional information on the auroral activity in two cases. They were provided by the OLS instrument, collecting the images across a 3000 km swath perpendicular to the satellite's trajectory footprint.

2.2.2 Other satellite data

WIND satellite

WIND was launched on 1st November 1994. The principal aim of the mission was to provide the information on the interplanetary medium (plasma-, energetic particles-, magnetic field- and wave-observations). Its orbit was ecliptic, reaching the distances of the Moon. Contrary to Interball, it is a relatively fast-rotating spacecraft (3 second spin period, with the axis perpendicular the ecliptic plane). It has 8 experiments on-board, mainly composed of multiple instruments. In this work, I used the data from two experiments : the magnetic field (3 or 49 second averaged) from the MFI (Magnetic Field Investigation, Lepping et al. 1995, [97]) and the EESA and PESA, the low energy-, electrostatic electron- and proton analyzers from the 3-D Plasma experiment (Lin et al. 1995, [98]). The energy range is of about 0.08 to 27.08 keV for PESA and 0.14 to 27.66 keV for EESA, divided in 15 log-spaced energy levels.

Other resources

It has to be pointed out that many other publicly available Key Parameter- and definitive data from different satellites have been searched for the features that would shed a light on Interball observations. These were the IMF- and the solar wind parameters and substorm signatures in the magnetosphere. In addition to the above mentioned, these were the observations from IMP8 and Geotail. Although not used in detailed analysis, they were important in the initial selection of the events. Also of great practical use were the satellite orbital data from the NASA Satellite Situation Center (SSC) accessed via Internet.

2.3 Electron pitch-angle data

2.3.1 The concept

Because of the satellite geometry, it was not possible to fully use the 360 deg. field of view of the top-hat analyzer (which would allow to get a full 3D spectrum during half a spin period). The analyzer was then mounted to cover a half-plane containing the satellite rotation axis (see the above Section) and the whole 4π solid angle was being scanned during one spin period.

The slow rotation of the satellite (nearly 120 sec spin period) appeared to be too long when analyzing some of the observed fast changing features reported here. It is, nonetheless, always possible to get at least a partial information on the electron pitch-angle distribution more frequently. Depending on how the instantaneous magnetic field vector is oriented relative to the rotating half-plane of the spectrometer (perpendicular, oblique, in-plane), a reduced range of pitch-angles might be sampled more frequently. In particular, every 3.75 sec. there is a detector whose line of sight is perpendicular to the magnetic field (in other words, there is always at least one straight

line on the plane, that is perpendicular to any other straight line, lying either in- or out- of that plane). This relative orientation and the instruments geometry is broadly sketched in Figure 2.2.

2.3.2 Database

The information on the pitch-angles of the electrons was not available routinely because of the failure of the FGM-I magnetometer (see Subsection 2.1.2 above). The generation of the pitch-angle data was then the first and essential step allowing for the observations and the analysis performed in this work. To this aim, the above concept of using the “instantaneous” magnetic field was applied to the MIFM instrument. It has been designed and performed as the contribution to the existing database of the ELECTRON- and the MIFM experiments, together with the software to generate and access the pitch-angle data. This was an inherent part of this work and the details are described elsewhere (Koperski *unpublished, internal reports of Space Research Center, Warszawa, 1998-2003*).

Such electron spectra, of relatively high time resolution but mostly of restricted pitch-angle range, are extensively used throughout this work.

2.3.3 Restrictions

The use of the data of different ELECTRON detectors in different time instants to get the pitch angles, based on their instantaneous orientation, requires some more comments.

(i) The magnetic field DC measurements from the MIF-M instrument with the sampling frequency 4 or 1 second have been used to calculate the mean pitch angles for each whole energy spectrum (3.75 sec) for each of 8 detectors. This is obviously averaged and inaccurate, as each of the analyzer’s 16 or 32 energy levels is scanned at slightly different moment of the rotation (changing every $\sim (3.75/16)$ -th or $\sim (3.75/32)$ -th second). It gives a reasonable estimate, however, when taking into account the slow rotation of the spacecraft, the analyzer geometry (22.5 deg. along and 6 deg. perpendicular to the spin axis) and the magnetic field sampling rate. Moreover, this allowed the software, developed to treat the data, to be much simpler and faster, as well as the volume of the data generated significantly smaller. These factors were important in the every day work.

(ii) Second is the equivalence of different detectors. The question is not about the sensitivity of the microchannel plates used nor the analyzer’s resolution ability- the response of detectors has been checked to be uniform within 96 percent (J.-A. Sauvaud, personal communication and [168]). What makes them not equivalent is electrostatic potential distribution of the satellite. This is one of the most serious yet difficult to analyze source of inaccuracy in the low-energy particle measurements in space. The conclusion from the data analysis is that there has been observed features in the electron spectra attributable to a nonuniform satellite charging, but they can be neglected in most practical situations. As long as a dense plasma is concerned (above few particles per ccm depending the on the mean energy) or the electron energies are above some 30 - 80 eV (or even more, depending on plasma density and mean energy), these effects are generally not seen. No detailed and systematic study, however, has been done relative to that. On the other hand, there are observations and theoretical considerations showing that even under such conditions in the magnetospheric plasma sheet, the satellite charging can be of great importance for particle measurements (see e.g. Popov et al. 1997, [149] and references therein).

(iii) Third, it is the question of the gyrotropy of the electron distributions. The gyro-period of electrons (nearly $1.8 \cdot 10^{-4}$ to $7 \cdot 10^{-3}$ second for typically observed range of B, 5 to 200 nT) is much shorter then the full spectrum scanning rate (3.75 second at best for the working modes used) or even than the single energy level scan time ($1/32^{th}$ of 3.75 or nearly 0.16 second at best). That means, the observed electron spectra are time averaged over multiple gyro-periods of electrons.

The gyro-radius of an individual electron would vary, for the B range as above, between nearly 67.9 and 1.8 km for a 10 keV energy electron moving perpendicular to \vec{B} , but it changes as sine of a pitch angle and it can be very small. The distance passed by the satellite during one full spectrum scan (3.75 sec.) varies between ~ 3 and ~ 18 km in the near plasma sheet, i.e. in some situations it might be comparable to- or smaller than the electron gyro-radius. Taking into account the plasma flows of several tens or hundreds km/sec it is, in principle, possible that the non-gyrotropic electron distributions would manifest in the observations. With the given instrument sampling time, however, this would require some special conditions (e.g. the bulk plasma flow similar to the spacecrafts actual velocity) and would influence only very specific part of the whole particle population.

To conclude, I will further assume that all the individual pitch-angle and energy spectra of electrons (obtained in 3.75 sec.) are gyrotropic, and the only effects that can disturb the observed gyrotropy are due to non-stationarity on the short time scale in the medium (below 3.75 sec. but not violating the “physical” electron gyrotropy, for given B and energy values).

2.4 Ground-based data

One of principal parts of this work was to relate the features of the plasma and the magnetic field observed locally on the Interball to the global state and the dynamics of the magnetosphere. To do so, I used, first of all, the standard magnetic data from the individual ground stations and sometimes the optical data.

2.4.1 Activity indices and the 1-minute geomagnetic data

Of the various geomagnetic activity indices, the 3- hour Kp index has been used mainly throughout this work. It is because of its availability and a broad use in various magnetic field models. The 1 minute AL, AU and AE indices, extensively used until recently in substorm-related studies, were still not available for the relevant time period until the moment of final preparation of this work. Also, as mentioned in the preceding chapter, these indices, though broadly applied, are of limited significance for the time- and space- localized case studies. Though the global “AE” indices (to denote the group as the whole) were not used throughout this study, the local “equivalents” based on latitude- limited data of stations of the IMAGE and the CANOPUS networks, has been used at the initial stage. Besides the above, also the hourly Dst index has been used. The source of these data was the World Data Center for Geomagnetism C2 in Kyoto.

The 1 minute- resolution geomagnetic data from several geomagnetic stations are routinely used to locally monitor the substorm- related activity. The source of this data for the purposes of my work was World Data Center (WDC) for Geomagnetism C1 in Copenhagen.

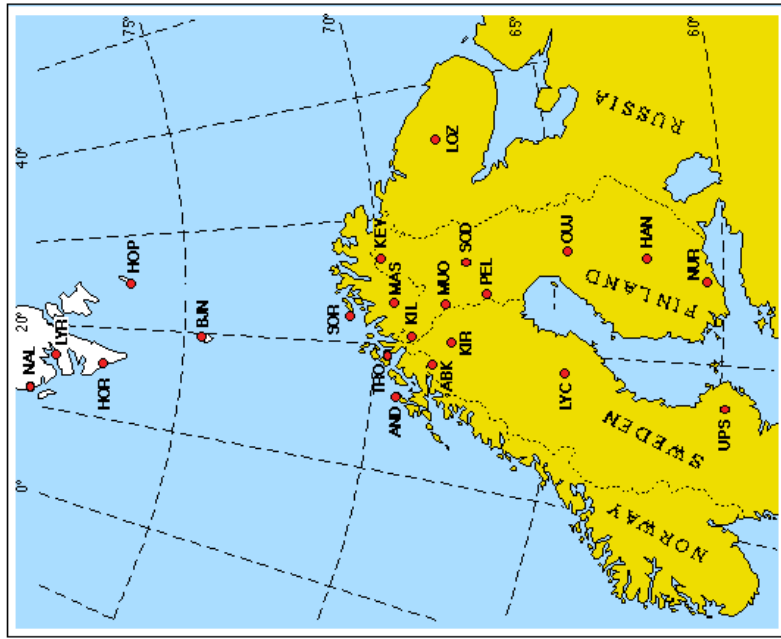
2.4.2 High-resolution magnetic data

The “high resolution” means here the frequencies sufficient to get the Pi2 pulsations (i.e. of periods of 40 - 140 seconds.). Such data are usually not recorded on many observatories nor collected in the WDC Geomagnetic data centers, but are available only from certain sites.

MM210 magnetometer network

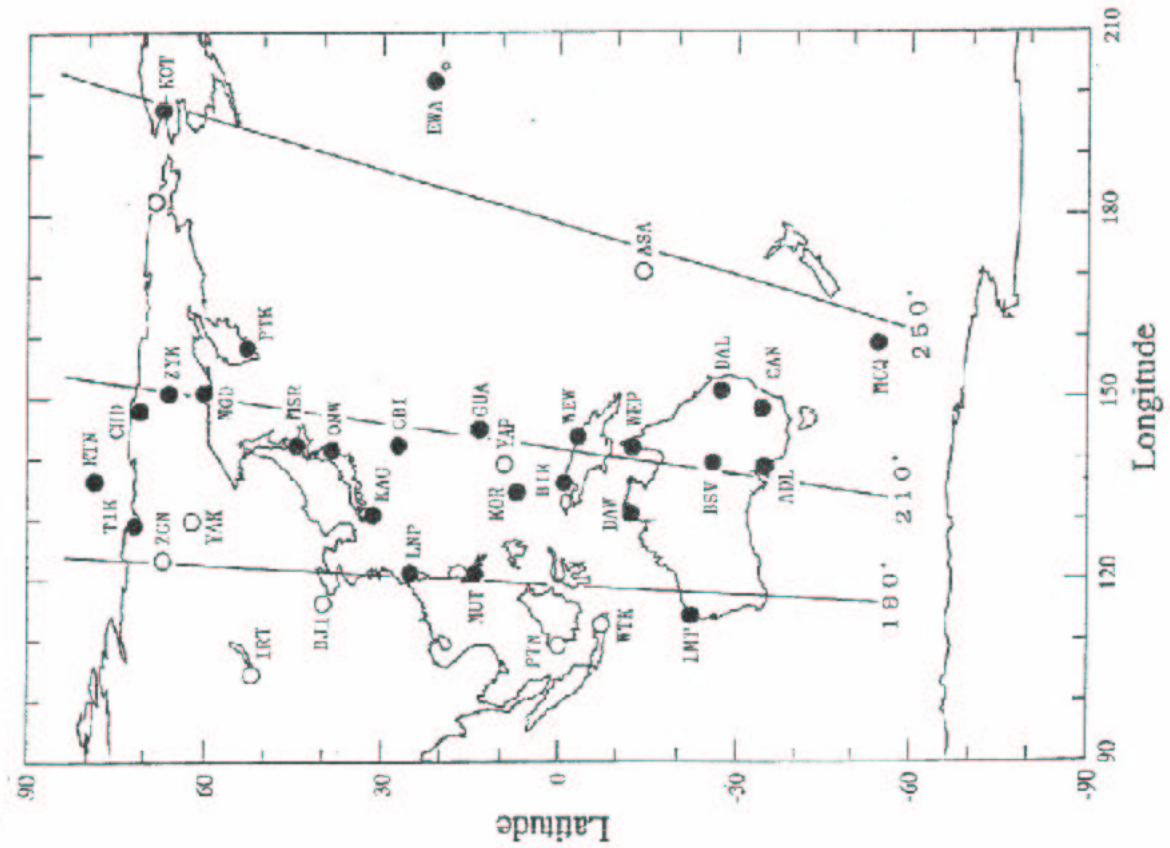
The name of this network, extending from the northern- to the southern auroral zone, come from its location- near the 210 Magnetic Meridian. The included stations are plotted in the left panel of Figure 2.3 Actually, after inclusion of more stations, the network has been named the Circum Pan- Pacific Magnetometer Network. It is deserved by the Solar-Terrestrial Environment

IMAGE Magnetometer Network



January 1999

Figure 2.3: Ground magnetic stations: (Left) of the MM210 network, (Right) of the IMAGE network.



Laboratory, at Nagoya University in Japan. For the purposes of this work, the magnetic data with the 2 second. resolution were used, from selected stations and in the limited time range.

IMAGE magnetometer network

The network of the magnetic, optical and radar observatories at high latitudes in Scandinavia is shown in right panel of Figure 2.3. It is an important and developing source of the ground observations. The magnetic data of 1 minute and of 10 second. resolution as well as the “local AE” index were used for the substorm related observations.

SAMNET magnetometer chain

These data come from the network of sub-auroral ($\sim 51^\circ$ to $\sim 65^\circ$ geographic latitudes) magnetic observatories between Scandinavia and Great Britain. Their locations are shown in the left panel of Figure 2.4.

Greenland Magnetic Stations

The map of the observatories is seen in the right panel of Figure 2.4. The Greenland’s magnetic data of high resolution (20 seconds.) were provided by Danish Meteorological Institute (the coastal observatories data) and by the Space Physics Research Laboratory at University of Michigan (the Greenland’s interior- observatories).

Conjugated Iceland- Antarctic Magnetic observatories

These data come from one antarctic station (Syowa, SYO) and the Iceland stations of the very near magnetic meridian (HUSA, ISAF, TJOR). The data are the relative, 1 second. sampling magnetic field components and were obtained from the WDC for the Aurora in Tokyo. The locations of the stations are shown in the upper panel of Figure 2.5.

CANOPUS magnetic data

The CANOPUS network is the source of 5 second. magnetic data used here. It is also the important source of the optical data (see below) and of the radar data (not used here). Station location is sketched in lower panel of Figure 2.5.

2.4.3 Other ground-based data

Only the optical ground data has been use at the final stage of the work and they were used only for the detailed, multi-point study of the event of 13/Jan/1996 in Chapter 3. As the additional, supporting source of information at the initial stage of selection of the ground events, I used however also the ALASKA radar- and the CANOPUS MSP optical data. After that, they were not further used in this work.

CANOPUS network- optical data

The Meridian Scanning Photometers (MSP) of the CANOPUS network are situated in PINA, GILL, RABB and FSIM sites. Also the All Sky Camera (ASP) data has been used from RABB. The locations can be seen in lower panel of Figure 2.5.

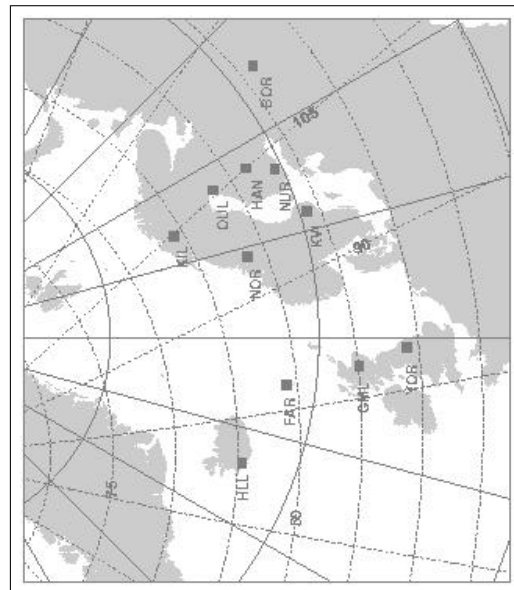
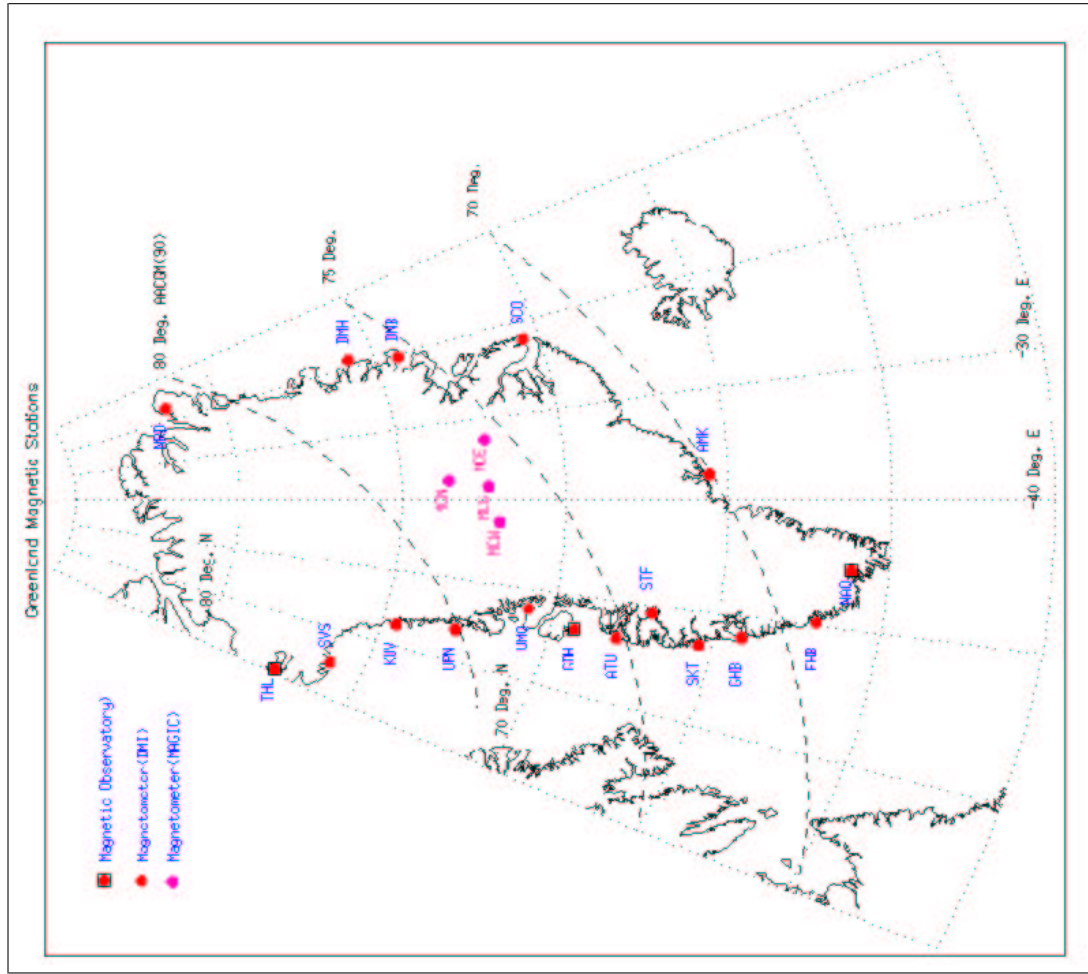
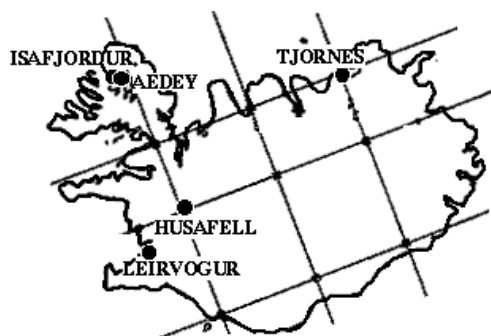


Figure 2.4: Ground magnetic stations: **(Left)** of the SAMNET network, **(Right)** of the Greenland network.

CONJUGATE OBSERVATION STATIONS IN ICELAND



Station Name	Geo.Lat. (deg)	Geo.Lon. (deg)	INV.Lat (deg)	MLON (deg)	L-value	MLT (hr)	B (nT)	D (deg)	I (deg)
HUSAFELL	64.67	-21.03	65.519	67.966	5.823	23.429	52191.0	-19.480	75.946
TJORNES	66.20	-17.12	66.526	72.299	6.303	23.718	52207.3	-17.916	76.588
AEDEY	66.09	-22.65	67.231	67.728	6.676	23.413	52552.4	-21.372	76.839
ISAFJORDUR	66.08	-23.13	67.295	67.323	6.712	23.386	52586.4	-21.670	76.864
SYOWA	-69.00	39.58	66.245	71.624	6.163	23.673	43433.5	-47.780	-63.959

Calculated with IGRF-95 model (epoch: 00:00 UT on January 1, 1998)

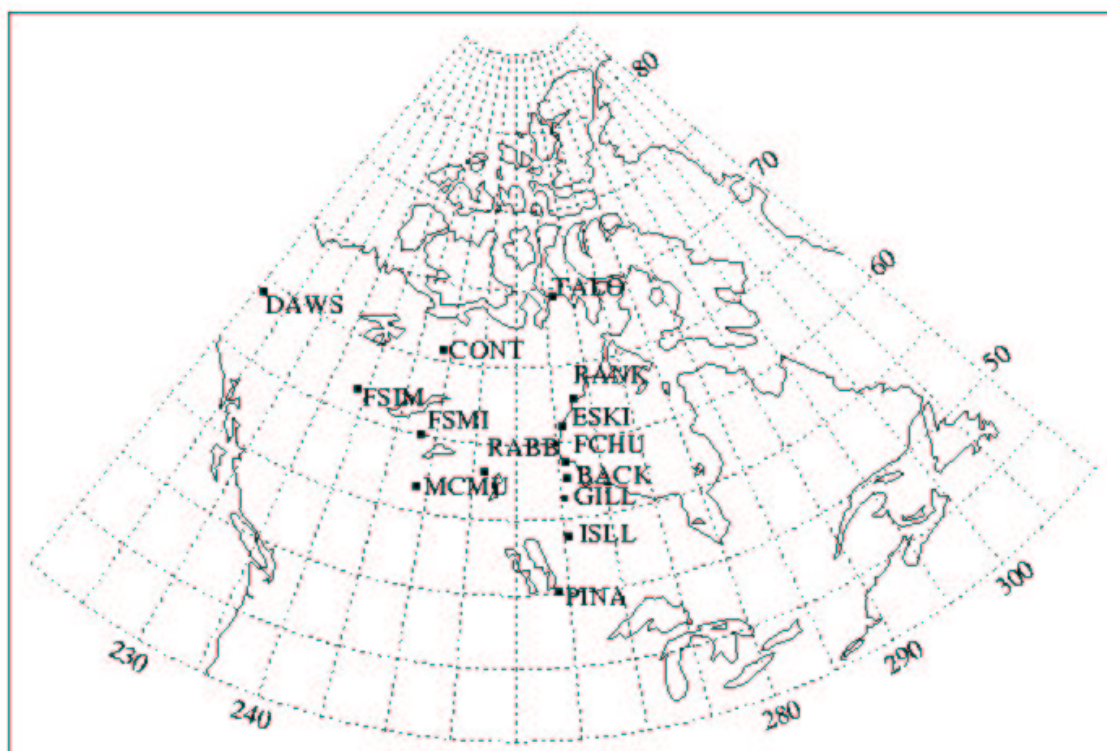


Figure 2.5: **(Top)** The magnetic stations of the Iceland. **(Bottom)** The stations of the CANOPUS network.

2.4.4 Software

Although only the WDC, 1 minute- resolution data were initially used, the need and the possibility to use the data with the higher sampling rates became evident during this study. This resulted in simultaneous use of the data of different origin, sampling rates and in different format. More precisely, 10 different data formats of high- resolution magnetic data, kindly provided by the owners has been used. To provide the necessary, unified access to all the ground magnetic data used, the small, simple data base and the software to access it was then developed. Although rather trivial, this work was the necessary- and the time consuming step to make. The information on this has been included here for the completeness, and the details were described elsewhere (in the internal activity report of the Space Research Center, Warszawa, for the year 2002; unpublished).

Chapter 3

Large-scale multi-point study of 13/January/1996 substorm expansion.

*The content of this chapter is the base for the article
“The January 13, 1996 substorm with multiple intensification: A multi-point study”
of P. Koperski, J-A. Sauvaud, G. K. Parks, S. Romanov
Submitted to Annales Geophysicae in May 2005.*

This chapter presents the multi-point, ground- and satellite based study of the substorm of 13 January 1996. This event offered a rare opportunity to observe multiple substorm intensifications, using the rich data set from the ground magnetic observatories and from the satellites located in nearly the same, pre-midnight local time sector, just above the mid-tail plasma sheet and in the near plasma sheet. Using also the data from other geostationary satellites, it was possible to observe the large scale changes related to the substorm expansion and to compare them with observations held on the ground. For one of the substorm intensifications, the tailward propagation of disturbance was observed and it was possible to compare it to the ground signatures.

3.1 Introduction

This chapter, focuses on the large scale dynamics and propagation characteristics of the substorm, leaving the microscopic features for the next chapter. Such detailed multi-point analysis of the events was necessary to properly relate the ground- and the space observed features. Similar analysis was applied for each of the finally selected Interball events (see the following chapter), even though the data set available was not always as rich as here.

3.2 Instruments and data used

The following satellite data are used in this study: the ELECTRON spectrometer and the MIF-M magnetometer from Interball Tail, the MFI magnetometer, the EESA and the PESA spectrometers from the 3DP on WIND, the SOPA electron spectrometers (on the 1990-095, 1991-080 and 1994-084 LANL spacecrafts), the GOES-8 high energy proton- and the magnetic field data, the visual range image from the OLS instrument on DMSP F-12.

The ground-based data shown are: the optical data from CANOPUS network (the all sky- and the meridian-scanning photometer), and the multiple magnetic data of the IMAGE, SAMNET, CANOPUS, Iceland and MIRAGE (Greenland) networks, the observatory Port-Aux-Francais (all these- the “high resolution” data allowing at least for the Pi2 filtering) as well as the 1-min. resolution data accessed through the WDC-1 geomagnetic data center.

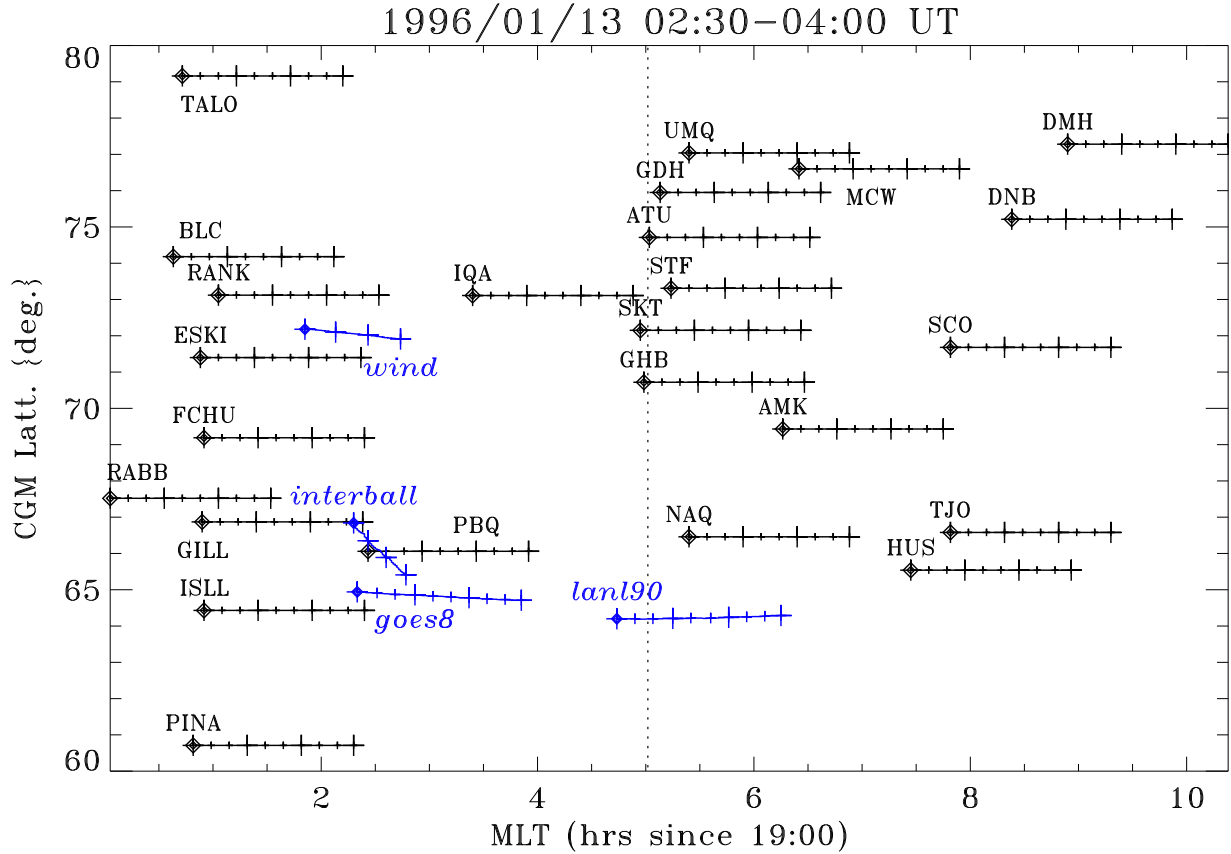


Figure 3.1: The localization of the geomagnetic stations and the satellite footprints in the Corrected Geomagnetic Latitude - Magnetic Local Time (CGL - MLT) coordinate system in the time range 02:30 - 04:00 UT. Each black line represents the "trajectory" of the instantaneous station position in the CGL - MLT, with small tick marks for every 10 minutes (except for Wind and Interball satellites with 30 min. tick-marks). The satellite footprint (100 km height, traced using the T89 Tsyganenko magnetic field model) are plotted in blue. The moment of 02:30 UT correspond to the leftmost, thicker points on each line. Thin dotted line marks the 00:00 MLT.

All the data and the instruments are further described in Chapter 2.

3.3 Observations

3.3.1 Ground based observations

Magnetic observations

Ground-based magnetic data for January 13, 1996 reflect a gradual activity increase starting around 02:30 UT, in a broad Local Time (LT) sector between 18:30 (Canada) and 04:30 (Scandinavia). The first five values of the Dst hourly index were 1,6,-7,-33,-45 nT (decreasing later down to -90 nT at 11:00 UT) and the first three values of the global Kp index for this day were 4,4,5.

Figure 3.1 shows the locations of the ground stations being analyzed from the Iceland-to-CANOPUS local time sector, in the Magnetic Local Time / Corrected Geomagnetic Latitude (MLT / CGL) coordinate system. No Scandinavian stations are shown, to get better local time resolution. The footprints of four satellites, located in the appropriate time sector, are also shown (traced at 100 km altitude, using the T89 Tsyganenko magnetic field model). Each line on the plot represents the "trajectory" of a station (or a satellite's footprint) between 02:30 and 04:00

UT; the small tick-marks for every 10 minutes (except for the Wind and Interball satellites with 30 min tick-marks). 02: 30 UT corresponds to the leftmost, thicker point on each line.

Figure 3.2 shows the northward component of the magnetic field measured at selected ground stations, in four LT sectors: (upper left) the Scandinavian IMAGE network region, (upper right) Iceland and East Greenland coast (the most westward station is here MCW), (lower left) on the Greenland's West Coast (the more eastward station is AMK), and (lower right) the CANOPUS Fort Churchill (FCHU) meridional chain, with two additional, more eastward located stations: IQA and PBQ. In each panel, the most equatorward (CGL) located stations are the lowermost ones. Two vertical lines mark the onset of low frequency magnetic fluctuations measured onboard Interball, as presented in the following subsection.

Multiple local intensifications of the westward oriented current are seen in the individual magnetograms as the sharp negative bay signatures. Some of them simply indicate the poleward expansion of the substorm current system. This can be found in lower left panel at SKT, STF, GDH and UMQ after 03: 12 UT, as well as in lower right panel for PBQ, GILL, FCHU and RANK after 03:29 UT. In the first panel (upper left), the Westward Electrojet (WEJ) develops near the MAS and KIL stations and suddenly expands northward to SOR after 03:05 UT

In addition to these poleward expanding features, further details can be found in the plot. The fadings and the intensifications of the electrojet observed locally at different stations are not purely local time, nor latitude-like organized. Instead they have mixed dependencies and can be grouped (anticipating the satellite observations shown in the following subsection) in three "intensification sequences".

The first "sequence" begins at lower latitudes, between about 02: 53 and 03:05 UT. The negative bay onset seen on AMK after 02:55 (third panel) coincides with the TJO and HUS onsets at 02:55 (second panel) and with, multiple disturbances over NAQ at 02:53-03:05 (third panel). Further inspection of the Z component (not shown) reveal that the WEJ starts to develop at 02:53 south of to AMK, TJO and HUS and then passes poleward over the HUS and NAQ at 02:58 UT. The WEJ over Scandinavia starts to expand close to that time at latitudes between MUO and SOR (first panel of Figure 3.2) and then develops poleward. Note also the WEJ intensification at 03:02 over the Canadian PBQ station (fourth panel, a weak one with a disturbance of the H- component of the order of 150 nT). The electrojet finally moves poleward over this station at 03:12 , which coincides well with the similar movement over the AMK at 03:13. It must be stressed that without the observations from more eastward located stations, the disturbance at PBQ could probably be classified as a pseudobreakup. It has to be pointed out that the above series of electrojet intensifications detected between 02:53 and 03: 05 has no counterparts at higher latitudes.

The second WEJ large intensification starts at 03:11 UT in AMK and NAQ (third panel). This intensification subsequently expands poleward, reaching UMQ at 03:14 UT (third panel). The above mentioned PBQ electrojet intensification near 03:12 UT is probably an element of the same sequence. Nearly simultaneously, a local intensification is seen west to Greenland and at higher latitudes: over the IQA station at 03:10 (fourth panel). Due to its high latitude and distant LT position relatively to AMK and NAQ, it is unlikely an element of the "03:11" sequence, being rather a localized and separate high latitude activation. It must be stressed that these electrojet changes at PBQ and IQA (panel d) are the only clearly identifiable negative bay signatures westward to the Greenland's West Coast. There is no typical signatures of WEJ intensification in the CANOPUS magnetic data before about 03:30 UT.

The third sequence is first observed over PBQ after 03: 29 UT. From that time the electrojet quickly develops poleward and reaches FCHU at 03:32 UT and RANK at 03:35 UT. A further, subsequent intensification is seen after 03:39 UT over FCHU. The negative bay is also well seen at 03:02 UT over the RABB station, located nearly one hour westward (data not shown). Near its onset around 03:02 UT, this intensification has no counterpart at higher latitudes east of the

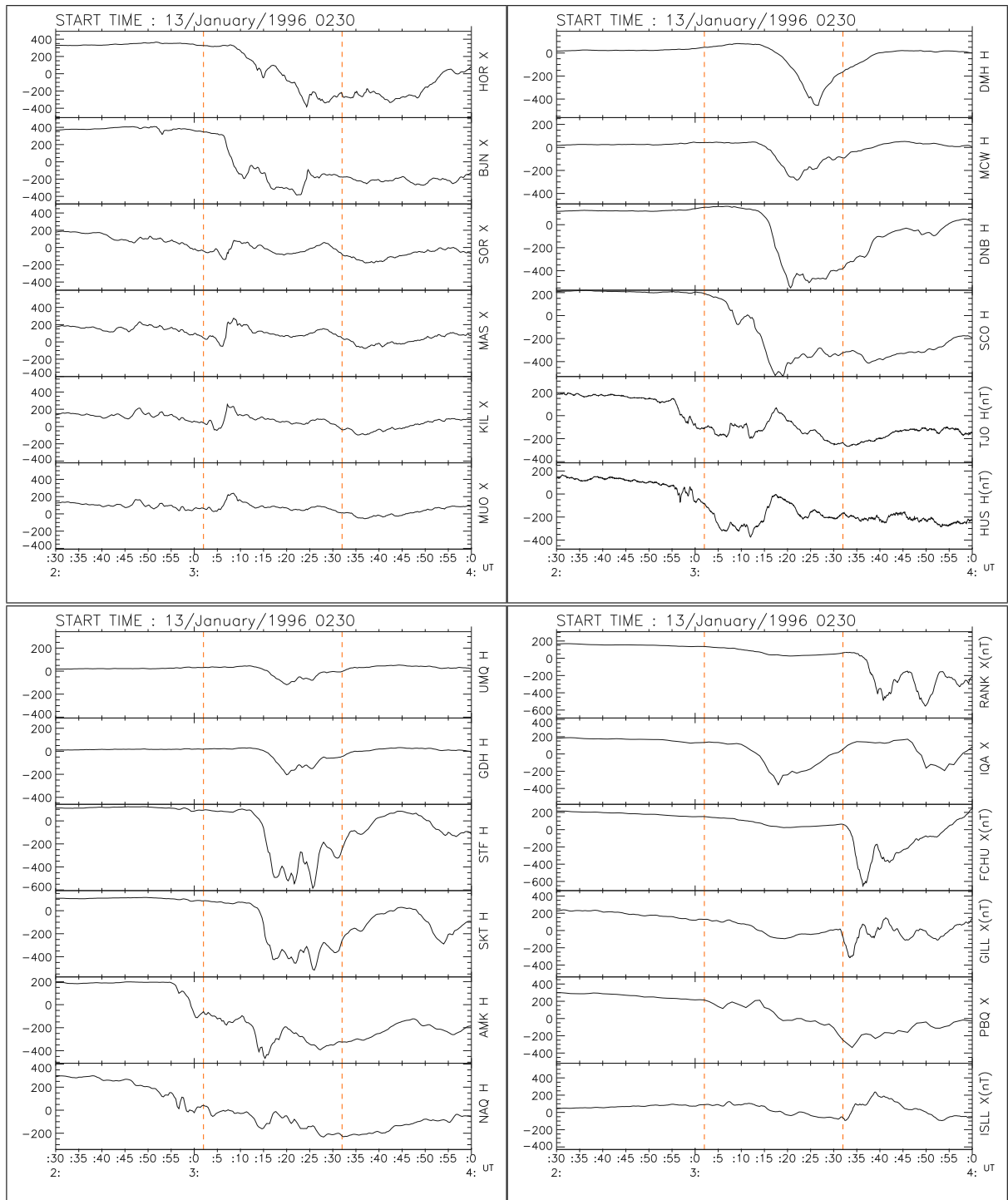


Figure 3.2: Ground magnetic observations of the substorm from four LT sectors: (upper left) Scandinavia, (upper right) Iceland and Greenland's east coast, with the more westward located station MCW, (lower left) Greenland's west coast with the more eastward located station AMK, (lower right) CANOPUS meridional chain with the two more eastward located stations, PBQ and IQA. Vertical dashed lines mark the beginning of magnetic fluctuations at Interball (see the following subsection).

CANOPUS. Only after 03:47 UT, the WEJ intensifies over IQA and, from 03:48 UT, over the Greenland's West Coast (see e.g. SKT and GHB in third panel).

The two last sequences are also seen in Figure 3.3, which shows the Z contour plots from the Greenland's West Coast and from the CANOPUS FCC magnetic networks. The reference "zero level" in the Greenland plot is chosen arbitrary but the WEJ fast poleward expansion is well seen there from 03:12 UT. It continues with oscillations with a 5 minutes period until about 03:35 UT. Note also the negative BZ at lower latitudes (NAQ) starting between 02:55 and 03:00 UT, which further evidence the WEJ poleward of it. Both these features are not seen over the CANOPUS chain, where a fast poleward WEJ expansion starts only after 03:31 UT. Soon after that time, the Greenland's WEJ disappear (03:35 UT) to reappear in a weaker, local form (GHB, STF) after 03:50 UT.

To further investigate the onset times and the locations of the electrojet intensifications, I used the latitude Pi2 pulsations. The high latitude Pi2, contrary to the low latitude ones, are confined in local time and are thought of to be more directly related to the Westward Traveling Surge (WTS) and to the field aligned currents (see e.g. Olson [137] and references therein and Uozumi et al. [199]). Thus, the use of middle and high latitude Pi2 as substorm intensification signatures is not biased with as much uncertainty as was found by Liou et al. [100] for low latitude Pi2. The filtered northward component of the magnetic field is plotted in Figure 3.4. This figure mostly shows the data corresponding to the 24 stations from Figure 3.2, except for IQA and PBQ (Figure 3.2, fourth panel) for which no data with the appropriate time resolution have been found and for MUO (Figure 3.2 second panel) and MCW (Figure third panel). In addition, there is also data from the mid-latitude station Port aux Francais (PAF) (southern hemisphere, located at about 07:40 MLT at 03:00 UT). In panel (b), data from the SYO station (magnetically conjugated with TJO on Iceland) are also shown, and records from PINA and ESKI are added in panel (d) (the CANOPUS chain, left side of Figure 3.1). Two dashed vertical lines mark the onset of magnetic fluctuations at Interball, as in Figure 3.2.

A strong increase of the Pi2 activity is first observed close to the equatorward side of the average auroral oval, in a broad LT range (TJO, HUS, AMK, NAQ) starting near 02:53 and continuing after 03:00 UT. This intensification is also seen at mid-latitudes: at PAF (located at flank side- bottom of third panel), and at KVI and NUR (southern Scandinavia- not shown) but not at higher latitudes, except in the Scandinavian sector. The weaker, smoothly starting disturbance observed after 03:00 UT at ISLL and GILL (panel d) seems to be a "westward edge" of this activity, as there was nothing similar found in more westward located high latitude stations like MCMU and RABB (not shown). Some weak Pi2 traces of the activity (but weaker than those near 03:00 UT) persists after 03:12 UT at ISLL and GILL but it is not seen elsewhere in the FCC time sector (Figure 3.4 (c)). More eastward Pi2 enhancements coincide with the second WEJ activation at 03:12 UT (see e.g. AMK-panel c) and Pi2 activation is shifted in time when moving northward which suggests the WEJ poleward expansion (panel b). This is consistent with the observed negative bay signatures described above.

After 03:29 the Pi2 activity sharply increases in the FCC sector, first at ISLL and GILL, then at PINA, FCHU and RANK, near 03:31, 03:32 and 03:33 UT respectively. Since that time, the Pi2's on the eastward side fade quickly and only some weak remnants are seen for a couple of minutes at SKT and STF on the Greenland's West Coast (panel b). Altogether, the ground based magnetic observations (both the "standard" and the Pi2) can be summarized as follows: The substorm under study does not have a simple form, where a clear, single growth, expansion and recovery phases can be easily distinguished on the ground over quite broad LT sector. Instead it shows multiple intensifications and a complex spatial and temporal structures. There are signatures of three substorm intensifications, starting at 02:53, 03:11 and 03:29 UT, each situated westward to the preceding one. At the equatorward edge, substorm intensifications are less clearly separated and occupy a broader LT sector. The middle and high latitude Pi2 intensifications follow closely

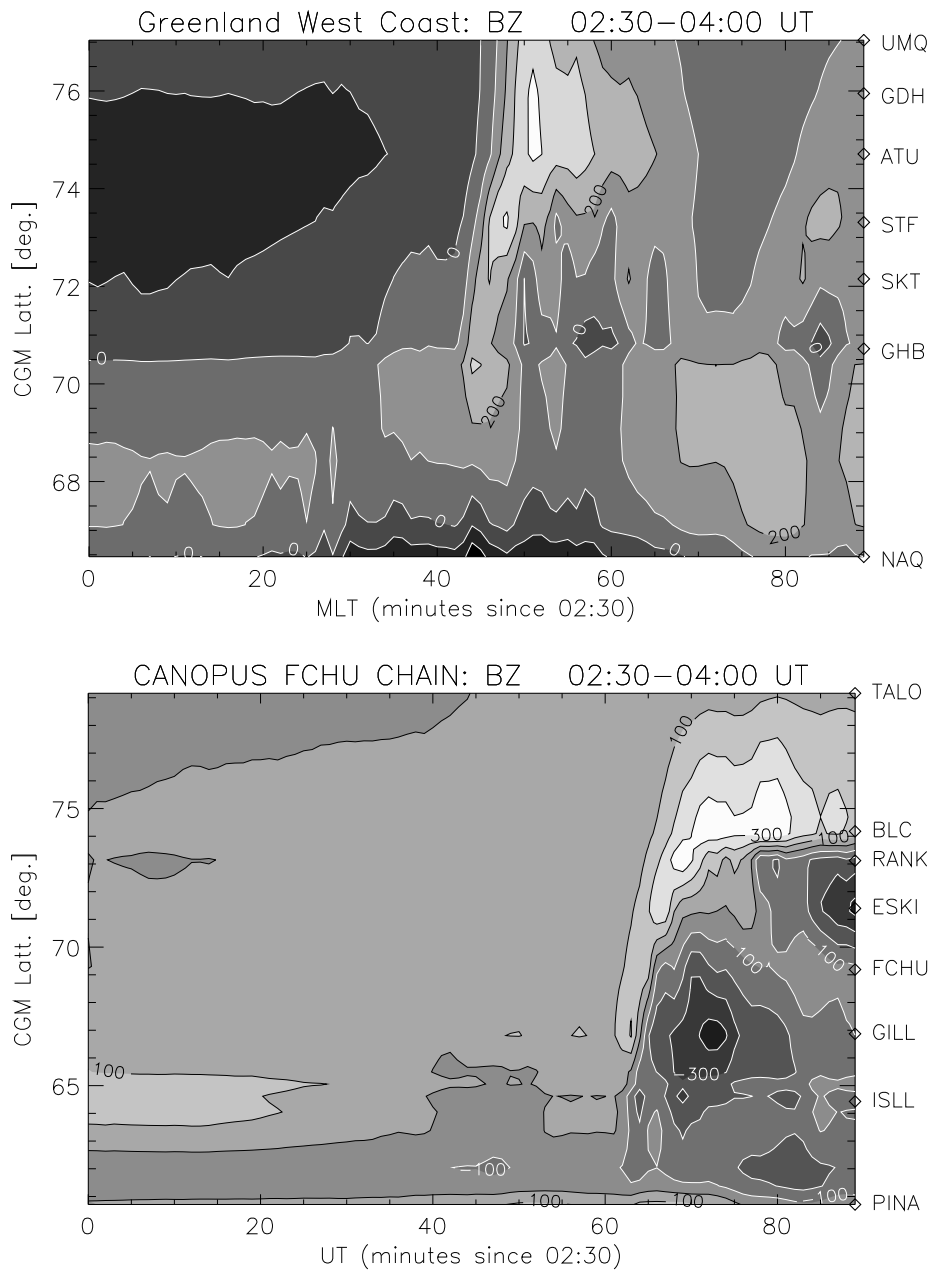


Figure 3.3: The contours of the BZ magnetic component in the time - Corrected Geomagnetic Latitude (UT - CGL) coordinate system between 02:30 and 04:00 UT: (Upper) for the Greenland's West Coast network and (Lower) for the CANOPUS FCHU meridional chain.

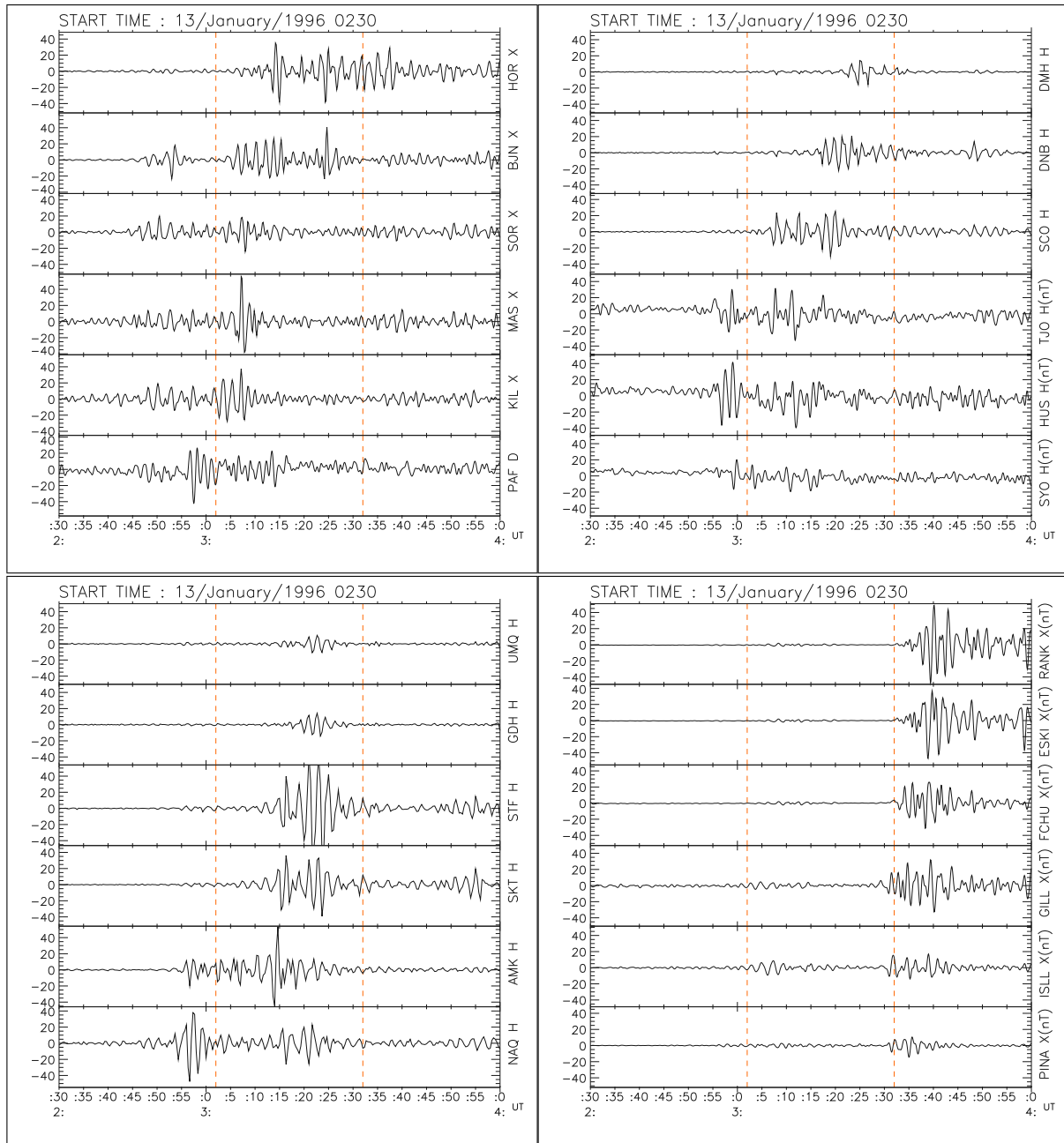


Figure 3.4: Pi2-range filtered-, northward oriented magnetic field component from selected stations (shown in Figure 3.2), between 02:30 and 04:00 UT. (Upper left) stations of IMAGE network and PAF (southern hemisphere, about 07:40 LT at 03:00 UT). (Upper right) stations of Iceland and the Greenland's east coast and SYO; (Lower left) stations of Greenland's west coast and the AMK; (Lower right) stations of CANOPUS FCC chain; Note, that stations SYO and PAF are not shown in Figure 3.2, while PBQ and IQA are not shown here (no high-resolution data could be found for them). Vertical dashed lines mark the beginning of magnetic fluctuations at Interball (see the following subsection).



Figure 3.5: The visible range auroral image from the DMSP F12 satellite taken between 03:06:43 and about 03:14:00 UT. The locations of the CANOPUS meridional chain geomagnetic stations are also marked (yellow diamonds) as well as the footprints of the satellites from the appropriate local time sector (red circles) footprints are obtained with the T89 mapping. The auroral spiral near the right edge was scanned between 03:08:38 and 03:09:44 UT.

the negative bay onset signatures.

Several important features are to be pointed out : i) The onset at 02:53 UT is only seen at the equatorward side of the average auroral oval west of Scandinavia, but the WEJ expands in a broad longitudinal sector reaching PBQ in the evening side, before the other intensifications appear; ii) The 03:11 UT intensification, clearly seen in Greenland, is only seen as a smooth bay at PBQ, ISLL, GILL (64 - 67 deg. CGL) and is not observed at higher latitudes westward of IQA, and; iii) The event of 03:29 UT is initially detected west of PBQ, expanding poleward until BLC. It further intensifies poleward of ESKI and develops eastward near IQA and SKT.

It follows however, that without supplementary information, even with a rich set of ground-based magnetic data as in our case, it is difficult to establish the fine structure and sequence of a substorm development. I will come back to this subject below.

Optical data

It has been concluded from series of multi-point observation studies, mainly using the POLAR mission observations, that the global, satellite based optical imaging of the auroral activity is the best mean to provide the exact timing of the substorm onset and the auroral activity in general (see e.g. Liou et al. [99], Liou et al. [100], Liou et al. [101]. Unfortunately, the POLAR satellite was not been launched yet at the time of the events reported. Here the ground based optical data from the CANOPUS/MARI chain are used and one fortuitously found image taken by the DMSP F12 satellite. The main interest is in observations from the time sector of the CANOPUS meridional Fort Churchill Chain (FCC), as the most closely related to observations of Interball Tail and Wind, and because of reach set of the available data. After all, other optical data related to this study could not be found.

The image taken onboard the DMSP F12 satellite in the visual wavelength range is shown in Figure 3.5. The image was taken between about 03:06 and 03:14 UT. Figure also shows the continent contours, the FCC stations and the footprints of the location of the Interball-

Tail, GOES-8 and WIND satellites (mapped at 03:06 UT with the Tsyganenko 89 model for the observed value, 5, of the Kp parameter). The thin auroral arc is located between the ISLL and the GILL. Near the right edge of the image the auroral spiral form is located (usually related to a Westward Traveling Surge) just equatorward of PBQ. Because of the way the atmosphere is scanned by the DMSP imager, it takes about 8 minutes to obtain the whole auroral image shown here. Specifically, the region of the spiral has been scanned between 03:08:39 and 03:09:44 UT. This observation follows the electrojet intensification, observed in the magnetic data which started around 02:53 UT more eastward and was reaching PBQ at 03:02 UT. It also lags behind the subsequent electrojet intensification, at 03:11 UT which will take place mainly eastward of the surge position displayed in Figure 3.5 (compare magnetograms from the PBQ, NAQ, AMK, TJO, HUS in Figure 3.2 and Pi2 signal from AMK, NAQ, ISLL in Figure 3.4).

Figure 3.6 provide additional data coming from the all sky camera located near GILL. It shows optical views of the sky with a 1 minute time resolution . The faint auroral arc seen before 03:05 UT is the remnant of a preceding one (not shown) that has started to intensify more poleward after about 02:40 UT and has reached its maximum intensity near 02:53 UT. Another weak arc intensification starts around 03:11 UT, but the most clear change is seen around 03:32 UT, when multiple arcs suddenly appear more and more poleward and dynamically evolve until they start to weaken after about 03:43 UT.

The meridian scanning photometer (MSP) data taken at GILL and RANK provide further details of the dynamics of the auroral arcs between 02:00 and 04:00 UT. Figure 3.7 shows the intensity-time plots for the auroral emissions at 5577, 4831 and 6300 nm from these two sites. Some possible uncertainties in the exact timing and location of arcs has to be taken into account due to clouds covering the sky, especially in GILL (see the "Cloud" bars in Figure 3.7 over the relevant panels), but the main features can be easily distinguished . These are: i) The slow and systematic equatorward movement of the auroral arc after about 02:00 - 02:10 UT (also seen one hour westward in LT at Fort Smith, not shown) followed by the slow increase of the intensity of the auroral emissions on the poleward side starting around 02:20 (features that usually correspond to a substorm growth phase); ii) Sharp emission enhancement and rapid latitudinal (mainly poleward) expansion of the auroral intensity starting at 03:31-03:32 at GILL and some minutes later, later at 03:34 - 03:35 UT at RANK; iii) Small and localized auroral intensification around 03:05 UT at GILL. This feature is consistent with the optical observations made at two other stations (not shown): PINA located more south and Fort Smith, situated about two hours westward. Note finally, that the magnetic negative bay in the FCC sector starts at latitudes close those where the main H_{β} emission (486.1 nm) is measured. This distinguishes the expansive phase onset from other auroral activation (Rostoker [159]).

To summarize, the available optical data support the sequence of magnetic substorm activations deduced from magnetic data. The first disturbance (near 03:00 UT) is seen expanding at lower latitudes and reaching the MLT sector of PBQ in Canada The intensification near 03:11 UT is not well seen in the available optical data set CANOPUS), in agreement with the magnetic observations there. As for the intensification of 03:31 UT, the optical data show clearly the auroral breakup and the following poleward expansion.

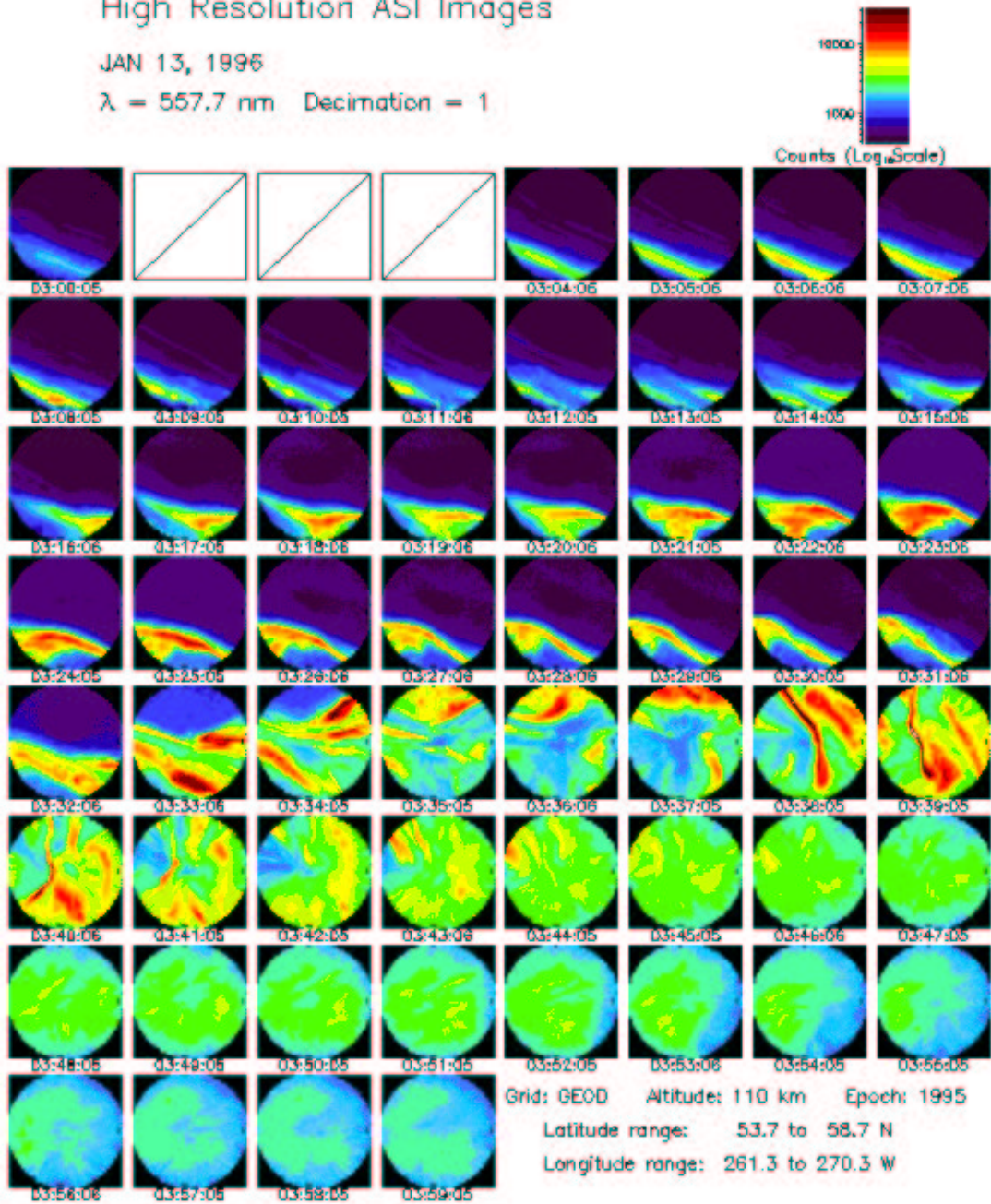
Summary of ground observations

Ground based observations over a large LT range and at different latitudes reveal the complexity of the substorm episode taking place after 02:30 on January 13, 1996. The persistent magnetic activity in the midnight sector inside the equatorward edge of auroral oval, between about 02:55 and 03:55 UT is accompanied by poleward expansions of the westward electrojet starting at lower latitudes. There seems to be three such expansions in different LT starting at different times (UT). In the case of the last one, taking place at 03:29 UT, it is possible to follow the auroral breakup in the proper LT sector using ground based optical measurements. Using a fortuitous

High Resolution ASI Images

JAN 13, 1996

$\lambda = 557.7 \text{ nm}$ Decimation = 1



CSA-ASC

Figure 3.6: The all sky camera images from the Gillam station (CANOPUS).

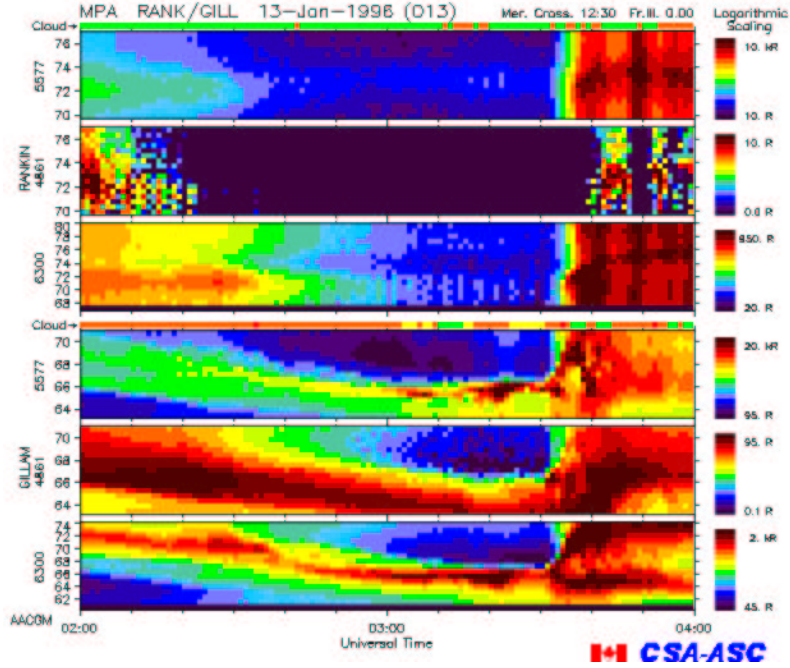


Figure 3.7: The CANOPUS chain meridian scanning photometer data from two sites, top to bottom: three plots from Rankin (in the wavelengths 5577, 4831 and 6300 nm respectively) and the same for Gillam. Note also the cloud bars showing the visibility conditions over each site.

multi-satellite configuration, I will search for the magnetospheric counterpart of the expansion phase related phenomena in the near magnetosphere.

A question can arise about the intensification events mentioned above: are they really separate, global scale substorm intensifications (or separate substorms) or small scale (of the order of 10 minutes or less), discrete auroral activations observed locally, that the substorms and pseudo-breakups are composed of (see e.g. Sergeev et al. 1996, 2001 [177]; Rostoker [158])

The possibility that we have to do with the three separate substorm intensifications, is further investigated below.

3.3.2 Satellite observations

The location (in the GSM coordinate system) of the satellites, the data of which has been used here, is shown in Figure 3.8. Unfortunately, there is no data available from the Solar Wind for the time range under study.

Pre- midnight tail and plasma sheet

Figure 3.9 shows the Interball Tail data (from top to bottom)- the magnetic field from the MIF-M instrument, the energetic electron- and ion fluxes from the SKA-2 instrument (Key Parameters), the ion- density, temperature and velocity from the CORALL instrument (Key Parameters), and the omnidirectional energy spectra from the ELECTRON instrument.

The satellite, located in the LT sector 21:00 - 21:30, traversed the hot plasma sheet moving southward and towards the Earth. The magnetic field (two upper panels) shows the substorm related changes (field stretching since 02:20 UT followed by two dipolarizations, about 03:02 and 03:32 UT) superposed on crossing of the neutral sheet near 02:50 UT (the minimum of the B total and the Bx changing sign) and the increase of B total due to approaching the Earth by the spacecraft. There is also two bursts of low frequency magnetic fluctuations seen at the beginning

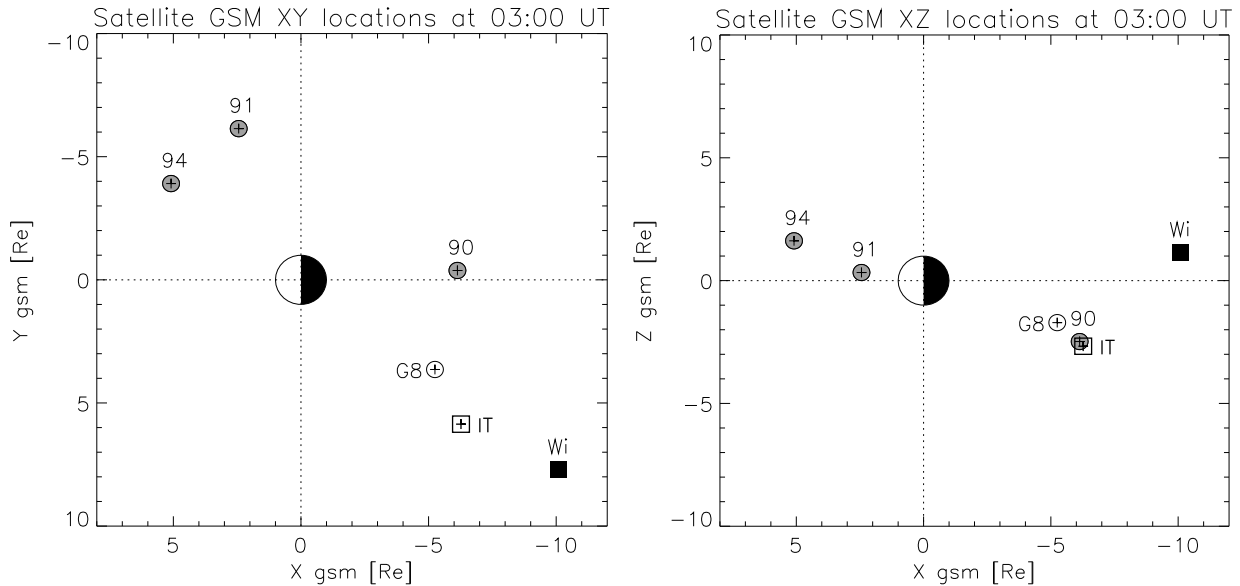


Figure 3.8: The GSM XY and XZ location of satellites at 03:00 UT. The satellites are marked as follows: IT for Interball Tail, Wi for WIND, G8 for GOES 8, 90 for 1990-095, 91 for 1991-080, 94 for 1994-084.

of dipolarizations. They are accompanied by two hot plasma recoveries/injections (the first of which is much weaker) seen in the ELECTRON- and the SKA data (bottom- and third panel).

The ion data from CORALL (fourth panel) show a weak, temporary decrease of the particle flux near 2 keV before 03:04 UT, accompanied by the strong earthward impulse in the velocity (up to +300 km/s in V_X GSM (and nearly -150 km/s in V_Y GSM, not shown). After the second magnetic field burst, since about 03:34 UT, the thermal energy of hot injected ions becomes slightly too high to be well detected by the instrument and mainly the low energy component contributes to the calculated moments of distribution function. This makes the density and the velocity calculations biased with uncertainty and the calculated (proton) temperature unrealistically low (contrary to what is observed in the SKA proton flux, increased at that time).

Significant, temporary dropouts of the parallel/anti-parallel electron flux are seen at few hundreds eV after 03:02 and 03:32 UT. Observed simultaneously with the magnetic fluctuations, they are signatures of a current disruption near the satellite and coincide well with the ground-observed expansion/intensification onset (The details of the observed electron pitch angle- energy distribution changes related to this- and similar substorm events are presented in Chapter 4 below).

Figure 3.10 shows the WIND data for the same time range (from top to bottom)- the EESA instrument electron temperature and omnidirectional fluxes, the proton (PESA instrument) density, velocity (GSM coordinates), temperature and omnidirectional fluxes. Below there is the 3 sec. magnetic field data from the MFI instrument (GSM components).

The WIND data show a different behavior, when compared to the Interball observations. This is related to the different location of the spacecraft. The decreasing fluxes of keV energy particles and increasingly tail-like configuration of the magnetic field before 03:00 UT are the signatures of the substorm growth phase and the plasma sheet thinning, observed also on Interball. Contrary to Interball, there is however nothing seen near 03:02 UT in the magnetic field or in the electron data. The two increases of the low energy ion flux and the resulting density increases took place at 03:08 and 03:25, but they are not accompanied by the magnetic field effects and should be thought of as the transient thickening/oscillations of the plasma sheet, seen from the outside. The related temperature increase (e.g. at 03:20 - 03:25 or 03:30 - 03:37) is an artificial effect

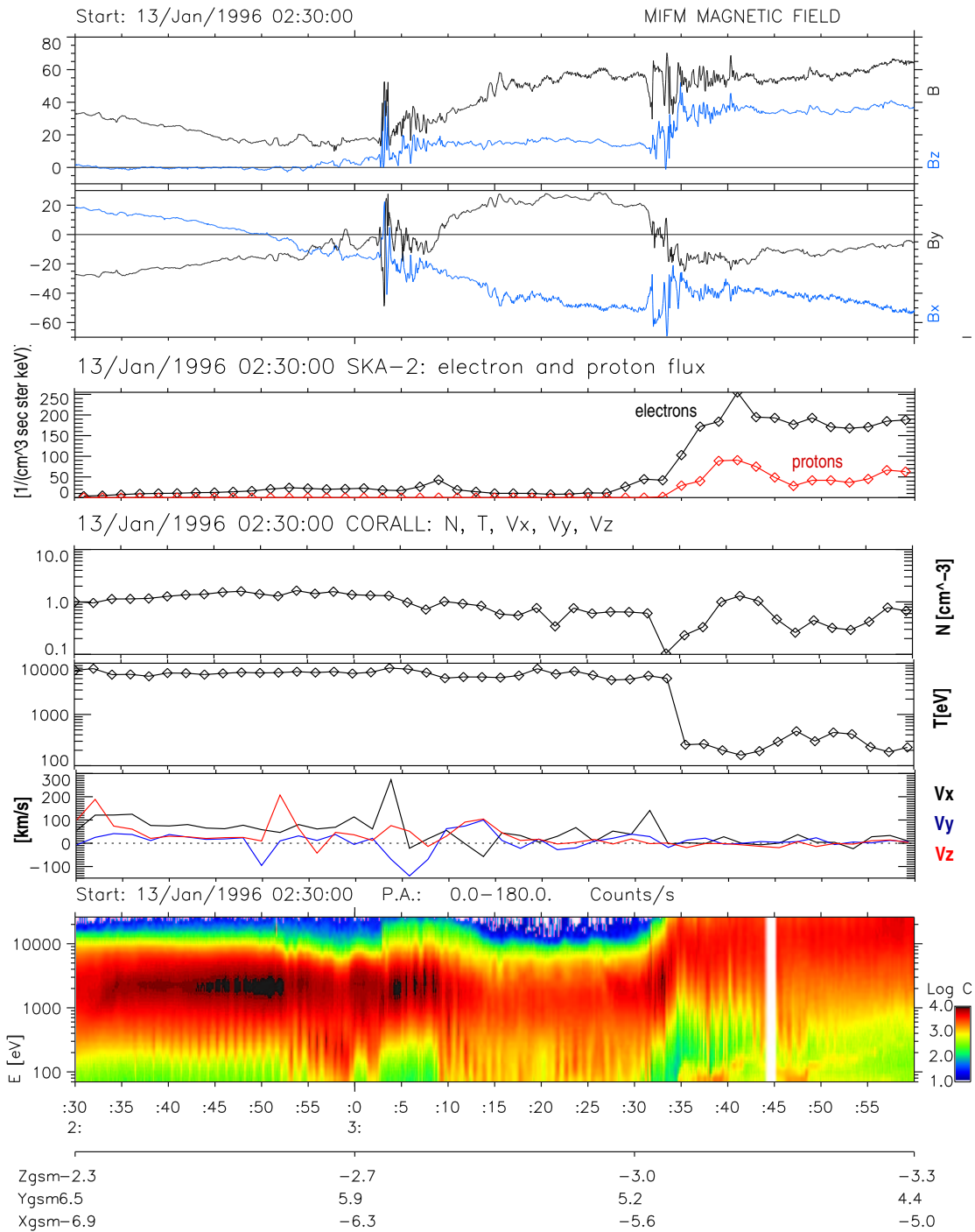


Figure 3.9: The Interball Tail observations, top to bottom: GSM magnetic field; the energetic electron- (black) and the ion fluxes from the SKA-2 (Key Parameters; the ion density (N), the temperature (T) and the velocity components (GSM) from The CORALL instrument; omnidirectional energy- time spectrogram of electrons (from the ELECTRON instrument).

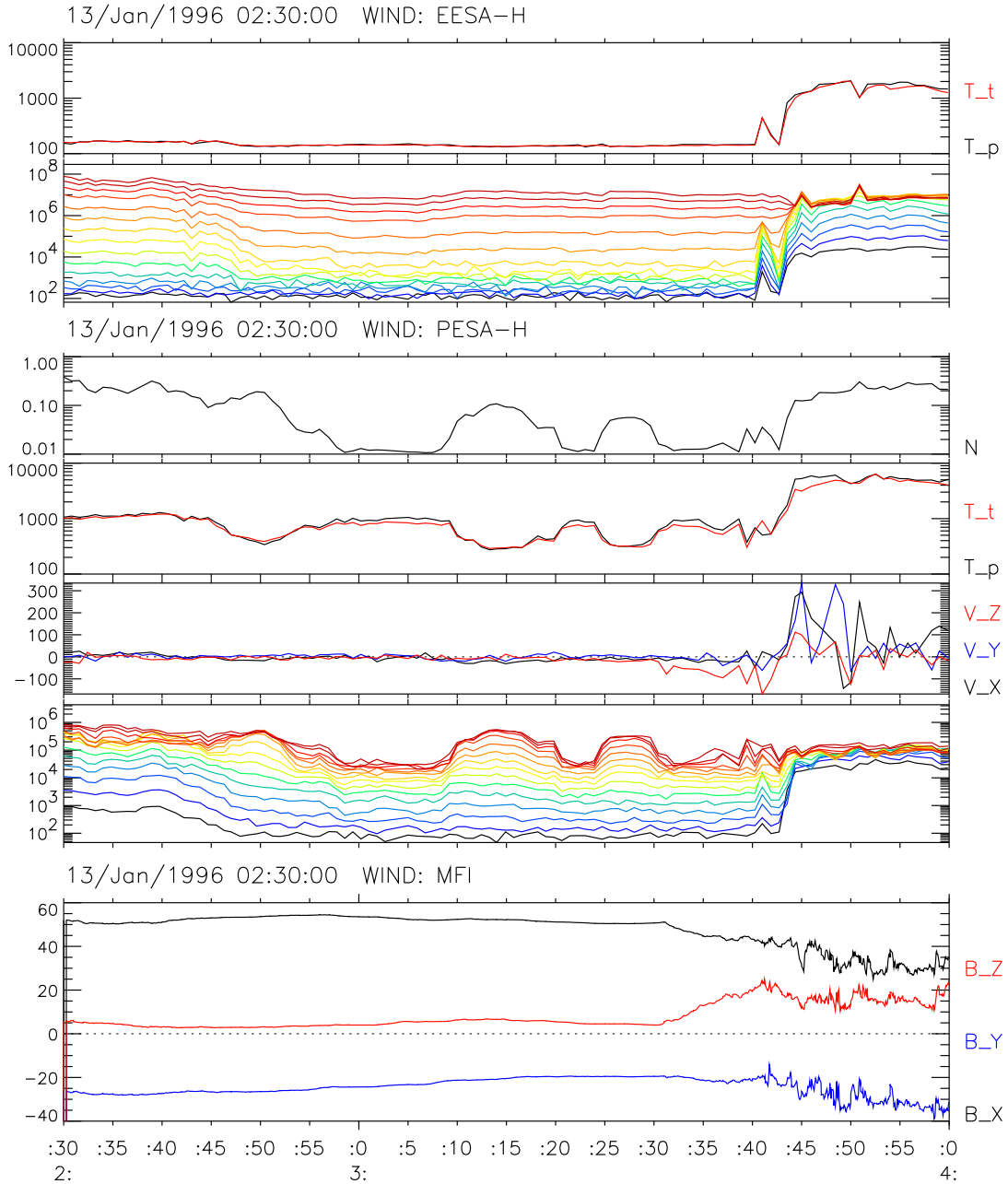


Figure 3.10: The Wind satellite observations- top to bottom: the electron temperatures (parallel- and anti-parallel to the magnetic field) and omnidirectional fluxes; the ion density, temperatures (perpendicular and parallel), bulk velocity components (GSM) and omnidirectional fluxes; the MFI, 3 sec. magnetic field: 3 components (GSM). See text for the details.

related to the very low ion density (compare the ion fluxes).

Another important difference between the Interball and the WIND observations is the time of the registered hot plasma injection, detected by WIND between about 03:41 (the first, week precursor and start of the velocity fluctuations) and 03:44 UT (the final hot plasma injection/recovery). This injection is shifted in time of about 12 minutes with respect to that on Interball, located earthward in the same LT sector.

Finally, compare the plasma- and the magnetic field behavior on WIND. The field smoothly changes since about 03:31 UT and the subsequent fluctuations appear only after the moment of injection, at 03:45 UT. The flow velocity increases simultaneously with the dipolarization (about 03:31 UT), initially in $-Z_{GSM}$ (perpendicular to the magnetic field). It then sharply increases in X and Y GSM at the moment of the hot plasma recovery, 03:44 UT, to reach the maximum of above 400 km/s just after 03:45. The magnetic field features on Wind are consistent with the tailward propagation of the cross tail current disruption of a limited vertical extent. I come back to the Interball and the WIND observations further below.

Geostationary orbit

The GOES- and the LANL satellite data has also been searched for signatures of the substorm. Two of the satellites, the GOES 8 and the LANL 1990-095 were located close to the region of the interest- at 22:03 LT and 00:30 LT respectively at 03:00 UT (compare also the MLT in Figure 3.1).

Figure 3.11 shows the data from geostationary satellites - GOES-8 (a, b) and LANL 1990-95 in (c). In addition, the records from LANL 1991-080 and LANL 1994-084, are shown in panel (d) and (e). Two last satellites were located at the morning flank, 07:42 and 09:52 LT respectively, at 03:00 UT.

The GOES 8 data shown are: (i) the 1 minute magnetic field in the local coordinates close to the GSE system (hn eastward-, he earthward-, and hp northward component) and (ii) the 5 min averaged proton fluxes, (p1, p2 and p3 in energy ranges 0.6 - 4.2 MeV, 4.2 - 8.7 MeV and 8.7 - 14.5 MeV respectively). The magnetic field plot clearly shows two dipolarizations taking place after 03:02 and 03:36, seen as the sharp increases of the northward component (hp). The second of them shows no significant change of the earthward component (he) and both are accompanied by decrease of the eastward component (hn). Note also the similar and significant, but slower effect of the field reorientation between 03:15 and 03:19 UT. It coincides with the northward expansion of WEJ at higher altitudes on the ground in Greenland, more eastward (see the previous subsection). There was no clear changes in the high energy electron fluxes (above 2 MeV, not shown) on the GOES 8, contrary to the proton data (ii). Although with the low, 5 minute time resolution only, they evidence the injection near 03:00 UT, in general accord with the time of the dipolarization (and with the Interball observation of dipolarization and weak electron injection). The observations at different energies may suggest the proton injection with a weak energy dispersion but low time resolution does not allow for more conclusions. The GOES 8 dipolarization of 03:36 UT is not accompanied with as strong increase of energetic proton fluxes as that of 03:02 UT, but it is seen in two higher energy channels (4.2 to 14.5 MeV) after 03:35 UT. There is also a significant (nearly 1 order of magnitude), sharp increase of the X ray intensity on GOES 8 (not shown) at that time (03:35 UT) which suggests the increase of electron flux below 2 MeV at that time (the injection).

The Los Alamos satellite 1990-095 (L90), 1991-080 (L91) and 1994-084 (L94) data on Figure 3.11 (three lowermost panels) are the SOPA instrument- energetic electron fluxes in the energy channels (top to bottom): 50 - 75, 75 - 105, 105 - 150, 150 - 225, 225 - 315 keV and 315 - 500 keV. There are two injections seen on L90, the first one with the small energy dispersion seen near 03:10 UT and the second seen after about 03:35 UT. These injections are also observed on L91 and L94, located in the morning sector, with the time shift of nearly 5 minutes. In addition, there

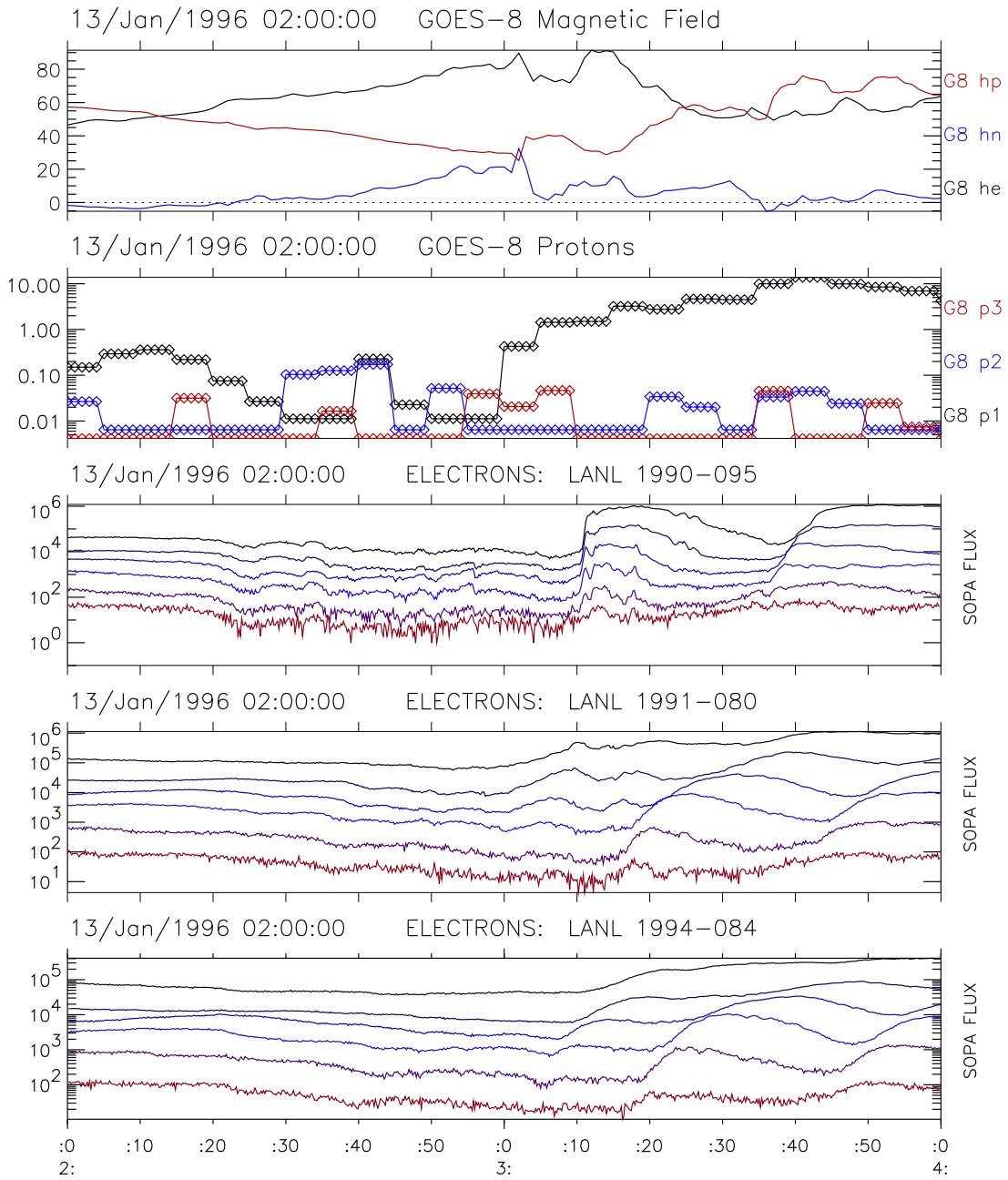


Figure 3.11: Geostationary satellite's data, from top to bottom: (i) three components of the GOES-8, 1 minute averaged magnetic field: northward (hp, red), earthward (he, black) and eastward (hn, blue); (ii) GOES-8 high energy proton fluxes (5 min. averages): the energy ranges for three channels, p1 (black), p2 (blue), p3 (red) are 0.6 - 4.2 MeV, 4.2 - 8.7 MeV and 8.7 - 14.5 MeV respectively; (iii) 1990-095 SOPA electron fluxes (channels e1 to e5); (iv) 1991-080 SOPA electron fluxes (channels e1 to e6); (v) 1994-084 SOPA electron fluxes (channels e1 to e6). (The energy ranges for the electron channels e1 to e6 are respectively: 50 - 75, 75 - 105, 105 - 159, 150 - 225, 225 - 315 and 315 - 500 keV.)

is also a smoother flux increase seen near 03:00 UT at the four lowermost energy channels (50 - 225 keV) on the L91 (d) which is even more clearly reproduced, with the appropriate time shift, in the L94 data (e). This injection is not seen in the L90 record, but closely follows the weak, temporary flux dropout at 02:56 UT. Similar features has been discussed by Sergeev et al. 1992, [176], who called them Drifting Electron Holes. The mechanism of their creation is principally the same as of "ordinary" injections (i.e. the change of the locally observed particle drift shells related to dipolarization and energization of particles). The final effect, decrease or increase of flux at given energy, depends on the degree of energization, the radial gradient of fluxes and the relative position of the satellite to the injection region. I come back to this subject below. Note that the injection starting near 03:10 UT on 1990-095 is in fact composed of multiple components of short duration (1- 3 minutes) continuing until almost 03:18 UT. They drift disperse, not being observed by the flank side satellites and can be related to the oscillations seen in the midnight sector magnetograms from Greenland (Figures 3.2 (c) and 3.4 (b)). Such "injectionlets" observed during a substorm expansion phase were reported and discussed by e.g. Sergeev et al. 1998, [178]. These smaller scale features should not be confused with the injections of larger scale reported here and won't be further discussed in this study.

It is well known, that the geostationary region (or closer) injections can show "echoes", when the injected particles trapped in closed drift shells disperse slow enough to be detected at the second (or subsequent) turn around the Earth (see e.g. Friedel et al., [54]). In the case of hundred keV particles, as in our case, the drift periods can be of the order of 20 or less minutes (above some 200 keV). Thus, one cannot apriori rule out the possibility that we do observe echoes and not the separate injections for the second or the third event above. In the following section it will be shown, that the simple model drift calculations support the hypothesis of three injections.

The LANL SOPA energetic proton data are not shown, cause they were not available from the L90 for this time range and do not show as clear effects as the electron data for L91 and L94.

Summary of the satellite observations

The satellite observations, both from the geostationary orbit and from the near earth, pre-midnight plasma sheet, show the features typical to a substorm expansion phase. More exactly, there are signatures of two or three plasma injections and magnetic field dipolarizations seen.

The signatures of three plasma injections are found in the geostationary region, accompanied by the dipolarizations. These (large time scale) injections support the ground observations (from the preceding subsection) of three substorm intensifications.

In the same pre-midnight sector, slightly further down-tail and just below the neutral sheet, two of the corresponding dipolarizations and electron injections are also observed by Interball (at 03:02 and 03:32 UT), but having the different amplitude and showing a time shift relative to the geostationary region. On the other hand, there is no sign of injection or dipolarization near 03:12 (see Figure 3.9). Another important feature observed by Interball is the strong magnetic field fluctuations preceding the dipolarizations and accompanying the disappearance of low energy, parallel electron fluxes. They can be explained as the in situ observations of current disruptions related to the substorm expansion phase (e.g. Lopez and Lui 1990, [102]; Roux et al. 1991, [160]; Lui 1996, [106]).

Yet further down-tail, in the same LT sector but just above the plasma sheet, the two first events are not seen except only the weak proton signatures suggesting the plasma sheet thickening or movements. Only after the third intensification onset has been observed closer to the earth and on the ground, the dipolarization and the following, nearly 12 minutes delayed, hot plasma recovery is seen there. The magnetic field and the plasma data here are consistent with the tailward propagation of the cross tail disruption region of a limited vertical extent.

3.4 Summary and discussion

3.4.1 Multiple intensifications

One can estimate the time (UT) and the location (MLT) of the near-geostationary injections from data of the geostationary satellites. I performed the backward tracing of the electron trajectories (more specific, the gyro-center drift paths of equatorially trapped energetic electrons) in the simplified electric- and magnetic fields, using the LANL SOPA data as the input. The drift was given by Equation 1.1 in Section 1.2. The model magnetic field was composed of the dipolar-, the ring current- and the tail current components as in e.g. Friedel et al. 1996, [54] (after Roederer; see equation A1 there for description, details and references). The electric field used was the Volland- Stern model for the cross tail- plus the corotation component, as used by e.g. Korth et al. [96], Friedel et al. 2001, [55], who modeled the plasma sheet access to the geosynchronous- and closer region. The Kp dependence of the electric field has been parametrized using both the "Maynard and Chen" and the "Gussenhoven" methods (so called after Korth et al. 1999, [96] - see there for the details and further references) and gamma, the "shielding parameter" of the electric field model, has been set to 2, 3 or 4 (we tried different values and choosed the ones to best model the observed electron data).

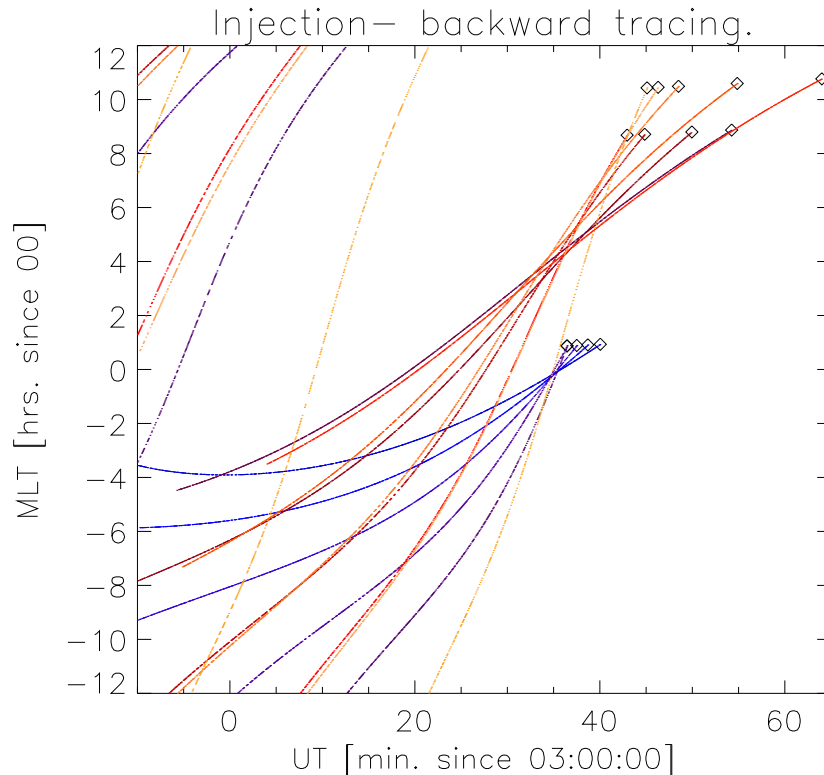


Figure 3.12: The example of backward tracing of electron trajectories for the third injection event (after 03:32 UT)- the MLT as function of the UT. Initial locations are marked with small diamonds and the different trajectories are marked in different colors. The values of the parameters used were: gamma=3, Kp=5 (see text for the description and discussion).

The results of such tracing, especially the particle energization near the injection region, strongly depend on details of the electric and the magnetic fields used and one may argue that some better models could be used in the drift calculations (as e.g. in detailed studies of the geostationary injections of Reeves et al. 1991, [153] and 1992, [154] or Sergeev et al. 1998, [178], who used the modified Tsyganenko T87 magnetic field model in the injection- related case study).

Without the information on the solar wind conditions it is, however, difficult to adequately model the magnetic- and the electric fields. Moreover, the dipolarization- related induction electric field models are poorly developed and not taken into account at all here, though it can play an important role in the injection. Finally, we are not interested in the small scale details of the injection (as e.g. the "injectionlets" with the time scale of about 1 - 3 minutes in Sergeev et al. [178]). In conclusion, these drift calculations can still be useful to estimate the time and the azimuth of the injection, at least while not exceeding too far the geosynchronous orbit.

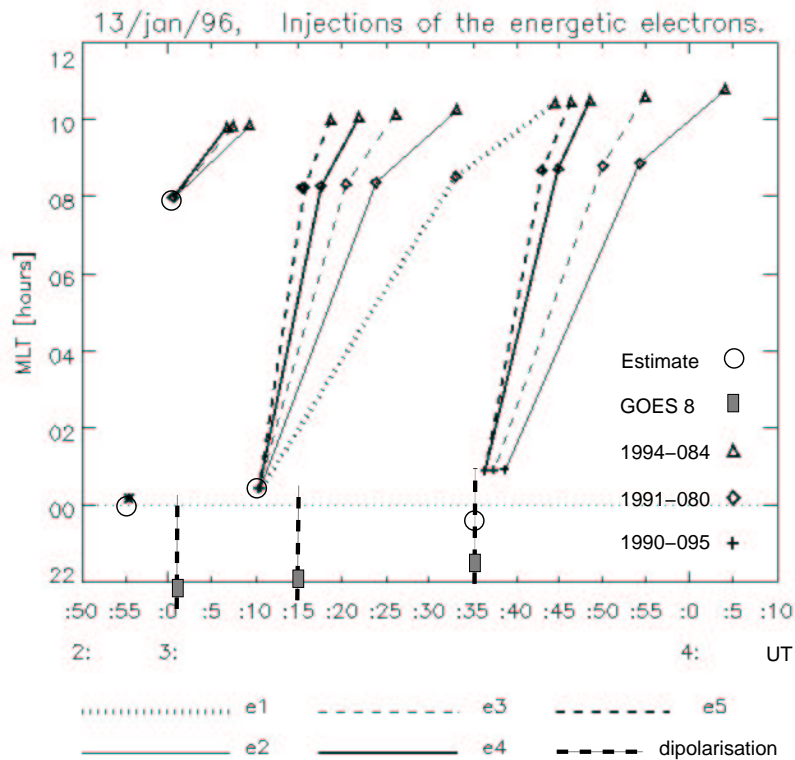


Figure 3.13: Estimated time and location (UT/MLT) of electron injections in geostationary region (marked by open circles), from the SOPA measurements on the LANL satellites 1990-095, 1991-080 and 1994-084. e1 to e5 correspond to energy channels 50 - 75, 75 - 105, 105 - 150, 150 - 225, and 225 - 315 keV respectively. The satellite position at the start of the injection seen in the specific energy channel is marked. In addition, the first dipolarization deduced from the Drifting Electron Hole on L90 is marked near 02:56 UT. The dipolarization times seen by GOES 8 and the satellite locations are also marked by thick, vertical dashed lines (the MLT extents of the dipolarizations are not meaningful). Note that the straight lines on the plot only join the points of the same energy at different satellites and DO NOT correspond to the trajectories.

The example of trajectory calculations in Figure 3.12 shows the MLT of the particles as the function of UT for the third injection. Here I took gamma of 3, Kp of 5 and used the "Gussenhoven" parameterization. The geostationary injection is clearly seen near 03:35 UT, at 23:31-23:56 MLT, inferred from the observations of 1990-095 (near 01 MLT). There is however another "focal point" of trajectories (from the data of 1991-080 and 1994-080 spacecrafts on the flank side) seen near 03:36:30 UT and 04:24-05:16 MLT. Such grouping of the morning flank side trajectories in a separate point was often found in our calculations, although the effect decreased with the increasing Kp and gamma values. I attribute this to inadequacy of the simplified electric- and magnetic field models, the formation of the injection front further out of the geostationary

orbit and of not taking into account the pitch angles different from 90 degrees. This also reflects the azimuthal extent of the injection front. I further use the times and locations of the estimated points on the westward side. Another feature in Figure 3.12 is that only the highest energy particles (above 250 keV) in the third injection could be the "echoes" of the more recent events. Only these particles would drift fast enough to be found near MLT midnight at 02:55 or 03:10 (see below), where the previous injections are supposed to occur. In the case of the second injection (near 03:10, see below), we found the same possibility for the particles above some 250 keV. Note however, that the diffusion processes can often lead the injected particle population to significantly disperse on shorter time scales and such echoes need not necessarily to be detected.

To conclude, the simple modeling can give the MLT range of geostationary injections and provide its sharp UT estimate. I apply the model to get the time and azimuth of the geostationary injections. It is shown in Figure 3.13, which shows the moments of the sharp electron flux increase, observed locally on the LANL satellites in different energies. Also the interpolated time-and-location points of dispersionless injection (open circles) are put there, as well as GOES-8 locations at the moments of the dipolarization (marked by thicker, vertical dashed lines).

Two estimated, well separated electron injections are surprisingly well seen at about 03:10 UT and 03:34 UT, located at 00:35 MLT and 22:52 MLT respectively. Note, that we are dealing with the large time scale injections and not with the small scale (1-3 minutes) "injectionlets" discussed e.g. by Sergeev et al. 1998, [178]. They are seen between 03:10 and 03:18 on 1990-095 in and Figure 3.11 together they constitute a larger- scale feature discussed here.

In the case of the another injection, chronologically the first one and observed only by the two dawn flank satellites, it is harder to find the injection region and the obtained value of 08 MLT is rather the exotic one. Using the (weakly) time dispersed signature of the small electron hole (see Sergeev et al. [176], [178]) in the L90 electron fluxes seen near 02:55 UT, I can roughly estimate the time (UT) of the dipolarization. The MLT of the obtained point (marked as the light square near 02:55 UT and 00:05 MLT in Figure 3.13) can also give us the estimate the westward boundary of the dipolarization and the injection region. In such a way I can localize the first (electron) injection somewhere eastward to 00:05 MLT (and westward to 08 MLT).

The above results, showing three distinct events, support the suggestions from the ground-based observations of three separate substorm intensifications. The observations show (e.g. Sergeev et al. 1998 and 1999, [178], [179]; Petrukovich et al. 1998, [145]) that the substorm activity is accompanied by transient auroral forms (streamers). They start on the poleward edge of the auroral oval, have the azimuth extent of the order of 1 - 2 hours MLT (ground) or below $3 R_E$ in the near tail. Their duration time is comparable to those of the BBF events (a few minutes) with which they are related to. They also show a significant north-south component of the optical pattern. Note however, that this is not the case, as we have to do with the poleward expansion events starting at the lower latitudes (see Figures 3.2, 3.4, 3.3). In this context, finding of Liou et al. 2001, [101] can be recalled, relating geostationary particle injections with substorm intensifications. Although the dispersionless injections are scattered in time relative to the start of the auroral breakup (-2 to +8 min. on average), they are mainly clustered within 1 hour MLT of the breakup longitude (as defined by the Polar UVI imager) in a broad MLT range between about 20 and 01 MLT.

In such a way, the second (03:10) injection should have its auroral bulge counterpart, and also the magnetic disturbance signature, located close to the Greenland West Coast. This is seen on Figures 3.2 (c) and 3.4 (b). Similar correspondence for the third injection (22:52 MLT at 03:34 UT) located eastward to the CANOPUS and very close to the PBQ, is worse. Both the UT of the first ground magnetic signatures (03:29 UT at PBQ, Figure 3.2) and the MLT of the first detected auroral intensification (about 21:30 MLT at 03:32 UT, see Figure 3.6) differ from the coordinates of the injection point in Figure 3.13. Note however, that the PBQ is located nearly 1.5 hour eastward to the all sky camera at GILL, whose field of view does not cover the

PBQ location and so a time shift in observed features between the two sites is possible. Also the injection locations in Figure 3.13 are only the crude estimates of their eastern boundaries. These two arguments can eventually explain the different location (UT/MLT) of the injection and of the auroral breakup. When applied to the first injection (02:55 UT, eastward to 00:05 MLT), the similar correspondence to the NAQ, AMK, HUS and TJO magnetic signatures are also good enough to accept the above estimated injections as related to the observed features.

There is a good agreement between the independent estimated values of the injection and the dipolarization times (UT), for the first and the third injection events. But the MLT sectors are only similar for the 03:34 event. There is also the discrepancy of about 4.5 min. UT between the estimated start of the second injection and the beginning of dipolarization recorded by GOES 8 more westward. Similarly, the difference in UT between the dipolarization at GOES-8 and the estimate based on L90 electron hole is about 5.5 min. What is similar between two first events is the positive time lag between the injection and the more westward observed dipolarization signatures. This can be interpreted as the effect of the azimuth expansion of the dipolarized region (the current wedge). The obtained expansion rates are discussed in the following subsection.

As to the Interball Tail and the WIND observations, there was no signatures of all the three injections. The narrow extent (below $3 R_E$ at $X = -12 R_E$) of the observed injection regions in the magnetotail (e.g. Petrukovich et al. 1998, [145]; Sergeev et al. 1999, [179] and 2000, [180]) could be a reason that we completely missed the second, and partially (on WIND) missed the first injection. Note however, that their observations are related to pseudobreakups and/or transients poleward intensifications and not to a substorm expansion/intensification. Recently Rostoker [159] discussed the criteria to identify and distinguish a legitimate substorm expansive phase from two another types of the auroral activity (compare also e.g. Rostoker [158] and Aikio et al. [1] and the references therein). The magnetic observations related to all three injections presented here show clearly the poleward expansion and suggest that we have to do with true substorm expansions/ intensifications. In addition, the onset of the magnetic disturbance at GILL, localized in the region of the maximum auroral H_β emission further support this suggestion (see Rostoker 2002, [159]) for the third event. Thus, the reported observation of three localized injections related to three separate substorm intensifications seems to be a new result.

3.4.2 Expansion rates of the disturbed region

With the times and the coordinates of local signatures of the onset, we can estimate the expansion rates of the "disturbance". In the case of 03:10 injection, we have the estimated MLT of the injection and the point where the dipolarization was observed by GOES-8 (Figure 3.13). For these two points, the distance from 00:37 MLT to 22:07 MLT is traversed in 4.5 min, which gives the azimuth expansion velocity of about 8.3 degree/minute, or 103 km/sec. on the geostationary orbit. The same estimation can be done for the first dipolarization, but the exact MLT location is not known, and the estimated geostationary injection at 08 MLT is rather exotic one. Taking the proper MLT somewhere between this value and that from the DEH on L90 (the light square, about 02:55 UT and 00:07 MLT in Figure 3.13) we have the expansion velocity of 4.7 - 16.9 degrees/minute, or 58 - 209 km/sec. on the geostationary orbit. These are not very different from the other observations and from the modeling results (e.g. Fok et al. 1999, [49] and Thomsen et al. 2001, [196]).

In Figure 3.14 I combined the MLT (a) and the CGL coordinates (b) of start points of selected ground- and satellite observed features: negative bays, injections and dipolarizations. The term "disturbance" is used below in a generic sense to denote the different kinds of a substorm expansion signatures. This approach helps to present the observations in a synthetic way, though it may assume that they are related to a single physical process, which need not necessary to be true. It seems that the substorm current wedge could be an acceptable candidate for an object described

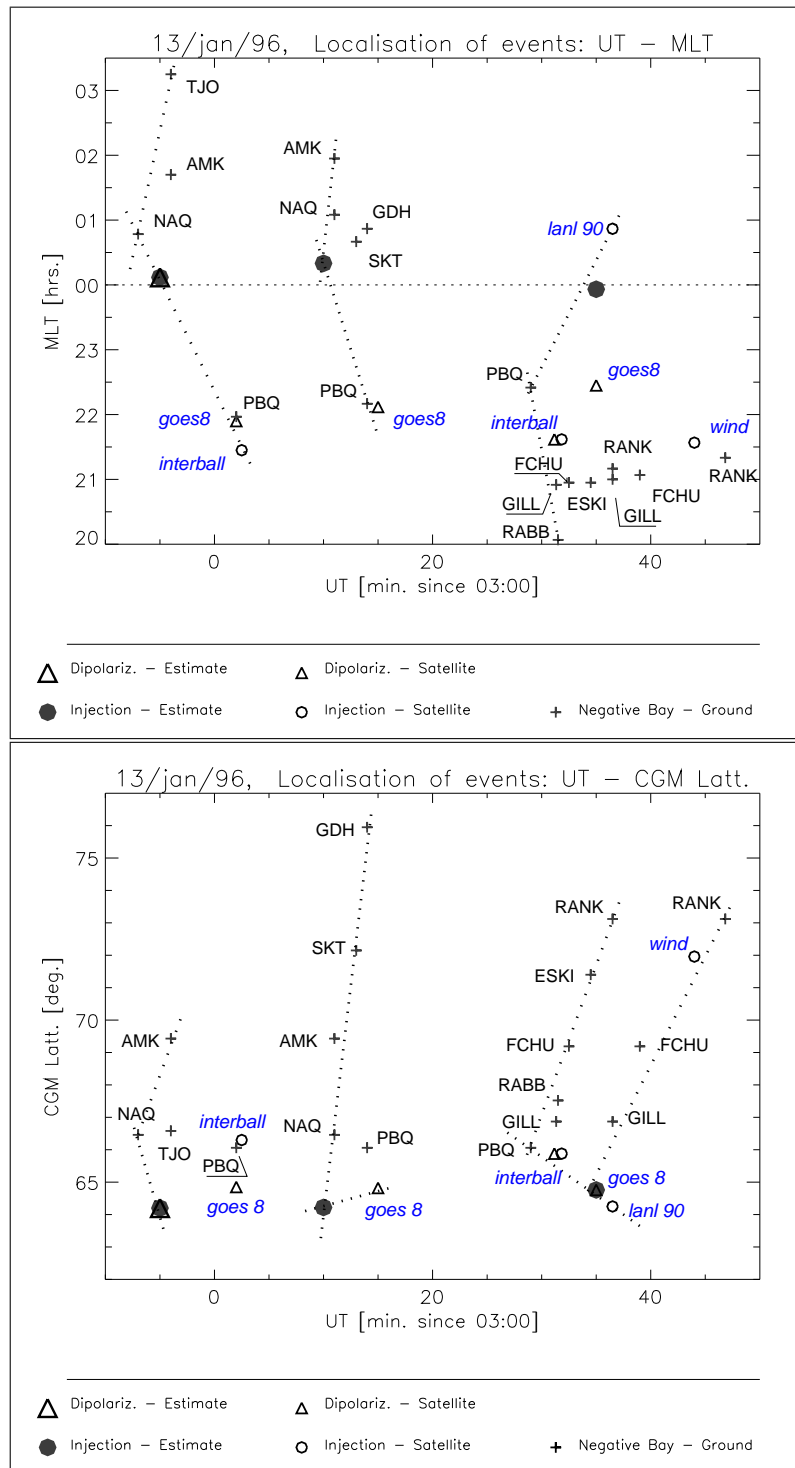


Figure 3.14: The MLT- (top) and the CGM Latitude coordinates (bottom) of selected ground- and satellite observed features: negative bays, injections and dipolarizations. The selection is made to better visualize expansions of disturbed regions for three observed substorm intensifications. Dotted lines help to delimit the disturbed regions.

in this way, but detailed considerations are out of scope of this work. We use such approach as a tool to apply to large scale aspects of the substorm expansion.

The injection events shown are the estimates obtained above (see Figure 3.13) as well as points from Interball and WIND. Only selected ground stations has been shown to clearly visualize the expansion process. Dotted lines are put in the plot, to delimit the regions where the start points of the observed disturbance fall into. In the CGL plot (b), the delimiting points are different than in the MLT (a). Note, that the same points on dotted lines in the UT-MLT (UT-CGL) plot may have different CGM (MLT) coordinates- compare (a), (b) and Figure 3.1. The points, not joined with the dotted lines all have the different CGL (MLT) coordinates. Because of that, dotted lines would rather provide a limiting values of the azimuth expansion rates. Note also, that only the limited range of MLT and CGL coordinates is considered.

The main things to find are: (i) All the observational points from the ground are well organized into three groups of events. It can be seen, that the estimated geostationary injection points fit well into them. For each group of points, there is the well defined start point in the MLT - CGL coordinate system, : the NAQ ground station at 02:53 UT, the estimated geostationary injection at 03:10 UT and the ground station PBQ at 03:29 UT. These points would correspond to the location(s) in space, where the substorm intensification start to develop. (ii) The azimuth expansion of the "disturbance" is easily seen in plot (a) (see the dotted lines). The expansion can explain the time differences between the observed geostationary dipolarizations and the injections or between the geostationary- and the ground onset signatures, mentioned above. E.g. the (azimuthal) expansion from the NAQ (02:53 UT) results in the time delay between the estimated geostationary injection, the GOES-8 dipolarization and even the Interball- observed features. The same can be seen for the PBQ expansion (03:29 UT) eastward to the LANL 1990 position. The eastward- and the westward expansion speeds are comparable, but change for each event. We estimate the expansion velocities from the points of similar CGL in Table 3.1 (a). (iii) The CGL expansion is seen in the plot (b). Two lines has been put for the third event in accord with the observations (see Figures 3.2, 3.3 and the next subsection). We put the estimated CGL expansion velocities for the points with similar MLT in Table 3.1 (b). (iv) The CGL of the start points in (b) show that the disturbances begin slightly outside the geostationary orbit in the first and in the third event, and then develop both tailward and earthward. It is clearly seen in both ground- and space data, especially for the third intensification, and is a very interesting observation (For the inward expansion, compare first of all the location and timing of events since 03:29 UT for PBQ and GOES-8, located very closely in MLT- 5 minutes or 1.25 deg. at 03:30 UT). Contrary to the above, the second intensification starts closer. Only outward expansion could be seen for third event, due to lack of the magnetic observatories south to Greenland.

The above estimates of the azimuth expansions of disturbed region can be compared to other observed and modeled values. E.g. Thomsen et al. 2001, [196] estimated the azimuthal expansion rates of the injection front from 43 geostationary injection events. For the electron injections, their values, especially the eastward expansion rates are mainly above 0.5 - and up to 2 LT hour/min. (see their Figure 10) and exceed slightly our estimates. On the other hand, values of westward expansion rates in the pre-midnight sector are more similar to ours. High dispersion and asymmetry between the pre- and post midnight sector also makes their- and our results similar. Modeling of plasma injection boundary of Fok et al. 1999, [49] resulted in 100 km/s azimuthal expansion rate, near- and outside of the geosynchronous region, which compares quiet well with our estimates (-62.7, -103.1, 115.5 km/s, obtained only with the points on the geostationary orbit in Table 3.1 and assuming the distance 6.7 R_E with $R_E=6371$ km.). The recent results on the auroral arcs expansion in the high latitude ionosphere of Safargaleev et al. [163] appeared when I was finishing this work. They obtained values of 2-3 km/s, comparable to earlier values the substorm current wedge- (a few km/s, Opgenoorth and Pellinen, [139]) or auroral bright spots expansion rates (order of 10 km/s e.g. Oguti, [132]). For the comparison, our observations related

	Event	Points used	MLT expn. rates [deg./min.]
(a)	1	NAQ, TJO.	12.3
	1	NAQ, Interball.	-5.3
	1	NAQ, AMK.	4.3
	1	NAQ, PBQ.	-4.7
	1	Estimate, GOES8, Interball.	-4.8, -5.3
	2	Estimate, AMK.	24.3
	2	Estimate, GOES8.	-8.3
	2	Estimate, NAQ.	11.3
	2	Estimate, PBQ.	-8.1
	3	PBQ, Estimate, LANL90	3.8, 4.9
	3	PBQ, GILL	-5.0
	3	Estimate, LANL90	9.3
	3	PBQ, Interball	-4.6

	Event	Points used	CGL expn. rates [deg./min.]
(b)	1	NAQ, AMK.	0.99
	1	NAQ, Estimate.	-1.13
	2	Estimate, SKT, GDH.	2.64, 2.93
	2	Estimate, NAQ.	2.24
	2	Estimate, GOES8.	1.15
	3	PBQ, FCHU, ESKI, RANK.	0.89, 0.97, 0.94
	3	PBQ, Estimate, LANL90.	-0.57, -0.51
	3	Estimate, GILL, FCHU, Wind, RANK.	1.41, 1.11, 0.8, 0.73
	3	GILL, FCHU, ESKI, RANK.	1.98, 1.43, 1.21
	3	PBQ, Interball.	-1.49
	3	(BZ contour plot)	1.33

Table 3.1: The MLT (a) and the CGL (b) expansion rates of the substorm disturbed regions [deg./min.] inferred from the observed points in Figure 3.14. Positive values correspond to eastward- and poleward directed expansion. Note that the different points are used to calculate the MLT- and the CGL expansion rates. The value in the last line in (b) is the estimate from the BZ contour plot (on lower panel of Figure 3.3) between 03:31:30 and 03:37:30 UT.

to the ionosphere at 70 deg. latitude result in values between 2.4 and more than 15 km/s.

The latitudinal expansion rates in ionosphere (at 100 km) take values between 0.95 and 2.8 km/sec in equatorward-, and 1.37 to 5.52 km/sec in poleward direction. This is lower than the azimuthal expansions (above) but clearly faster than the usual velocities of northward |southward expansion of an individual arc (of the order of 100 m/s) reported in the mentioned work of Safargaleev et al. [163] or earlier by Haerendel et al. [59] (below 500 m/s). Such big difference, nearly one order of magnitude, is significant but need not to be discriminating validation of our estimates. They are not based on individual arc expansions neither on short (a few minutes) electrojet- or injection- structures. Such fine scale auroral structures and "injectionlets" are the components of the large scale structures, that were used to obtain our estimates.

Looking back at the BZ contour plot from FCHU chain (see lower panel of Figure 3.3), we see the poleward movement of WEJ for the third intensification. It continued with the constant speed until 03:37:30 UT and stopped at 03:48 UT (see the 0 value contour line). WEJ expanded then both poleward and equatorward between 03:37 and 03:48, then started to intensify (without displacement). The poleward movement rate of WEJ obtained from from this (put into the last line in Table 3.1) is comparable to other estimates.

Taking into account the time shift in the observed features on the WIND and on the Interball satellites (about 12 minutes for the 3-rd event) and the distance between them (nearly 4.3 R_E in X_{GSM}), one gets the tailward expansion velocity about 38.0 km/s. It is significantly less than the tailward propagation velocities reported earlier: e.g. 160 - 260 km/s (between the geostationary region and $X_{GSM} = -13 R_E$, Jacquy et al. 1991, [74] and 1993, [75]) or 270 - 380 km/s (downto nearly -35 R_E , Sauvaud et al. 1996, [169]), but such simplified estimate does not seems to be appropriate. In the following section, I further explore the opportunity of simultaneous multi-point observations in the same LT sector for the third event. As it is shown there, a higher propagation rate is obtained with the more careful analysis of the observation.

3.4.3 The 03:30 UT substorm intensification

I can further investigate some details of the last substorm intensification using the ground based- and the satellite data from nearly the same LT sector. The footprints of three satellites: WIND, Interball and GOES-8, found in Figure 3.1 are very close to the station PBQ and the FCHU chain. The MLT location of satellites was not the same as for the stations though, and did not fall into the field of view of the all sky imager at GILL (Figure 3.6). In particular, the Interball footprint was situated about 40 minutes MLT-, or 10 degrees eastward along a constant latitude to the nearest stations ISLL and GILL at 03:32 UT. Similarly, at 03:44 UT the Wind footprint was about 17 min. MLT-, or over 4 deg., eastward to the RANK station. Further eastward, GOES-8 footprint position differs only slightly in MLT (5 MLT minutes at 03:32 UT) from position of PBQ (22:28 MLT at 03:32 UT), while the CGL of the satellite's footprint is lower than the PBQ coordinate (of about 1.29 deg. at 03:32 UT for our mapping, and permanently lower for different mapping parameters).

The inward expansion of the disturbance mentioned above can easily be found in various kinds of data: PBQ- and CANOPUS chain magnetic observations, near-geostationary particle injection (LANL, GOES-8 and Interball data), magnetic observation in space (GOES-8, Interball) and in some other data not shown here (the timing based on the X-ray data from GOES-8 and Interball, the energetic particles- and the AKR- data on Interball is consistent with the above estimates). The time delay between the onset at PBQ and the signatures on GOES-8 is about 6 minutes. It is nearly the same as between PBQ and the estimated geostationary injection, situated at least 1.5 MLT hr eastwards. The onset at Interball, which has the intermediate CGL position, fits well between two above points (Figure 3.14). Relatively slow inward expansion of disturbance, as compared to azimuthal expansion, qualitatively agrees with expectations- the magnetic field dipolarization can not penetrate too close earthward, as well as the injected plasma- the flow is

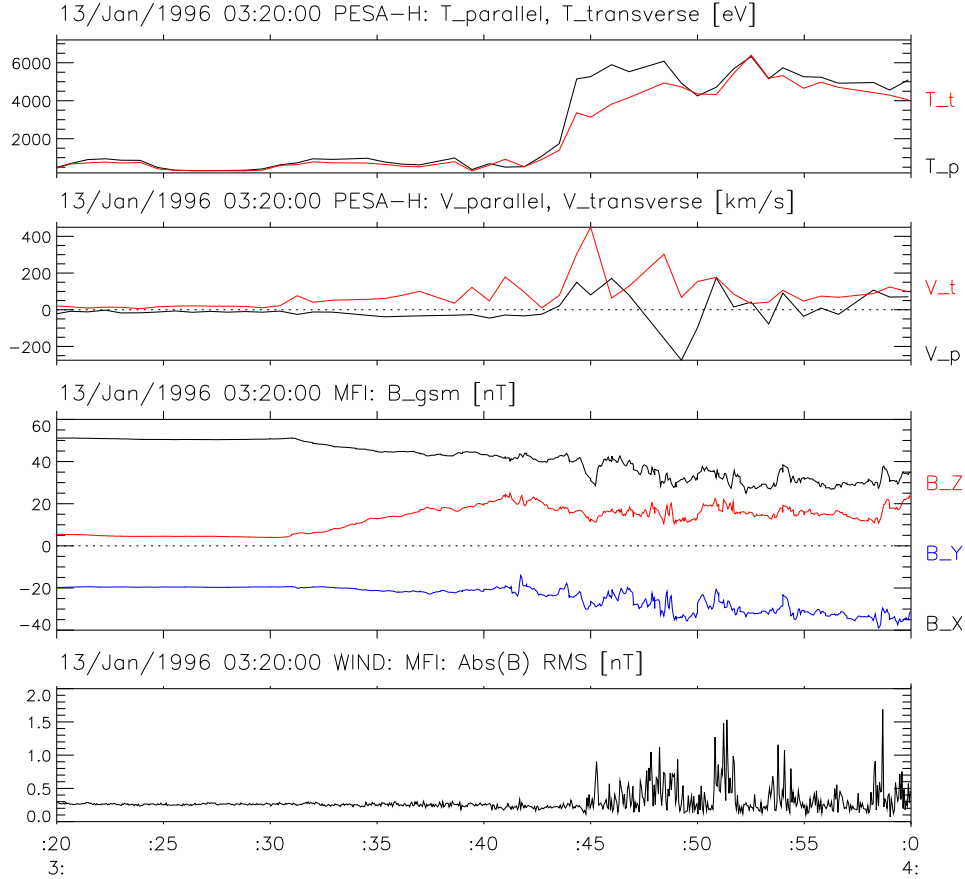


Figure 3.15: WIND ion and magnetic field data for the 3-rd intensification, 03:20 - 04:00 UT. Top to bottom: Proton temperatures, parallel (T_p) and transverse (T_t) to the magnetic field; Flow velocities (parallel and transverse); 3 sec. sampled magnetic field (GSM); Root mean square of 3 sec. fluctuations of $|\vec{B}|$. Note the time delay between the maximum of B_Z and the beginning of the plasma sheet recovery (almost 2 minutes) and the onset of the magnetic fluctuations (nearly 4 minutes).

braked and diverted towards flanks in region of increasing magnetic field (e.g. Birn and Hesse 1996, [12]; Shiokawa et al. 1997, [182]).

The disturbed region is simultaneously expanding tailward, as follows from ground- and satellite observations, especially when comparing the Interball and the WIND observations. The disturbed region in this case corresponds to the current wedge as follows from the magnetic- and plasma data. The estimation of tailward expansion rate from time delay and distance of two satellites, done in the previous subsection, leads to expansion rates significantly lower than published elsewhere (4 to 10 times). The more careful analysis performed below, provides a better result.

Looking back at the Wind data, we find an interesting feature in the magnetic field (as compared to the plasma, see Figure 3.15). The field starts to change (slowly dipolarizing) since 03:31:40 UT, almost simultaneously with dipolarization close to the earth, but the changes are smooth. No fluctuations are seen before the hot plasma recovery, at about 03:44:50 UT. While the B_X and the B total constantly decrease, the B_Z reaches maximum near 03:41:10 UT and then starts to decrease, staying positive. The plasma flow is initially weak and transverse to \vec{B} (southward, compare Figure 3.10). It sharply increases near 03:43:30 together with the temperature. Note the significant, parallel anisotropy of temperature and parallel flow since that time. In the Interball data (see Figure 3.9) we find signatures of current disruption at 03:31:30 UT and hot plasma

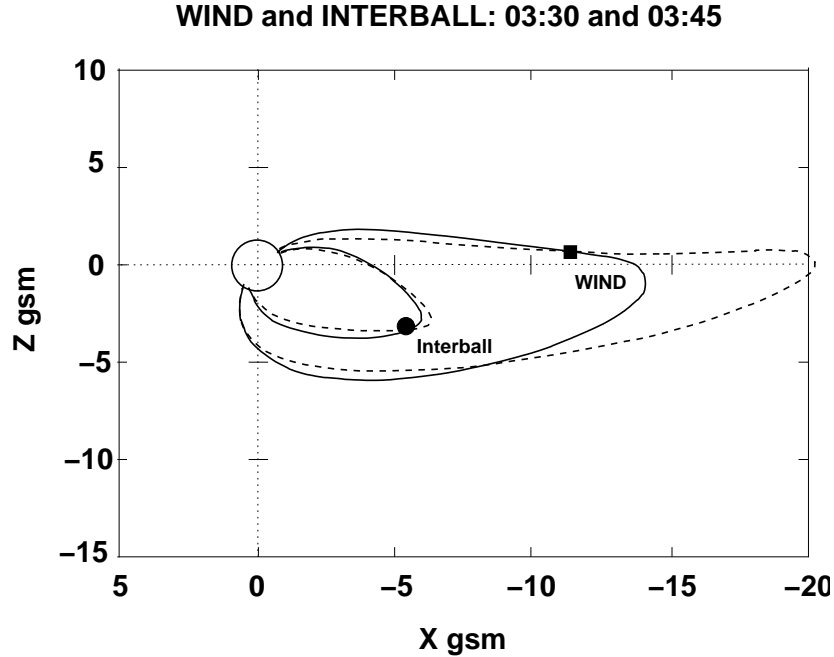


Figure 3.16: The model magnetic field lines (T96) passing by 2 satellites. Dashed line (03:30 UT)- just before the dipolarization/injection seen on Interball; Solid line (03:45) just after the plasma sheet recovery on WIND. Two spacecrafts separated by nearly $4.3 R_E$ are magnetically connected to more distant points of the neutral sheet (here, the separation is above $14 R_E$).

injection shortly after (03:32 UT). These two features occurred almost simultaneously, in contrast to the WIND observations.

This behavior can be understood in terms of a tailward propagation of the current disruption region (compare e.g. Jacquy et al. 1993, [75]; Sauvaud et al. 1996, [169]). Figure 3.16 shows the model magnetic field lines traced from the locations of the Interball and the WIND satellites at two instances, 03:30 and 03:45 UT, just before the dipolarization at Interball and just after final plasma sheet recovery at WIND, respectively. The model magnetic field (T96 and T89) used for the mapping, depend on the solar wind parameters, which are not known. The comparison of the observed magnetic field and the model output for various solar wind parameters has been done, assuming the negative Z component of the interplanetary magnetic field, in accord with the prolonged period of increasingly negative Dst index. Varying other model parameters (the dynamic pressure, the values of IMF B_Z , and B_Y) the attempt was made to get the values similar to observed locally on two satellites. The fully satisfactory result was not obtained, which can be attributed to properties of the models, especially to their statistical character and not adequacy to the expansion phase of a substorm. The principal result, however, is that the model field more similar to what was observed resulted in the field lines reaching further downtail, usually between 20 and $40 R_E$ and not closer than $17 R_E$ in X_{GSM} in case of mapping of the WIND position. The WIND is then magnetically connected to a region more distant in the neutral sheet than the spacecraft's position. It should be taken when considering the expansion rates.

Reaching the maximum by the B_Z suggests that the disturbance is close behind the WIND X-position, but is not reaching its Z position, staying confined near the neutral sheet. Note that the Wind is located above the plasma sheet and even in the increasingly dipolar configuration more earthward, the B_Z can stay positive if the current disruption takes place in a vertically confined region. Figure 3.17 illustrates this scenario. At time t_1 (03:31), a current disruption occurs close to the Interball position (the field line labeled "1"). The current wedge, with dipolarized magnetic field, thickened plasma sheet and "active" region of thin current sheet disruption, propagates

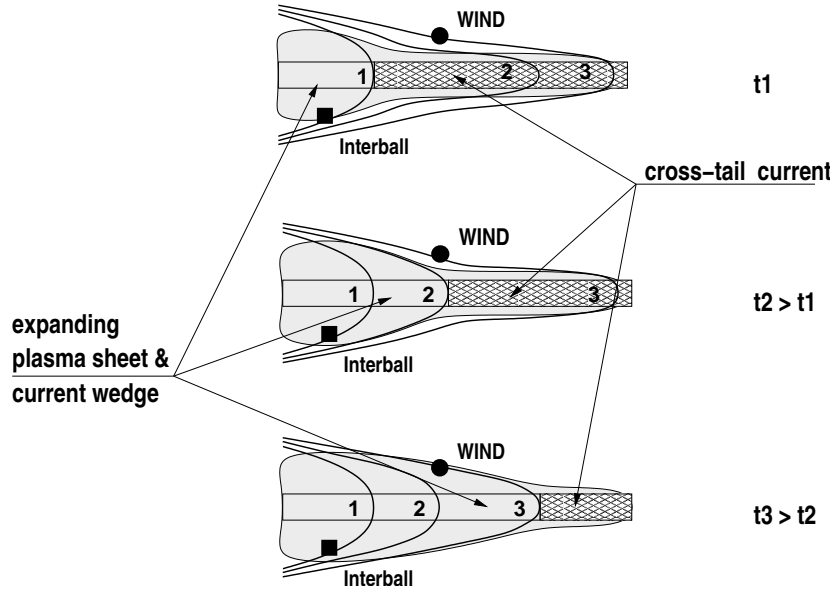


Figure 3.17: Sketch illustrating propagation of the current disruption region and the expanding plasma sheet near the WIND. See text for the description.

tailward. If the current layer is thin enough and if the disruption propagates primarily within it, the “active” region reaches the position of WIND in time $t_2 > t_1$ (the field line labeled “2”) and moves tailward, before the WIND can observe the recovered plasma sheet. When the current disruption reaches, at time $t_3 > t_2$, the point further downtail, magnetically connected to the satellite (the field line labeled “3”), the magnetic fluctuations and the parallel accelerated particles can first reach the satellite.

This scenario is supported by detection of the increased magnetic fluctuations and the field aligned-, earthward directed anisotropy of particle fluxes (not shown, but reflected in the enhanced temperature- and the velocity records since about 03:45 UT in Figure 3.15). Nearly 1.5 minute delay between plasma sheet recovery and start of fluctuations also supports the point of view of a quite distant “active” point. These plasma features can be the consequence of a heating/acceleration near the reconnection point in the tail current sheet (see e.g. Delcourt et al. 1990, [35]; Smets et al. 1999, [186]; Hoshino et al. 2001, [65]).

In the above scenario, the proper estimate of tailward propagation speed of the disturbed region would be obtained using the points, where the field lines cross the neutral sheet. The WIND and the Interball, spatially separated by about $5 R_E$ ($4.3 R_E$ in X_{GSM}), are magnetically connected to the regions in the neutral sheet at X_{GSM} of respectively, about $7 R_E$ and somewhere between 17 to $40 R_E$ (e.g. they are separated by nearly $14 R_E$ for the configuration in Figure 3.16). The magnetic field signatures are used of the current disruption at Interball at 03:31:30 UT and of the beginning of magnetic fluctuations at WIND at 03:45:00 UT. Furthermore I take into account the propagation time between the current WIND position and the distant “active” point, assuming the fluctuations are the parallel propagating Alfvén waves of velocity 1000 km/sec (For Interball such propagation time is neglected). The propagation time of the Alfvén waves is between about 0.5 and 3 minutes (about 1 minute for projection in Figure 3.16). Subtracting this time from 13.5 minutes that separate the events on two satellites, we have the tailward (in X_{GSM}) propagation rate between nearly 82 and 333 km/s (119 km/s for the configuration in Figure 3.16). When compared to other results (e.g. 160 to 260 km/s tailward propagation velocity of current disruption, Jacquy et al. 1991, [74] and 1993, [75] or 270 - 380 km/s at slightly larger distances, Sauvaud et al. 1996, [169]) the obtained estimates are acceptable, especially for the preferred projections of the WIND position further than $20 R_E$ downtail.

The results concerning the third substorm intensification are summarized as follows. (i) The multi-point observations are consistent with the initially localized disturbance, expanding both tailward and earthward (and also in azimuth). It has started slightly out of geostationary orbit in the pre-midnight MLT sector. The onset was accompanied by the signatures of a current disruption on Interball and followed by the hot plasma recovery and magnetic fluctuations on WIND further tailward. (ii) The sequence of events on WIND and on Interball suggests a tailward expansion of the “active” region of current disruption, in the sheet of vertically limited extent. This could be a tailward- propagating rarefaction wave, possibly accompanied with a reconnection at the distance between about 17 and 40 R_E downtail. (iii) The estimated tailward propagation rate of the current wedge (between 82 and 333 km/sec) is similar to other observations only for the above scenario of the propagation. The earthward expansion rate is lower, even than the azimuthal expansion and does not depend on the above scenario

3.5 Conclusions

A multi-point, ground- and satellite- based case study of has been presented of the substorm with multiple intensifications. I focused on the large scale aspects of expansion. Main findings can be summarized as follows:

1. Different kinds of observations are combined (ground- based magnetic data from middle- and auroral latitudes in the broad LT sector, optical data from selected, rather limited range of locations, geostationary particle- and magnetic field data, near plasma sheet- and tail observations from WIND and Interball) to get times and locations of the local onset of a substorm- related “disturbance”.
2. It was possible to identify and separate three different, large scale intensifications (time scale of the order of 10 min.) of the substorm. Each intensification was well localized in the MLT, expanding in azimuth and in latitude. The observations are consistent with the near earth substorm initiation and the current wedge expanding tailward-, but in the case of two intensifications, also earthward.
3. The expansion rates were estimated of the “disturbance” (best characterized as the substorm current wedge/ current system), using both ground based- and satellite observations. The azimuth expansions have the velocities between -4.3 MLT degrees per minute (westward directed), and 12.3 (or even 24.3, eastward directed) MLT degrees per minute, in accord with other observations and simulations. The latitude expansion rates was between -1.49 (equator ward-) and +2.93 (poleward directed) Corrected Magnetic Latitude degrees per minute. Compared to expansion rates of individual auroral arcs in ionosphere (hundreds m/sec , these values are nearly order of magnitude higher. This difference is attributed to the fact, that the estimates concern the larger scale features, usually composed of individual small scale structures.
4. The observations of WIND and Interball satellites, located at different distances in the same MLT sector of the magnetotail, allowed to follow the third of intensification in space and to compare this with the CANOPUS chain magnetic- and optical observations. The observations are consistent with a tailward expansion of the cross-tail current disruption in a vertically limited layer. Such expansion is probably accompanied with the reconnection site located not far down-tail (below 40 R_E). Also the inward expansion of the disturbed region was observed in this case.
5. For the above scenario, the tailward expansion speed of the “active” region is comparable to other observations (between 82 and 333 km/sec , with the higher values slightly preferred).

The exact values of the estimated distance and the tailward expansion rate depend however on the magnetic field model.

6. The interesting finding, unexplored here, is the drastic change of the electron energy- pitch angle characteristics at the moment of the enhanced magnetic fluctuations observed by the Interball. The Pi2- and higher frequency fluctuations are accompanied by the disappearance of the low energy, field aligned electron population in the space region magnetically close to ground active region. This suggest a direct link to the upward current region in the ionosphere and can be explained by a current disruption mechanism proposed by e.g. Roux et al. 1991, [160].

In the following chapter I present the results of the search for and of the large scale geophysical analysis of the similar events on Interball Tail. The aim is to select the events for the ongoing investigation of microscopic properties of the electron plasma component.

Chapter 4

Changes of the electron distribution function in the plasma sheet related to the onset of substorm/pseudobreakup.

4.1 Introduction

The large scale, substorm- related phenomena in the magnetosphere are well documented thanks to the multiple satellite observations. These observations, reviewed in Section 1.4 provided the main ideas on the process of substorm initiation and development (the phenomenological models of substorm, in Subsection 1.4.4). The easily observed features are the crossings of plasma sheet boundaries, manifesting themselves as the decreases and increases of the energetic (few keV to tens of keV) particle fluxes. It is interpreted as a thickening/thinning or a movement relative to the spacecraft and reflects the plasma sheet dynamics. Related to the substorm expansion onset on the ground, the observed plasma sheet behavior changes with the position of the observing spacecraft. While impulsively thinning at distances above some $20 R_E$ (e.g. Sauvaud et al. 1984, [166] and 1996, [169]), it exhibits the opposite behavior closer to the Earth, manifesting in the near- geosynchronous region as the hot plasma injections (e.g., McPherron 1972, [146]; Sauvaud and Winckler 1980, [165]).

Klumpar et al. 1988 , [89], reported two events of bursts of field-aligned electron fluxes below ~ 1 keV at $9R_E$. Johnstone et al. 1994, [80], found similar features in the $\sim 100 - 1000$ eV electron data at closer distances on the CRRES satellite. They suggested that the events could be related to substorm activity, though no direct correspondence to the substorm was shown nor investigated. The low-energy electron-flux dropout was found on the geostationary orbit by Roux et al. 1991, [160]. The event was related to the substorm onset on the ground, showing the in situ signatures of the current disruption and the dispersionless injection. They proposed the ballooning mode instability to explain this event and more generally, as a possible mechanism leading to the substorm onset (the associated mechanism of disruption of the magnetic field-aligned current was proposed by Perraut et al. 1993, [142] and 2000, [144] and references therein; see also Subsection 1.4.4).

The fast changes of field-aligned fluxes of low-energy electrons observed in the near-Earth edge of the plasma sheet can be a signature of a transient current /acceleration along the field line. Regarding the adiabatic of the electron trajectories in the quiet near- Earth plasma sheet (see Section 1.3), they should be treated as indicators of fast processes during the disturbed periods. If field-line connected to the active auroral region, such processes are essential for the substorm development (e.g. Lui 2001, [109]; Ohtani 2001, [134]).

At the moment when this work was started, there was no reports (up to the author's knowl-

edge) on the details of plasma properties in the magnetospheric source region of the substorm currents at the onset. Of course, the electron distribution functions are well known from the various regions of the magnetosphere and the plasma sheet, in particular. (e.g. Frank et al. 1981, [51]; Christon et al. 1989 [29] and 1991, [30]; Onsager et al. 1990, [138]). These distributions were also compared to the low-altitude observations, to obtain e.g. the current- voltage relationships for the auroral field lines (see e.g. Shiokawa et al. 2000, [183] and other references in Section 1.3). The observations of the DMSP, Viking and Freja satellites provided important information on the details of the electron distributions on the auroral field lines near the acceleration region (1-2 R_E). More recently FAST added the information from below (4000 km), while POLAR from the above of that region (~ 4 to $7.5 R_E$). See Section 1.3 for more informations and references. In particular, the few hundreds eV electron beams (called the SupraThermal Electron Bursts, STEB) are known to occur at low altitudes near the edge of a disturbed auroral region, but their origin is an open question (e.g. Meng et al. 1978, [120]; Miyake et al. 2001, [124]; Ivchenko et al. 2002, [71]).

Only at the final stage of the large scale analysis presented in this chapter, the report appeared of the Cluster and the DMSP particle observations, from the nearly conjugated regions at low- and high altitude ends of the auroral field lines (Vaivads et al. 2003 [200]). The outer (magnetospheric) end was however located in the PS boundary, contrary to what is considered here. In the recent work on statistics of the electric field distribution near the upward current region field lines, Hull et al. 2003 ([67]) also reported details of the particle distributions in the magnetosphere. This was however not the main topic of their analyzes and the question on the relations to the ground onset was not directly addressed. No direct comparisons were reported between the low-altitude auroral zone and the connected magnetospheric region observed in situ at the moment of a substorm onset.

In the Interball data, the events were found of the hot plasma injections, accompanied with the changes of the electron distribution function and the signatures of cross-tail current disruption. Observed in the near-Earth plasma sheet, this directly coincided with the substorm onset on the ground. The large scale, multi-point case study of one such substorm is presented in Chapter 3. In this chapter, I show the results of the search for the similar events- the hot plasma injections and the current disruptions, related to the localized events of the pseudobreakup-/substorm onset. For such events, properties of the electron distribution function are investigated. There is still need of such kind of observations and I believe that these results can be an important add on to the subject of magnetosphere-ionosphere coupling and the auroral electron acceleration during the substorm development.

4.2 Data selection

General remarks

It is important here to relate the Interball- observed features not only to the onset time of the ground disturbances (i.e. a substorm expansion or a pseudobreakup) but also to its location as closely as possible. In such a way, it would be possible to better investigate any potential relation between them.

As it is known, (e.g. Aikio et al. 1999, [1]) there are multiple ways to determine the time and location of an individual ground substorm onset and each has its advantages and inconveniences. The mostly used methods relay on: (i) identification of optical auroral arc brightening, (ii) finding a "negative bay" signatures in local magnetograms in the auroral zone, (iii) finding an onset of the high latitude PiB pulsations- and (iv) middle latitude Pi2 pulsations, (v) other methods, e.g. radar sounding of the ionosphere or the satellite observations of Auroral Kilometric Radiation (AKR) activity.

For the purposes of this work, the procedure of identification was based first of all on the individual, local magnetic measurements from multiple ground observatories near the auroral zone. The motivation for this is as follows: (i) The global optical, space based monitoring of the auroral activity, provided by the instruments on the POLAR satellite and extensively used elsewhere, was not operating yet at that time. The other optical measurements, as e.g. the DMSP satellites- or the ground based- images, often suffered from a missing the interesting place due to the very localized observations or the bad weather conditions. Also the individual ground-based optical data were not always available. (ii) The magnetic observations in the Pi2 frequency range from the low latitudes are provided by a sparse network of stations, so they miss the local time effects and may not always give a proper onset time (see e.g. Olson 1999, [137]; Liou et al. 2000, [100]). (iii) Other means, as e.g. the ground based ionospheric radar- or the satellite AKR observations (e.g. Liou et al. 1999 and 2000, [99] and [101]) are not always available and less easy to interpret. (iv) On the other hand, the ground magnetic data of 1 min. resolution from the multiple stations are easily available via e.g. the Internet and could have been easily used during the initial data selection, the necessary stage of the work.

At this point, a comment has to be done on using the global magnetic activity indices, as the AE/AU/AL (the "AE indices" to denote the group as a whole). In the context of substorm-related research they are often used as a common, 1 min. time resolution, global tool to determine the activity level in general, and the substorm onset time in particular. However, based on the data from the limited group of magnetic stations, they may miss some localized events at lower- and higher latitudes and by definition miss any local time information. Moreover, as pointed out by e.g. Rostoker 1998, [158], the AU (and in the consequence the AE) contain the information on the convection electrojet (see Section 1.2 and Figure 1.3) and the onset time determined using the AE is often incorrect. For the time range under consideration, the definite values of the global AE indices have not been available even until the moment of finishing this work so they could not be used. Their "local analogues", independently calculated for the Image- and the CANOPUS network stations are however easily accessible via Internet. With the above limitations of the AE indices, and with the main interest on the localized (in longitude) phenomena, the "local AE" values were used only as a secondary helping tool in this work.

Selection routine

The data selection routine applied was, first, to visually search for the magnetically disturbed events on the ground first, during the days when the satellite was in the magnetosphere. Then the corresponding Interball events were selected that fulfilled the following criteria:

- i For the whole time range the spacecraft was located in the magnetosphere and the event took place in the Plasma Sheet (determined on the basis of the electron energy flux- it had to have a maximum at energies typical for the plasma sheet);
- ii The hot plasma injection was seen in the ELECTRON data, preferentially accompanied with changes of fluxes at hundreds eV;
- iii They were accompanied with \vec{B} fluctuations and/or evident changes in time scale of minutes or shorter.
- iv They took place at geocentric distances closer than about $-12 R_E$ in X_{GSM} .

These criteria help to exclude the crossings of the tail / plasma sheet boundary (PSBL) and/or the outer, cold plasma sheet further downtail or at flanks, the regions where the field aligned fluxes are continuously observed and which (PSBL) are usually thought to be connected to a more distant reconnection sites in the magnetotail. They had to be excluded from the analysis, as interest here is to investigate the events in the near plasma sheet.

DATE	TIME	KP	WHERE & WHAT	X_{GSM} Y_{GSM} Z_{GSM}	MLT
06/Oct/95	09:00-09:30	3+/5	Canopus, MM210; E	-4.5, -8.2, 2.2	04:07
21/Oct/95	13:15-13:45	4-	MM210, YKC; E	-6.4, -7.0, 0.6	03:11
02/Dec/95	10:00-10:15		Canopus, MM210; O	-5.6, -1.7, -3.2	00:43
09/Dec/95	23:15	1+	NAQ,LRV;Pi2; P	-8.3, 1.2, -3.6	00:04
25/Dec/95	01:15-02:15	3-	GILL,NAQ,PBQ; P	-11.2, 5.2, -2.3	22:23
28/Dec/95	20:45	1-	Image,Iceland; P	-10.2, 5.8, -2.4	22:53
13/Jan/96	03:00	3+/5	Image, Iceland, Greenl.; O	-6.3, 5.9, -2.7	21:27
-, -	03:30	5	Canopus; I	-5.6, 5.2, -3.0	21:37
16/Jan/96	19:45-20:00	2+	Image, Iceland; O	-8.5, 9.3, -0.9	21:27

Table 4.1: List of the selected ground substorm / pseudobreakup events related to Interball Tail injections / electron pitch angle- distribution changes. Observed on ground between October 1995 and January 1996. Accuracy is within 15 minutes and the Interball coordinates correspond to a half hour just preceding the first time (when *:15, *:45) or exact at that time (when *:00, *:30). The Magnetic Local Time position of the Interball is also shown, at the beginning of the observed event. The field “where” means the approximate region and/ or the network of magnetic stations, where the event was observed; P, O, I and mean, respectively, the pseudobreakup or the onset-, and the intensification- of the expansion phase E of substorm, as deduced from the ground magnetograms.

The alternative way has also been tested in which, as the first step, the events of the same category were selected (according to the (i) - (iv) criteria above). As the second step, each of the cases selected was tested against the proximity of a substorm expansion/ intensification onset at the initial stage. This procedure was not very fruitful, as the selection of the injection-like events was rather arbitrary, leaving (according to the energy range being analyzed) different number of cases to compare with the, time consuming, ground data analysis. On the other hand, some cases passed by the selection routine appeared not to be related to any detectable ground activity too, so that this selection routine was finally not applied.

In the time range considered, between October 1995 and January 1996, the Interball spent most of the time in the nightside magnetosphere. For this period, at least 30 separate pseudobreakups and 148 well separated substorm expansion/ intensification events were identified for the purposes of this work, using the above mentioned substorm identification method and for which the spacecraft was located inside the magnetosphere (but beyond the radiation belts). After eliminating the cases for which ELECTRON and/or the MIFM data were missing or erroneous, there was 127 substorm- and 29 separate pseudobreakup events left. This number is however not definite. Especially the pseudobreakups, which are the weak, localized phenomena, are less easy to identify with the sparse network of ground magnetic stations. Moreover, the substorms often develop through multiple, more or less localized and separated expansions and may be preceded by pseudobreakups. All such "short scale" and not well separated activities were missed when looking for a "large scale" (above some 30 minutes long) events. To better follow such activities, the global optical monitoring of the auroral zone was proved to be a more convenient method than the ground magnetic data used here (e.g. Liou et al. 1999, [99]). Although all the ground activity events that coincided with the Interball events were further regarded more in details (as e.g. for the 13/January/1996) and tested against the Pi2 activity, some substorm / pseudobreakup events could be however missed due to the selection method applied. 40 of the above events took place close enough to perform the detailed search in the Interball data.

After selection of the Interball events according to the above criteria (i) - (iv), there were 9 cases left for further analysis (including two separate events of 13 January 1996 (see also Chapter 3). They are listed in Table 4.1, and the satellite locations for these events are shown in Figure 4.36 in

the summary section below. Although the number of the satellite events might seem drastically low in comparison to the whole number of substorms identified, suggesting that the features choosed are very exotic, it is not so, actually. The spacecraft approached the Earth once in almost 4 days. Due to the highly inclined orbit ($\sim 65^\circ$ relative to the ecliptic plane) and its elongated shape (the apogee of $\sim 23R_E$), the spacecraft traversed the near-Earth plasma sheet ($|X_{GSM}|$ below $\sim 15R_E$) in nearly 8 hours. Taking into account the fact that the geomagnetic substorms are quite randomly distributed in time, that the ground station coverage is sparse in some LT sectors and that the satellite observations suffered sometimes from technical problems, the number of cases left to study is satisfying. It is worth to note, that the number of selected events obtained here is comparable to those reported in other studies (e.g. Frank et al. 2000 and 2001, [52] and [53]).

To increase the number of events, the Interball data were subsequently searched for the similar events in the time range of October 1996 to December 1997. Except the one, doubtful and not definitely investigated case in October 1996, no similar events were found for these time range. This result seems to be related to the satellite's orbit evolution- the orbit became more inclined and did not cross the appropriate region of the near-Earth, equatorial plasma sheet for the time long enough. Also, some degradation of the instrument sensitivity made the search more difficult. With such discouraging results, no systematic analysis of the substorm activity on the ground and on the geostationary orbit was performed and no additional events were finally included to the analysis. Although indirect and not definite, the above negative result is consistent with the limited spatial extent of the observed events (see below).

4.3 Review of selected events

In this section, the Interball data, the relevant ground based data and the additional selected satellites observations will be presented to show the basic character of the events. The most important details of Interball observations for each of events will also be shown. The summary of observations and the conclusions will be presented in the next section. The events are reviewed below in chronological order. Anticipating the results, the most interesting cases start since end of December 1995 (see Table 4.2 in the next section).

4.3.1 06/October/1995- an “unclear” case

Interball was situated near the 04 geographic Local Time (LT) sector at 09:00 UT. Upper panel of Figure 4.1 shows the GSM positions of the Interball and some geostationary satellites after the injection and near the moment of the observed magnetic field disturbance at 09:30 UT. The bottom panel of Figure 4.1 shows the ground projection of the Interball trajectory and the locations of selected geomagnetic stations in the neighborhood, in the Magnetic Local Time - Corrected Geomagnetic Latitude (MLT-CGL) coordinates. Projected trajectories of two geostationary satellites from the similar MLT sector, GOES-8 and LANL90, are also shown.

Geophysical situation

Detailed inspection of the magnetograms of the whole CANOPUS chain (not shown) reveals strong substorm starting at about 08:12 UT more westward (near the FSIM station, at about 23 MLT). Since 09:00, the westward electrojet further develops in the whole MLT sector between FSIM and GILL, north to ISLL and south to GILL (see Figure 4.1). This is seen in the left panel of Figure 4.2, that shows the northward magnetic component measured on ground, between 08 and 10 UT, in stations located close to the satellite footprint. In particular, the negative bay starts to develop about 09:01 at FCHU and GILL (about 1.5 MLT hour westward to the Interball) with

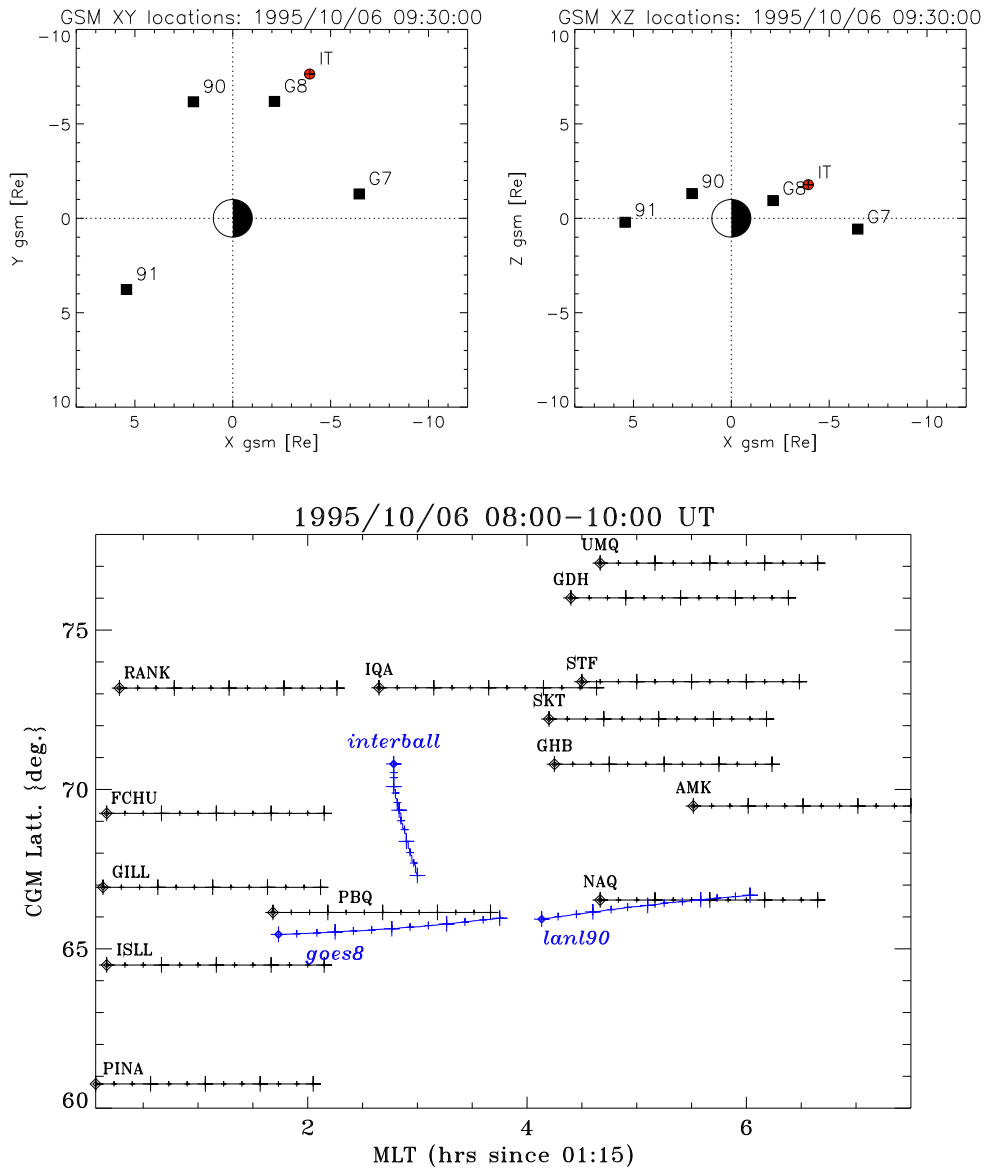


Figure 4.1: The **06/October/1995**- localization of the event. (**Top**) The GSM XY and XZ location of satellites at 09:30 UT. The satellites are marked as follows: 90 and 91 - for LANL 1990-095 and 1991-080, G7 and G8 for GOES-7 and GOES-8 respectively. (**Bottom**): The Interball trajectory (also with the projected trajectories of two geostationary satellites) projected on earth in the Magnetic Local Time - Corrected Geomagnetic Latitude (MLT- CGL) coordinates and positions of the selected ground magnetic stations between 08 and 10 UT. Each trajectory (of a station or of a satellite) begins at the leftmost (thicker) point at 08:00 UT and the tick-marks are separated by 10 minutes UT. The coordinates and the satellite's trajectory footprints have been obtained using standard T98c model with $K_p=3$ and the IGRF model for the 1995 epoch.

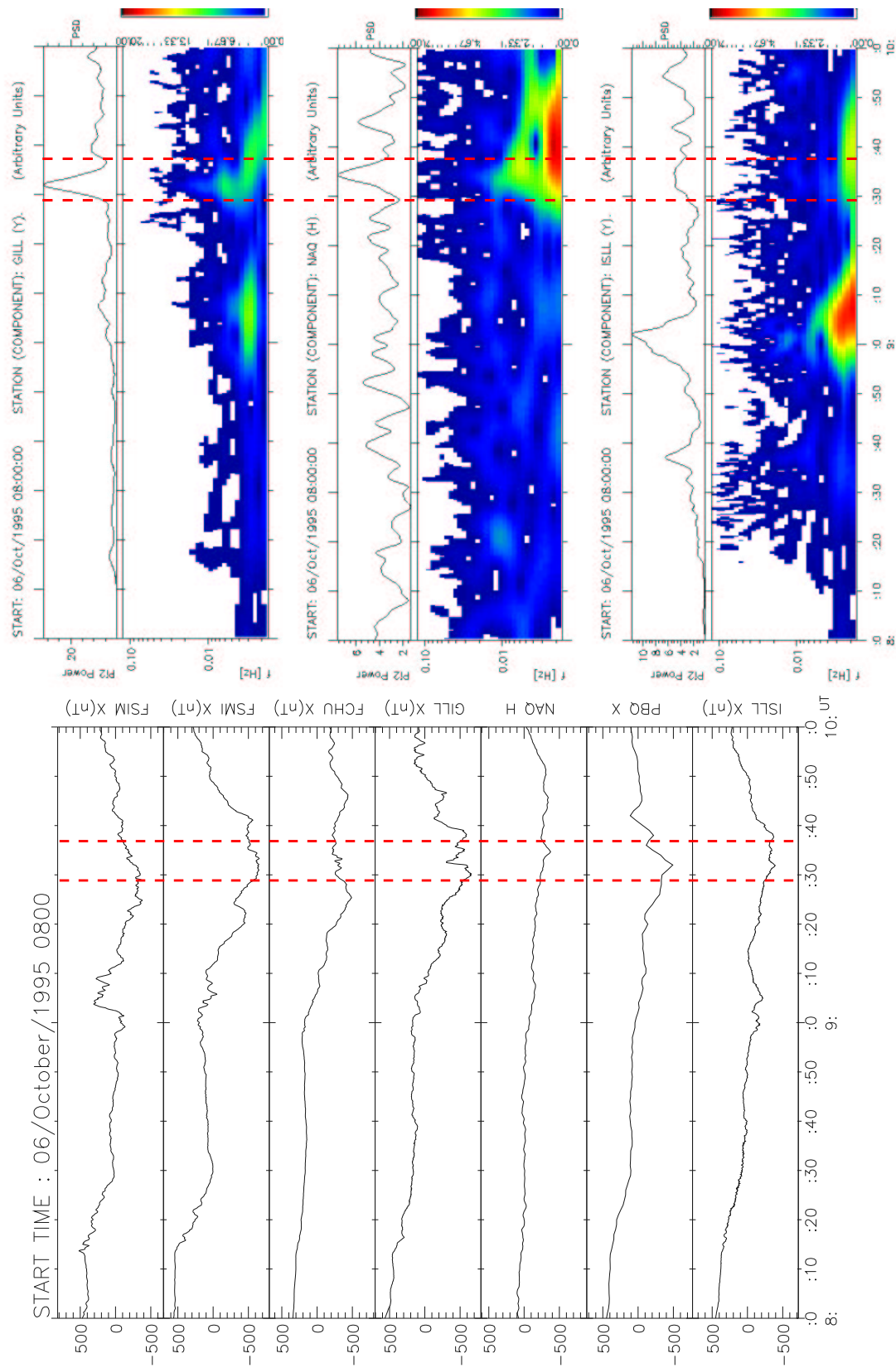


Figure 4.2: Ground based magnetic observations between 08 and 10 UT on 06/October/1995: **(Left)** Northward magnetic field component from selected stations near the Interball trajectory footprint (compare Figure 4.1). **(Right)** Dynamic spectra (color panels) of magnetic pulsations in the Pc5 - Pc3 frequency range (1.67 - 100.0 mHz) and total power of the Pi2 pulsations (black curves). The data of the northward component from three selected stations, ISLL, NAQ and GILL are shown and the units are arbitrary.

further intensification at 09:22 in PBQ (close to the Interball MLT position). Two red, dashed lines delimit the time range of the magnetic disturbance seen by Interball (see below).

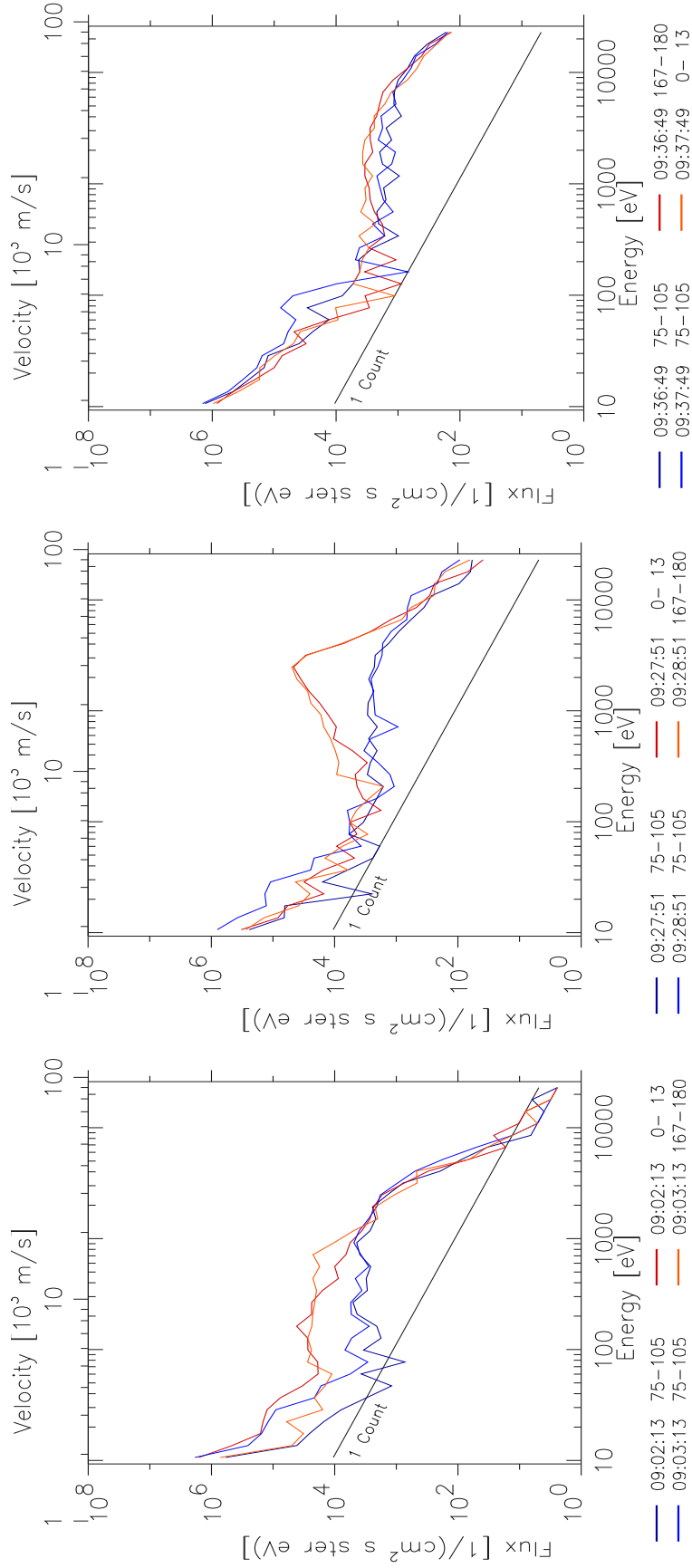
The dynamic spectra of the northward magnetic component and the total power in the Pi2 frequency (see Figure 1.10) range are shown in the right panel of Figure 4.2, from three stations: ISLL (bottom), NAQ and GILL. Only the most representative data are selected for the plot, but the data from all the stations in Figure 4.1, were investigated for the Pi2 pulsations bursts. As the result, no evident, strong Pi2 peaks were seen simultaneously with Interball, eastward to its footprint (see NAQ, where the noisy Pi2 is permanently observed of amplitudes slightly lower than on two other stations). However, the nearby located stations (GILL, FCHU) detected enhanced Pi2 at the same moment as the Interball did. Furthermore, these stations did not see the onset related enhancement of Pi2 around 09:00 UT, contrary to the stations at lower latitude (e.g. ISLL). It should not be surprising- the dependence of such kind of the Pi2 observations on latitude is well known (e.g. Olson [137]). Dashed, red line in Figure 4.2 marks the beginning of the enhanced magnetic fluctuations on Interball (see below). They coincide with the end of the WEJ intensification observed locally in PBQ and GILL, the two ground stations located closest to the trajectory footprint. (It is seen as the temporary decrease in the northward component of magnetic field in the left panel of Figure 4.2).

The local time sector of the Interball (and of the stations shown in Figure 4.1) is not the pre-midnight one, where the substorm current wedge- and the upward, field- aligned substorm currents are usually found. It follows from the ground magnetic observations, that the substorm onset/intensification at 09:00 UT started near 01 MLT, more than 2 MLT hours westward to the Interball footprint position. No signatures of the Westward Traveling Surge (WTS) or the substorm upward FAC were observed close to the Interball footprint. This should not be surprising for such MLT sector, but it suggests, that the burst of the magnetic pulsations observed on Interball this time are not related to the substorm, field-aligned upward current.

The IT observations

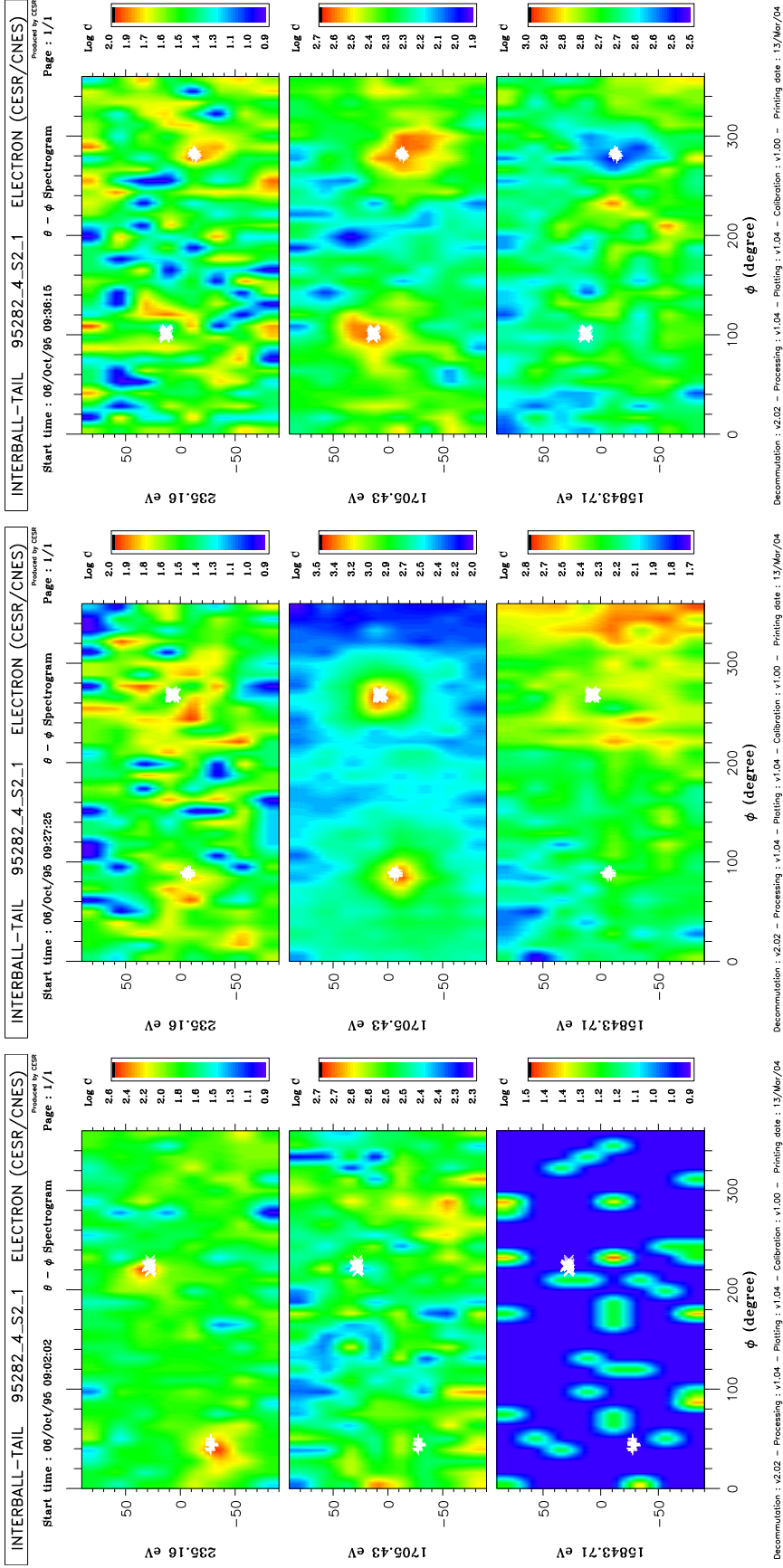
The Interball data shown in Figure 4.3 for the 08 - 10 UT time range are, from top to bottom: the omnidirectional energy- time spectrogram of low- energy electrons from the ELECTRON instrument, the electron fluxes at 3 energy levels and 3 pitch- angle ranges (perpendicular, parallel and anti-parallel to the local magnetic field), the dynamic spectrogram of the B_X GSM component in the Pc5 - Pc3 pulsation range (0.00167 - 0.1 Hz) and the GSM components of the magnetic field. Electron- and magnetic field data (in top and bottom panels) show that the satellite was located in the outer edge of the Plasma Sheet. Increase of the magnetic field, and its subsequent reorientation near 09:16 is a behavior typical for a substorm growth phase followed by the magnetic field dipolarization at- or shortly after the substorm onset. The electron data evidence the slow plasma sheet thinning followed by an injection- like signatures (near 09:08 and 09:16 UT), in consistency with changes of the magnetic field. Actually, the keV electron fluxes raise quite slowly, except for the sharp increase of the field aligned fluxes near the energy 2 keV, between 09:16 and 09:36 UT (the blue curve in the second panel from the top). The energetic particles seen by DOK2 instrument (not shown) also evidence the injection since about 09:13 UT. An interesting feature is seen in the electron- and in the magnetic field data at about 09:32 - 09:35 UT. Temporary excursion of the B_X below zero is accompanied by enhanced magnetic fluctuations. They extend up to the Pc1 frequency region and are clearly seen despite increasing instrument noise near the 0.01 and 0.03 Hz. It is a current disruption signature. Near that time, the keV fluxes sharply drop off, and shortly after the field aligned anisotropy disappears too.

The details of the electron distributions and their changes are seen in Figure 4.4. There are cuts through the 3D electron flux distributions in perpendicular- and in parallel/anti-parallel (to the magnetic field) shown in three instants, in the sub-figure 4.4(a). They were taken before the injection, near 09:03 UT, during enhanced magnetic disturbances (just before the current



(a) Cuts through the electron 3D flux, (perpendicular to B, the blue and green curves, and parallel/anti-parallel to B, light blue and red). (Left) Before-, (Middle) during-, and (Right) after the increased magnetic pulsations.

Figure 4.4: Electron distributions at three instances of 06/October/1995. Compare also Figure 4.3 and see text for more details.



(b) Full 3D (i.e. taken during one spin period) counts at three energies. The direction parallel to B is marked with the white “x”. (Left) Before-, (Middle) during-, and (Right) after the increased magnetic pulsations.

Figure 4.4: Electron distributions at three instances of 06/October/1995 (continued). Compare Figure 4.3 and see text for more details.

disruption near 09:28 UT) and after (09:37 UT, see Figure 4.3). The exact timing is found in the Figure, and the necessary comment about it is that the parallel/anti-parallel directions are not sampled simultaneously and the closest measurements (parallel and anti-) are plotted in each panel. For both cuts, the perpendicular spectra taken simultaneously are also shown. The sub-figure 4.4(b) shows the full 3D angular dependence of the particle count rates at three energy levels (0.235, 1.7 and 15.843 keV). Each panel corresponds to one full satellite's spin period, that begins at the time marked on top of it, and the cuts in the top row are taken during that time range. The abscissa (theta coordinate) is the angle to the satellite's spin axis (compare Figure 2.2) and the value of 90 (-90) deg. denotes the sunward (antisunward) direction. The phi (ordinate) is the phase angle of the satellite rotation, and the representation is the analogue of the standard Mercator cartographic projection with the equator at theta of 0. The directions of the instantaneous magnetic field are represented by "+" (for parallel-) and "x" signs (for anti-parallel direction). Together, two sub-figures of Figure 4.4 show the properties of the electron distributions. First of all, one can see that the pitch angle- dependencies are monotonic- no flux maxima are observed in the intermediate pitch angles (within the limits imposed by the instruments angular- and time resolution and temporary changes of the medium), and the "field aligned components" in left and middle column are really field aligned. The main differences between the three distributions shown are as follows: (i) The temperature increase and the isotropisation takes place after the injection (compare the left- and the right column). While anisotropy in the first case is typical for the outer plasma sheet (compare e.g. Fujimoto 1997, [57]), the "empty" cone observed at highest energies in the rightmost column is typical for the inner, hotter plasma sheet, where the Interball is immersed in after the injection. (ii) The enhanced anisotropy (in the middle column) is due to the presence of the additional, highly accelerated and rather cold component (see Figure 4.4(a)). Its shape is the same as a typical "inverted- V" event- electron spectra observed at much lower altitudes in the active auroral regions. Such and similar spectra are one of the key features investigated here. For this case, however, it won't be further explored, as explained below. (iii) the non-stationarity is seen in the middle column as the increasing high energy- and decreasing middle energy- fluxes. In fact drastic changes of the magnetic field and plasma properties took place only during the following 2 minutes. Detailed inspection of the electron energy spectra (not shown) show the cold (tail lobe- like) plasma traversed during 8 to 12 seconds (3 full energy spectra of 3.75 sec.)- the effect too short to be further investigated (see below). (iv) There is the difference in the properties of field-aligned components between the left- and middle panels (i.e. before- and during the injection. These point will be further explored in the next chapter.

Diagnosis

The observed changes of the electron distribution, for this case, are not directly related to the substorm current system near the onset. This is due, first, to location of the event (eastward, four hours away from the midnight MLT where the substorm initiates) and, second, by the time delay from the ground onset. Also, the lack of the detailed in situ observations (e.g. optical) near the satellite footprint makes the investigation of a possible connections impossible. Finally, the very short time of the current disruption observed by Interball did not allow to obtain the necessary information on electron distributions during this event. In such a way this case, though allowing for further exploration of the macro scale magnetospheric dynamics, for the purposes of this work has to be classified as not directly related to the magnetospheric source region of the substorm current at the onset (see also the next section).

4.3.2 21/October/1995

The Interball was located near 03 local time at 13:00 UT. The upper panel of Figure 4.5 shows its GSM location at 13:45 UT, while the bottom panel- its trajectory projected onto the earth in the

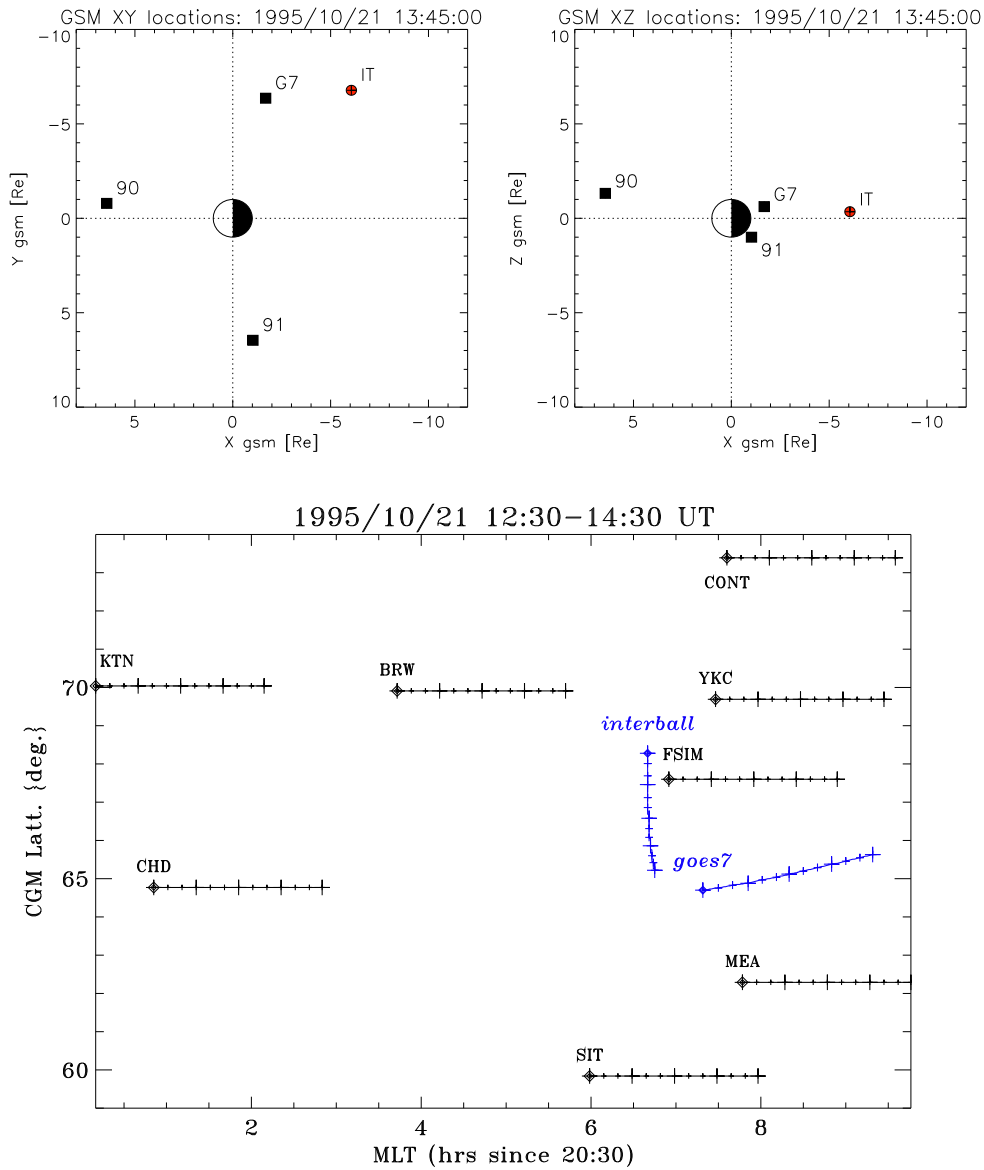


Figure 4.5: The **21/October/1995-** localization of the event. (**Top**):The GSM XY and XZ location of satellites at 13:45 UT. The satellites are marked as follows: IT for Interball, G7 for GOES-7, 90 and 91 for LANL 1990-095 and 1991-080. (**Bottom**): The Interball trajectory projected on Earth (also with footprints of the geostationary GOES-7 satellite)in the Magnetic Local Time - Corrected Geomagnetic Latitude (MLT- CGL) coordinates and positions of selected ground magnetic stations at 12:30 UT. Each trajectory (of a station or of a satellite) begins at the leftmost (thicker) point at 12:30 UT and tick-marks are separated by 10 minutes UT. The coordinates and the satellite footprints have been calculated using standard T98c model with $K_p=5$ and the IGRF model for the 1995 epoch.

MLT- CGL coordinates. The projected trajectory of the GOES-7 is also shown and locations of selected geomagnetic stations. As in the preceding case (06/Oct/95), the satellite was approaching the Earth in the post- midnight sector (03:09 - 03:19 MLT between 11:30 and 14:30 UT).

Geophysical situation

Northward component of the magnetic field, recorded on the ground in a broad MLT sector (compare Figure 4.5) are shown in the left panel of Figure 4.6. There was no activity recorded on stations in the Interball MLT sector (MEA, FSIM, YKC). Contrary, the stations from the pre-midnight sector (CHD at 22:20, and KTN at 21:40 MLT at 13:30 UT) show clearly the northward (substorm) electrojet development since 13:31 UT over CHD, expanding northward near 13:36 over KTN and intensifying further between CHD and KTN between 13:43 and 14:05 UT. The slow and systematic decrease of northward component at BRW however, is probably not related to the substorm-, but rather to the westward convection electrojet. The onset of the substorm near 13:30 is seen in the Pi2 pulsations from the low latitude Kakioka observatory (about 13:31 UT, not shown) and in the dynamic spectrograms shown in the right panel of Figure 4.6 (stations CHD, FSIM and KTN). As in the preceding case, the high latitude Pi2's are clearly seen to increase near the substorm onset at CHD (13:30 - 13:50), where the substorm initiates and at KTN, while they are almost not seen far from this MLT sector at FSIM (the middle panel; note the different scale in plot of the Pi2 power there).

Observations of the other satellites

The geostationary satellites show the injection related to the substorm, as e.g. the LANL 89 SOPA energetic electrons, since about 13:41 UT.

The IT observations

There is a lot of details in the electron fluxes and anisotropy plots, seen between 12:30 and 14:30 UT in two top panels of Figure 4.7 (format is the same as in Figure 4.3). The magnetic field shows that the satellite was located, most of the time, in the plasma sheet but away from the neutral sheet, before about 13:51 UT. The main interest here is to relate the Interball observations to the substorm onset on the ground (see below) so the flux and anisotropy changes observed before 13:30 UT are not considered.

Since 13:38 UT, the electron temperature gradually decreases until about 13:50 UT. Simultaneously, at 13:34 - 13:36 UT there was injection of the energetic particles observed by the DOK2 instrument (in the energy range of about 30 - 300 keV, not shown). In the ELECTRON energy range, enhanced fluxes above some 15 keV appear since 13:46 UT.

The magnetic fluctuations of low level are biased by the instrument noise near 10 mHz (see weak amplitude in the fourth panel of Figure 4.7). Weak Pi2 range enhancements are seen, however, around 13:00 UT and between 13:47 and 14:02. The second of them coincides with crossing the neutral sheet (the Bx changing sign near 13:52 UT at the bottom panel) and with the weak, temporary magnetic field enhancement. Note also, that the few keV fluxes (the blue curves in the second panel) become isotropic, when the Pi2- fluctuations level reaches maximum and shortly after.

Details of changes of the electron distributions are plotted in Figure 4.8. The format is similar to that of the Figure 4.4 except the energies in the lower panels (near 450, 2200 are 13000 eV). The left side- and the middle spectra are nearly isotropic. The maximum of the particle flux may serve as a simple proxy for the temperature and one can see that (in the instrument energy range) the post-onset, injected plasma is actually colder than the pre-onset (see the maximum of the left spectrum near 10 keV and of the middle- about 4 keV). This is probably related to the changed

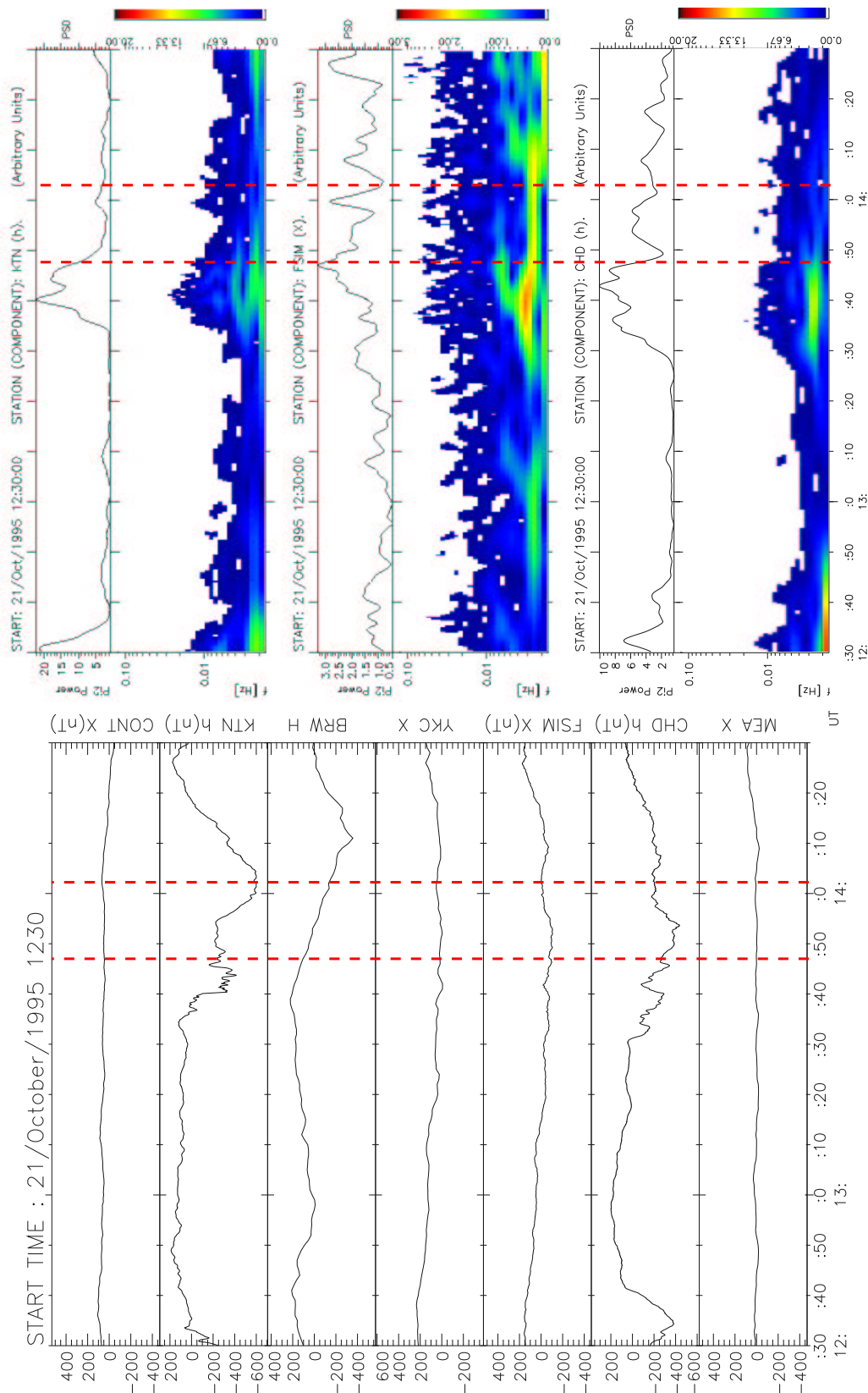


Figure 4.6: Ground based magnetic observations between 11:30 and 14:30 UT on 21/October/1995: **(Left)** Northward magnetic field component from selected stations near the Interball trajectory footprint (compare Figure 4.5); **(Right)** Dynamic spectra (color panels) of pulsations in the Pc5 - Pc3 frequency range (1.67 - 100.0 mHz) and total power of the Pi2 pulsations (black curves). The data of the northward component from three stations, CHD, FSIM, KTN are shown and the units are arbitrary.

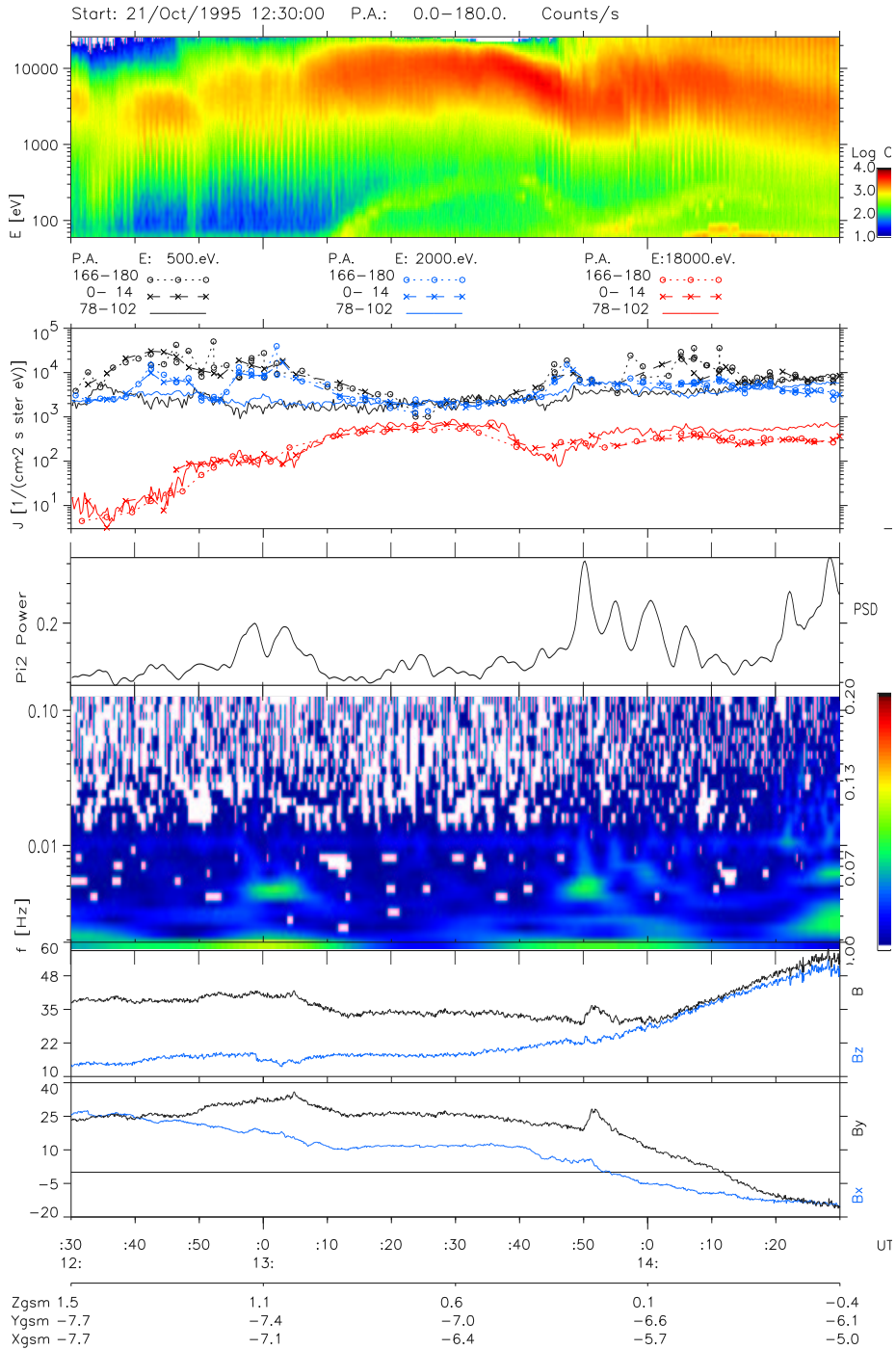
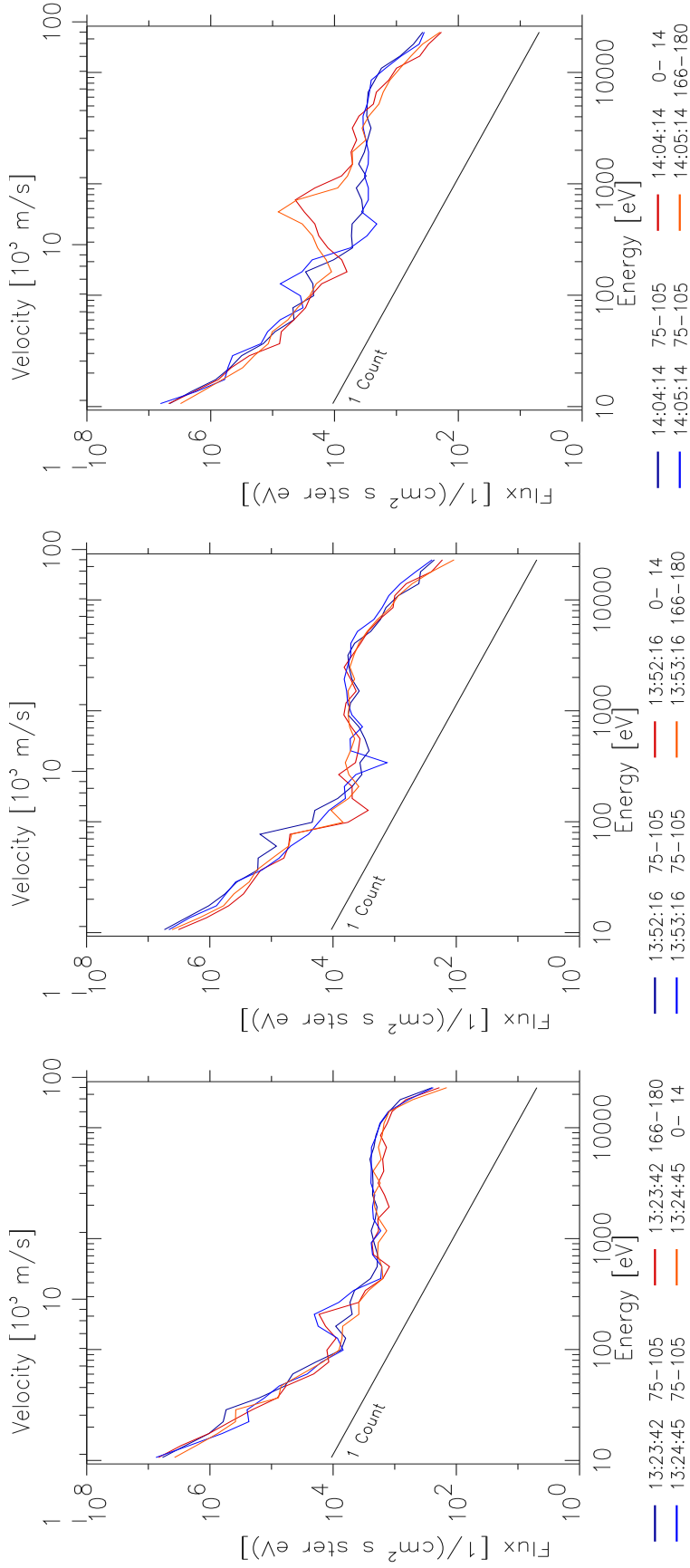
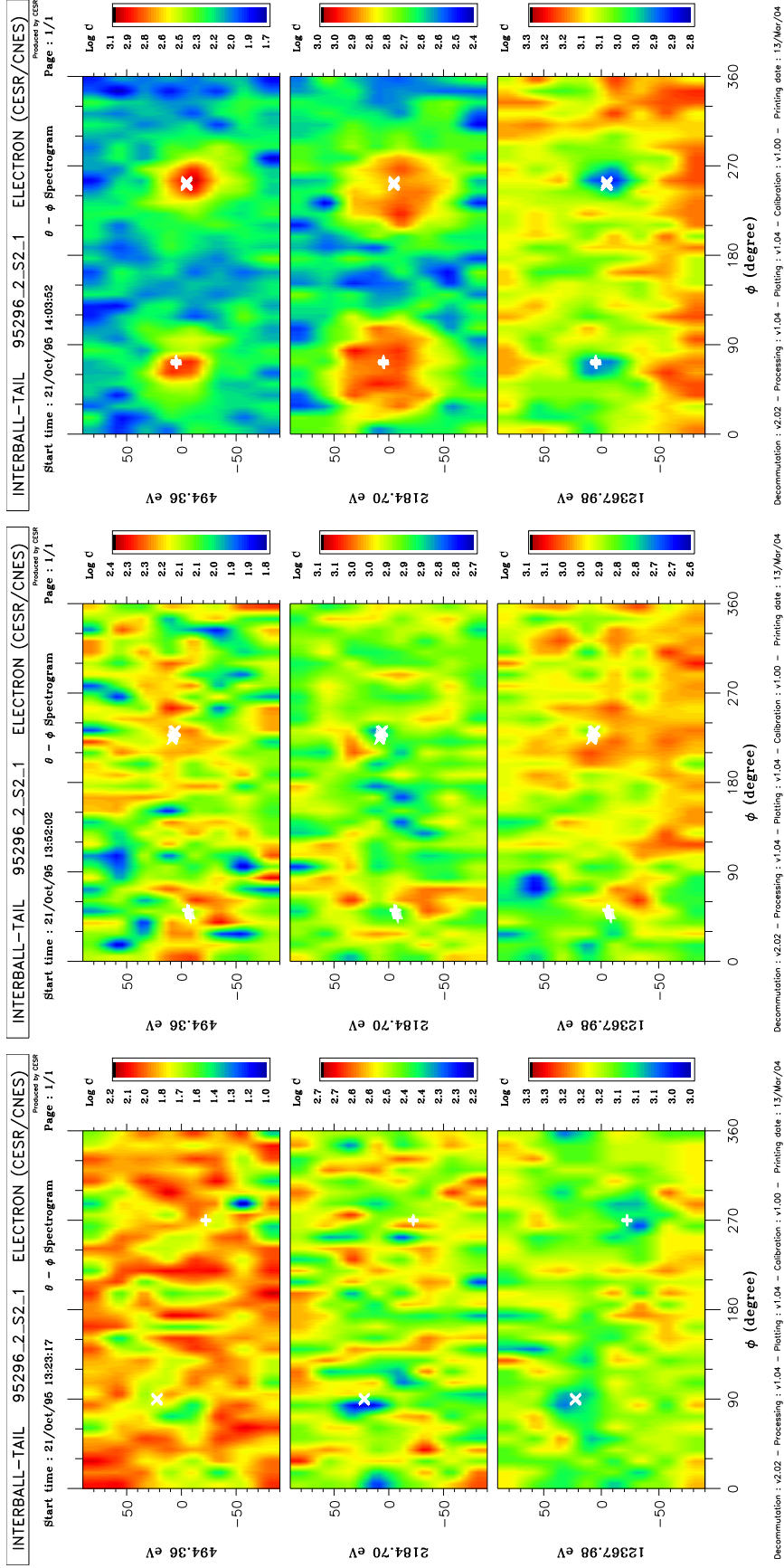


Figure 4.7: The Interball observations in the time range 12:30-14:30 UT on 21/October/1995. Format the same as in Figure 4.3.



(a) Cuts through the electron 3D flux.

Figure 4.8: Electron properties at three instances of 21/October/1995. Format the same as in Figure 4.3, except for the energies at the bottom panels. See text for the details.



(b) 3D counts at three energies. **(Left)** Before-, **(Middle)** during-, and **(Right)** after the increased magnetic pulsations.

Figure 4.8: Electron properties at three instances of 21/October/1995. Format the same as in Figure 4.3, except for the energies at the bottom panels. See text for the details.

shape of the Plasma Sheet. Note also a less steep, high energy tail of the second distribution- it is no longer maxwellian during and after the injection. In the next chapter, the details of the spectral shape of electrons are further explored in a more systematic way and this statement will be justified. An interesting feature in the plot is the appearance of the additional, rather cold and field line- accelerated component in the right column. It peaks near 600 eV and is the source of the observed, strong flux anisotropy. Note its approximated parallel / anti-parallel symmetry. It is not possible to state whether there is an empty loss cone in the distribution, as it is too narrow for the instrument at the magnetospheric location.

Diagnosis

This case is easier to analyze than the preceding one. The Interball, located in the post-midnight MLT sector and away from the onset site, did not see the magnetic signatures of the current disruption. The plasma injection, the pitch angle distribution changes and the magnetic effects are delayed with respect to the ground onset by 5 to 15 minutes. Weak traces of magnetic fluctuations are not related to the ground magnetic activity in the same MLT sector.

4.3.3 02/December/1995

The Interball was located in the midnight sector- between 00:48 and 01:08 LT since 09:00 until 10:00 UT, staying in 00:30 - 01:00 MLT sector during that time. Its location, and the location of the geostationary GOES-7 satellite at 09:57 UT are shown in upper part of Figure 4.9. Bottom panel shows the earth projection of the satellite trajectory and locations of selected ground stations in the MLT - CGL coordinates. This time the satellite was located closer to the Earth but below the neutral sheet (see below) and still traversed the auroral zone- field lines. Although the projection onto the southern hemisphere would be more appropriate in this case, there was no ground magnetic station close to the projected satellite trajectory, so the northern projection, and the data of the northern ground stations are used below.

Geophysical situation

In the magnetograms in left panel of Figure 4.10, there is the negative bay seen in BRW and KTN, but there is no effect close to the Interball MLT sector. A possible scenario deduced from the analysis of the magnetograms (of all the components and all the stations shown in Figure 4.9) is as follows: at 09:51 - 09:53 UT the eastward electrojet (EEJ) intensifies south to BRW and CHD; then the WEJ develops at 10:06 south to BRW and at 10:07 south to KTN; finally, at 10:14 WEJ moves northward over KTN. The Pi2 pulsations in the right panel of Figure 4.10 further support this point of view. They raise at CHD and ZYK (not shown) at 09:52 and then again at 10:02. At KTN, the maximum intensity of Pi2 is reached since 10:10 UT. Contrary to this, the Pi2 pulsations in the Interball MLT sector significantly decreased at that time.

Observations from the other satellites

The above picture is consistent with the optical data of the DMSP F12 satellite (not shown) that evidence the developing auroral spiral slightly eastward to CHD, scanned between 09:59 and 10:02 UT. The substorm onset and the related injection is also confirmed by the high energy particle data (of SOPA instrument) from the geostationary LANL spacecrafts (not shown).

The IT observations

As in the previous case (21/Oct/95), the satellite crossed the hot, near-Earth plasma below the neutral sheet (see the negative B_X in the bottom panel in Figure 4.11). The only features found

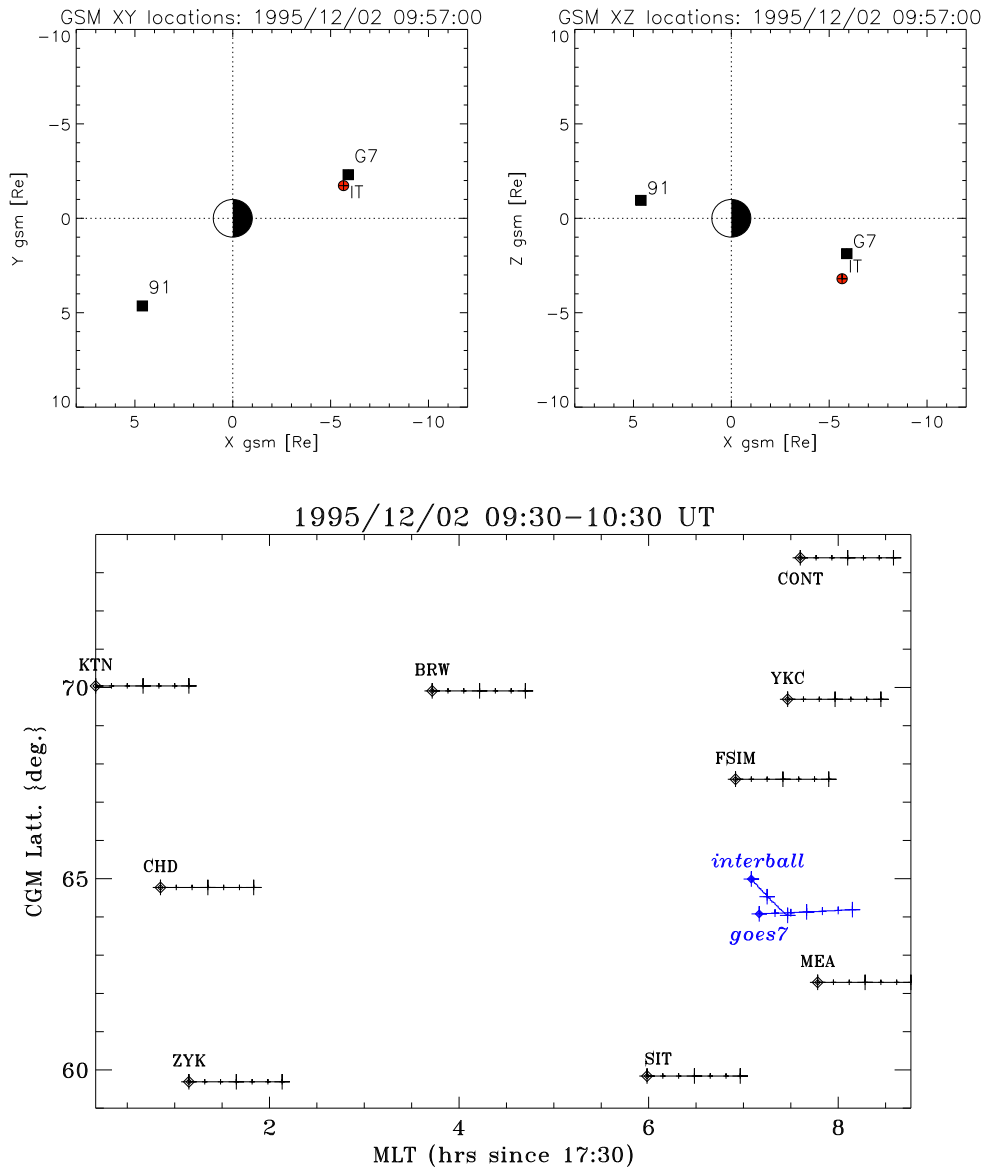


Figure 4.9: The **02/December/1995**- localization of the event. (**Top**):The GSM XY and XZ location of satellites at 09:57 UT. The satellites are marked as follows: IT - Interball Tail, G7 - GOES-7, G8 - GOES-8, 90 - LANL 1990-095, 91 - LANL 1991-080, 94 - LANL 1994-084. (**Bottom**): The Interball trajectory projected on Earth in the MLT- CGL coordinates and positions of the selected ground magnetic stations (also with trajectory footprints of the geostationary satellite GOES-7). Each trajectory (of a station or of a satellite) begins at the leftmost (thicker) point at 09:30 UT and tick-marks are separated by 10 minutes of UT. The coordinates and the satellite footprints have been calculated using standard T98c model with $K_p=3$ and the IGRF model for the 1995 epoch.

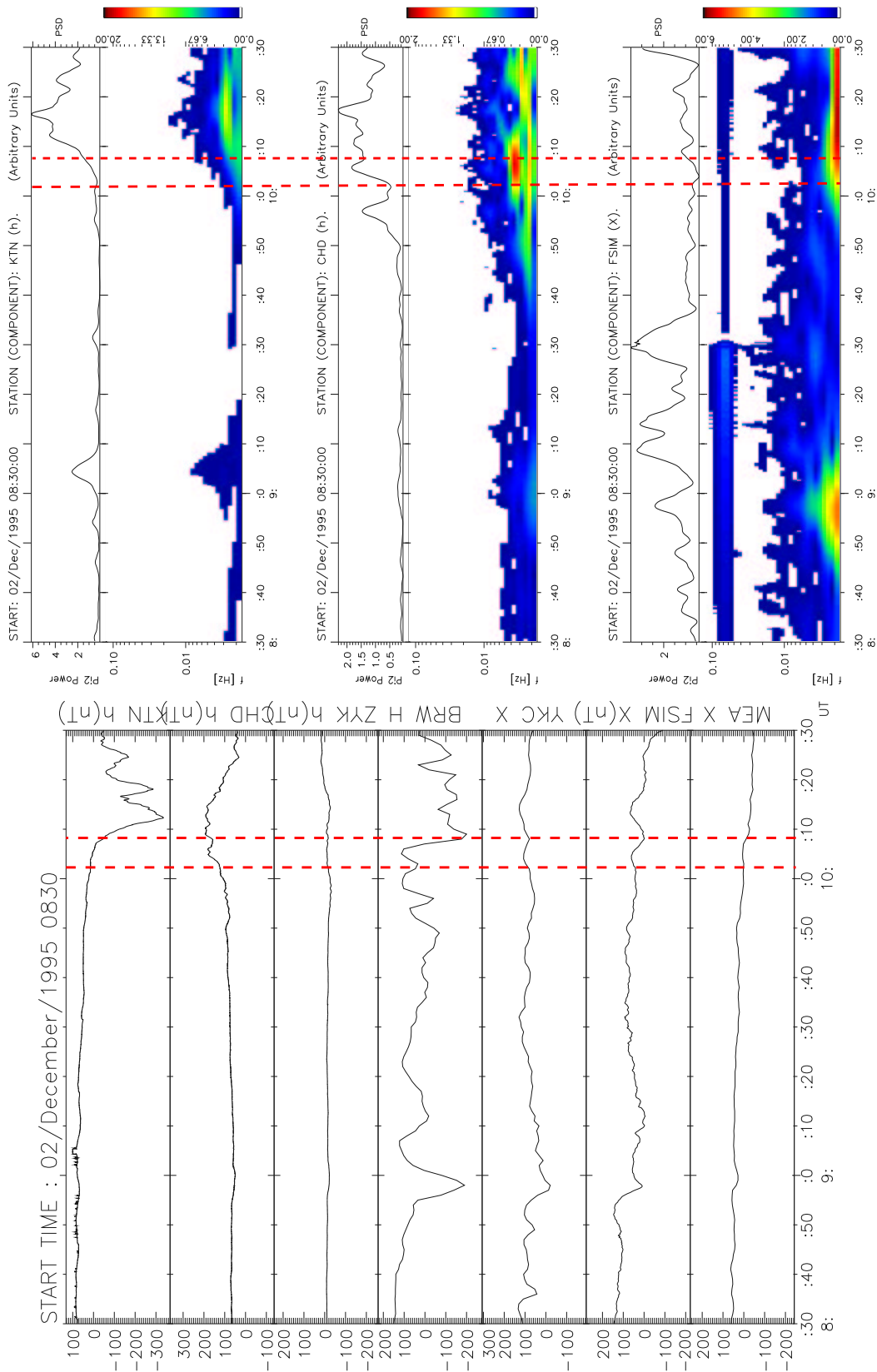


Figure 4.10: Ground based magnetic observations between 08:30 and 10:30 UT on 02/December/1995: **(Left)** Northward magnetic field component from selected station near the Interball trajectory footprint (compare Figure 4.9); **(Right)** Dynamic spectra (color panels) of the magnetic pulsations in the Pc5 - Pc3 frequency range (1.67 - 100.0 mHz) and total power of the Pi2 pulsations (black curves). The northward component from three stations, FSIM, CHD and KTN are shown and the units are arbitrary. The enhanced intensity in the range 0.05 - 0.09 Hz of the bottom panel is an artificial effect of the instrument noise.

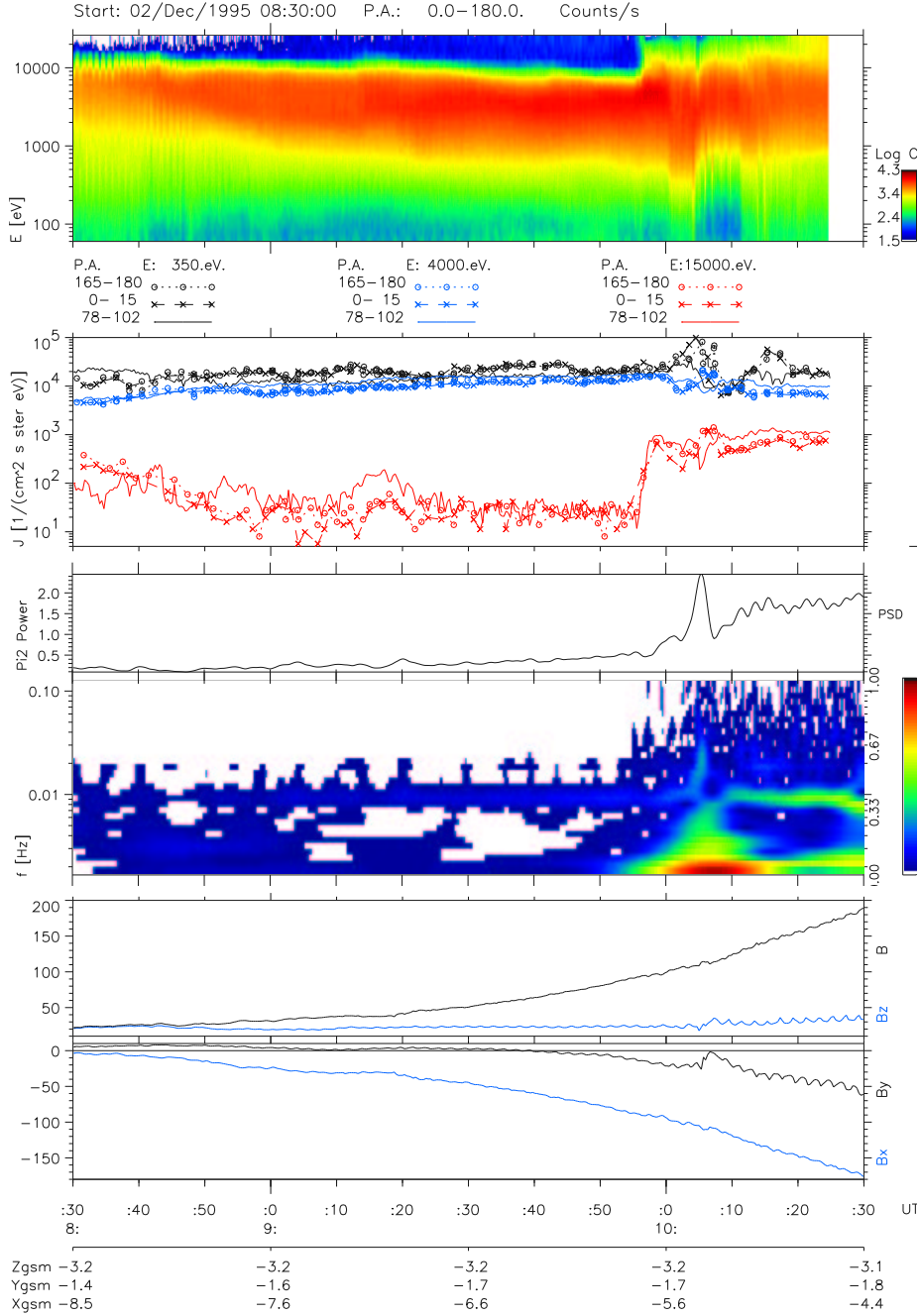


Figure 4.11: The Interball observations in the time range 08:30 - 10:30 UT on 02/December/1995. Format the same as in Figure 4.3.

in B are the weak disturbance near 10:05 (mainly in B_Y). and impulsive increase of rather weak fluctuations (10:02 - 10:08 UT). The enhanced intensity near the band 0.01 Hz in the third panel is the instrument noise, but it does not totally obscures the “real” fluctuations. More careful investigations of other components reveals, that they continue until 10:08 to finally fade near 10:13 UT, while the Pi2 power after about 10:15 UT is mainly artificial.

The ELECTRON data are consistent with the crossing of the hot and quiet near Earth plasma sheet until 09:55:45 UT. An injection at highest energies was found at this time (see the two top panels in Figure 4.11). Between about 10:01 to 10:08, the field aligned fluxes dominate slightly at few keV and below. This anisotropy disappears temporarily just after the magnetic field disturbance (10:08-10:14 UT).

Details of electron distributions and their changes are similar in some aspects to those of the preceding case, but some important differences are also seen (see Figure 4.12, (a) and (b)). (i) Electron distribution function become slightly hotter but first of all not maxwellian during and after the injection (see the highest energies). (ii) This time, the field aligned anisotropy is also observed in the “main” population (middle panel). (iii) The additional, streaming component is not related to the magnetic disturbance (compare the middle- and the right panel). The anti-coincidence of these two features, as in the above- or (first of all) the following cases does not hold or is obscured by the additional temporal changes. (iv) The asymmetry of the parallel-anti-parallel fluxes continues for several minutes.

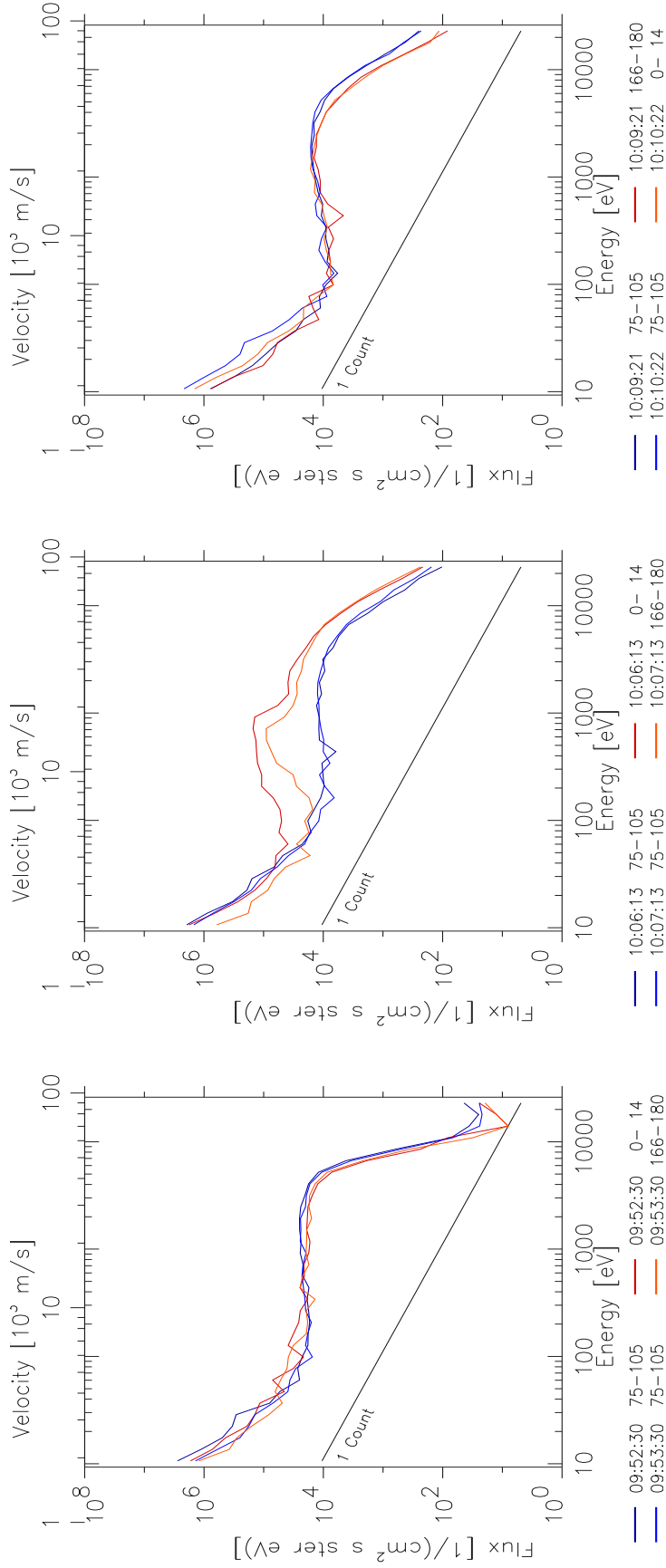
4.3.4 09/December/1995

At 23:00 UT, the Interball was located in about 23:30 LT sector(see upper panel of Figure 4.13), staying between 23:59 and 00:09 MLT since 22 until 00 UT. The projection of the satellite trajectory is found close to the TJO and HUS stations on Iceland (see lower panel of Figure 4.13. In particular, at 23:15 UT the distance to the TJO was nearly 35 minutes MLT.

Geophysical situation

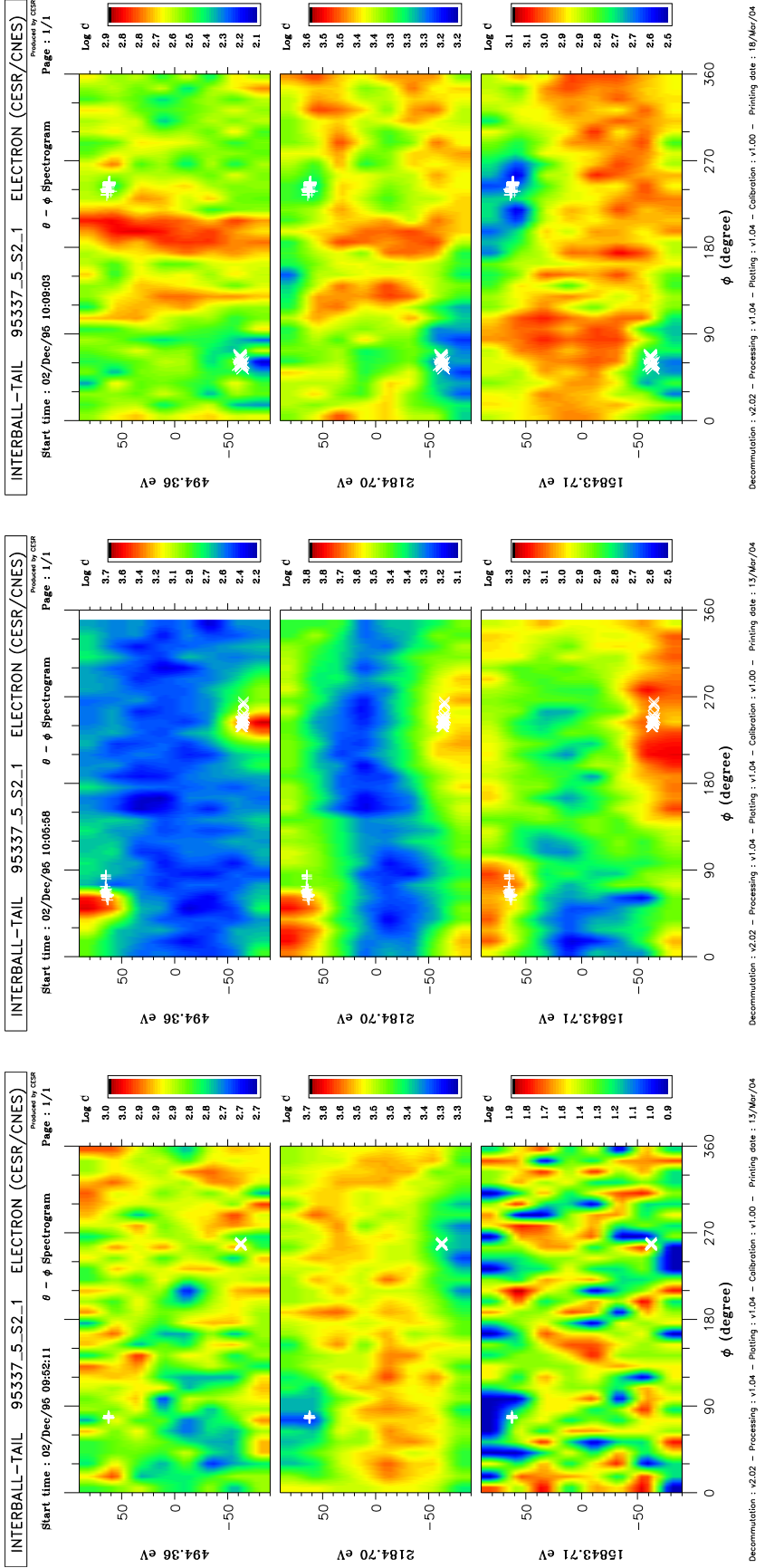
Ground magnetic data in the left panel of Figure 4.14 show no activity in MUO, TRO, SOR and BJN (located approximately 2 hrs MLT eastward to the satellite’s footprint), contrary to HUS and TJO (about 30 min. MLT westward to the footprint). The weak (120 nT deep) but sharp negative bay started to develop at about 23:13 over TJO and HUS, as well as over ISA and the magnetically conjugated SYO in southern hemisphere (not shown). More careful investigation of the magnetic data from the multiple stations reveals that the westward electrojet moves poleward over SYO near 23:13:15 and 23:14:20 over HUS. Simultaneously, since about 22:30 UT a systematic intensification and equatorward displacement of westward electrojet over the Scandinavia took place (not shown) until the substorm onset about 00:30. Further northward (SCO) and westward AMK (22:00 MLT at 23:15 UT, not shown), there is no magnetic bay signatures, except a weak one (100 nT) at NAQ between 23:27 and 23:23 (21:15 MLT then). Ground magnetic pulsations intensify at that moment (see right panel of Figure 4.14) close to the satellite (TJO, 23:13 UT) and at the conjugated point in southern hemisphere (SYO, 23:13 UT), but not or weakly in the stations located more eastward (TRO and, not shown, LOZ). At middle latitude, however, in the same MLT sector as TRO, pulsations are easily seen at e.g. OIJ and NUR (not shown).

The event of 23:13 UT, weak and localized, can be thought of as a pre-substorm pseudo-breakup.



(a) Cuts through the electron 3D flux. **(Left)** Before-, **(Middle)** during-, and **(Right)** after the increased magnetic pulsations.

Figure 4.12: Electron distributions at three instances of 02/December/1995. Format as in Figure 4.4. See text for more details and compare Figure 4.11.



(b) Full 3D counts at three energies. The direction parallel to B is marked with the white “+” signs and the opposite- by “x”. (Left) Before-, (Middle) during-, and (Right) after the increased magnetic pulsations.

Figure 4.12: Electron distributions at three instances of 02/December/1995 (continued). Format as in Figure 4.4. See text for more details and compare Figure 4.11.

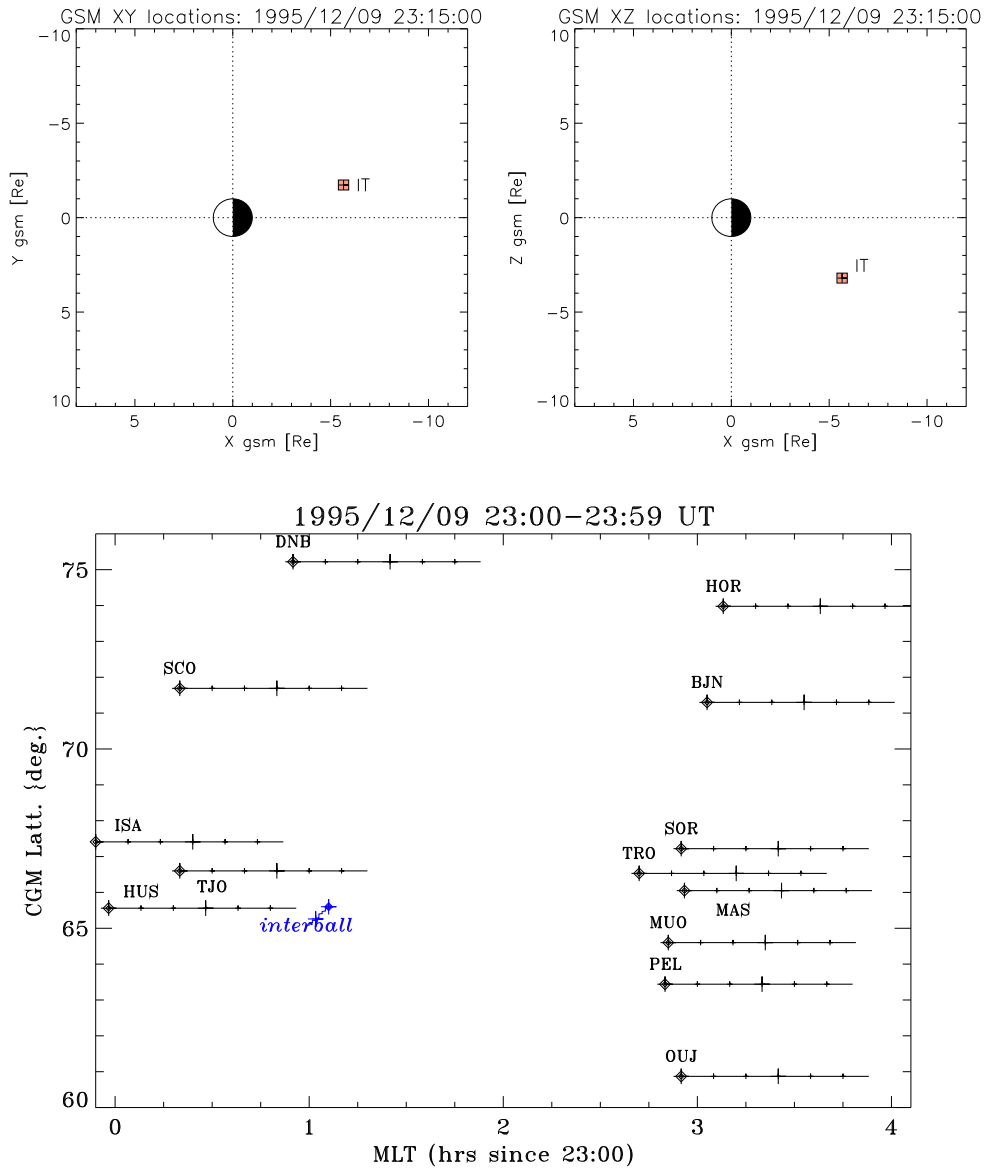


Figure 4.13: The **09/December/1995**- localization of the event. (**Top**): The GSM XY and XZ position of Interball at 23:15 UT. (**Bottom**): The Interball trajectory projected on Earth in the MLT- CGL coordinates and positions of the selected ground magnetic stations. Each trajectory begins at the leftmost point at 23:00 UT. Other details as in the previous cases.

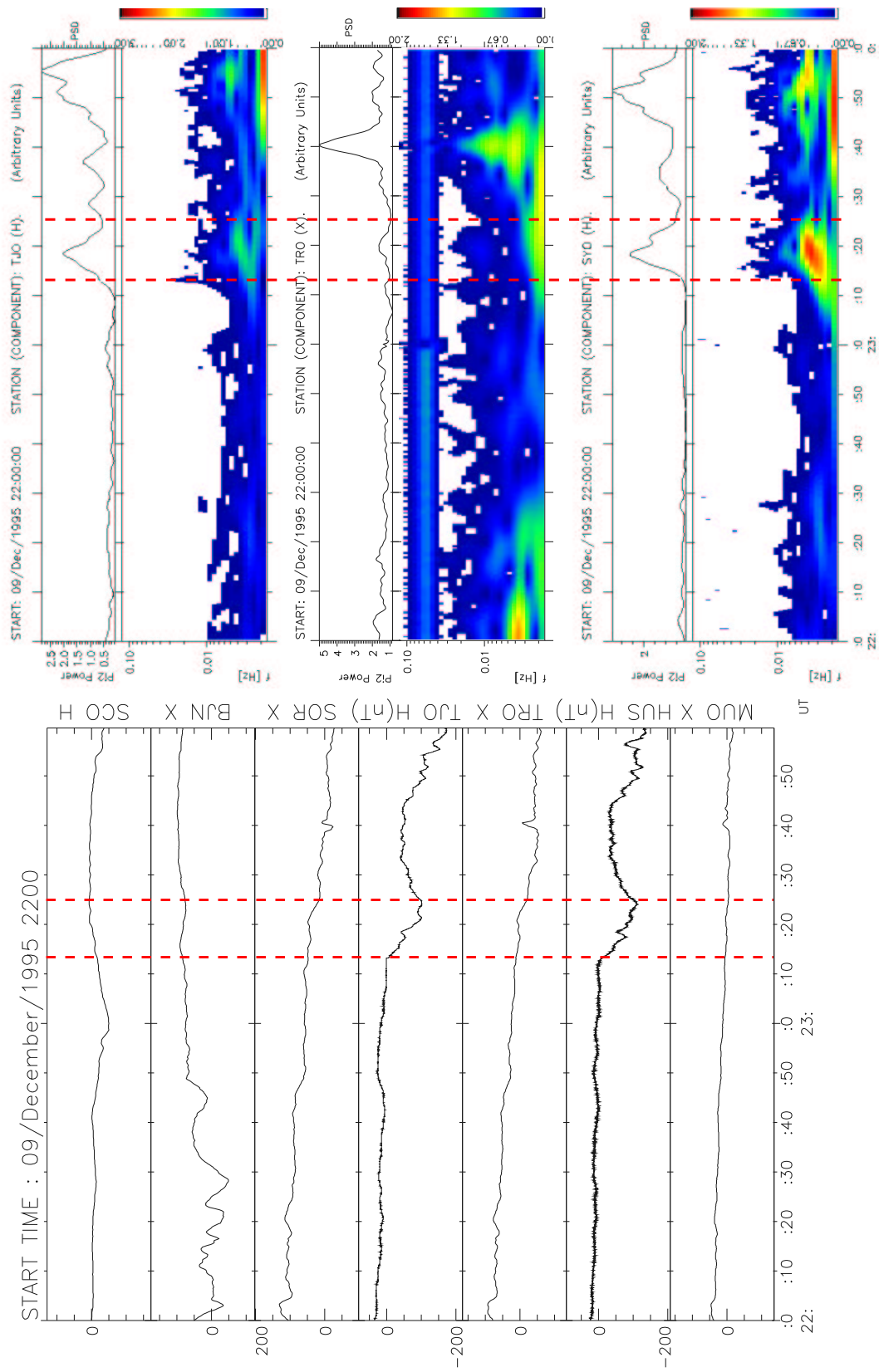


Figure 4.14: Ground based magnetic observations between 22 and 00 UT on 09/December/1995: **(Left)** Northward magnetic field component from selected stations near the Interball trajectory footprint (compare Figure 4.13); **(Right)** Dynamic spectra (color panels) of pulsations in the Pc5 - Pc3 frequency range (1.67 - 100.0 mHz) and total power of the Pi2 pulsations (black curves). The data of the northward component from three stations, TRO, TJO and SYO (magnetically conjugated, southern hemisphere) are shown and the units are arbitrary. The enhanced intensity in the range 0.05 - 0.09 Hz of the second panel (TJO) is an artificial effect of the instrumental noise.

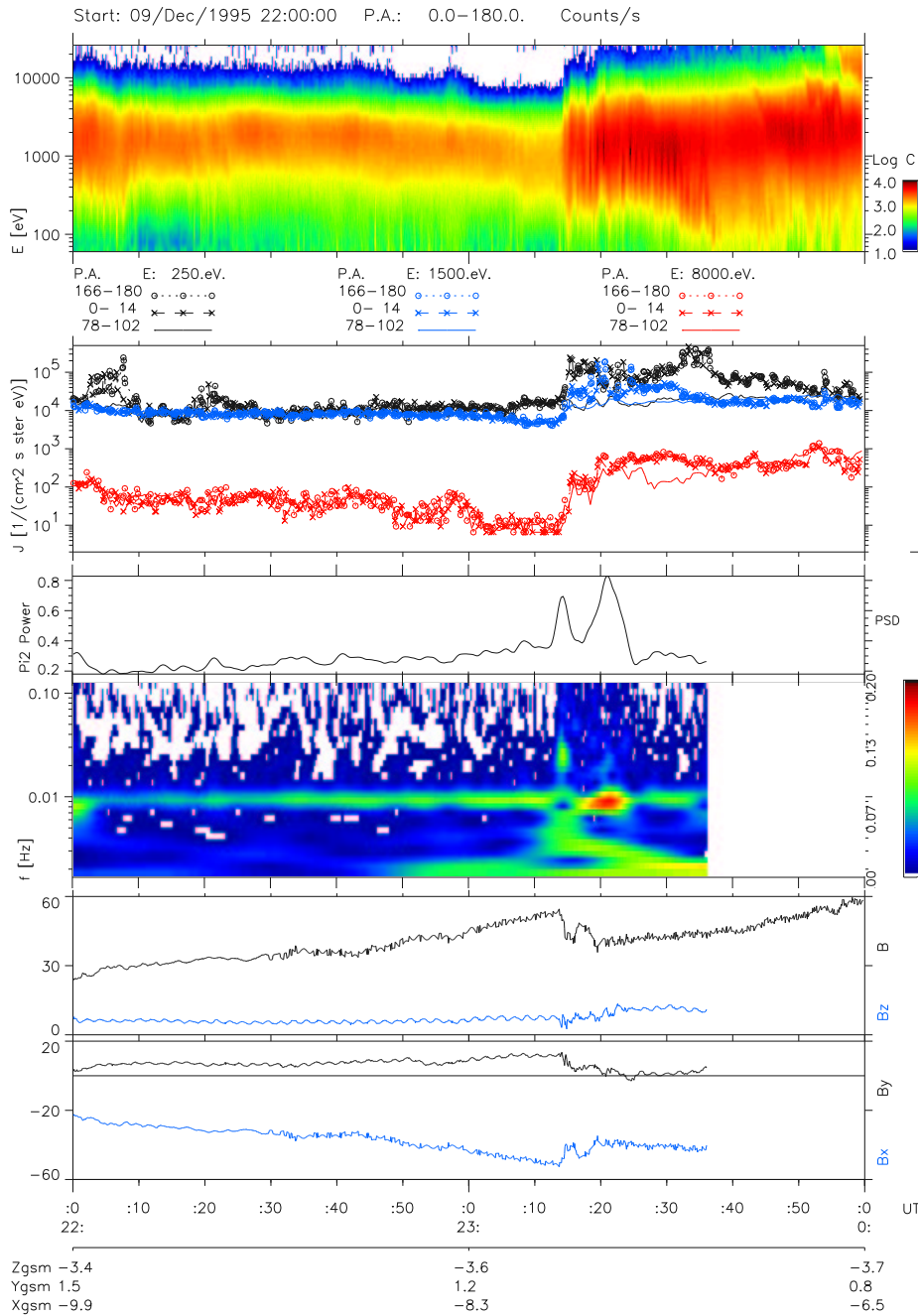


Figure 4.15: The Interball observations in the time range 22 - 00 UT on 09/December/1995. Format the same as in Figure 4.3.

The IT observations

The most evident feature found in Figure 4.15 is the sharp increase of fluxes at 23:14:30, seen in two top panels. Electron population, rather cold and isotropic before-, became slightly hotter but first of all much more anisotropic after this time. Note the energy dispersion effect observed below about 2 keV until 23:37:19 UT. The injection was preceded by the magnetic disturbance (since 23:13:45) of the type of dipolarization, also seen in Pi2 and Pc1 frequencies (since 23:13). The enhanced power in the frequency band near 0.01 Hz is an artificial, instrumental noise, but do not cover totally the weak magnetic disturbance, observed at all components (not shown). High value of the B_X component shows, that the event was observed far from the neutral sheet.

The electron distribution in Figure 4.16 exhibit clearly the above changes: (i) The anisotropy is realized by the appearance of the additional, colder and streaming component (ii) There is the time/energy dispersion (compare the upper middle- and right panels) seen in the colder component (iii) There is no evident effect attributable to the appearance/ disappearance of the magnetic fluctuations in distributions of the injected electrons.

Diagnosis

The location of the satellite's footprint, eastward and slightly southward to the weak and localized ground event, the distance to it and a typical geometry of the similar events suggests, that the Interball is probably not connected to the upward field aligned current related to this ground pseudobreakup.

4.3.5 25/December/1995

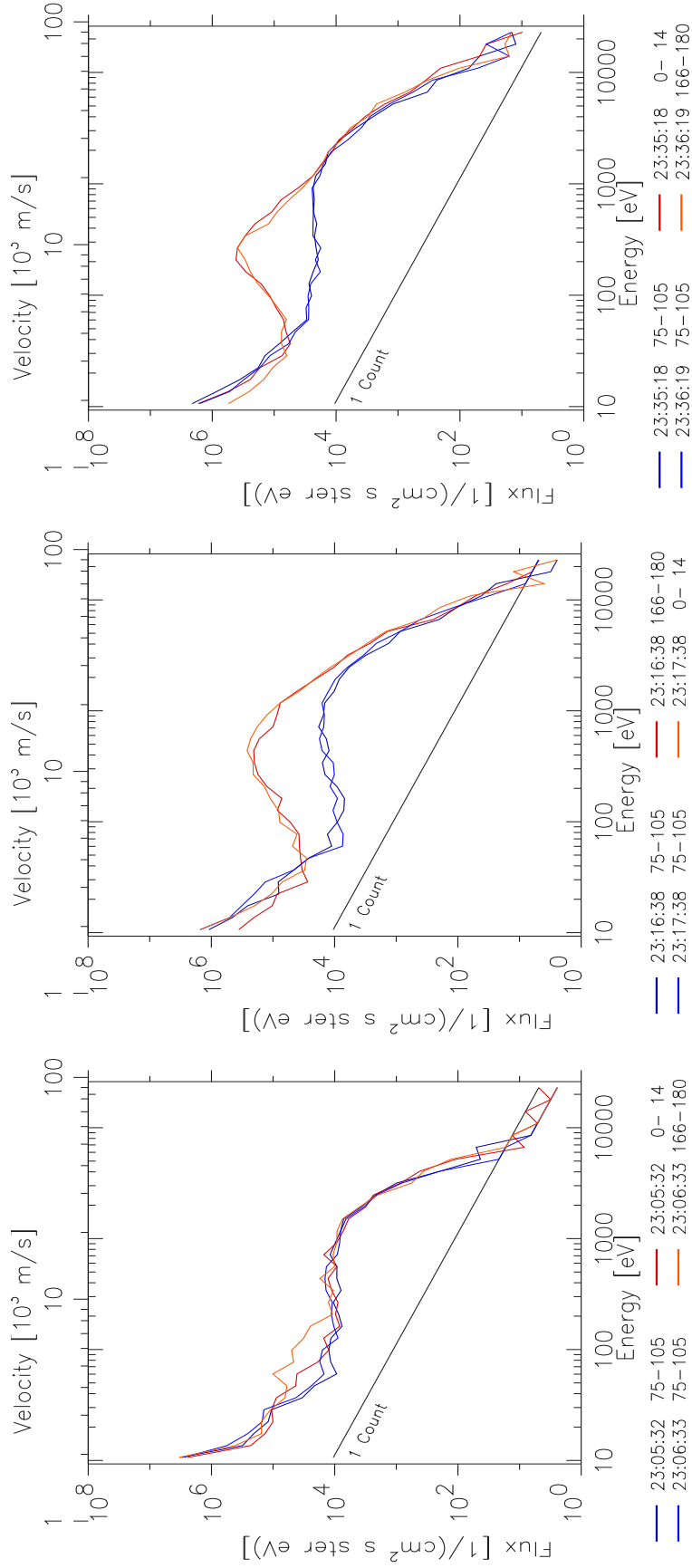
The satellite was located near the 22 LT, and the localization is shown in Figure 4.17.

Geophysical situation

As seen in Figure 4.20, there was no significant activity in the broad sector between PINA and AMK (nearly 6 hrs MLT). Quiet surprisingly, the Interball- detected, not very strong magnetic fluctuations coincide well with the pulsations at the lower edge of the auroral zone NAQ, ISLL. Also the more distant geomagnetic stations (e.g., not shown here, the middle latitude KVI and NOR of the SAMNET network or the low latitude KAK) observed the weak, but easy to identify Pi2 power increase near 01:30 UT. Contrary to lower latitude, there are no evident pulsations higher in the auroral zone (GHB and other stations, not shown). There is also a weak westward electrojet signature coinciding with the IT observations in NAQ, the closest station to the Interball trajectory footprint.

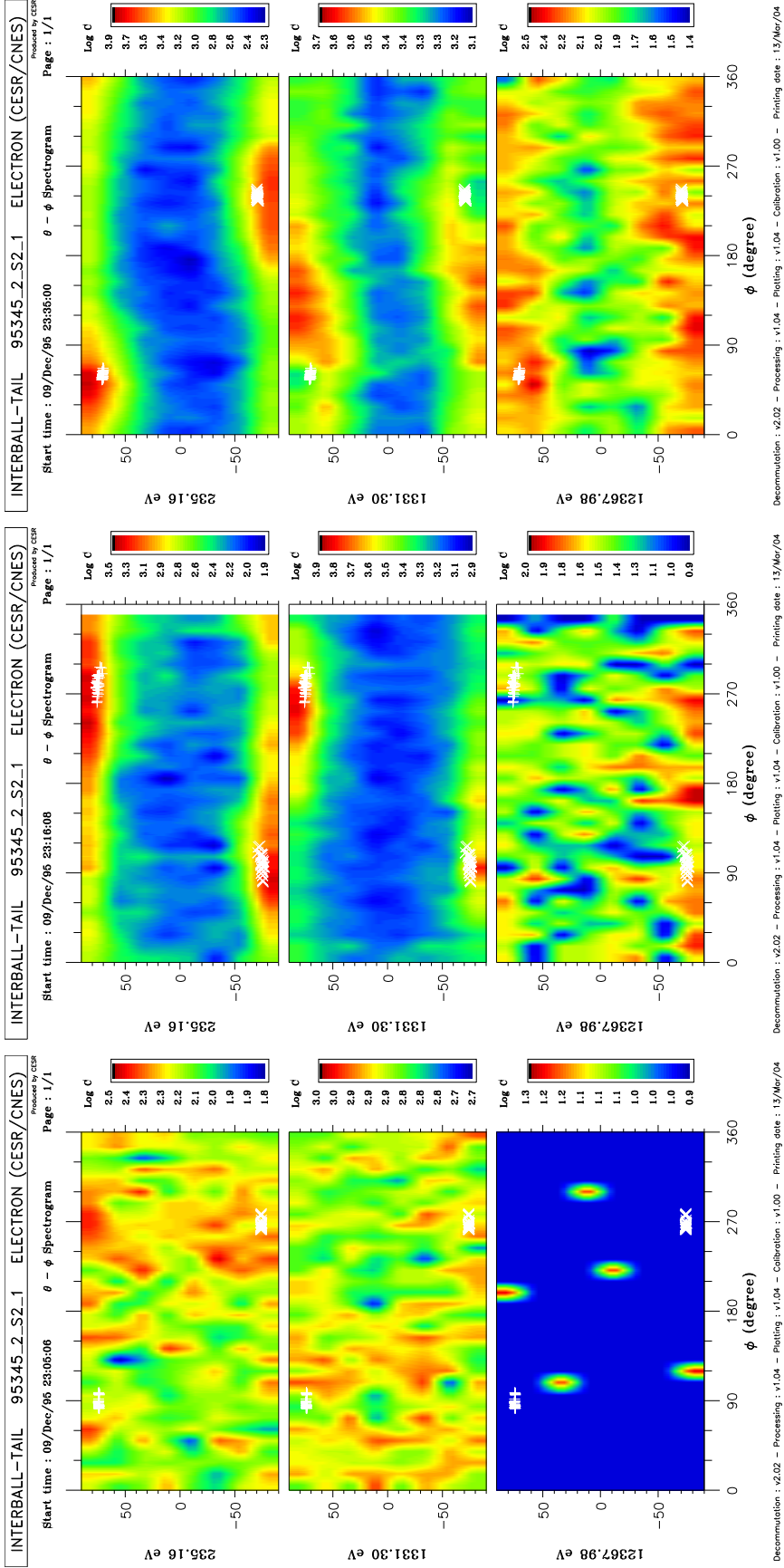
The optical observations

Two visual images taken by the DMSP F12 satellite are shown in Figure 4.19. The projected Interball positions at the moment of the scan is marked by the blue dots, while the position corresponding the moment of interest (01:30 UT) is represented by the red circle. The DMSP passed over the region of interest before- and after the event under study, so there is no direct image, but the displacement of the bright auroral spiral (typical to rather weak disturbances) confirms, that the Interball had to pass through the field lines of the auroral arc between the moments where the two images were obtained. Two comments on the above crossings of the auroral arc (blue dots) have to be done. First, that there was no magnetic field data on Interball after 01:42 UT, so the well confirmed pass of the Interball through the active auroral field lines (see the blue dot in the right panel) can not be explored. Second is that near the similar crossing (in the left panel of Figure 4.19) there was no injection nor enhanced magnetic fluctuations seen



(a) Cuts through the electron 3D flux, (perpendicular to B, the blue and green curves, and parallel/anti-parallel to B, light blue and red). (Left) Before, (Middle) during, and (Right) after the increased magnetic pulsations.

Figure 4.16: Electron distributions at three instances of 09/December/1995. Format as in Figure 4.4. See text for details.



(b) 3D counts at three energies. (Left) Before-, (Middle) during-, and (Right) after the increased magnetic pulsations.

Figure 4.16: (continued) Electron distributions at three instances of 09/December/1995. Format as in Figure 4.4.

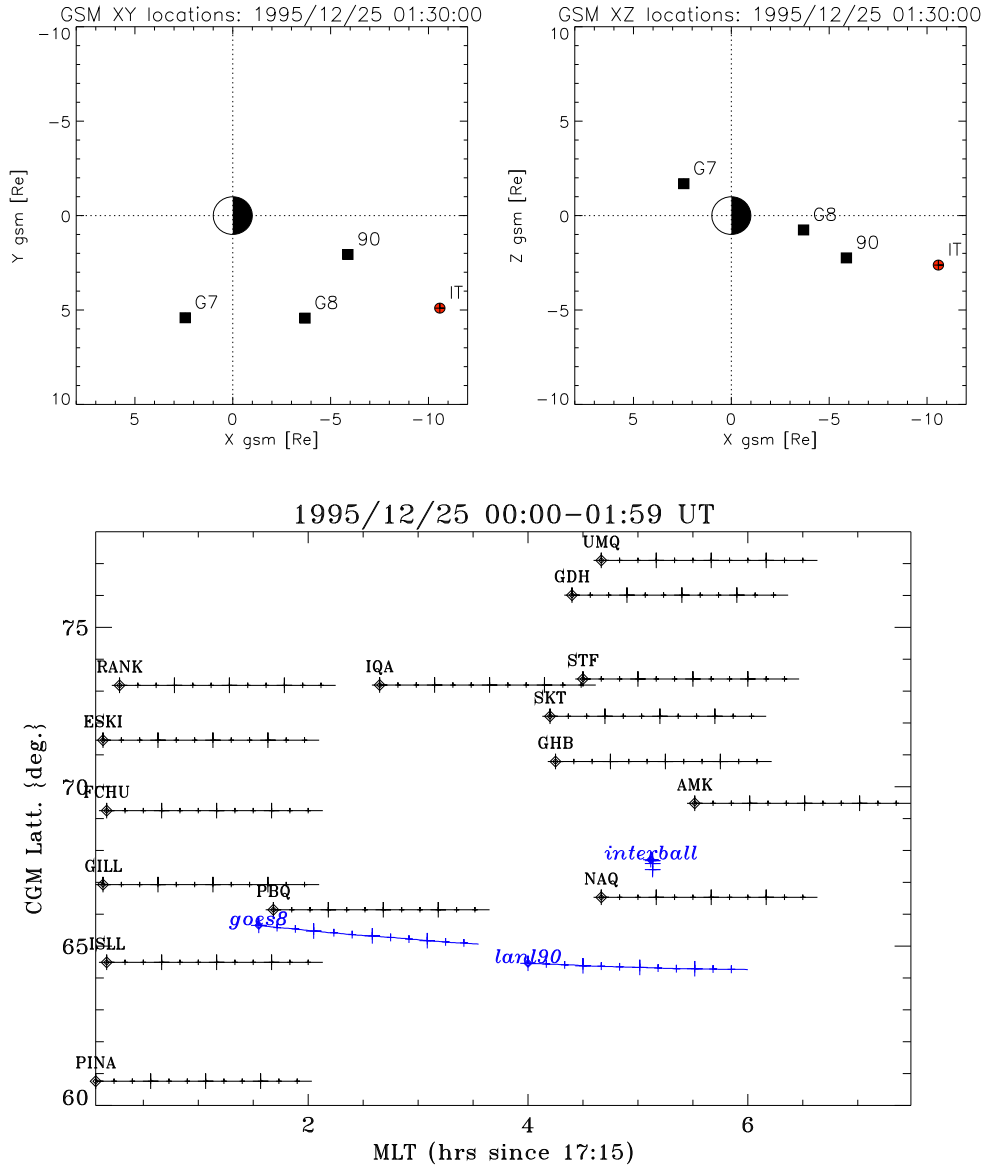


Figure 4.17: The **25/December/1995**- localization of the event. (**Top**):The GSM XY and XZ location of satellites at 01:30 UT (the satellites are marked as in previous cases). (**Bottom**): The Interball trajectory projected on Earth (also with the trajectory of geostationary satellites GOES-8 and LANL 90) in MLT- CGL coordinates and positions of selected ground magnetic stations. Each trajectory begins at 00:00 UT and other details are as in the previous cases.

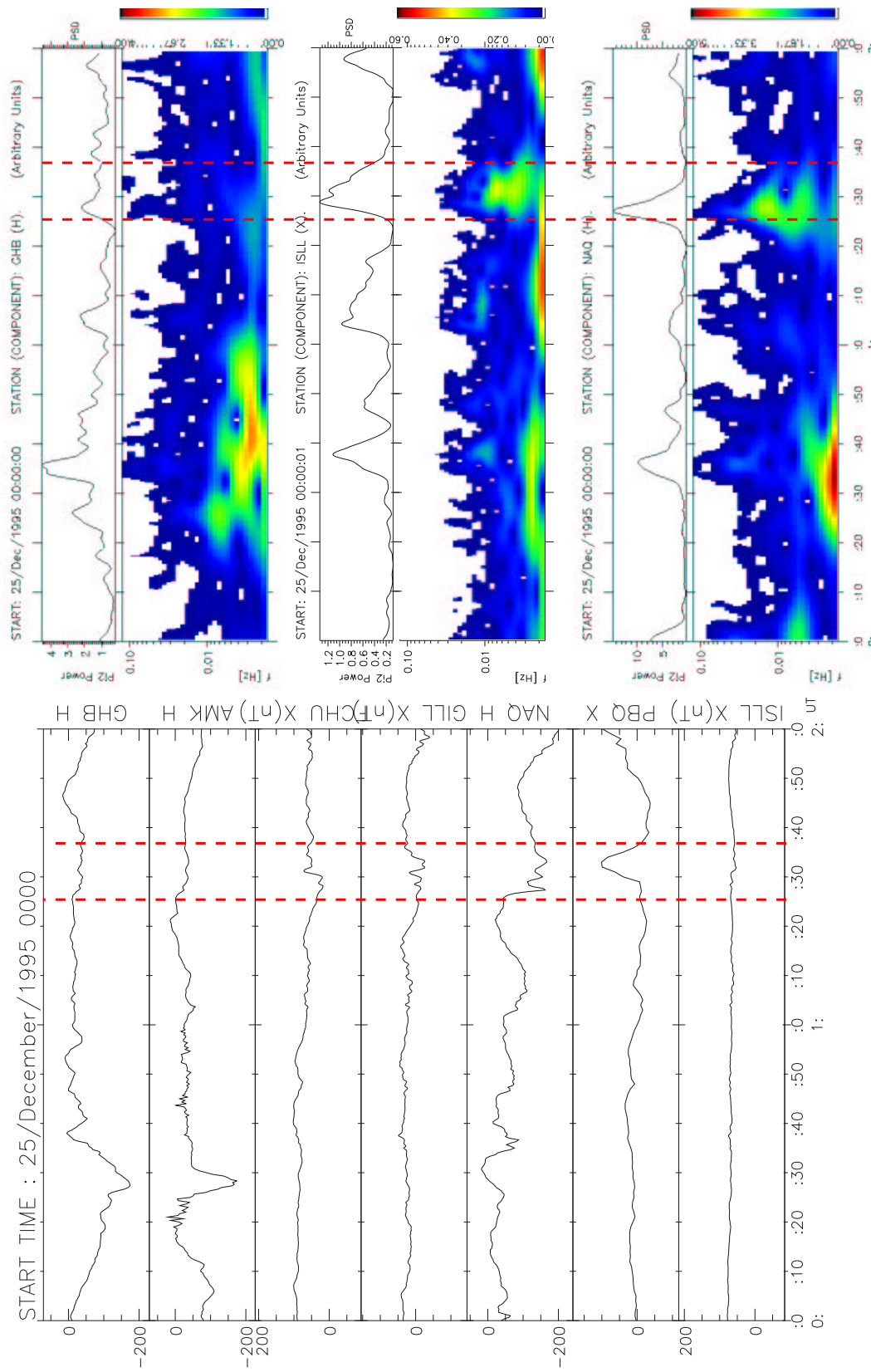


Figure 4.18: Ground based magnetic observations between 00 and 02 UT on 25/December/1995: **(Left)** Northward magnetic field component from selected stations near the Interball trajectory footprint (compare Figure 4.17); **(Right)** Dynamic spectra (color panels) of pulsations in the Pc5 - Pc3 frequency range (1.67 - 100.0 mHz) and total power of the P12 pulsations (black curves). The data of the northward component from three selected stations, NAQ, ISLL and GHB are shown and the units are arbitrary.

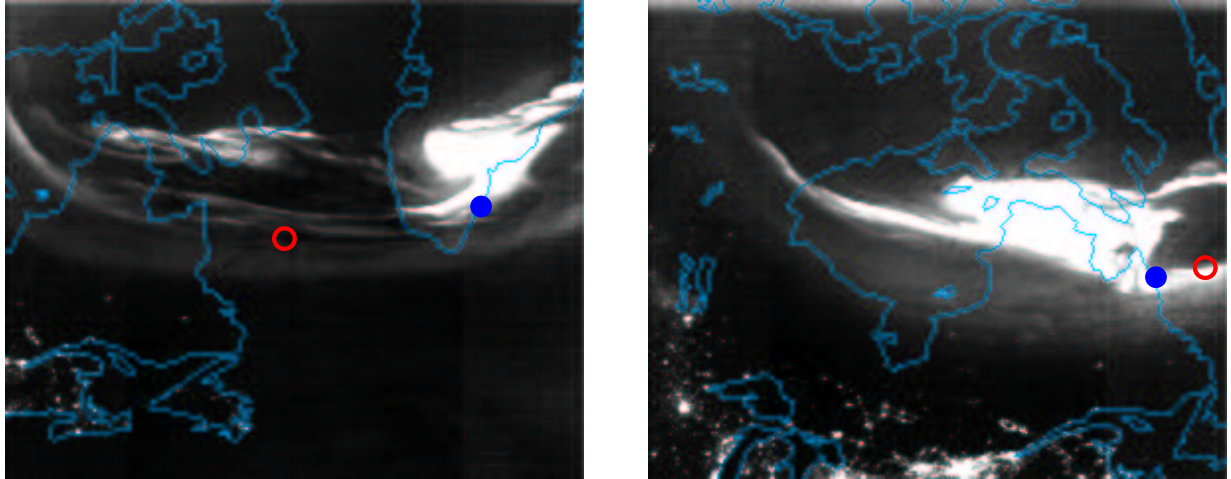


Figure 4.19: Two visual range images of the region of interest taken by the OLS instrument on the DMSP F12 satellites on 25/December/1995. Projected Interball position at the moment of scan is marked as the blue dot, while the position at the time of the discussed event (01:30 UT) by the red circles (note that at 01:30 UT the DMSP F12 was located elsewhere and the discussed event fits between the two images shown). **(Left)** Before the discussed event: the bright auroral spiral far eastward, over Greenland, was scanned between about 00:13 (lower edge) and 00:17 (upper edge) UT. **(Right)** After the discussed event: the bright auroral spiral, slightly westward to Interball (red circle) was scanned between about 01:54 and 01:57 UT. The conjunctions with the auroral spiral (blue dots) are not discussed in this study (see text for explanations).

(see the Interball observations below), so this case is not included into this study (it will be analyzed in a separate work).

These results, together with the lack of the clear injection and dipolarization signatures in the geostationary satellites (GOES-8 and LANL 90; not shown) allow to classify the case of 25/Dec/95 01:25 UT, as a localized, weak disturbance (as a pseudobreakup could be).

The IT observations

There was no attitude data for the satellite for that case, so the magnetic field is plotted in the satellite (rotating) frame of reference. The dominating value of the B_X (not rotating) and the electron spectra in Figure 4.20 show that the spacecraft traversed the hot plasma quite far above the Neutral Sheet. Between 01:26 and 01:37 UT there is the enhancement of the magnetic fluctuations (in the Pi2 and Pc3 range) that accompany the signatures of a current disruption. At this time the previously existing, field aligned flux anisotropy at few keV disappears (01:27 - 01:37 UT). There is also the hot plasma injection (or a Plasma Sheet thickening) seen just before the magnetic disturbance.

The changes of the electron distributions presented in Figure 4.21 are quite evident. The key points are: (i) The temperature increases and the high energy, non-thermal tail in the distribution increases after the beginning of injection. (ii) The field aligned anisotropy is, at least partially, realized by the presence of the additional, colder component streaming/accelerated along the field line and peaked near 1 keV (this statement will be justified, and the details will be further explored in the following chapter) (iii) During the magnetic disturbance (on Interball), the additional, field aligned flux component (almost) disappears and the spectra have more turbulent/non-stationary character.

Contrary to the previous cases, this time the satellite MLT position was westward (about 60 min. at 01:30 UT) to the station, where the ground disturbance is best seen (NAQ). If the

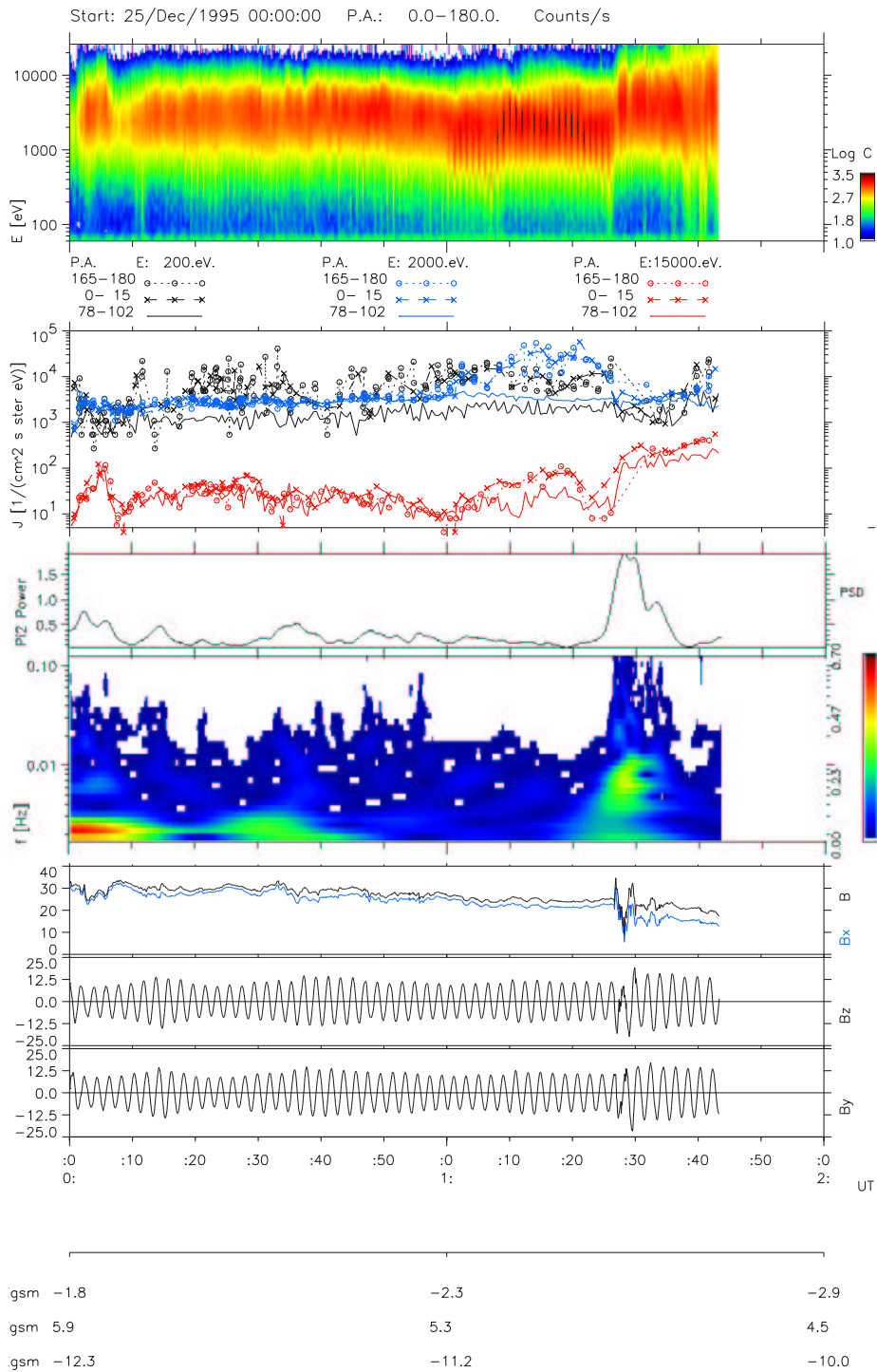
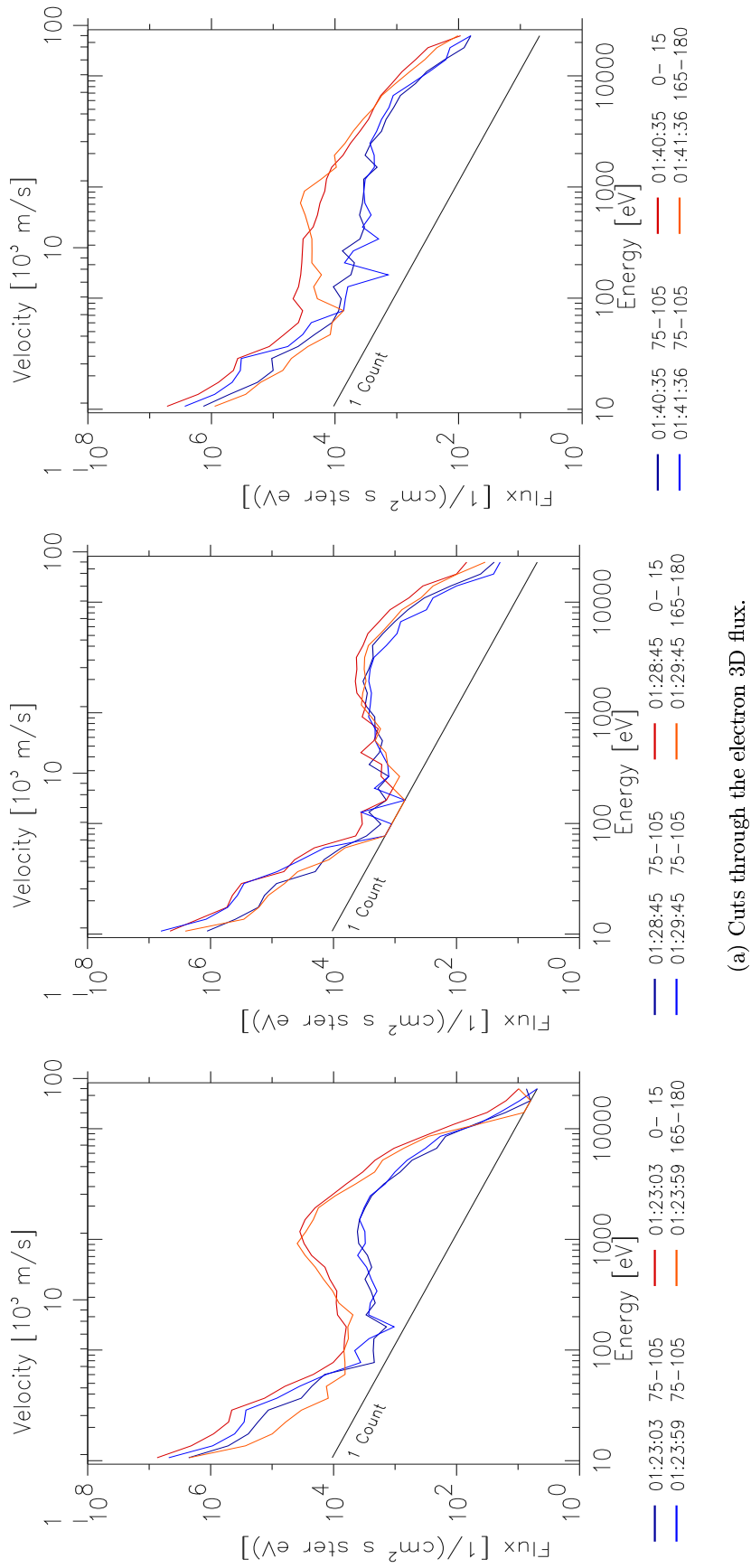
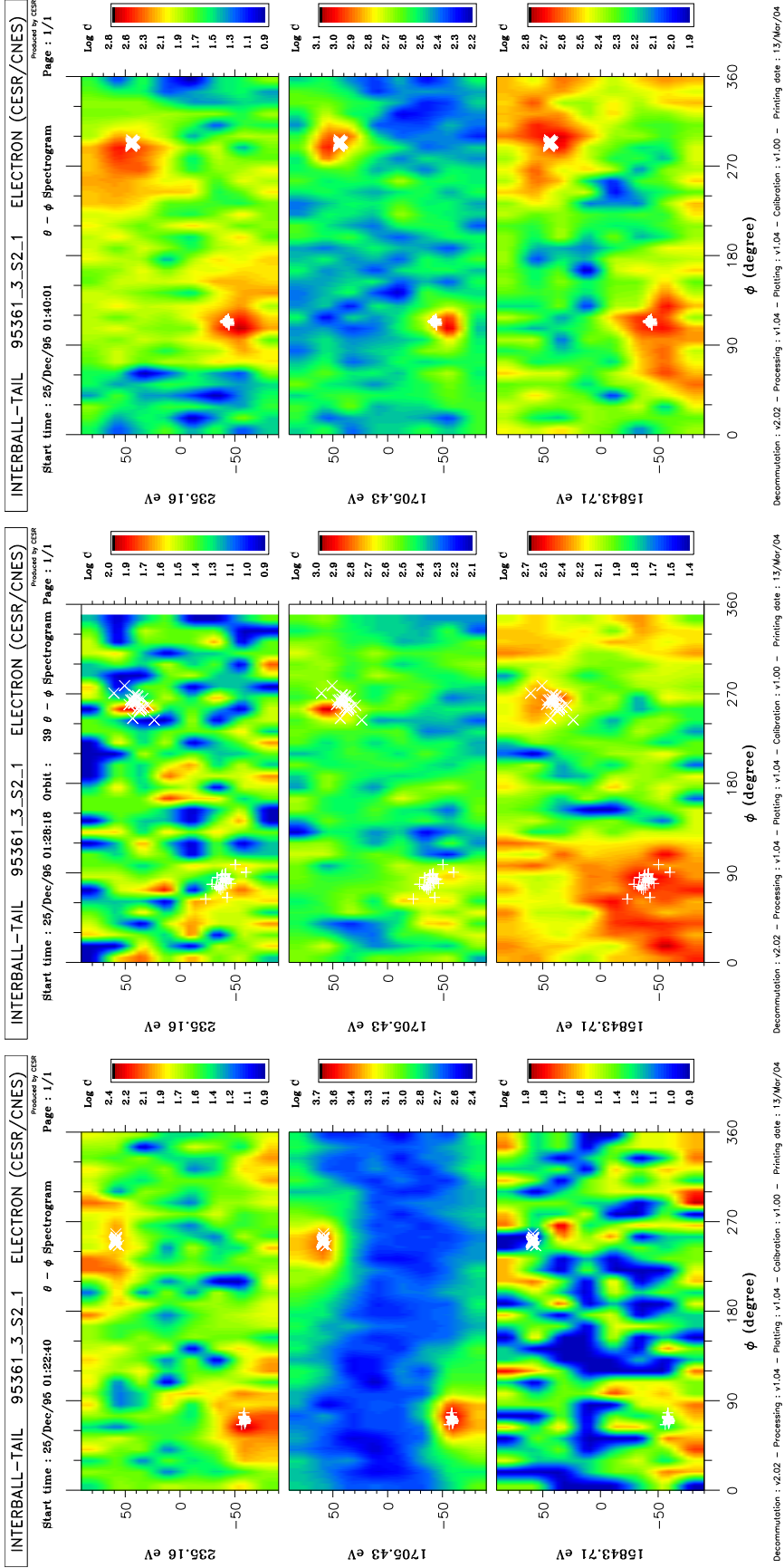


Figure 4.20: The Interball observations in the time range 00 - 02 UT on 25/December/1995. Format the same as in Figure 4.3.



(a) Cuts through the electron 3D flux.

Figure 4.21: Electron distributions at three instances of 25/December/1995. Format as in Figure 4.4. See text for details.



(b) 3D counts at three energies. (Left) Before-, (Middle) during-, and (Right) after the increased magnetic pulsations.

Figure 4.21: (continued) Electron distributions at three instances of 25/December/1995. Format as in Figure 4.4.

ionospheric currents develop in a similar way (westward and poleward) for such weak disturbance as for the case of a usual substorm, then the Upward Field- Aligned Current (UFAC) should easily reach the proximity of the Interball magnetic footprint, and the particle and magnetic field signatures could be observed by the spacecraft. It seems to be so, and it is further suggested by the optical observations of DMSP F12 (though not proved). The character of this case (the late evening MLT sector and stronger magnetic turbulence lasting longer than in the preceding cases) makes it similar to the following cases presented below.

4.3.6 28/December/1995

The satellite was located all the time at about 22:05 LT, near the IMAGE network sector, as shown in upper panel of Figure 4.22 for 20:45 UT. Projected satellite's trajectory and selected geomagnetic stations, between 19:30 and 21:30 UT, are seen at the bottom panel. Although the satellite was located below the neutral sheet, (see below) the northward projection of trajectory is shown as the station coverage of the appropriate region in the southern hemisphere was too poor.

Geophysical situation

The evolution of the ground event is illustrated on the contour plot in Figure 4.23. It shows the B_Z magnetic field component in the UT - MLT coordinates. The dark structure that begins at 20:45 UT and expands poleward, shows clearly the position and the time of its beginning. Note the footprint of the Interball position at 20:45 UT - it was located about 35 minutes MLT westward to the ground event.

Northward component of the magnetic field from selected stations is plotted in the right panel of Figure 4.24. Weak but clear signatures of a substorm- like current system activation are also seen here, since 20:45 UT, at relatively higher latitude. Careful examination of the magnetic data on stations in the auroral zone (from broad LT sector, about 18 to 03 MLT) has been performed to find that it was a very localized event, as a pseudobreakup could be. The westward current developed slightly southward to SOR at 20:45, then it intensified and moved northward near 20:46 UT. It passes poleward over BJN at 20:52. Simultaneously, the eastward current develops over- and south to TRO since about 20:46:30. This event, though localized, was easily detected by the Pi2 enhancements at even distant stations. Right panel of Figure 4.24 shows the dynamic spectra of the northward magnetic components from TRO, OIJ (at lower latitude) and more westward (nearly 2.5 MLT hours) located TJO.

The IT observations

Interball traversed the plasma sheet below the neutral sheet at X_{GSM} of -11.0 to -9.0 R_E , in the pre-midnight MLT sector. On the top- and on the bottom panel of Figure 4.25, two slightly 'disturbed' regions are seen, near 20:00 - 20:20 UT and near 20:40 - 20:55 UT. For the second of them, the increase of electron fluxes above 10 keV is observed between 20:43 and 20:53 UT. It is accompanied by the enhanced magnetic fluctuations in the broad frequency range (Pc5 to Pc1), near 20:41 - 20:52 UT. Note the difference in amplitude and frequency range between this event and the preceding disturbance near 20:00 - 20:20 UT. Note also, how this case differ also from the preceding cases (21/Oct/95, 02/Dec95) by the time range and the amplitude of the magnetic fluctuations (Figures 4.7 and 4.11). After the magnetic fluctuations cease, since 20:53, an enhanced electron flux anisotropy (of the field- aligned type) increases at low energies (above about 100 eV).

Changes of distributions in Figure 4.26 are similar in some aspects to those of other cases: (i) After the injection, the non- maxwellian, higher energy tail of distribution appears and the

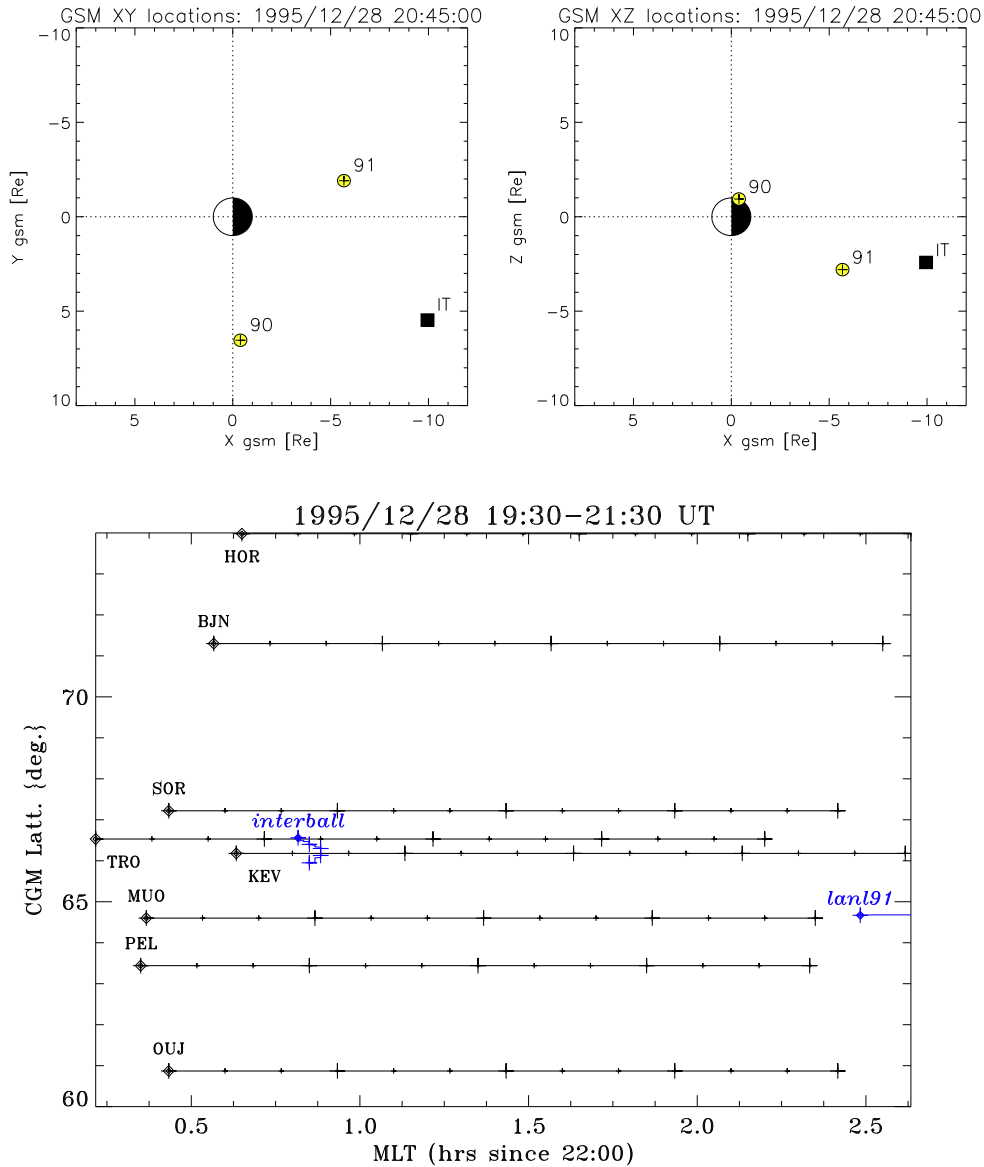


Figure 4.22: The **28/December/1995**- localization of the event. (**Top**): The GSM XY and XZ location of the Interball at 20:45 UT. (**Bottom**): The trajectory of the Interball (and of the geostationary satellite LANL 90) projected on Earth in MLT- CGL coordinates and positions of the selected ground magnetic stations. Each trajectory begins at the leftmost (thicker) point at 21:30 UT and tick-marks are separated by 10 minutes UT. The coordinates and the satellite footprints have been calculated using standard T98c model with $K_p=2$ and the IGRF model for the 1995 epoch.

temperature increases. (ii) Stronger non-stationary effects are seen in fluxes during the magnetic disturbance (the middle panel). (iii) When the magnetic fluctuations fade, the additional accelerated/streaming population appears with the flux maximum at few hundreds eV and it is the main source of the enhanced anisotropy. (iv) Note however, that this time, the direct anti-coincidence between this component and the fluctuations is obscured by non-stationary effects.

Localization of the event (westward to the position of ground pseudobreakup), the weak plasma injection related to it and stronger fluctuations (than in four first cases), makes this case similar

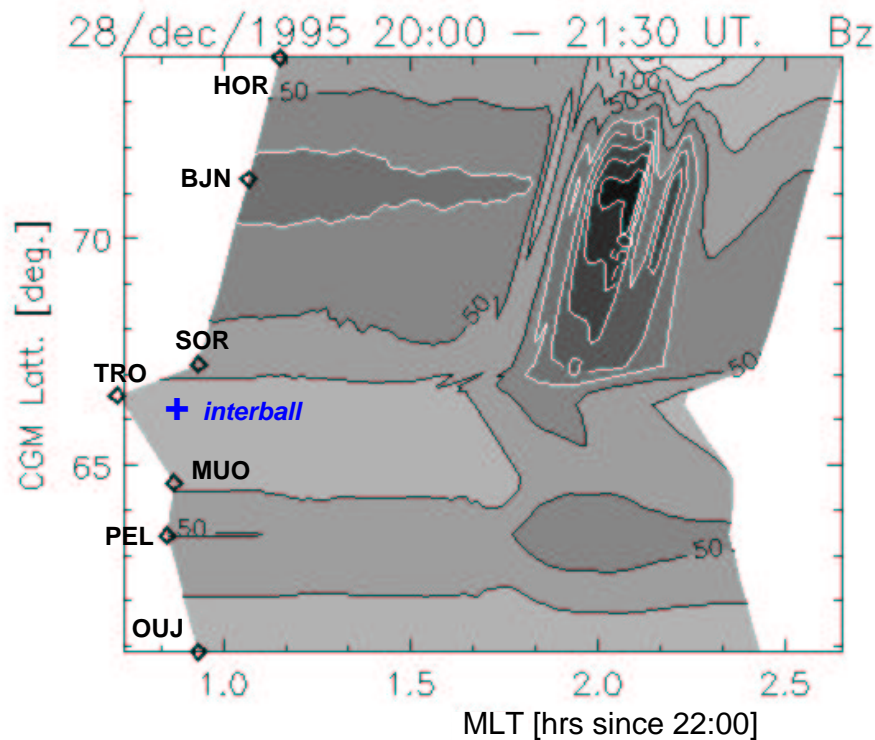


Figure 4.23: Contour plot of the B_z magnetic component at selected IMAGE stations in MLT-CGL coordinates. The Interball position at 20:45 is also marked.

to the preceding one and to the three following cases, presented below.

4.3.7 13/January/1996

This case consists actually of two injections, related to two separate intensifications of the substorm studied in detail in Chapter 3. They will be considered as two separate cases. The satellite was located in the late evening MLT sector, as shown in Figure 4.27 (compare also Figure 3.8).

Geophysical situation

To recall the results of Chapter 3, the ground data showed high activity level in the broad LT sector, with three substorm intensifications, two of which coincided with the Interball observations (see below). The magnetic records from some of the relevant stations are shown in Figure 4.28 in the format as before. The Interball events, marked by red dashed lines, correspond well to intensifications shown in magnetograms- at NAQ, AMK and PBQ (near 03:02 UT) and at GILL, FCHU (near 03:32 UT).

The IT observations

Two injections are seen in the ELECTRON spectrogram in Figure 4.29 (the first weaker, but both clearly seen in the SKA energetic particle data, not shown). They coincide almost exactly with the onset of the strong magnetic field fluctuations. The fluctuations extend up to the Pc1 frequencies and accompany two dipolarizations. The satellite is located in the hot plasma, in the pre-midnight sector. The second event took place away from the Neutral Sheet as seen in the magnetic field record. The fluctuations show the signatures of the current disruption observed

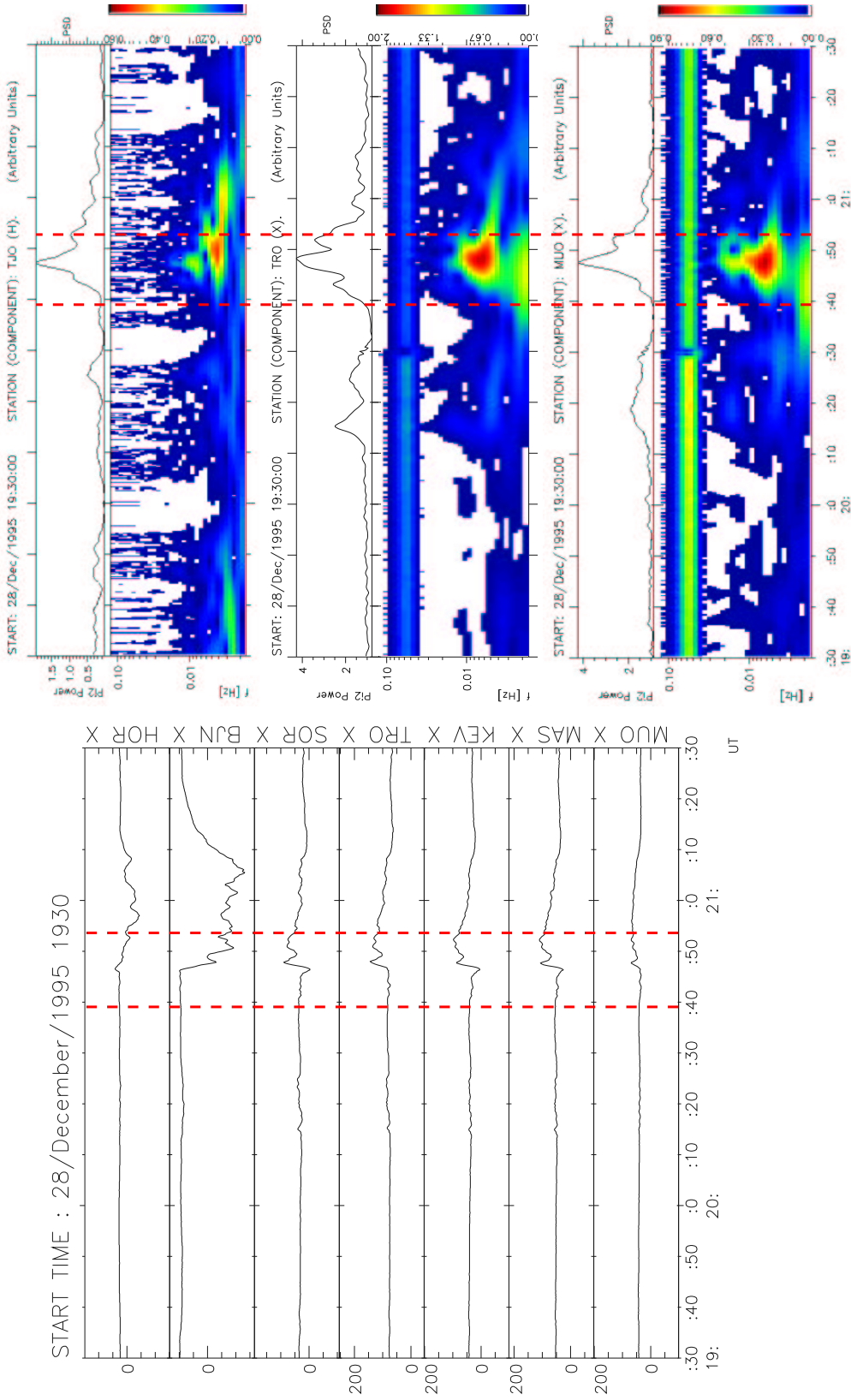


Figure 4.24: Ground based magnetic observations between 19:30 and 21:30 UT on 28/December/1995: **(Left)** Northward magnetic field component observed on selected stations near the Interball trajectory footprint (compare Figure 4.22); **(Right)** Dynamic spectra (color panels) of pulsations in the Pc5 - Pc3 frequency range (1.67 - 100.0 mHz) and total power of the Pi2 pulsations (black curves). The data of the northward component from stations, MUO, TRO and BUN are shown and the units are arbitrary. The enhanced intensity in the range 0.05 - 0.1 Hz is an artificial effect of the instrument noise.

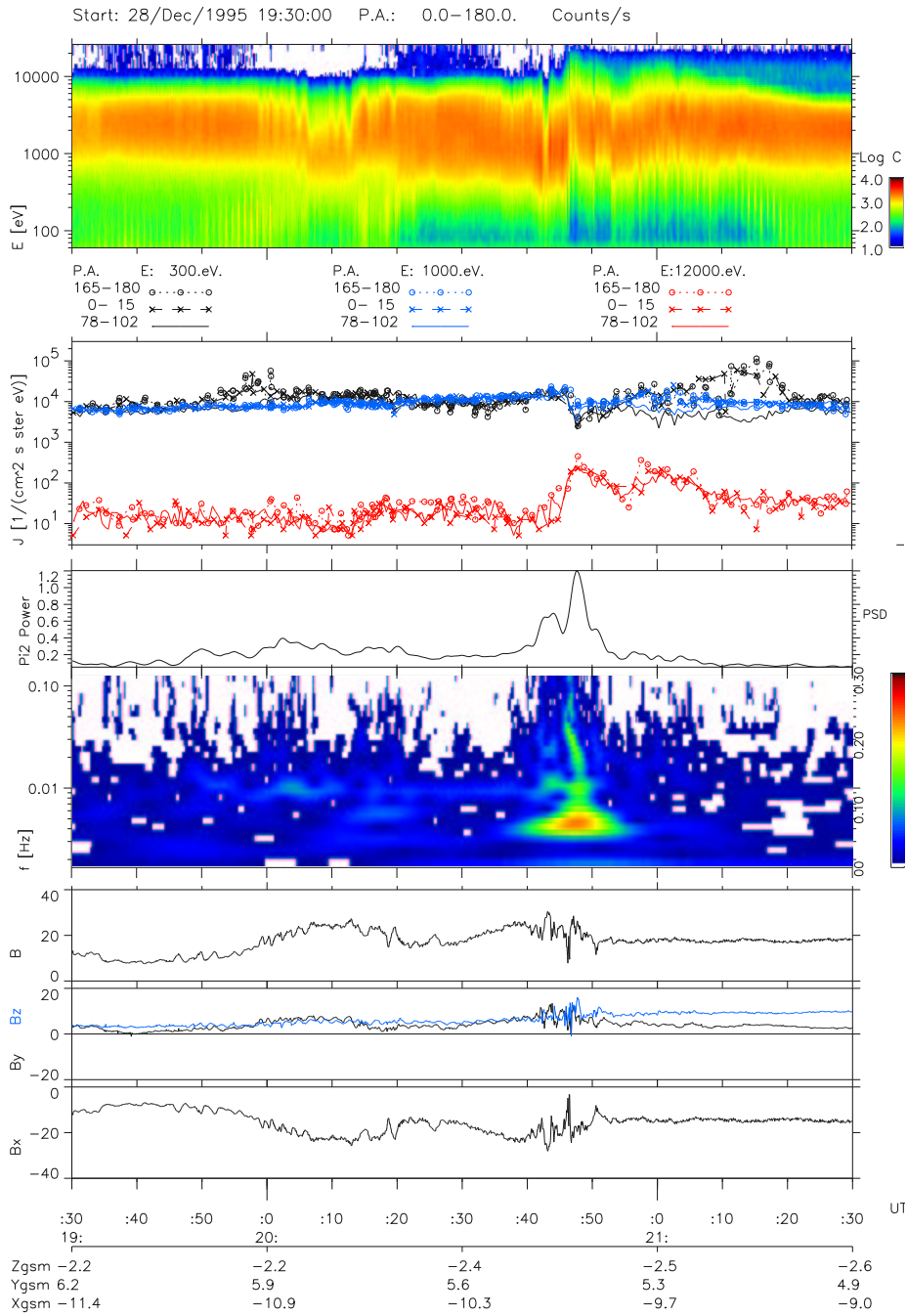
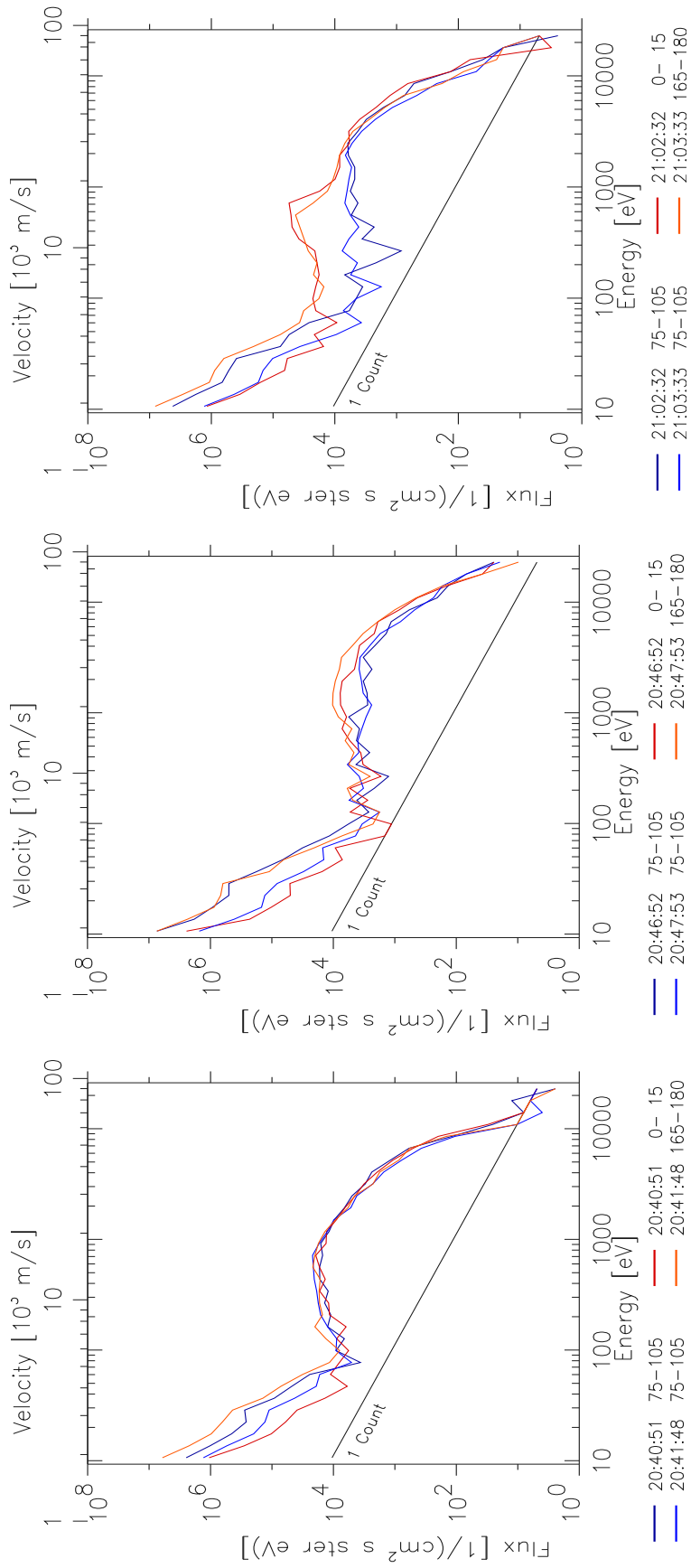
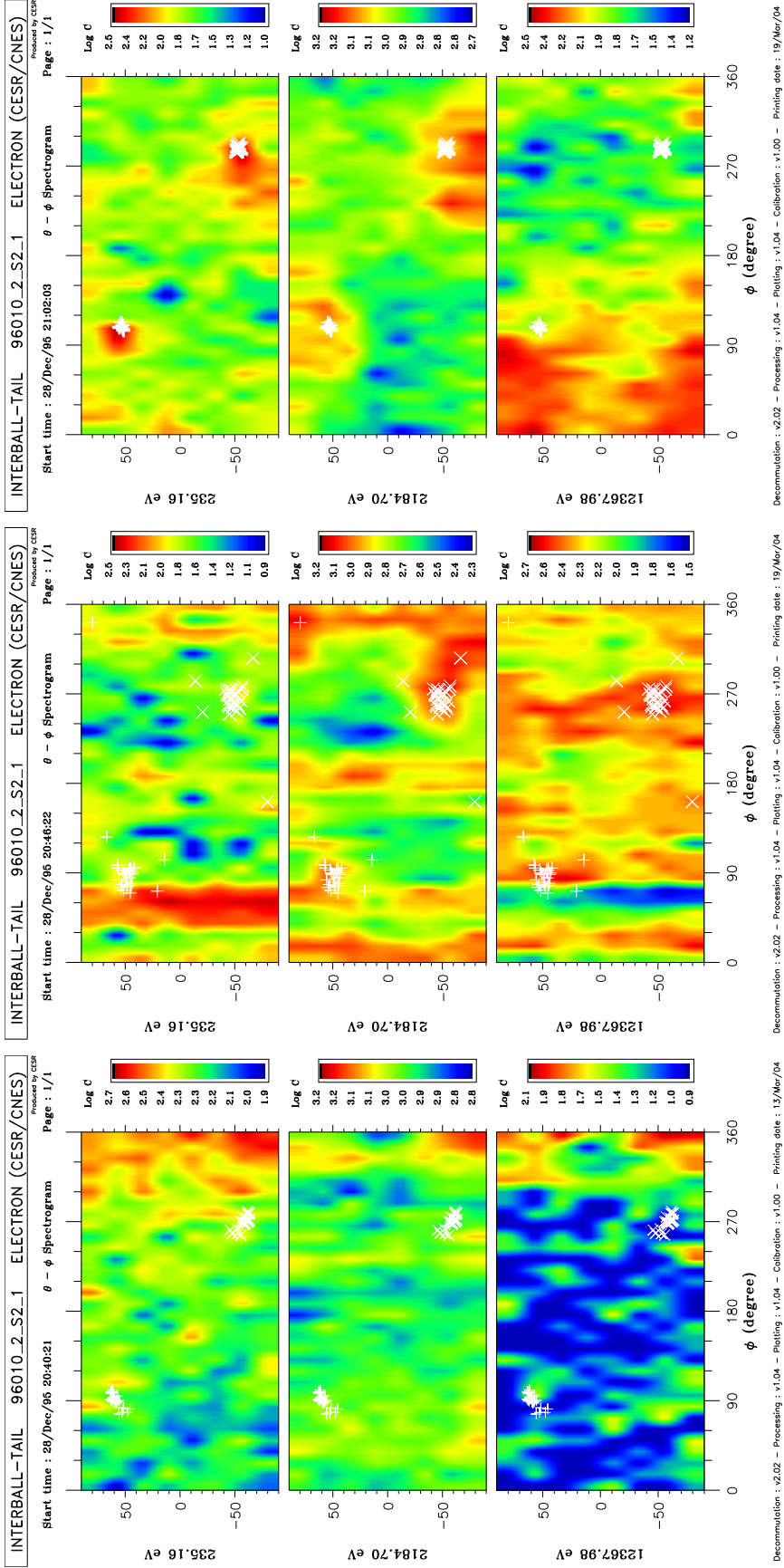


Figure 4.25: The Interball observations in the time range 19:30 - 21:30 UT on 28/December/1995. Format the same as in Figure 4.3.



(a) Cuts through the electron 3D flux.

Figure 4.26: Electron distributions at three instances of 28/December/1995. Format as in Figure 4.4. See text for details.



(b) 3D counts at three energies. (Left) Before-, (Middle) during-, and (Right) after the increased magnetic pulsations.

Figure 4.26: (continued) Electron distributions at three instances of 28/December/1995. Format as in Figure 4.4. See text for details.

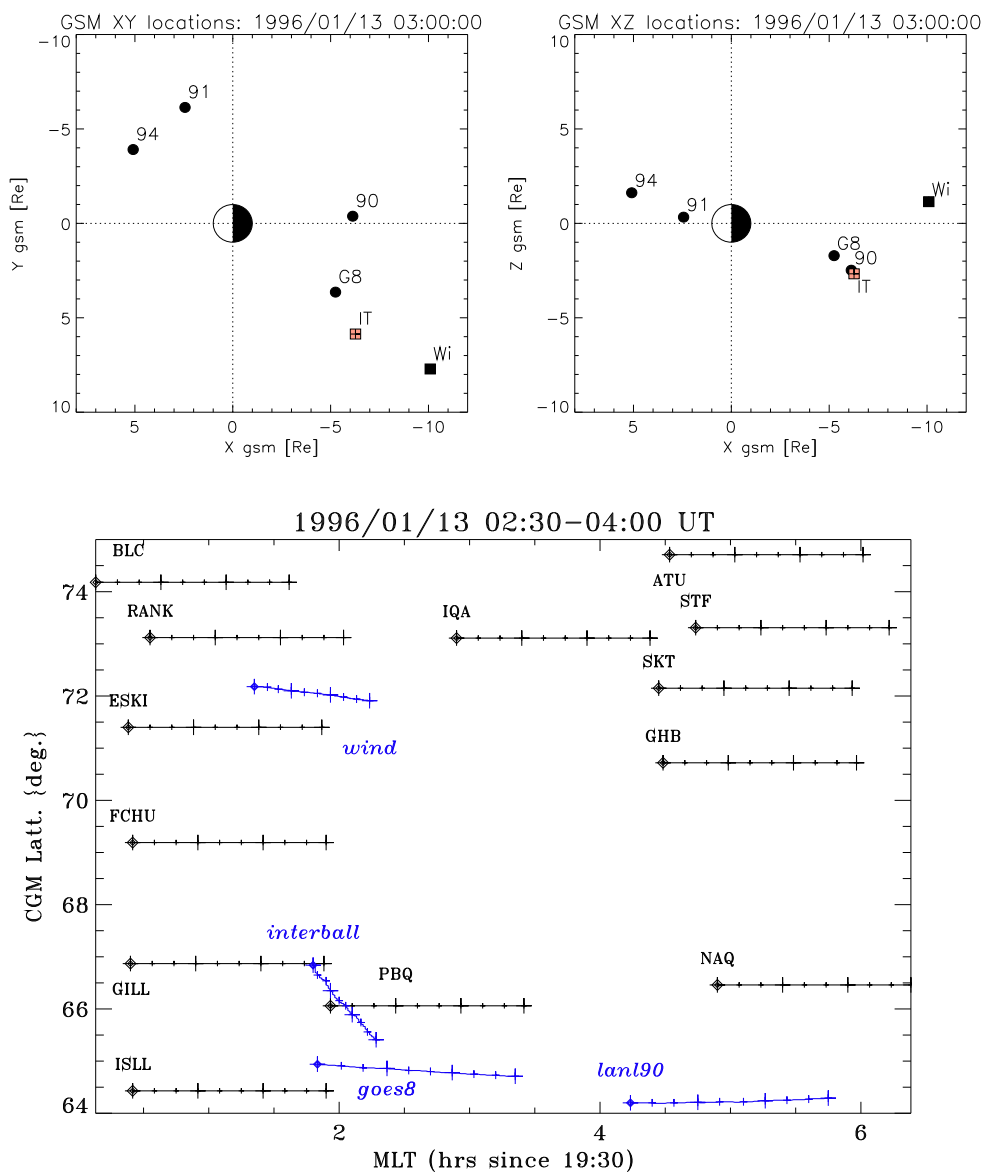


Figure 4.27: The **13/January/1995**- localization of the event. (**Top**):The GSM XY and XZ location of satellites at 03:00 UT (the geostationary satellites are marked as before and the WIND satellite is denoted by WI). (**Bottom**): The Interball trajectory projected on Earth (also with footprints of satellites GOES-8, LANL 90 and WIND) in the MLT- CGL coordinates and positions of the selected ground magnetic stations between 02:30 and 04:00 UT. Each trajectory begins at 02:30 UT and the coordinates and the satellite footprints have been calculated using standard T98c model with $K_p=3$ and the IGRF model for the 1995 epoch. See the detailed analysis of these two cases in Chapter 3 for more.

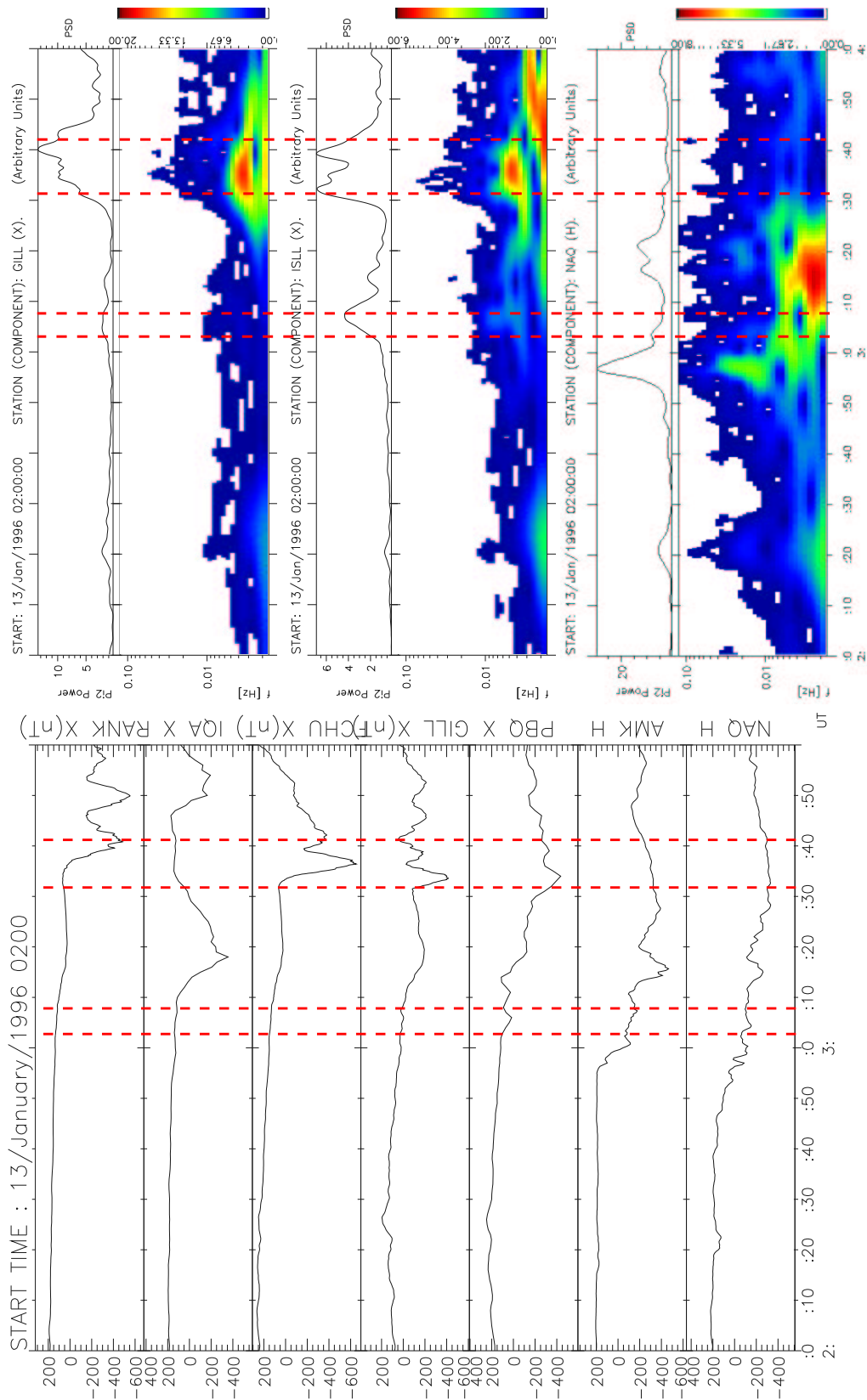


Figure 4.28: Ground based magnetic observations between 02 and 04 UT on 13/January/1996: **(Left)** Northward magnetic field component from the selected stations near the Interball trajectory footprint (compare Figure 4.27); **(Right)** Dynamic spectra (color panels) of pulsations in the Pc5 - Pc3 frequency range (1.67 - 100.0 mHz) and total power of the Pi2 pulsations (black curves). The data of the northward component from stations, GILL, ISLL and NAQ are shown and the units are arbitrary.

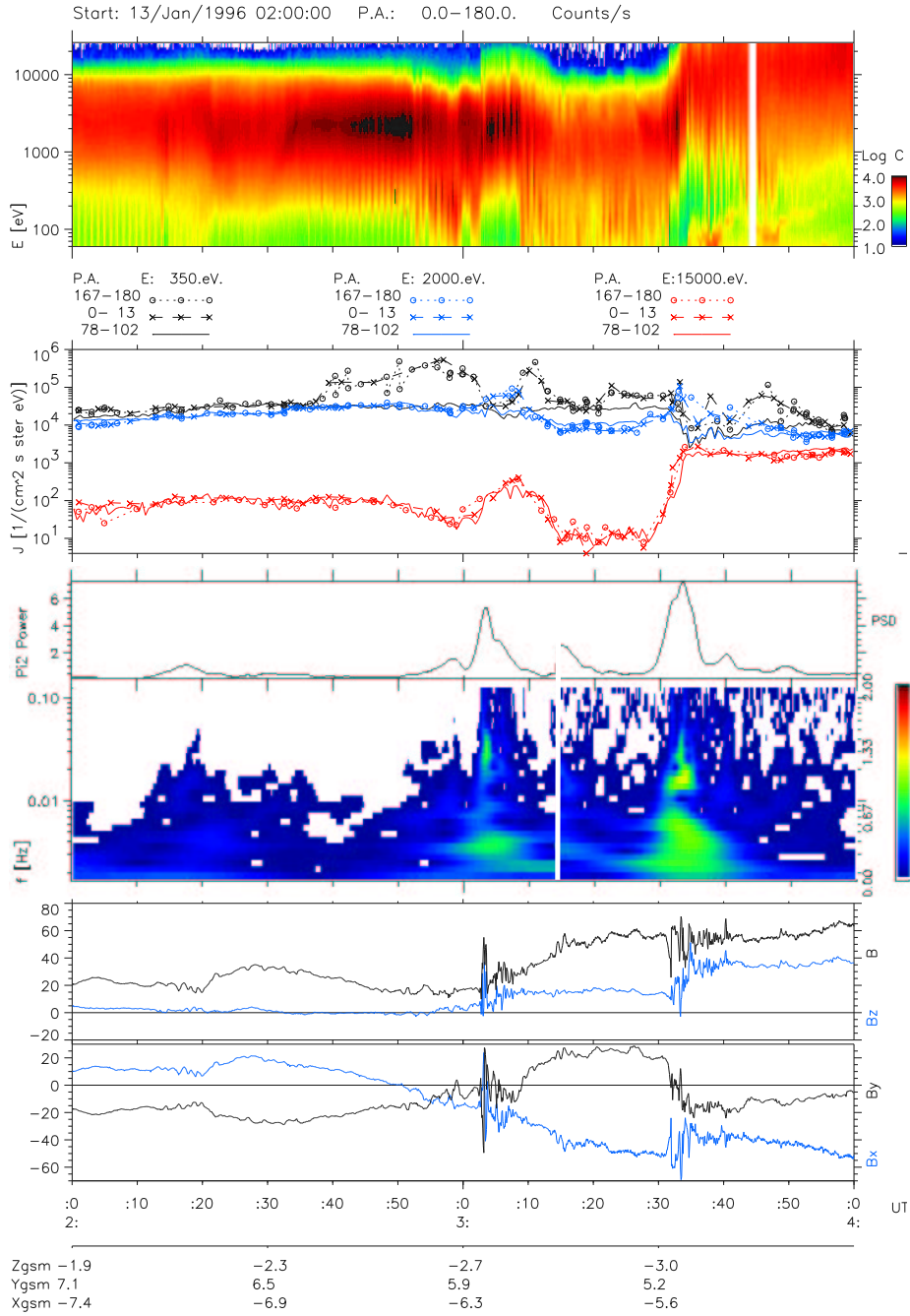


Figure 4.29: The Interball observations in the time range 02 - 04 UT on 13/January/1996. Format the same as in Figure 4.3.

nearly “in situ” (see e.g. Lopez et al. 1990, [102]; Lui et al. 1990, [104]; Roux et al. 1991, [160]). The very striking feature are the sharp changes of the electron fluxes. At the moment of fluctuations, the strong, field aligned anisotropy of low energy flux disappears while it appears (weaker) in “middle” energies (about 2 keV).

Changes of the distribution function during the first event are shown in Figure 4.30. The effect is very clear this time: (i) Colder, field-aligned streaming/ accelerated component disappears during the extended magnetic fluctuations. Note, that the distribution in the left panel is not an ephemeral one but is typical for the region of the Plasma Sheet traversed during at least 5 minutes before the onset of the magnetic fluctuations. (ii) Despite the above disappearance, there is still a rather weak, field- aligned anisotropy near 1 - 2 keV (middle panel) (iii) There is the asymmetry (in the parallel/anti-parallel direction) of the colder component (see the left- and the right panels). It is also the long lasting effect in that case. (iv) After the injection, the temperature does not change much, but the high energy tail develops (see nearly one order of magnitude increase near 12 keV). (v) There is significant level of fluctuations/temporary changes seen in the electron fluxes

The second event is illustrated with Figure 4.31. During this case: (i) The temperature strongly changes (reaching values close to the instrument upper energy limit). (ii) with the enhanced magnetic fluctuations, the anisotropy is evident in the whole main, hotter component while the colder one almost disappears contrary to the quiet regions (iii) Weak empty cone- and ring-type distributions (i.e. flux maximizing obliquely to B) are observed at higher energies after and before the fluctuations (iv) The asymmetry (parallel / anti-parallel) is stronger in the quiet regions (v) the temporal changes are even more important then before.

4.3.8 16/January/1996

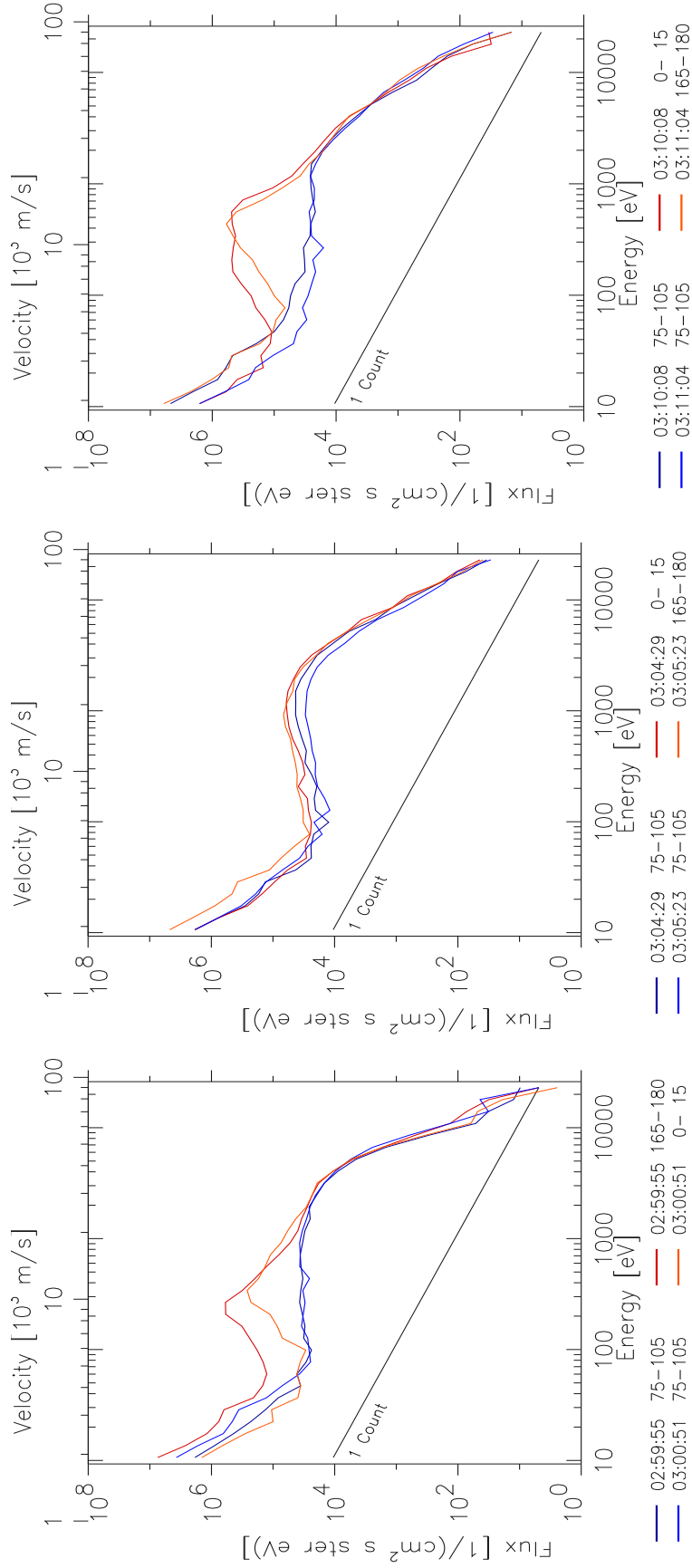
Interball was located around 20:50 local time between 19 and 21 UT. Its location at 19:45 UT is seen in upper part of Figure 4.32, and the projection of the trajectory onto northern hemisphere (in MLT - CGL coordinates) in the lower part, together with the positions of the selected geomagnetic stations.

Geophysical situation

The weak substorm between Scandinavia and Iceland was detected to develop since about 19:45 UT. In the left part of Figure 4.33, the northward component of the magnetic field is seen, from selected stations (see Figure 4.32) ordered with increasing CGM latitude and decreasing MLT. The negative bay starts to develop over SOR at 19:45, and the ionospheric substorm current system is seen expanding northward over MUO, AND and SOR since 19:46 UT. At 19:56 westward electrojet moved northward over BJN and developed between TJO and SCO more westward (see four top stations in the left panel of Figure 4.33). Bursts of the magnetic pulsations confirm the global character of the event. They are seen in distant stations, e.g. NAQ or LOZ (not shown, 18:39 and 23:56 MLT respectively, at 19:45 UT) and in the closely located stations, as shown the right panel of Figure 4.33.

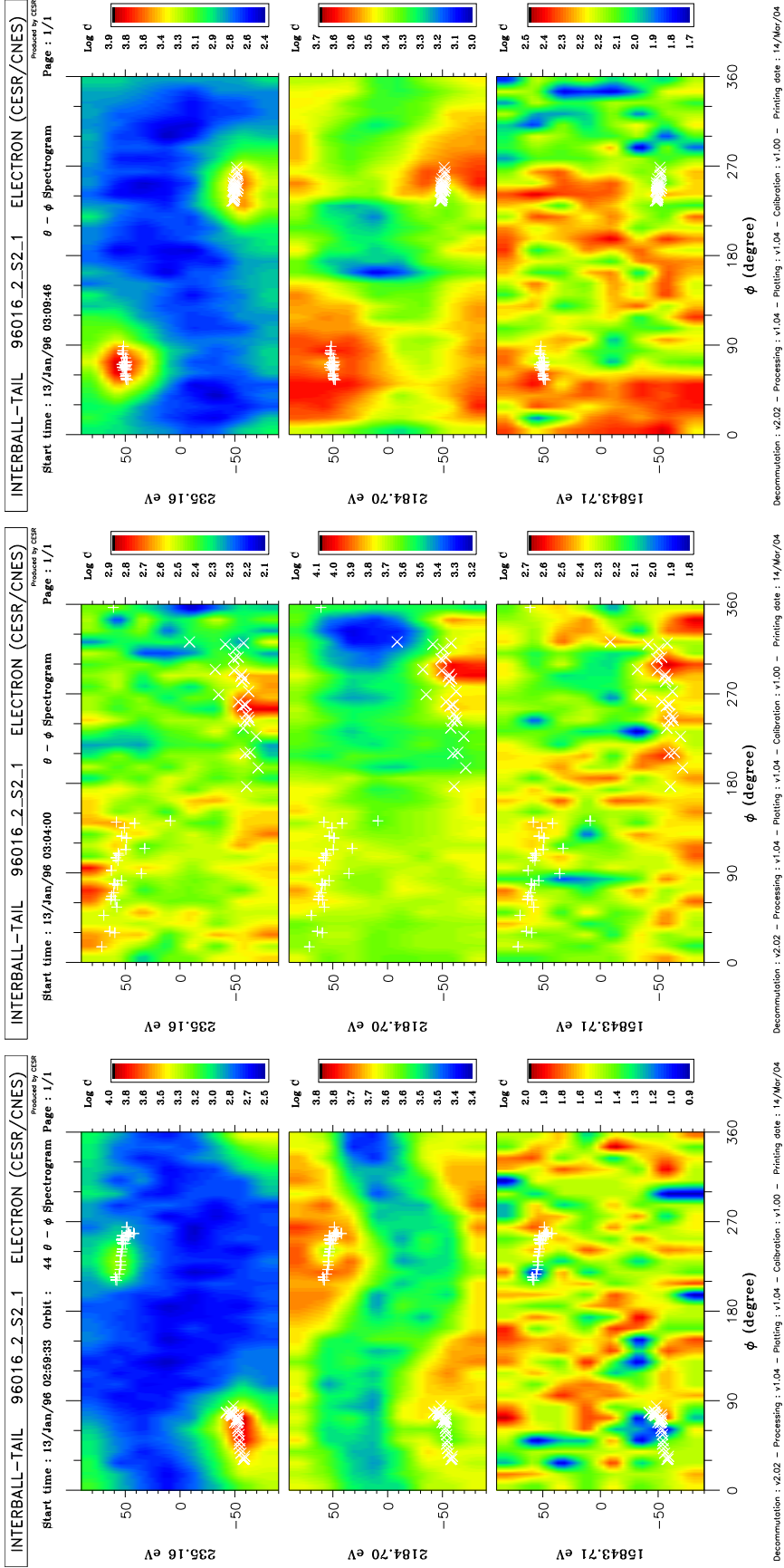
The IT observations

There are two signatures of the cross- tail current disruption seen in bottom panel of Figure 4.34 (as the B_X changing sign). The second of them, about 20:45 UT, is followed by dipolarization. It is also accompanied by the stronger, long lasting magnetic fluctuations in the Pc5 - Pc1 range, since about 19:42 until 20:12. The weak signature of injection at high energies in the ELECTRON data is confirmed by the DOK2 energetic electrons data at 19:43 (as is also the first ‘disruption’, at about 19:24 UT; not shown). There are also the changes of the flux anisotropy, the most evident



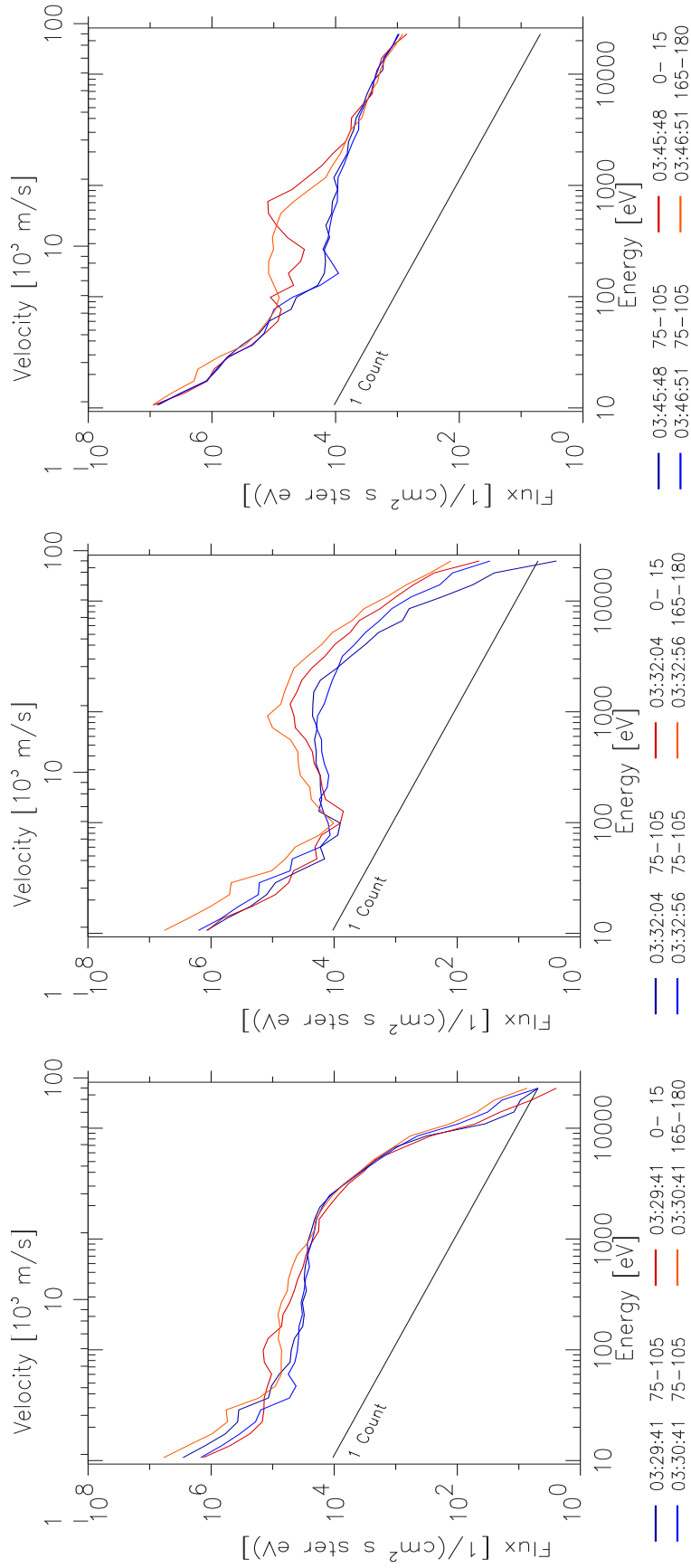
(a) Cuts through the electron 3D flux, (perpendicular to B, the blue and green curves, and parallel/anti-parallel to B, light blue and red). (Left) Before, (Middle) during, and (Right) after the increased magnetic pulsations.

Figure 4.30: Electron distributions at three instances of the first event of 13/January/1996. Format as in Figure 4.4.



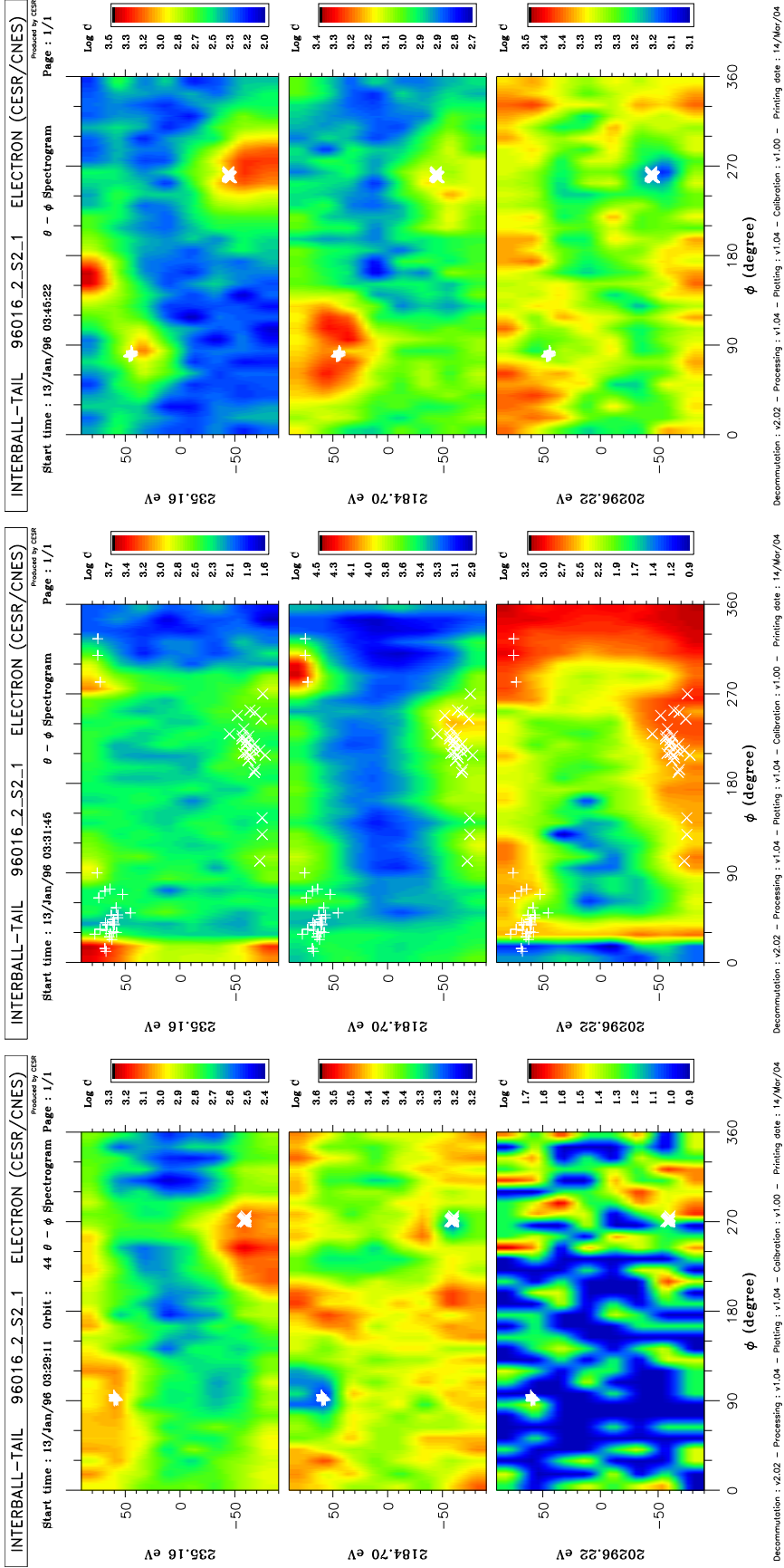
(b) 3D counts at three energies. (Left) Before-, (Middle) during-, and (Right) after the increased magnetic pulsations.

Figure 4-30: Electron distributions at three instances of the first event of 13/January/1996. Format as in Figure 4.4.



(a) Cuts through the electron 3D flux, (perpendicular to B, the blue and green curves, and parallel/anti-parallel to B, light blue and red). (Left) Before, (Middle) during, and (Right) after the increased magnetic pulsations.

Figure 4.31: Electron distributions at three instances of the first event of 13/January/1996. Format as in Figure 4.4.



(b) 3D counts at three energies. (Left) Before-, (Middle) during-, and (Right) after the increased magnetic pulsations.

Figure 4-31: Electron distributions at three instances of the second event of 13/January/1996. Format as in Figure 4.4.

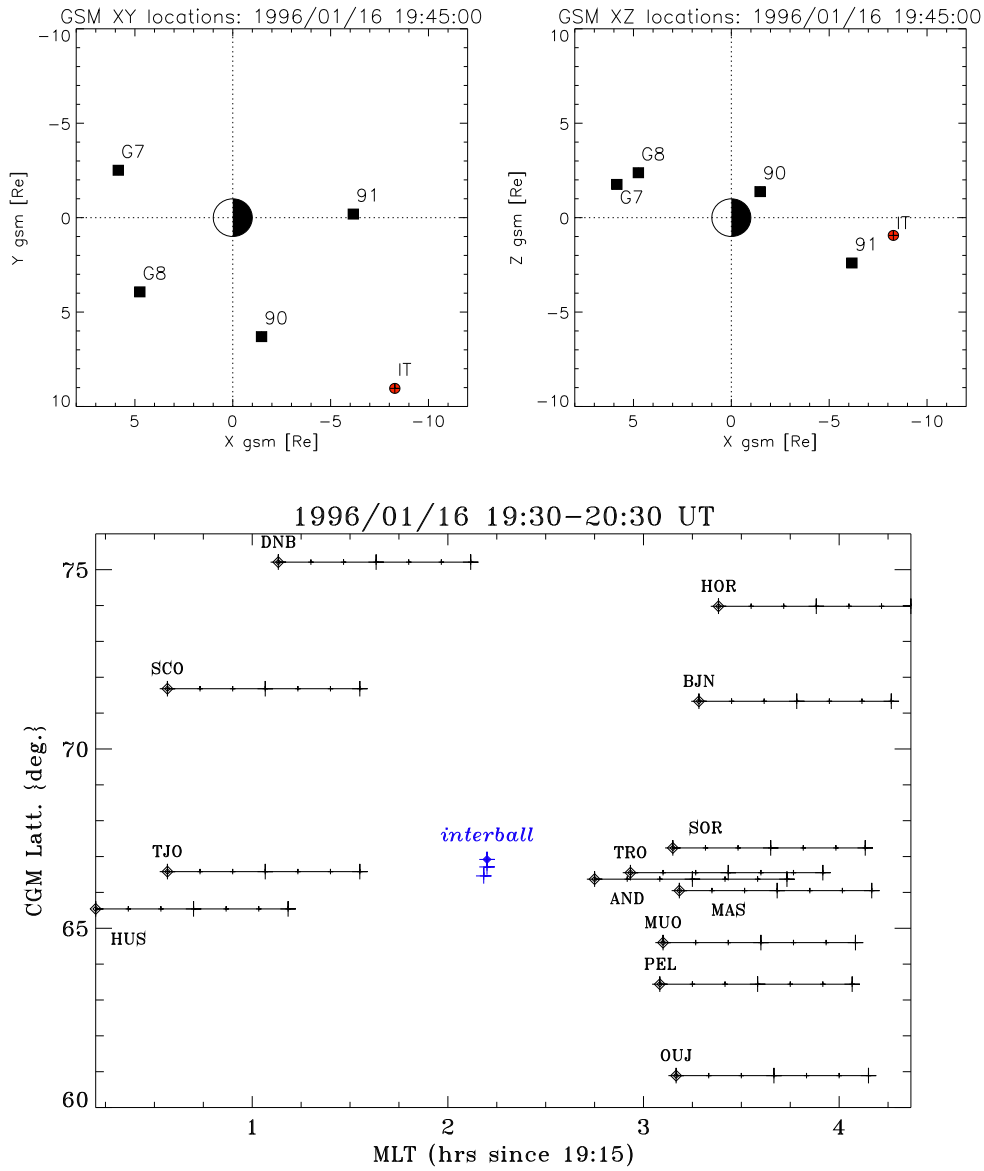


Figure 4.32: The **16/January/1996-** localization of the event. (**Top**):The GSM XY and XZ location of Interball at 19:45 UT. (**Bottom**): The Interball trajectory projected on Earth in MLT- CGL coordinates and positions of the selected ground magnetic stations. Each trajectory begins at 19:30 UT and other details are as before.

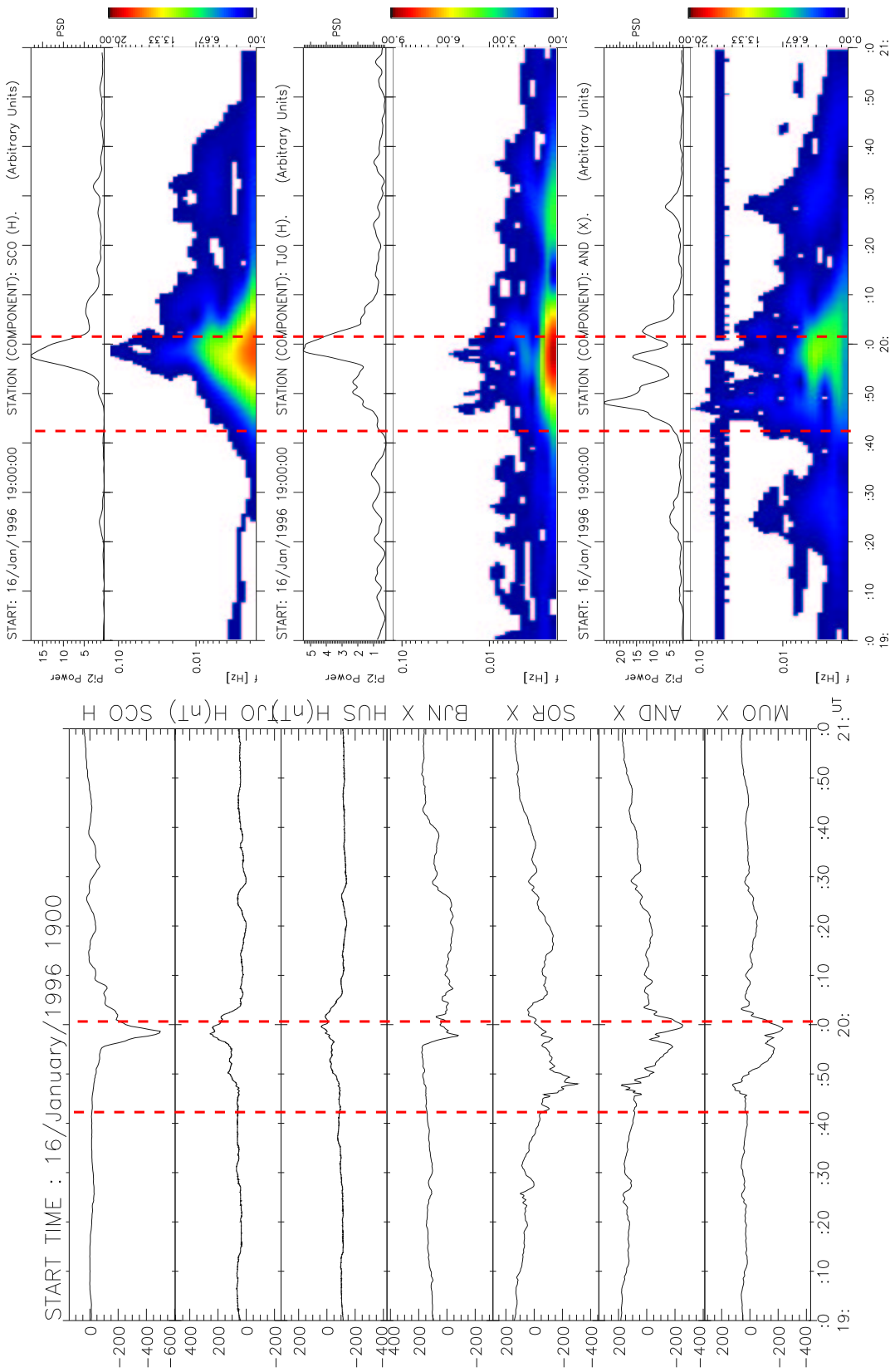


Figure 4.33: Ground based magnetic observations between 19 and 21 UT on 16/January/1996: **(Left)** Northward magnetic field component from selected stations near the Interball trajectory footprint (compare Figure 4.32); **(Right)** Dynamic spectra (color panels) of pulsations in the Pc5 - Pc3 frequency range (1.67 - 100.0 mHz) and total power of the Pi2 pulsations (black curves). The data of the northward component from stations, AND, TJO and SCO are shown and the units are arbitrary. The enhanced intensity near the range 0.06 Hz of the bottom panel (AND) is an artificial effect of the instrumental noise.

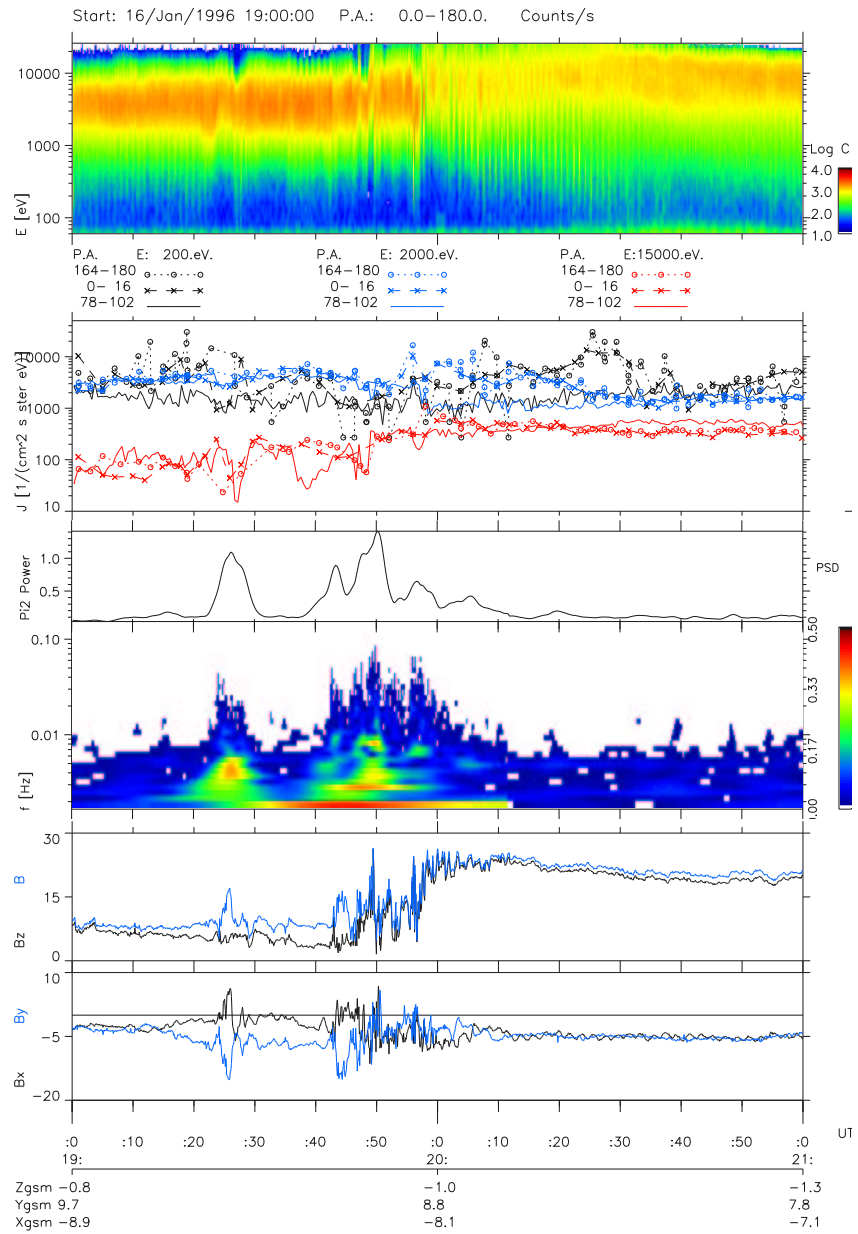


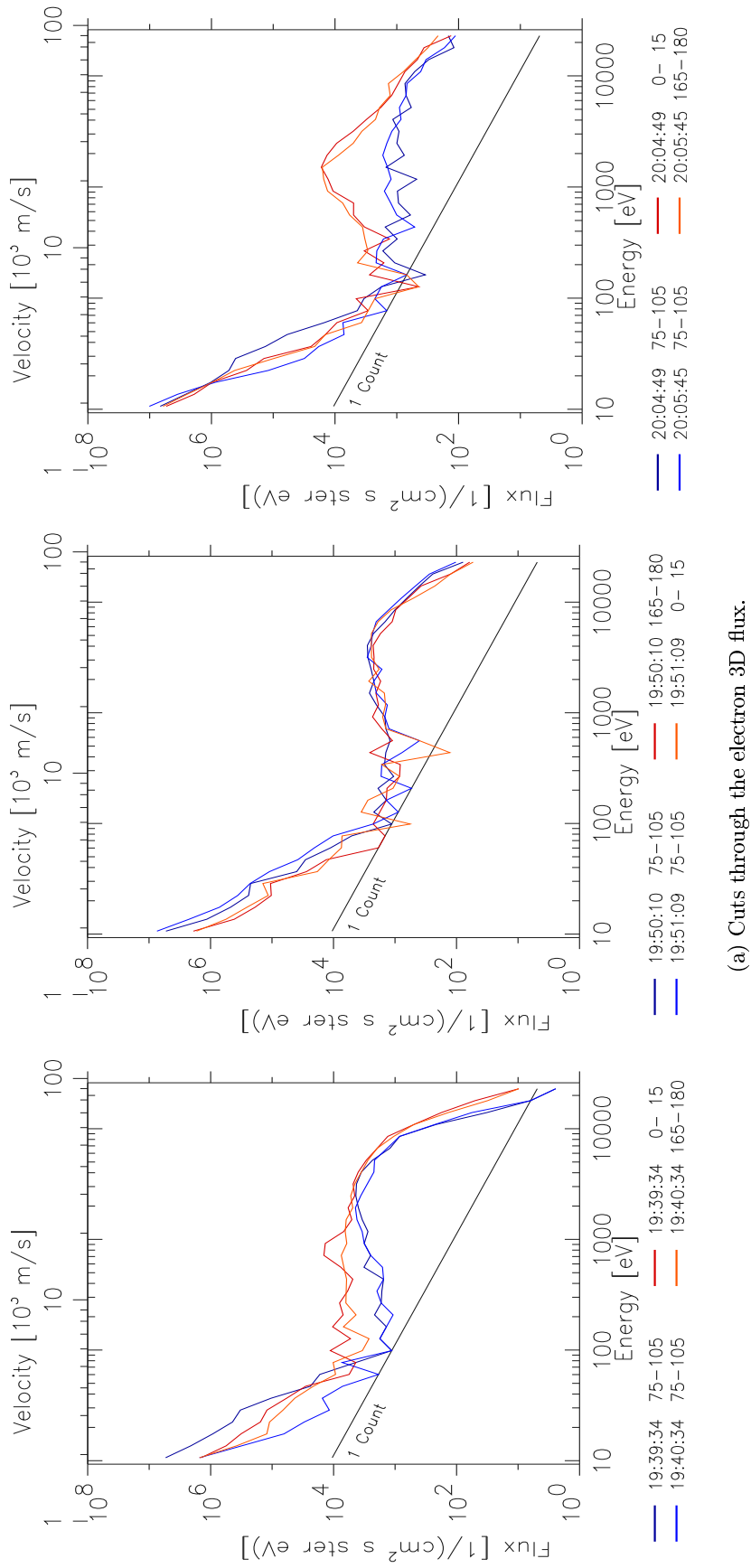
Figure 4.34: The Interball observations in the time range 19 - 21 UT on 16/January/1996. Format the same as in Figure 4.3.

being the sharp increase of the field- aligned flux near 2 keV, when the magnetic fluctuations start to fade after 19:56 UT.

Figure 4.35 illustrates the details of the electron distributions and their changes: (i) The temperature increases after the injection/dipolarization, (ii) The field- aligned flux anisotropy disappears during the enhanced magnetic fluctuations and the plasma is more turbulent then (iii) The anisotropy before and after the injection/fluctuations is due to the additional, field-line accelerated-, and relatively cold electron population. More detailed investigations shows that the higher energy tail also developed after the burst of magnetic fluctuations. Similar, but less dense and less accelerated component is also seen before, in the left panel.

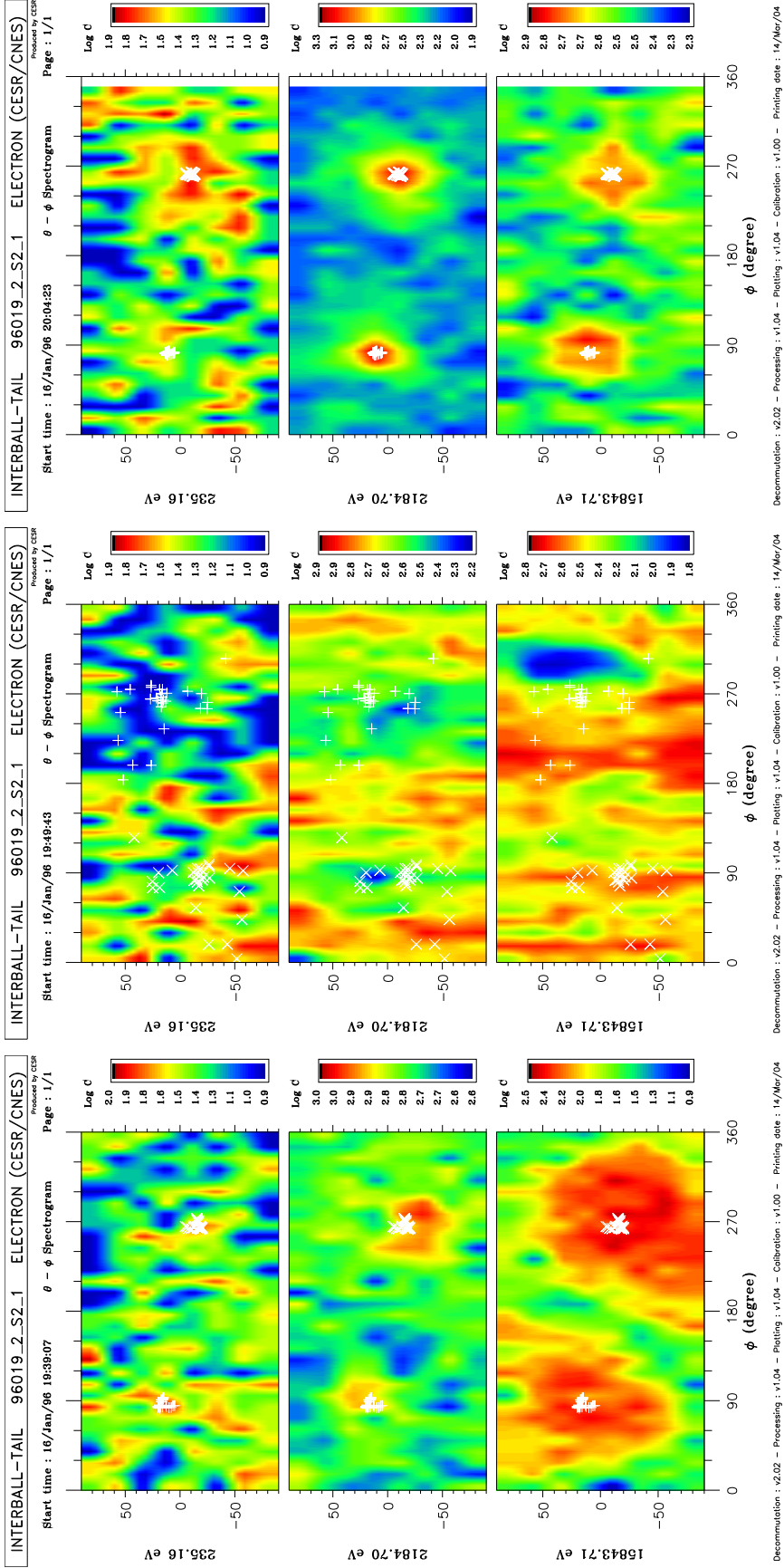
It is tempting to consider the presence of the parallel / anti-parallel flux asymmetry as a current- or an empty/decreased loss cone signature. This would help to estimate the strength of a possible field aligned current and / or the possible losses of the precipitating particles. The asymmetry found in the first and the third panel (lower row), should be taken with care because of the non- simultaneous measurements in direction parallel- anti-parallel and because of the insufficient angular resolution (for the ionospheric loss cones in the magnetospheric conditions). Details of electron distributions will be further explored in the following chapter.

The proximity of the satellite's footprint to the MLT sector where the substorm begins strongly suggest the magnetic connection between the Interball and the ionospheric substorm current system in this case.



(a) Cuts through the electron 3D flux.

Figure 4.35: Electron distributions at three instances on 16/January/1996. Format as in Figure 4.4.



(b) 3D counts at three energies.

Figure 4.35: Electron distributions at three instances on 16/January/1996. Format as in Figure 4.4.

4.4 Summary of large scale observations

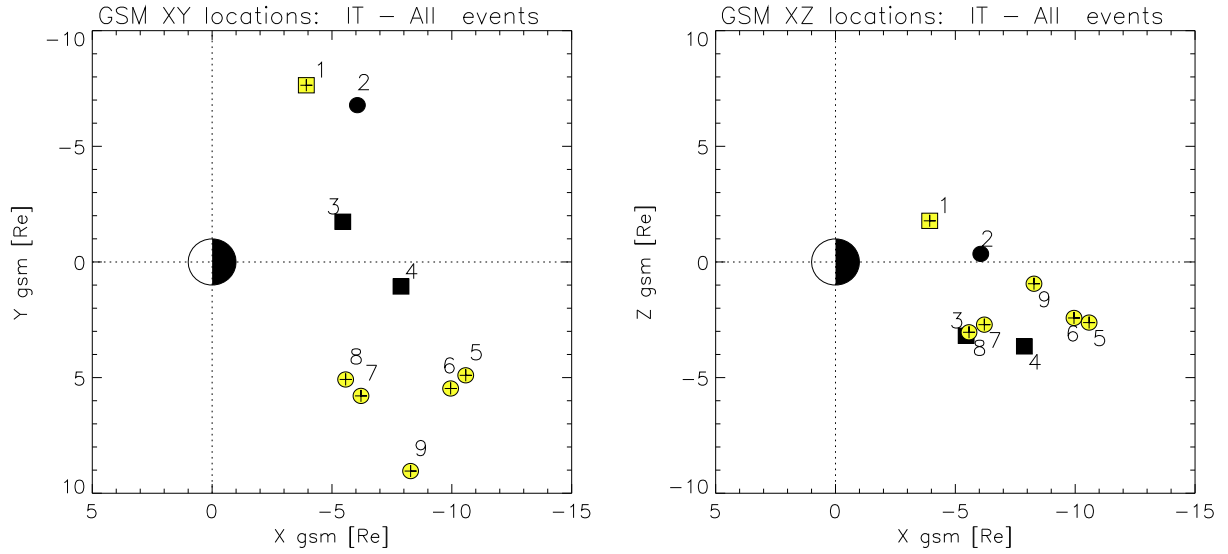


Figure 4.36: Location of the Interball events described above, in the GSM XY and XZ coordinates. **Light (black)** symbols denote the events with (without or unclear) the intensive magnetic fluctuations. **Circles** mark the events for which the additional, colder component disappears during the fluctuations, while **squares**- the events, where this relation did not hold. The events are labeled in order they have appeared in this] section: 1- 06/Oct/1995; 2- 21/Oct/1995; 3- 02/Dec/1995; 4- 09/Dec/1995; 5- 25/Dec/1995; 6- 28/Dec/1995; 7, 8- 13/Jan/1996; 9- 16/Jan/1996.

The injections observed by the Interball Tail, occurred in the near Earth plasma sheet ($X_{GSM} > -12R_E$) and coincided with the magnetic field dipolarizations (of variable strength) and with a substorm- or a pseudobreakup development on the ground. In some cases, they were accompanied with the bursts of magnetic fluctuations (the signatures of the current disruption) and with the changes of the pitch angle-energy distributions of electrons. The observations can be summarized as follows:

- According to the selection criteria (see Section 4.2), only the events in the Plasma Sheet have been reported (no traversing of tail lobes boundaries were considered, defined as a transition to/from the cold, and more dilute plasma of temperatures below some 500 eV);
- The injections closest in time to the ground onset occurred when the satellite was in the same MLT sector (or slightly westward to it) before the midnight. The injections observed more eastward were less steep and delayed in time (regarding the ground onset);
- Strong magnetic fluctuations accompanied by the most violent changes of electron distributions occurred only for the pre-midnight, closely onset- related events;
- The changes of flux were related to the presence/ absence of the additional, colder and field line- accelerated population of electrons and also to changes of the temperature anisotropy;
- The strongest fluctuations, in the Pi2 - to Pc3 frequency range accompanied the disappearance of the colder, streaming/accelerated electron population.

Figure 4.36 shows the GSM locations of the events described above. Light (black) symbols represent the Interball position when the enhanced magnetic fluctuations were (were not) observed.

Case	Ground signature		Interball signature	
	Pi2	B_X	δB	$\Delta J_E > 0$
25/Dec/95	01:23:00, NAQ 01:25:30, GILL 01:25:30, ISLL	01:26:00, NAQ 01:29:00, PBQ	01:25:50	01:26:30
28/Dec/95	20:41:30, MUO 20:42:00, TJO; 20:43:00, SOR 20:45:00, MUO.	20:46:00, BJN.	20:41:50 20:45:00	20:46:20
13/Jan/96	02:52:00, NAQ 03:02:00, ISLL.	02:52:00, NAQ 03:02:00, PBQ	03:02:20	03:02:50
13/Jan/96	03:29:00, ISLL 03:31:00, FCHU	03:29:00, PBQ 03:31:00, GILL 03:34:00, FCHU	03:31:10	03:31:50
16/Jan/96	19:43:30, AND 19:44:00, OUJ 19:53:00, SCO 19:54:00, OUJ 19:56:30, AND	19:46:00, AND 19:47:00, TJO 19:56:00, SCO; 19:57:00, BJN.	19:46:30 19:55:50	19:46:30 19:58:10

Table 4.2: The Interball- and the ground event timing for the cases, where both the bursts of the magnetic fluctuations (δB)- and the changes in the low energy electron fluxes (ΔJ_E) was detected. Columns 2 and 3 show the times of the beginning of the ground onset signatures (Pi2 and negative bay, $\Delta B_X < 0$) from the selected stations, located close to the satellite position. (compare Figures 4.17, 4.22; 4.27 and 4.32 for the location). Columns 4 and 5 show the features observed in situ by the satellite The time for the ground signatures is rounded to 30 sec. and 1 min. respectively for the Pi2 and the $\Delta B_X < 0$, while the satellite signatures- to tens of sec.

Circles denote the situation, when the additional, colder component disappeared/weakened with the enhanced fluctuations, while squares- the situations when such feature did not hold or was unclear. The events are numbered in order, their descriptions have appeared in the preceding section. The events are non uniformly distributed in the GSM coordinates (see below). This is the result of the specific selection criteria (mainly (i) and (iv) in Section 4.2) and of the specific of the Interball's orbit. Its geometry influenced the spatial distribution of events as it crossed the Neutral Sheet region close enough (in X_{GSM}) only out of the 00 LT sector. The striking feature is the dawn/ dusk asymmetry- the events with the enhanced fluctuations and the parallel flux changes (cases: 25Dec, 28Dec, 13Jan-a and 13Jan-b, 16Jan) are located in the pre-midnight LT sector and are well separated from others. Table 4.2 summarizes the Interball- and the ground timing for the above events (where both the bursts of the magnetic fluctuations- and the changes in the low energy composition was detected). It shows the time of the beginning of the specific ground onset signature from the selected stations located close to the satellite's projection (compare Figures 4.17, 4.22; 4.27 and 4.32 for the location) and of the features observed in situ by the satellite. The time for the ground signatures is rounded to 30 sec. and 1 min. respectively for the Pi2 and the "dc" B_X , while the satellite signatures- to tens of sec. With the properly choosed ground stations, the time delay between the various satellite- and ground signatures is not longer than 1 minute, which confirms the close relation between the ground- and in situ observed processes.

It is not possible to make any significant statistical considerations based on the spatial distribution- the number of events is too small. Despite this limitation, some conclusions are possible.

- The MLT localization of the "turbulent" events and their proximity (mainly from the west-side) to the regions of the ground onsets strongly suggests a connection to the substorm upward field-aligned current (UFAC), developing in the western part of the disturbed auroral region (the Westward Traveling Surge).
- Turbulent events have the signatures of a current disruption: the localization, the amplitudes, frequencies and duration and finally the coincidence with the onsets/intensifications of the ground disturbances. (Lopez et al. 1990, [102]; Lui 1990 and 1996, [104] and [106]; Roux et al. 1991, [160]; Perraut et al. 2000, [144]).
- Regarding two above points, the presented observations of microscopic electron properties are important for the substorm models and for the auroral acceleration models. As pointed out above, there is generally a lack of the in- situ observations of the plasma properties in the "active" magnetospheric regions at substorm. One category of such regions is the magnetospheric source region for the field aligned, substorm currents. E.g. the existing models of the auroral acceleration (see Section 1.3.3) suffer from the insufficient knowledge of the plasma properties at the high-altitude magnetospheric edge (above some $\sim 4 - 6 R_E$).
- Some mechanisms of the cross- tail current disruption, (e.g. Perraut et al. 2000, [143]; LeContel et al. 2000, [32]) require the field- aligned anisotropy of the low-energy electron fluxes in the near- Earth edge of the Plasma Sheet. The field-aligned current they support, can be disrupted by the current- driven Alfvén waves (near 1 Hz), which leads in turn to the disruption-and-diversion of the cross- tail current (see also Section 1.4). One of the signatures of such process are the disappearing field- aligned, low- energy electron fluxes. The observations reported here, i.e. the anti-coincidence between the strong magnetic fluctuations (current disruption) and the presence of the additional, colder electron component are the independent confirmation of the occurrence of such process near- and beyond the geostationary orbit.

In the next chapter, the properties of electrons will be further explored to allow the more quantitative considerations.

Chapter 5

Properties of electron distribution and signatures of acceleration.

5.1 Introduction

The analysis from Chapter 4 provided the information on the occurrence of the specific features in the electron component of magnetospheric plasma, and on their relations to the substorm/ pseudobreakup disturbances. Distribution functions were explicitly shown in the near- Earth, plasma sheet- end of the auroral field lines, before- and during the “active” events: injections and enhanced ULF magnetic turbulence, observed in situ. For the five cases where the projected spacecraft trajectory was close to the developing auroral disturbance, the key features observed in the electron distribution are:

- i enhanced parallel anisotropy of the electron flux at 0.1 to 1 keV, observed *before-* and *after*, the bursts of magnetic turbulence near the onset of a substorm/ pseudobreakup.
- ii this flux anisotropy at (seemingly supported by the additional colder, counter-streaming population) disappears *during* the magnetic bursts (in the Pi2 - Pc3 range);
- iii the isotropy, and eventually the anisotropy *above* some 2 keV developing during the bursts, over the single electron population (contrary to the non-turbulent case, where the field-aligned anisotropy of flux is supported by another colder component);
- iv the non- maxwellian character of distributions, with the enhanced energetic “tail”.

This is the potentially important information, when regarded in context of the substorm development, the substorm current system and the auroral acceleration processes. Several previous works concerning these topics did not take into account the real properties of the magnetospheric source (see the introductory review in Sections 1.3 and 1.4). The generic, representative plasma properties were used instead due to the lack of the appropriate observations, though the meaning of a more realistic magnetospheric plasma model for such considerations was recognized several times. The observations presented in this work can help to validate/improve some assumptions made before.

The detailed properties of electrons are explored in this chapter. To this aim, the moments of distribution function are first given. Based on the observations, the simple model distribution function is proposed as a tool to reduce and to analyze the data. Fitting the model function is performed and the results are used to further analyze and interpret the observations.

5.2 Quantitative characteristics of electron distributions

5.2.1 Moments of the distribution function

The moments of distribution function for the five “positive” cases from Chapter 4 are shown in Figures 5.1 – 5.4.

The curves plotted are (top to bottom): density, “temperatures” (from the measurements in the limited range of P.A., black/green/blue, corresponding to directions parallel/ anti-parallel/ perpendicular to \vec{B}), parallel/anti-parallel fluxes of particles and of energy and pitch angle- integrated (within the cone of ~ 45 deg) parallel energy flux, in the whole energy range- and below 1.8 keV (blue and red curves). Alternatively, parallel/ anti-parallel fluxes of the particle- or of the energy are replaced by the net fluxes (positive parallel do \vec{B}) obtained from the time- interpolated data. In such cases, the upgoing / downgoing fluxes are marked in blue / red. Two bottom panels show: the Alfvén velocity (assuming proton density equals the observed electron density), and the integral power of fluctuations of one of the magnetic components, in two frequency bands: 1.67 to 6.7 mHz (the Pc5 frequencies) and above 6.7 to 125 mHz (the Pi2 – Pc3 range). Note, that the second band extends higher than the Pi2, shown in plots in Chapter 4. Vertical dashed lines mark periods of enhanced fluctuations δB , when they are above 1/3 of maximum value.

The moments were calculated for energies above 100 eV to reduce the influence of the satellite electrostatic potential. The range of the pitch angles selected is the compromise between the angular resolution and the number of data points, resulting from the angular resolution of the instrument. Because of the observational constraints (see Chapter 2), some of the moments are not fully “3D” values, taken during the full rotation of the satellite. In particular, the parallel and perpendicular “temperatures” is obtained from the unidirectional observations and rescaled, so it can be influenced by the anisotropy of flux. In other words, the observed differences between the parallel- and the anti-parallel temperatures follow from the parallel drift velocity of electrons. The finite angular resolution of the instrument, combined with the effects of the satellite charging is partially responsible for the 2-min. oscillations appearing when the magnetic field was highly stretched (e.g. around 01:15 UT on first sub-figure or 03:15 on third sub-figure). These effect are less important for the higher order moments and were removed when calculating the net fluxes (upgoing/downgoing).

Before pointing out the common features of interest, I briefly review the main features observed. In two first cases the spacecraft was located further from the neutral sheet and the related geomagnetic disturbances were weaker than in three other cases. The direction of magnetic field is not the same all the time- as found in relevant plots in Chapter 4, it is pointing “downward” (towards the earth) for the whole time in the first case (25 December 1995) and is opposite in all other cases, but there are also the episodes of the earthward orientation on 13 January and 16 January, near the substorm expansion.

25/Dec/1995: Increased fluctuations in the Pi2 – Pc3 (01:26 - 01:36 UT) correspond to the decreasing particle flux along \vec{B} (third panel) and the increasing temperatures (it is also seen in the pitch angle- integrated energy flux in fourth panel). Anisotropy of the temperature (perpendicular is dominating) may seem contradictory to the parallel flux anisotropy (cf Figure 4.20). This results from the appearance of the secondary, colder and streaming component. The P.A.- integrated, net energy flux (5-th panel) show weak oscillations in the Pc5 range. The magnetic fluctuations in this range remain rather weak (blue curve at the bottom panel).

28/Dec/1995: The intensity of magnetic fluctuations, δB , is not much higher than in the preceding case (the lowermost panel). As above, the spectral characteristics of the magnetic field oscillations changes temporarily- higher frequencies dominate (red curve at the bottom panel) around the event detected on the ground. The parallel particle- and energy fluxes increases downward with it (third, fourth and fifth panels) except for the maximum of δB (about 20:47 UT). There is also the episode seen of weaker fluctuations and increased downgoing flux near

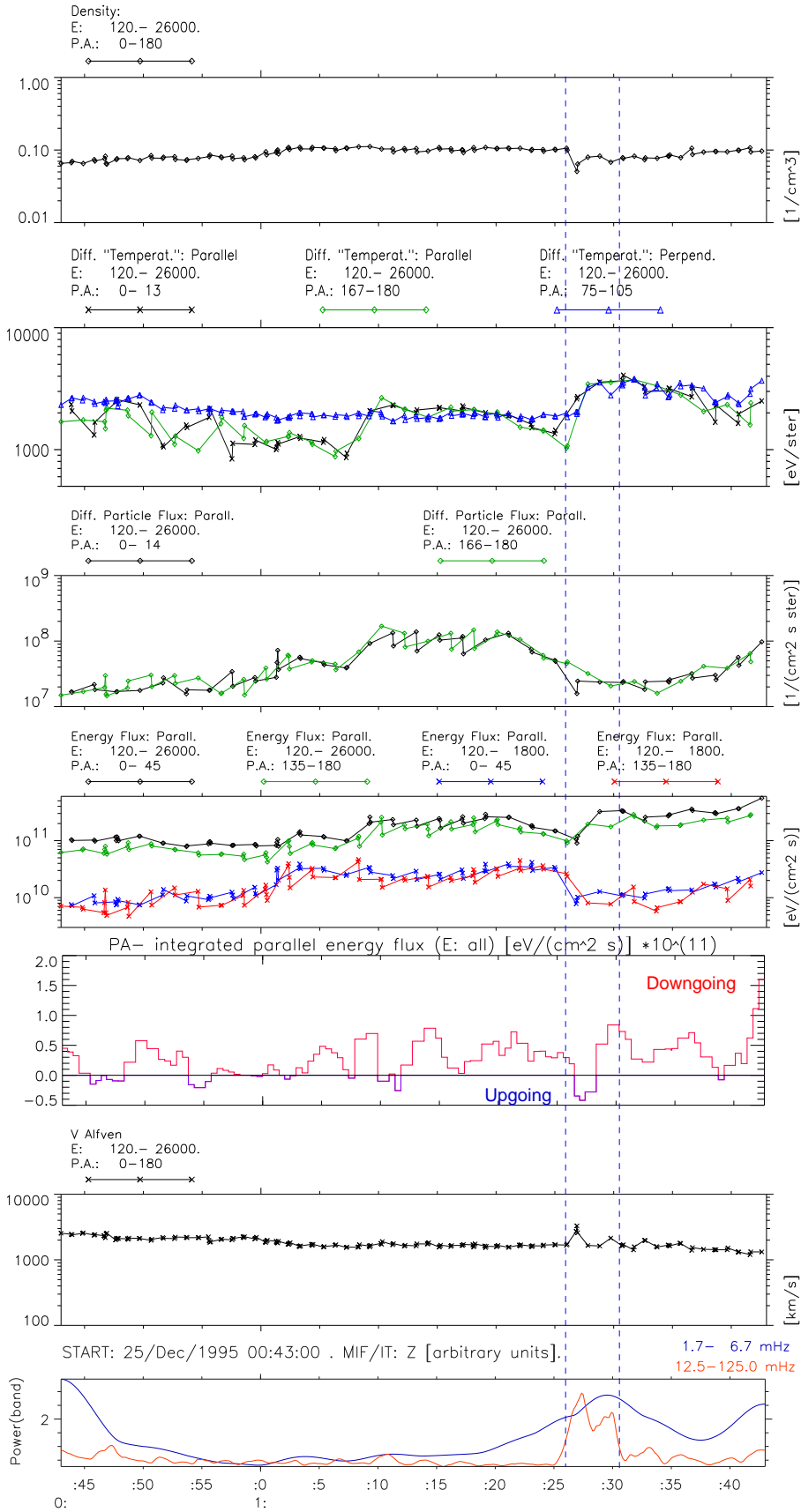


Figure 5.1: 25/December/1995, 00:43 - 01:43 UT. Moments of distribution function (see text for the details). From top: density, $[cm^{-3}]$; "temperatures"- parallel / anti-parallel / perpendicular to \vec{B} [eV]; particle flux along / opposite to \vec{B} , $[1/(cm^2\text{ster})]$; energy fluxes (P.A.- integrated within the 45 deg. cone) in two energy ranges, $[eV/(cm^2\text{s})]$; net energy flux along \vec{B} , $[eV/(cm^2\text{ster})]$; Alfvén velocity, $[km/s]$. Bottom: power of magnetic fluctuations.

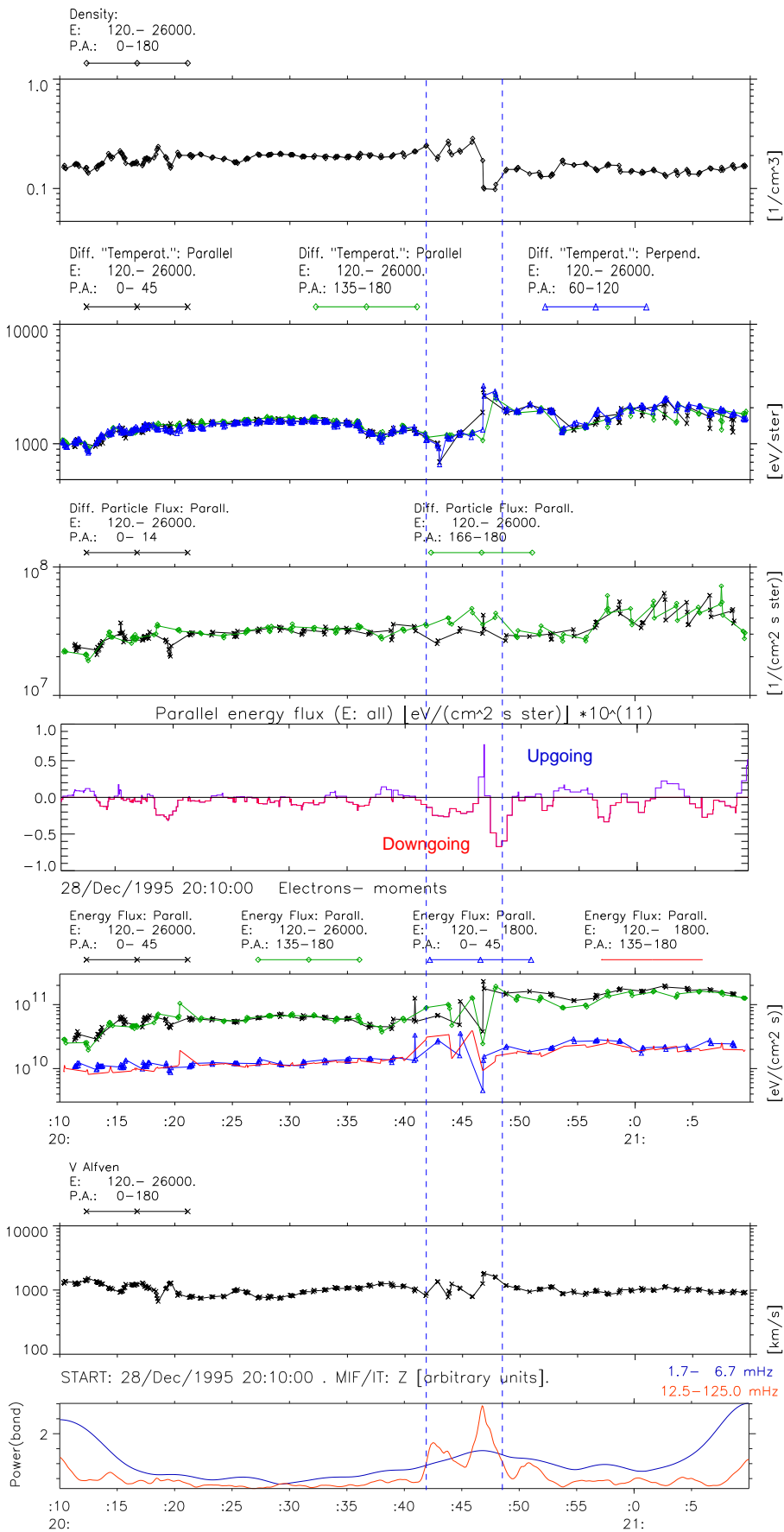


Figure 5.2: 28/December/1995 02:10 - 21:10 UT. Moments of distribution function. From top: density, [cm^{-3}]; "temperatures", [eV]; parallel / anti-parallel particle fluxes, [$1/(cm^2 s ster)$]; P.A.- integrated energy fluxes (within 45 deg. cone) in two energy ranges, [$eV/(cm^2 s)$]; net energy flux along \vec{B} , [$eV/(cm^2 s)$]; Alfvén velocity, [km/s]. Bottom: power of magnetic fluctuations.

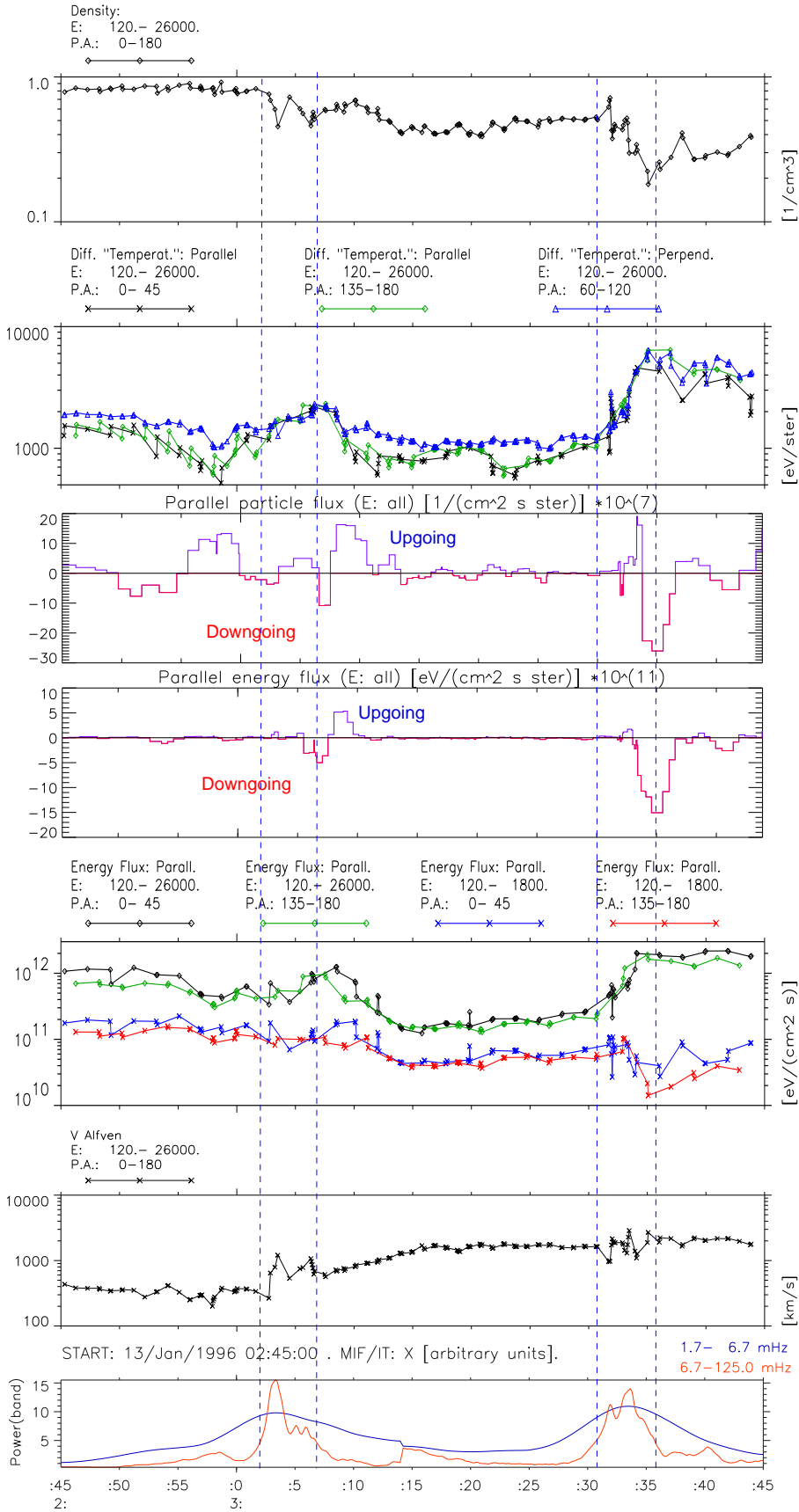


Figure 5.3: 13/January/1996 02:45 - 03:45 UT. Moments of distribution function. From top: density, [cm^{-3}]; “temperatures”, [eV]; net particle flux along \vec{B} , [$1/(cm^2 s ster)$]; net energy fluxes along \vec{B} , P.A. integrated (within the 45 deg. cone) fluxes of energy along \vec{B} , [$eV/(cm^2 s)$], in two energy ranges; Alfvén velocity, [km/s]. Bottom: power of magnetic fluctuations.

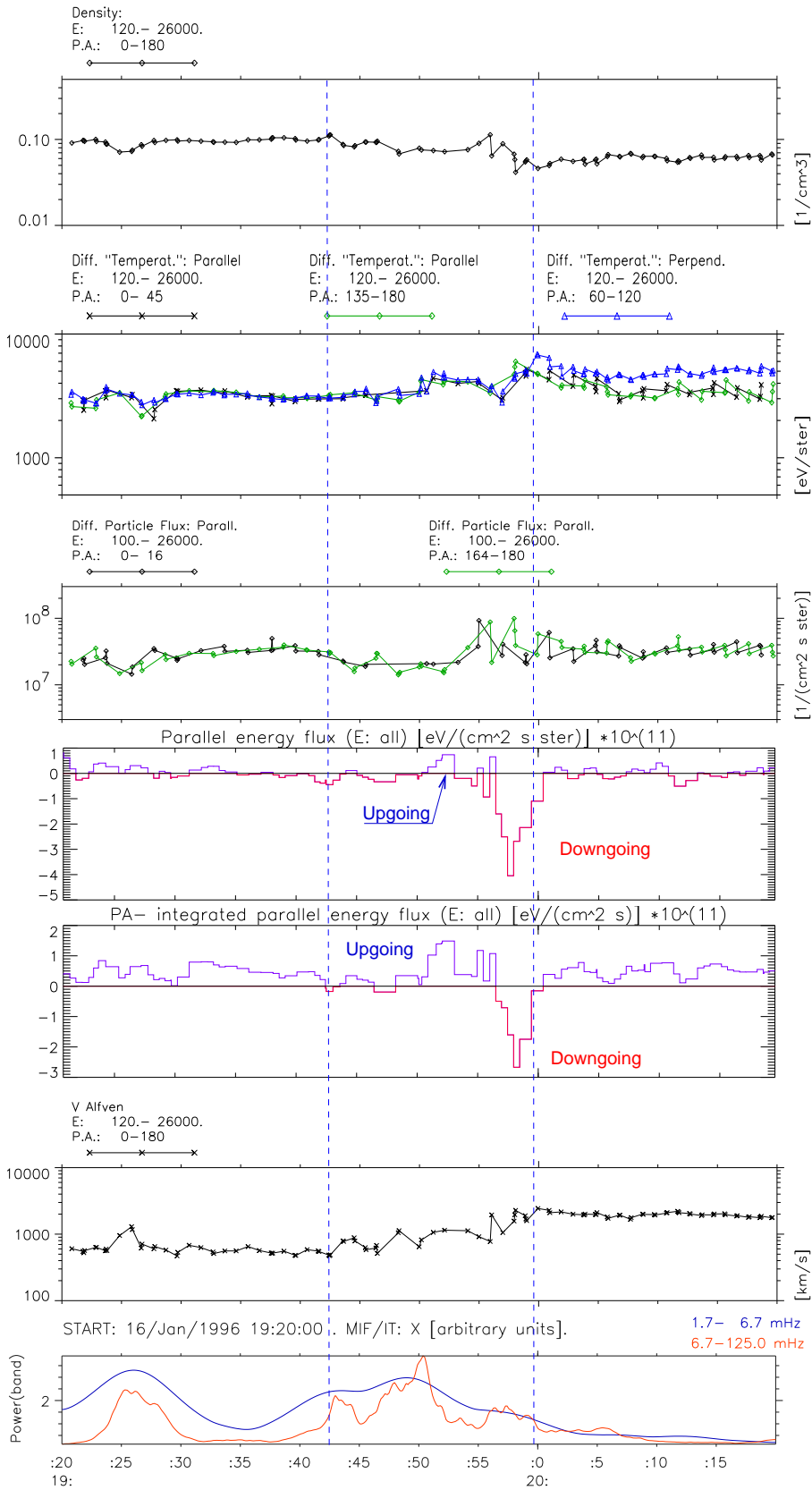


Figure 5.4: 16/January/1996, 19:20 - 20:20 UT. Moments of distribution function. From top: density, $[cm^{-3}]$; “temperatures” - parallel / anti-parallel / perpendicular to \vec{B} , $[eV]$; particle flux along / opposite to \vec{B} , $[1/(cm^2 s ster)]$; net flux of energy along \vec{B} , $[eV/(cm^2 s ster)]$; P.A. integrated (within the 45 deg. cone) fluxes of energy along \vec{B} , $[eV/(cm^2 s)]$; Alfvén velocity, $[km/s]$. Bottom: power of magnetic fluctuations.

20:20 UT, but its relation to the ground activity could not be established. Electron fluxes are isotropic this time *before* the δB episode, but the anisotropy at low energies appears *after* it.

13/Jan/1996 a, b: Density and perpendicular temperature change more than before and the magnetic fluctuations are also stronger- these two cases correspond to the intense substorm (studied in Chapter 3). Sharp changes of parallel fluxes are clearly seen- especially the parallel/anti-parallel asymmetry in the energy flux. These two events occurred in quite distinct conditions (compare the magnetic field in Figure 4.29)- the first occurred closer to (but still out of-) the neutral sheet and the main body of the injection were located more eastward. In the second case, the injection (after 03:30 UT) occurred “in situ”. Both cases show nevertheless quite similar features.

16/Jan/1996: The wave intensity is weaker during this substorm than in the two preceding cases as is also the strength of the ground magnetic signatures. The case is more “patchy”- three intensifications of δB are seen, and the final transient earthward flux occurs only near the last magnetic burst. This character can be attributed to the localization (most westward) and to the low time/pitch angle resolution of the instrument and won’t be. The net effect of the parallel energy flux is still clear- the downgoing impulse occurs after the maximum of the higher- frequency fluctuations.

Figure 5.5 shows each of 5 events in the records of 20 min, to better present the time ordering of the wave- and particle effects. (see also Table 4.2).

Case	net J_N [nA/m^2]		net J_E [mW/m^2]	
	Quiet	Transient	Quiet	Transient
25/DEC	8	32	0.05	0.08
28/DEC	5	25	0.04	0.10
13/Jan a	8	160	0.08	0.80
13/Jan b	8	400	0.08	2.40
16/Jan	8	80	0.08	0.40

Table 5.1: Representative values of the net (parallel minus anti-parallel) particle flux J_N (current), and energy flux J_E carried by the electrons: during the “quiet” times- and in the “disturbed” (δB) episodes.

The important common features are as follows:

- i The density (0.1 to 1.0 cm^{-3}) and the temperature (perpendicular- mostly between 1 and 3 keV) confirms that the events reported occur in the plasma sheet and *not* on crossing the plasma sheet- tail lobe boundary. The records of the magnetic field (shown in Chapter 4) show that the satellite was in the plasma sheet.
- ii The clear effect is seen in the net field- aligned fluxes. Well balanced most of the time (even if the differential fluxes change), they temporarily increase near the onset of the magnetic fluctuations. The effect last for 3 to 6 minutes- long enough to be detected even by the slowly rotating satellite as the Interball. The changes are not the same for the particle- and for the energy fluxes nor for the lower- and the upper energies. It is stronger for the substorm (global) event than for the localized one. The representative values of the parallel particle- and energy fluxes, obtained from the electron data, are shown in Table 5.1. Transient flux values are high, compared to other satellite observations (see Section 5.4 below) especially for the substorm events 13 and 16 January when the fluxes increase more than order of magnitude from the “balanced” level (Figures 5.3 and 5.4). E.g., the net flux of 10^8 *particles/cm²s* corresponds to the (field aligned) electric current of $0.16 \mu A/m^2$, if not accompanied by the ions. The energy fluxes are even more spectacular: the peak values of the local field aligned energy flux exceed $0.8 mW/m^2$.

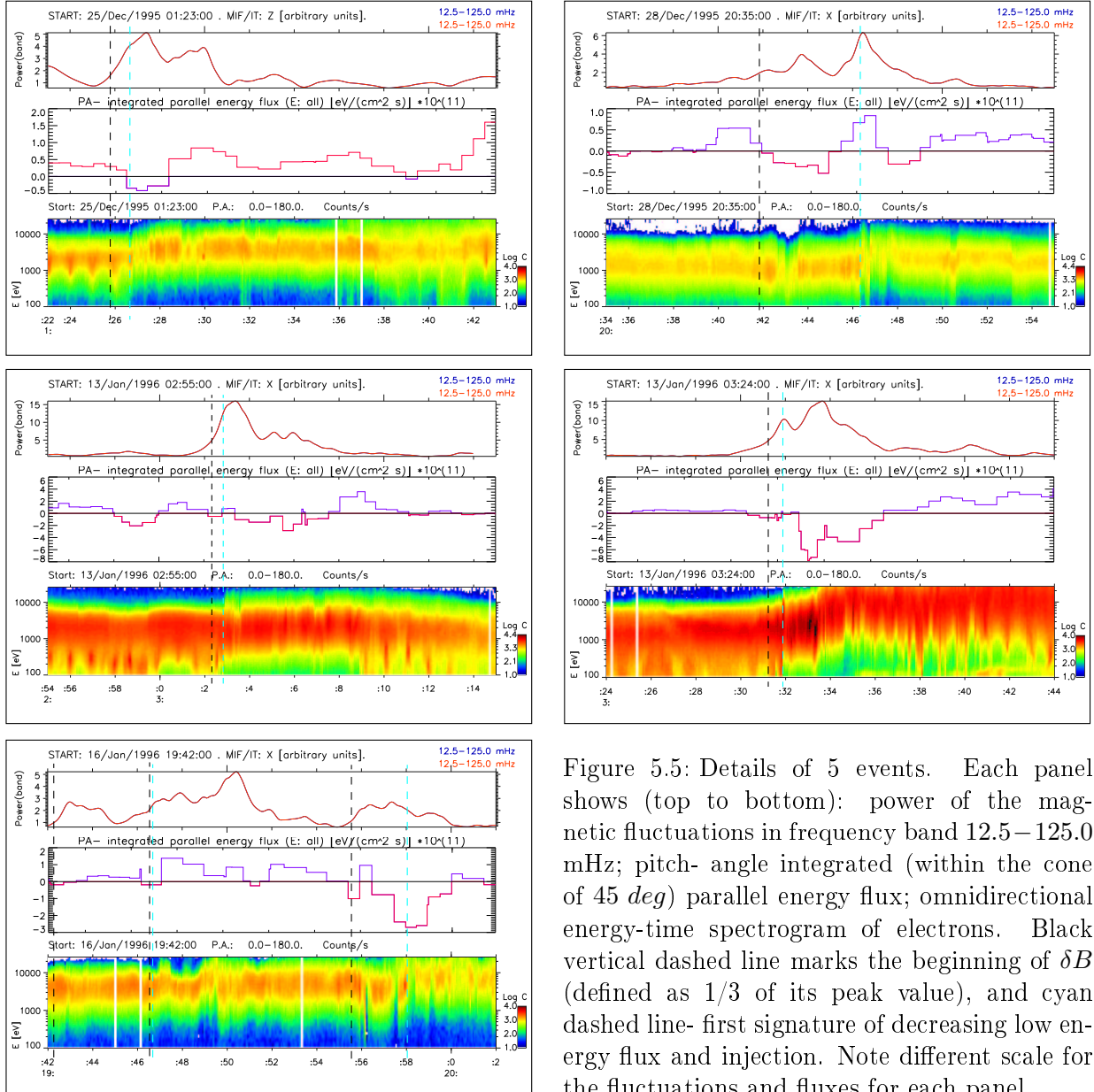


Figure 5.5: Details of 5 events. Each panel shows (top to bottom): power of the magnetic fluctuations in frequency band 12.5–125.0 mHz; pitch-angle integrated (within the cone of 45 deg) parallel energy flux; omnidirectional energy-time spectrogram of electrons. Black vertical dashed line marks the beginning of δB (defined as 1/3 of its peak value), and cyan dashed line- first signature of decreasing low energy flux and injection. Note different scale for the fluctuations and fluxes for each panel.

- iii The enhanced magnetic fluctuations in the Pi2 - Pc3 range (red curves at the bottom of Figures 5.1 - 5.4) coincide with the changing density and temperature of electrons (the “gradient” effect). More careful comparison shows, that the magnetic burst begin *before* the decrease of low energy flux and the transient earthward energy flux. There are also the oscillations in the parallel particle number- and energy fluxes with the periods of 3 to 5 minutes (Pc5 range). They form the “trains”, that the transient, intensive downward energy fluxes seem to be the part. Similar oscillations are seen in the magnetic data, as the enhanced amplitude at lower frequencies (blue curves) and modulation of the higher frequency part (red curves), but no clear 1:1 correspondence can be found. There are also the weak signatures of such oscillations in the density, but no systematic investigation has been done. Note that the frequency range corresponding 80 - 150 sec., was excluded from considerations, to avoid the bias from the satellite rotation (about 119 sec.) The amplitude of higher frequency bursts exceeds that of the Pc5 range at- or before the moment of transient earthward energy flux and only for the short time. This is a signature of a new wave mode excitation and probably of the turbulence.
- iv The *estimated* Alfvén velocity (assuming the equal proton- and electron densities) is generally between $1 - 3 \cdot 10^3 km/s$, but is changing. It decreases to nearly 270 km/s before 03:00 UT on 13/January and reaches above $6.5 \cdot 10^3 km/s$ about 01:27 UT on 25/December. These values are lower than the most probable velocities of the “hotter” electron population ($\sim 15 - 20 \cdot 10^3 km/s$) but become closer (still below) to that of colder electrons ($\sim 6 \cdot 10^3 km/s$ for $\sim 100 eV$). The estimated *electron* “beta” (β_e not plotted) is slightly above 1 (and below 1.2) only in the first event of 13 January, just before 03:00 UT- in all the other cases β_e was close to 0.1 or even lower. The main input to the total plasma beta (e.g. Lui 2004, [110], and references therein) is done by protons, the data not used in this work. Assuming the proton-to-electron temperature ratio between 5 and 7 (typical in the plasma sheet) one can see that *plasma* beta is still far below 50 or even below 10, expected by the cross-field current- or the ballooning mode instabilities to develop just before the current disruption in the cross-tail current sheet (see e.g. Cheng 2004, [27] and Lui 2004, [110]). I will come back to this issue below.

5.2.2 Microscopic details

It follows from the above, that the magnetic “bursts” can significantly influence the energy flow along the field line. Alternatively, they can be only a signature of another mechanism(s) that transfer the energy downward. The field- aligned, low energy electron fluxes weaken/ disappear near that times. This two effects may seem contradictory though need not to be, depending on details of the distribution function. The “moments of the distribution” approach does not provide such details.

The representative electron distributions and their changes can be found in Figures 5.6 - 5.9, showing the parallel/anti-parallel cuts through the 3D particle fluxes, and the pitch- angle distributions of the energy- integrated fluxes.

The observed properties of electron distribution functions can be summarized as follows:

- i The features in the parallel fluxes are quite subtle- they are well seen in the integrated quantities but may be missed in the individual energy spectra.
- ii If present, the enhanced field- aligned fluxes *in the absence* of the magnetic bursts, are well balanced (in parallel- anti-parallel direction) and only result in the weak net fluxes of particles. They can be involved in the low frequency oscillations of rather low amplitudes, usually not influencing significantly the parallel energy flux.

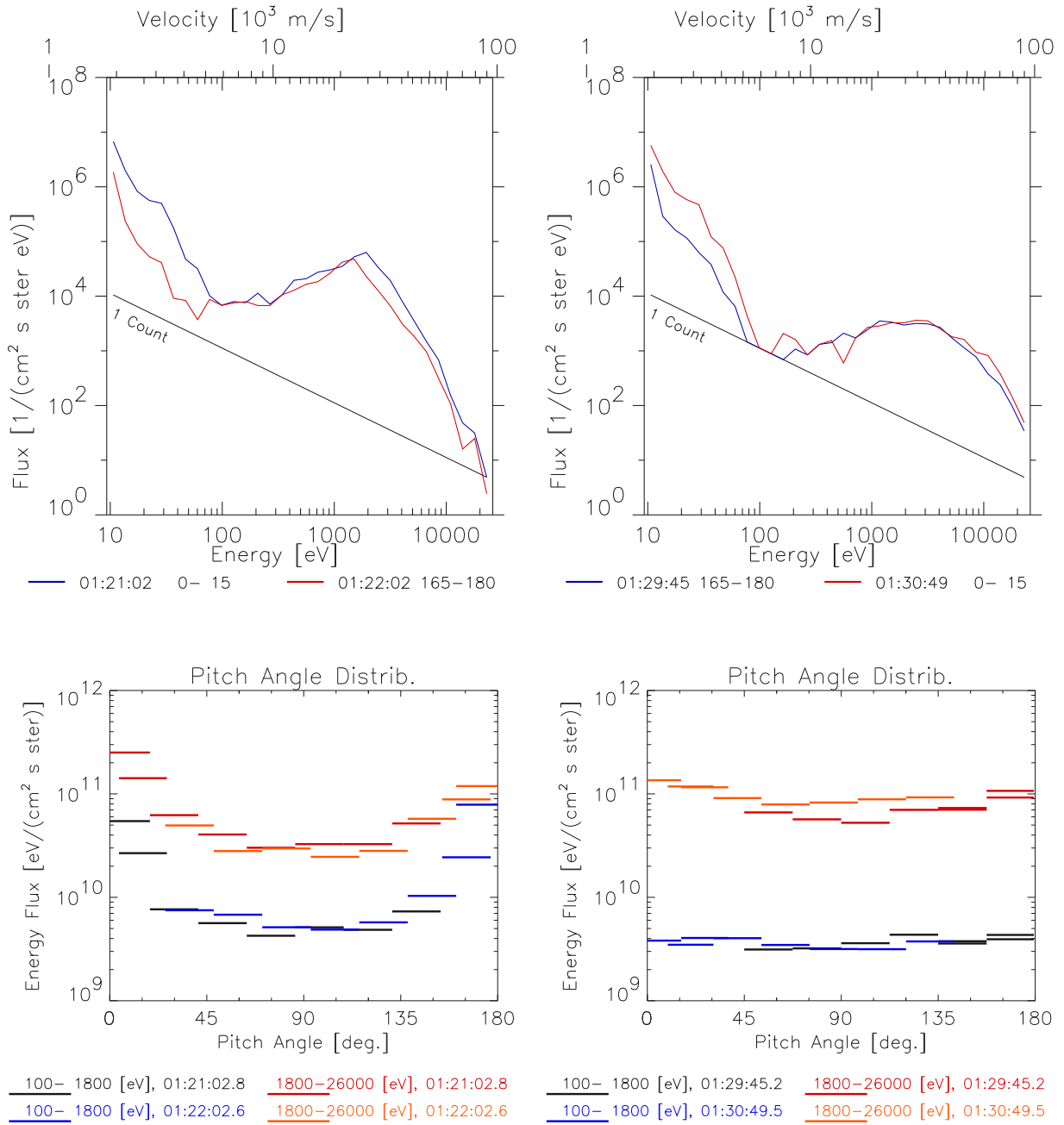


Figure 5.6: Sources of the features observed in parallel electron fluxes on 25 December 1996 (compare Figure 5.1). (Upper) Parallel (to \vec{B}) and anti-parallel cuts through the 3D particle flux; (Lower) Pitch angle dependence of energy flux. Lower- and higher energy part are shown (blue- and red curves). (Left) Slightly asymmetric (in parallel / anti-parallel), and highly anisotropic (cigar shape) distribution before the magnetic disturbance; (Right) More isotropic, single component distribution- time changes during the magnetic disturbance (about 01:26 to 01:31 UT) result in transient flux enhancement this time.

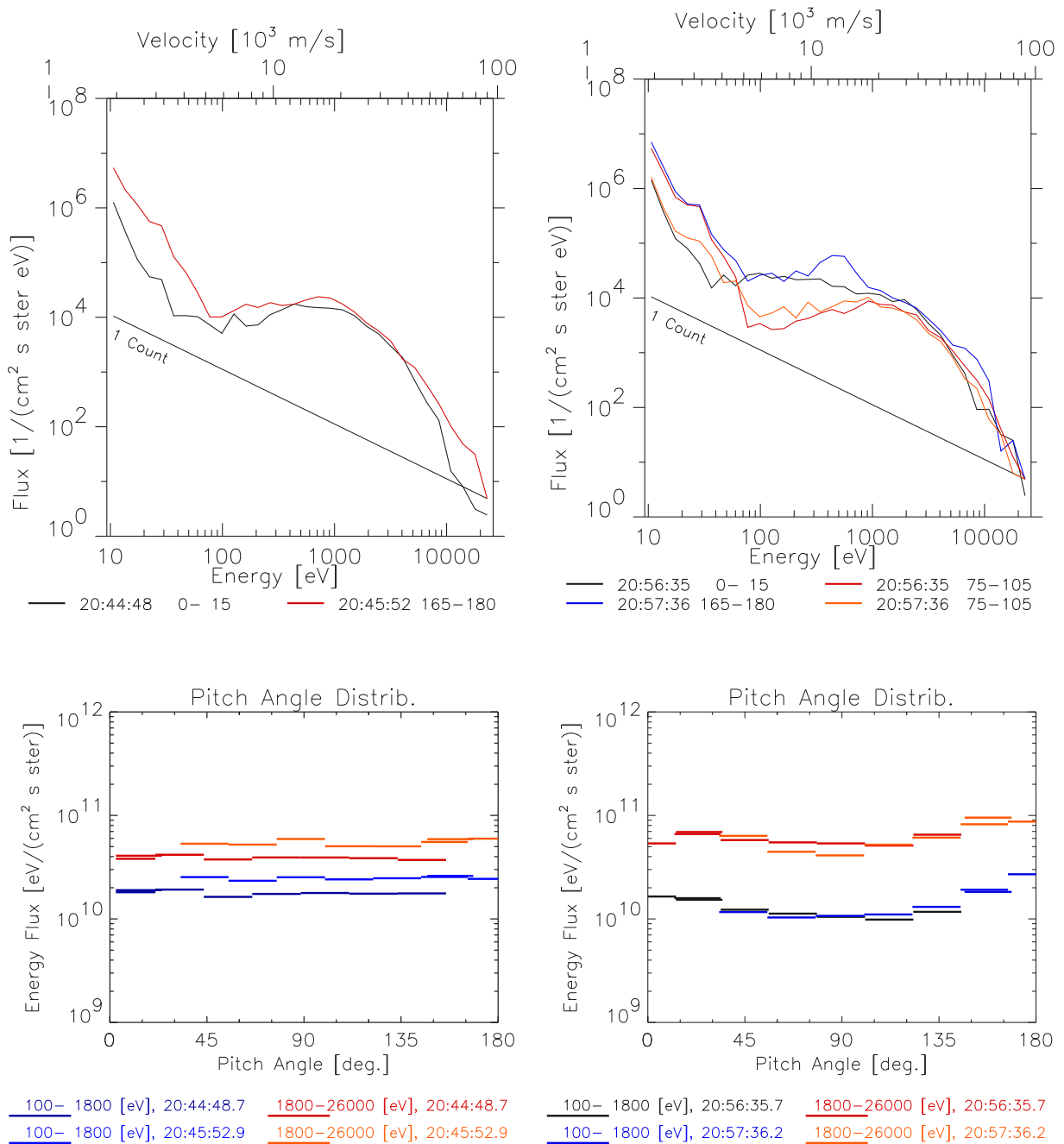


Figure 5.7: Sources of the features in parallel electron fluxes on 28 December 1996 (compare Figure 5.2). (Upper) Parallel and anti-parallel cuts through the 3D particle flux (perpendicular cuts added for the comparison in the right plot) (Lower) Pitch angle dependence of energy flux. Low- and high energy part plotted separately (blue- and red curves). (Left) Nearly isotropic-time changing distributions result in the enhanced net downward energy flux during the magnetic disturbance (about 20:40 to 20:49 UT). (Right) Distribution after the magnetic disturbance, with the field-aligned anisotropy and the additional weak, streaming component. Significant parallel particle flux below ~ 2 keV (upper right) does not influence significantly the energy flux (lower right).

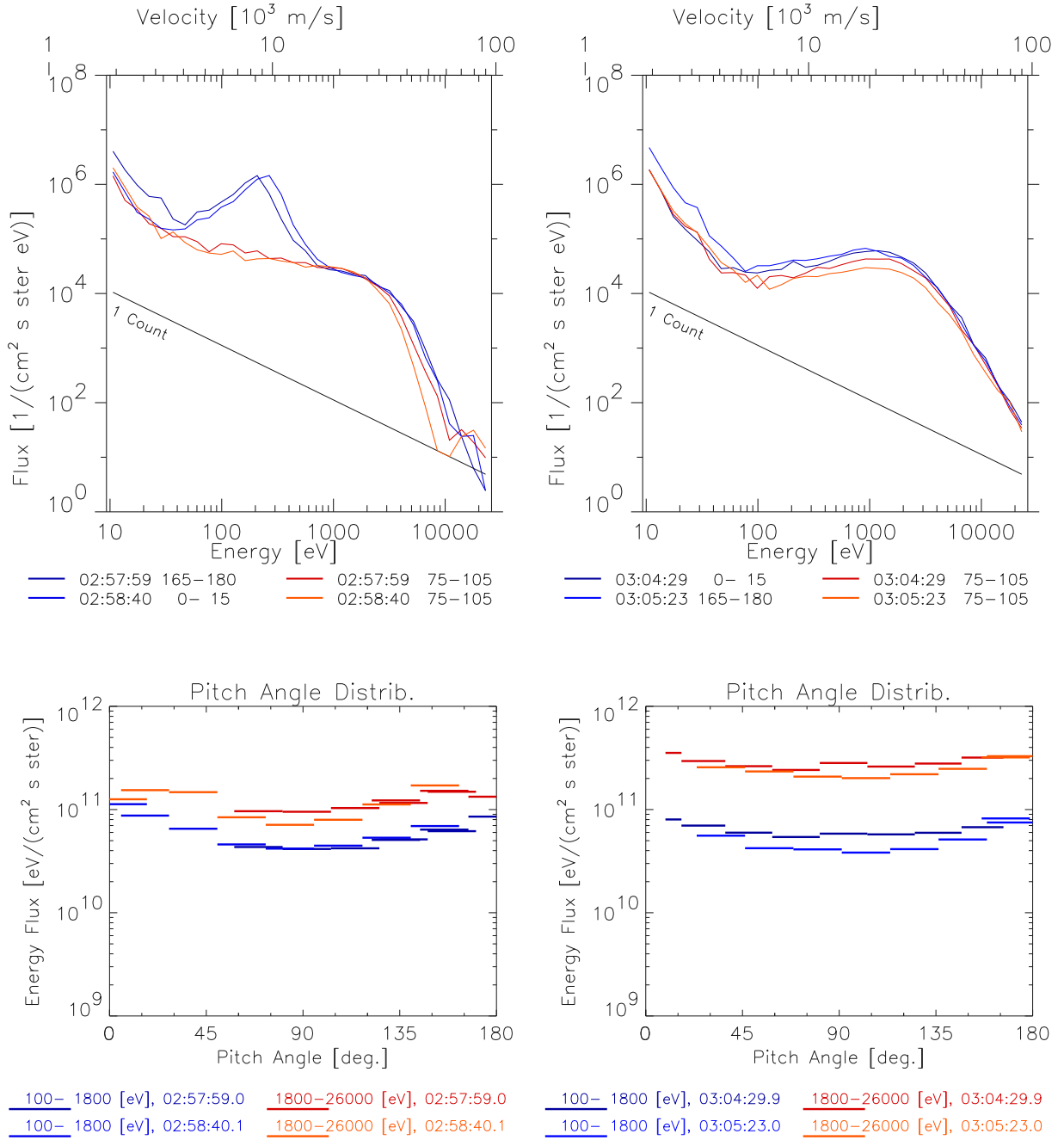


Figure 5.8: Sources of the features observed in net parallel electron fluxes for the substorm of 13 January 1996 (compare Figure 5.3). (Upper) Cuts through the 3D particle flux (perpendicular cuts are shown for the comparison- red curves); (Lower) Pitch angle dependence of the energy flux: Low energy- (blue) and high energy (red) parts are displayed separately. (Left) Distribution with two components before the magnetic disturbance. The energy flux added by the colder component is almost as significant as that carried by the hotter component; (Right) Changing, single component and field-aligned spectra resulting in the enhanced downward energy flux during the magnetic disturbance.

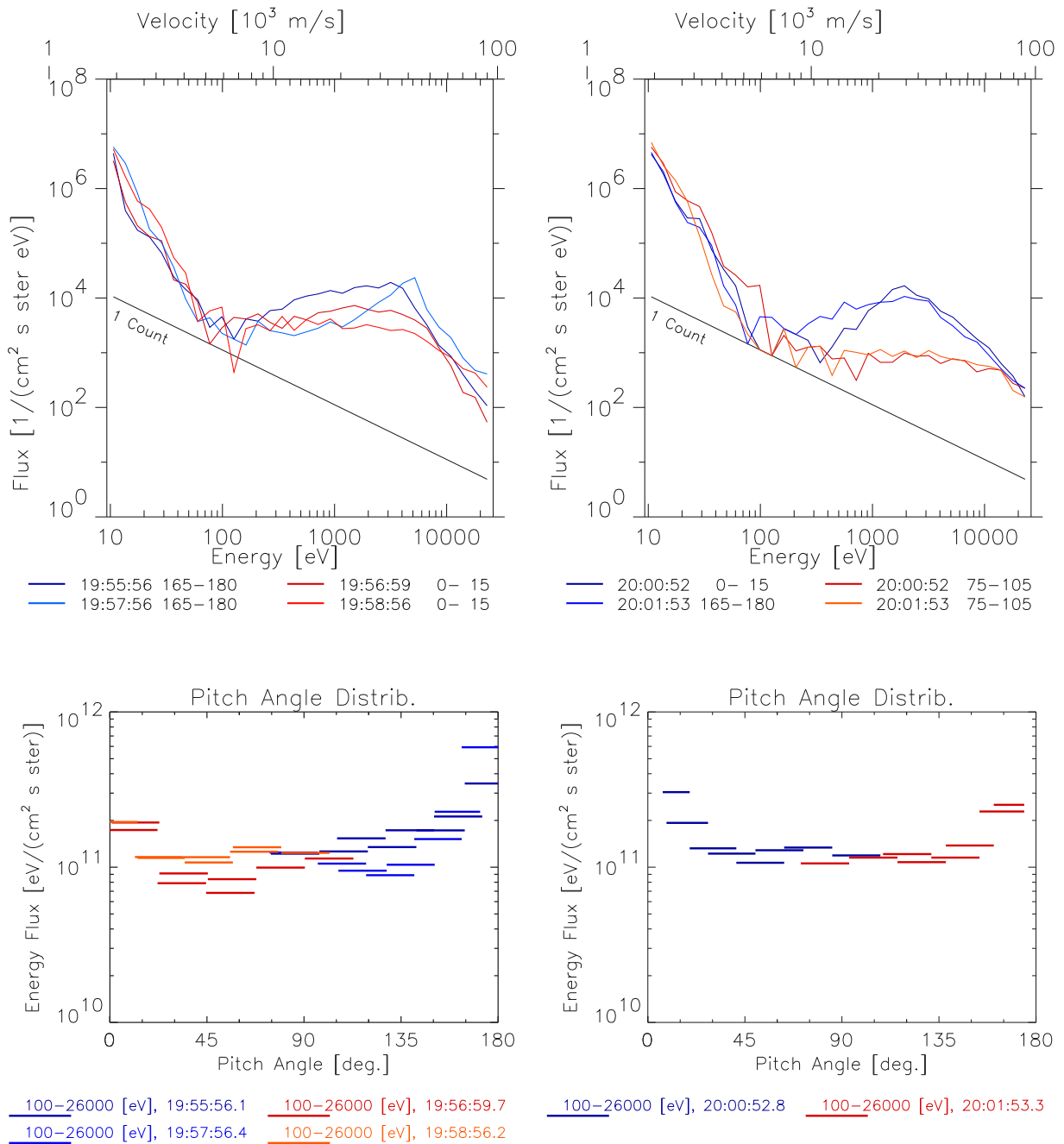


Figure 5.9: Sources of the features observed in parallel electron fluxes on 16 January 1996 (compare Figure 5.4). (Upper) parallel, anti-parallel cuts through the 3D particle flux (perpendicular cuts are added for the comparison *only* in the right plot); (Lower) pitch angle dependence of energy flux. (Left) Sequence (about 19:56 - 20:00 UT) of transient parallel fluxes resulting in the enhanced downward energy flux during the magnetic “disturbance”: *downgoing* flux intensity increases (two blue curves at upper left and at bottom left), while the *upgoing* is less changing (compare blue and red curves at upper left). Note also significant changes of the pitch angle distributions. (Right) Distribution during the following “undisturbed” period (perpendicular flux in upper right is shown in red).

- iii The density and the energy effects related to the enhanced parallel electron fluxes below ~ 1 keV (e.g. Roux 1991, [160]) are variable. They are well described as an additional, colder population, that is (using the terminology of the low altitude particle observations) of the type of the Supra Thermal Electron Bursts (STEB, maximum flux at a few hundreds eV)- or of the “inverted- V” population .
- iv The transient energy fluxes of duration of 3 to 6 minutes, related to the injections and the enhanced magnetic fluctuations result from the unbalanced, time changing parallel fluxes. The significant anisotropy can develop in the electron distribution during the bursts, but the colder, streaming component disappears at that times.
- v The description of the electrons by the single maxwellian, using the observed moments of distribution function is not adequate for the reported events (due to the expected presence of two populations as well as due to the development of higher energy tail of distribution).

5.3 Data modeling

The “moments-of-distribution” approach from the previous section ignores the details of the distribution function. This is important if the function differs significantly from the maxwellian.

Another method is applied here to further analyze the observations in the large scale. The model function is proposed to represent the properties of electrons. The approach to be used is to fit the parameters of the selected model function to the observed electron distributions. The parameters change to follow the observed features of the distribution function and the changes can be attributed to the physical processes going on and be used to analyze the observations.

Modeling of the magnetospheric plasma through fitting the single kappa distributions has previously been performed on the large data volume (Christon, 1989, [29] and 1991, [30]). It was also used in case studies related to the plasma sheet structure and dynamics (Koperski et al. 1992, [94]; Popielawska et al. 1993, [148]) and the generation of the plasma waves (Blecki et al. 1994, [15]). The approach used here differ in that it has better time resolution, it is oriented towards the specific events and the model function is more complex, depending on larger number of parameters (the details are given in Appendix A.1).

5.3.1 Model of the distribution function

The proposed model distribution is the sum of two anisotropic kappa functions (see Equation A-1) depending on two sets of parameters and describing two electron populations. The parameters to fit are: temperatures (T_{\parallel} and T_{\perp} , parallel and perpendicular respectively), density N , power indices (κ and λ , independent in the parallel- and perpendicular directions) and parallel streaming velocity, $V0$ for the second (colder) component. Note the slightly different form of the kappa function has been used here (than in the Equation 1.17, usually applied in this context). Note also that the parameters T_{\parallel} and T_{\perp} have the sense of the “true” thermodynamic temperatures (see Appendix A.1 for more details and references). Expressed as the particle flux density, dependent on the energy and the pitch angle, the fitting function applied is:

$$j(E, \tau) = j1(\mathbf{P1}; E, \tau) + j2(\mathbf{P1}; E, \tau) + j_p \quad (5.1)$$

where $\mathbf{P1} = \{N_1, T_{\perp 1}, T_{\parallel 1}, \kappa_1, \lambda_1\}$ and $\mathbf{P2} = \{N_2, T_{\perp 2}, T_{\parallel 2}, \kappa_2, \lambda_2, V0\}$ are the sets of parameters. The bi-lorentzians $j1$ and $j2$ are both of the form of Equation A-3 but in $j1$ the parallel drift is set to zero. j_p is the power law function introduced to exclude the “photoelectron” part of distribution at lowermost dozens of eV, not discussed here.

This specific form of the function has been choosed to follow the principal properties of the observed distributions (anisotropy, parallel drift, power- law tail, two components), and to be

relatively simple. In particular, the well known “partial shell” distribution type met at lower altitudes on the auroral field lines (e.g. Ergun et al. 1998, Strangeway et al. 2001) are not easily observed by the Interball Tail (the atmospheric loss cone is too narrow at its location). Though some weak signatures of the depleted cone can be sometimes found after the injection, this type of distribution is not considered here.

This approach was applied in the data reduction and representation for the two events of 13 January, and partially, to the event of 16 January. The results are presented in two following subsections. Details concerning the method and its constraints are to be found in A.1.

5.3.2 Quality of the method

The examples of fitting are shown in Figures 5.10 - 5.11 for the case of 13 January, and in Figure 5.12 for 16 January. There is the electron flux in the parallel/anti-parallel directions and in the simultaneously observed perpendicular direction. The data are represented by diamonds and plus signs, while the fitting functions by solid lines. The fitting parameters are also printed. (The N^* parameter on the individual spectra plots is not the “true”-, but the scaled density, resulting from the nonlinear fitting routine and depending on the temperature. In the following plots (Figures 5.13 to 5.16), the true density is used instead).

The three plots show the observed fluxes representative for the features of interest- the mixture of two populations in the “stable” situations and the single component during the magnetic disturbance. It can be found that the main features of the measured spectra are well reproduced by the fits.

Figure 5.13 shows the bulk effect of the modeling. Temperature vs. density is plotted for the two populations, obtained for 13 January. Despite the high variability of the second (“colder”) component, two populations are well separated, according to the observations. The above results further confirm the ability of the modeling approach to detect the desired details in the observed distribution functions.

5.3.3 Results of modeling

Despite the significant variance of some parameters and the low number of points obtained (see Appendix A.1 for the constraints), this method provided the valuable results. Selected fitted parameters of two populations are shown as the function of time in Figure 5.14, for the events of 13 January 1996. There are (from top to bottom): the densities, the parallel drift- and the Alfvén velocities (assuming the proton density equal to the electron density), parallel temperatures (T_p), temperature anisotropy (the temperature parallel over the perpendicular, T_p/T_t), and the *electron* beta parameter, obtained separately for the parallel- and for the perpendicular electron pressure. Power of magnetic fluctuations is added in the bottom line. Several features are found in the figure.

- i Dropout of density N_2 of the secondary component with the enhanced fluctuations is evident in two cases (03:03 and 03:32 UT).
- ii The velocity V_0 decrease is also seen around that times, though in the second case (03:35 UT) it fluctuate significantly. Such strong increase is the artificial effect of the fitting and does not change significantly the effect of decreased current carried by the secondary electron population, $N_2 \cdot V_0$.
- iii Other parameters of the secondary population change too- the significant effect is the highly variable temperature anisotropy in the second half of the magnetic disturbance (i.e. when the transient parallel energy fluxes were detected- see the previous section). This would suggest the principal role of secondary population in the energy transport. It is however not

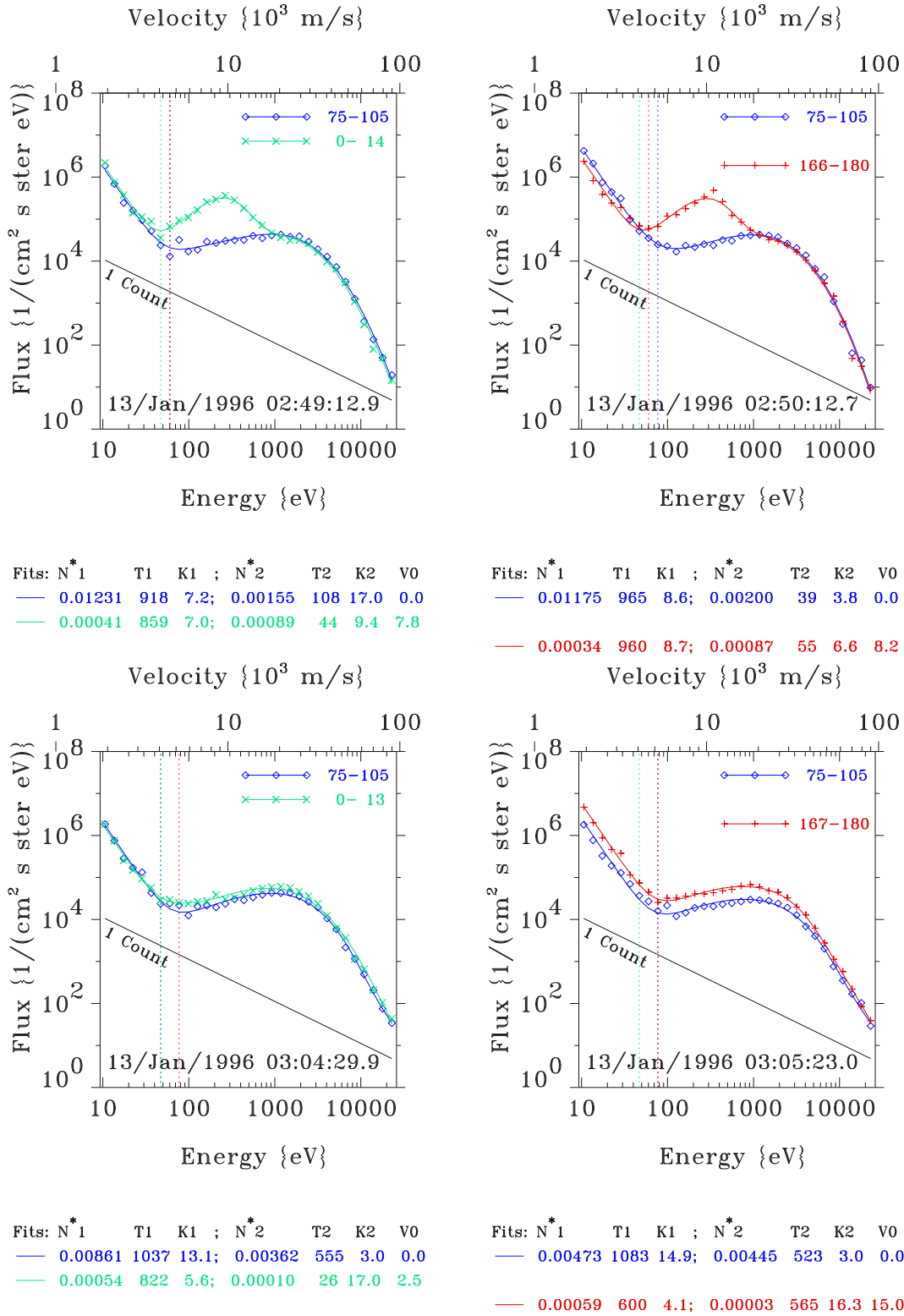


Figure 5.10: Parallel | anti-parallel (**Left** | **Right**) cuts through the 3D particle flux and, simultaneously taken perpendicular cuts (relative to the magnetic field direction). The observed spectra (points) were taken before the enhanced magnetic fluctuations (**Top**), and during that time (**Bottom**). Fitting model distributions are overplotted as solid curves, and the fit parameters are plot in the figure. (Note that the N^* is not the true particle density- see text for the details).

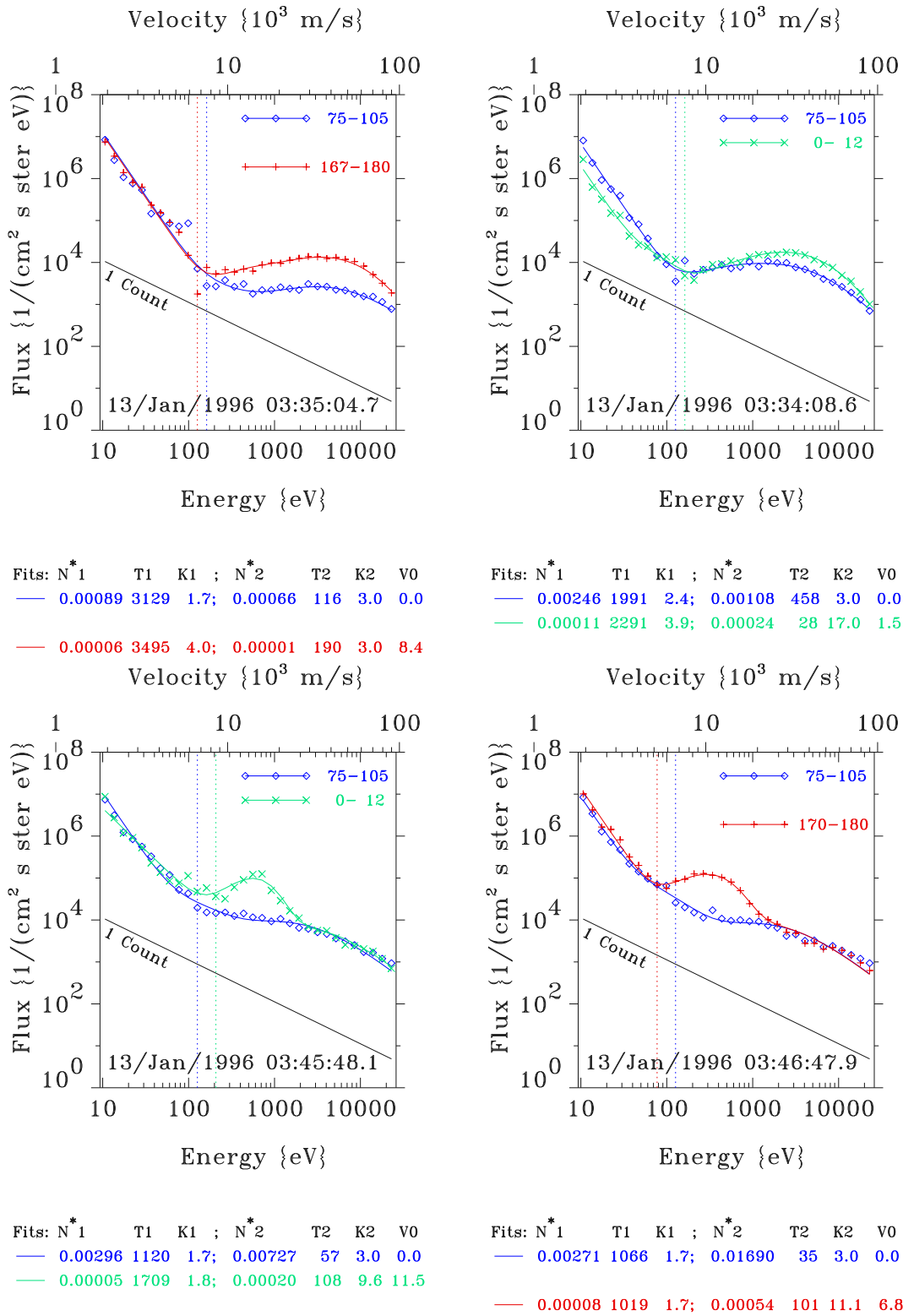


Figure 5.11: Parallel | anti-parallel cuts through the 3D particle flux (**Left** | **Right**) and, simultaneously taken perpendicular cuts. The observed spectra (points) were taken during the enhanced magnetic fluctuations (**Top**), and after that time (**Bottom**). Fitting model distributions are overplotted as solid curves, and the fit parameters are plot in the figure. (Note that the N^* is not the true particle density- see text for the details).

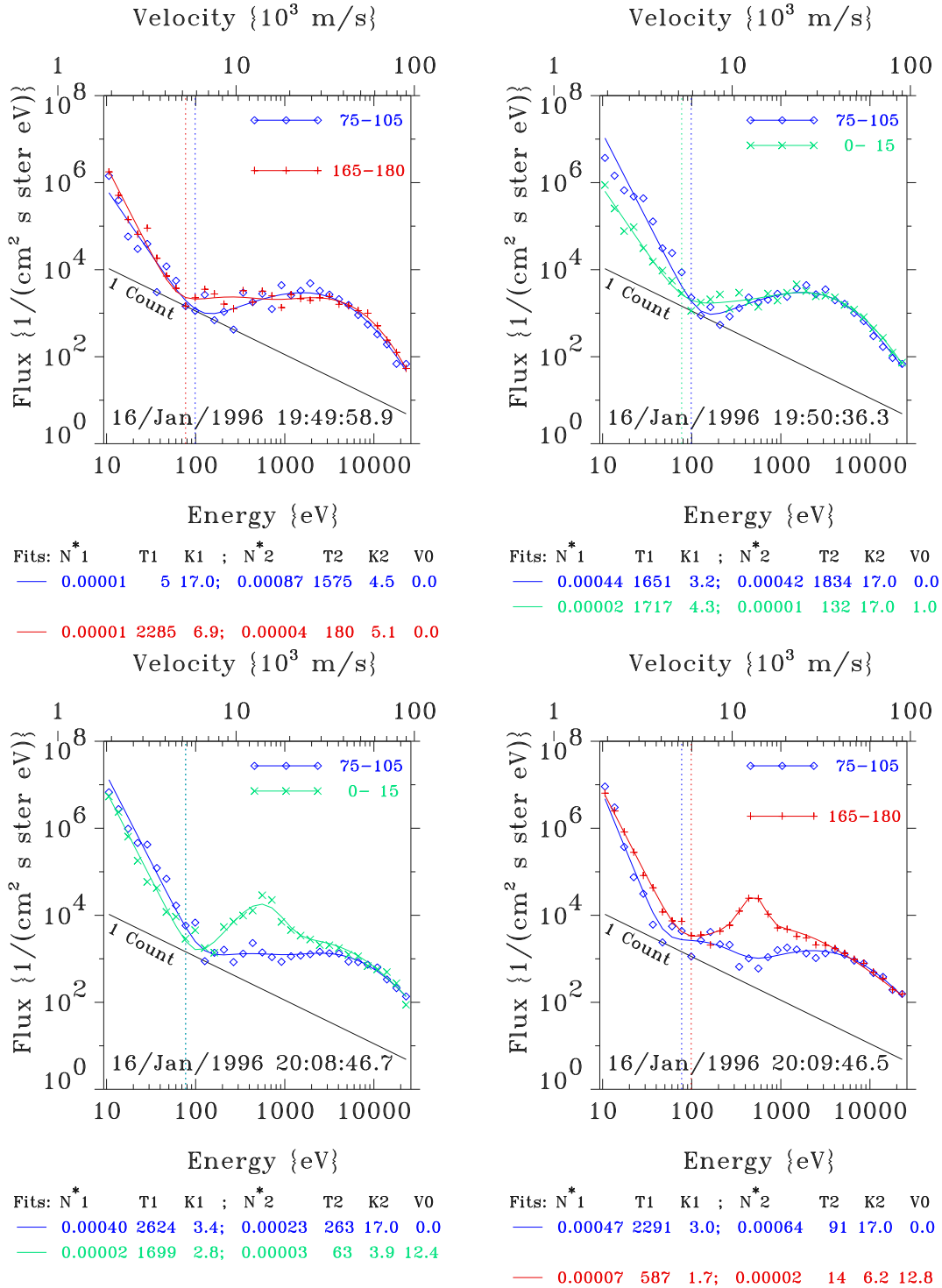


Figure 5.12: Parallel | anti-parallel cuts through the 3D particle flux (**Left** | **Right**) and, simultaneously taken perpendicular cuts. The observed spectra (points) were taken during the enhanced magnetic fluctuations (**Top**), and after that time (**Bottom**). Fitting model distributions are overplotted as solid curves, and the fit parameters are plot in the figure. (Note that the N^* is not the true particle density- see text for the details).

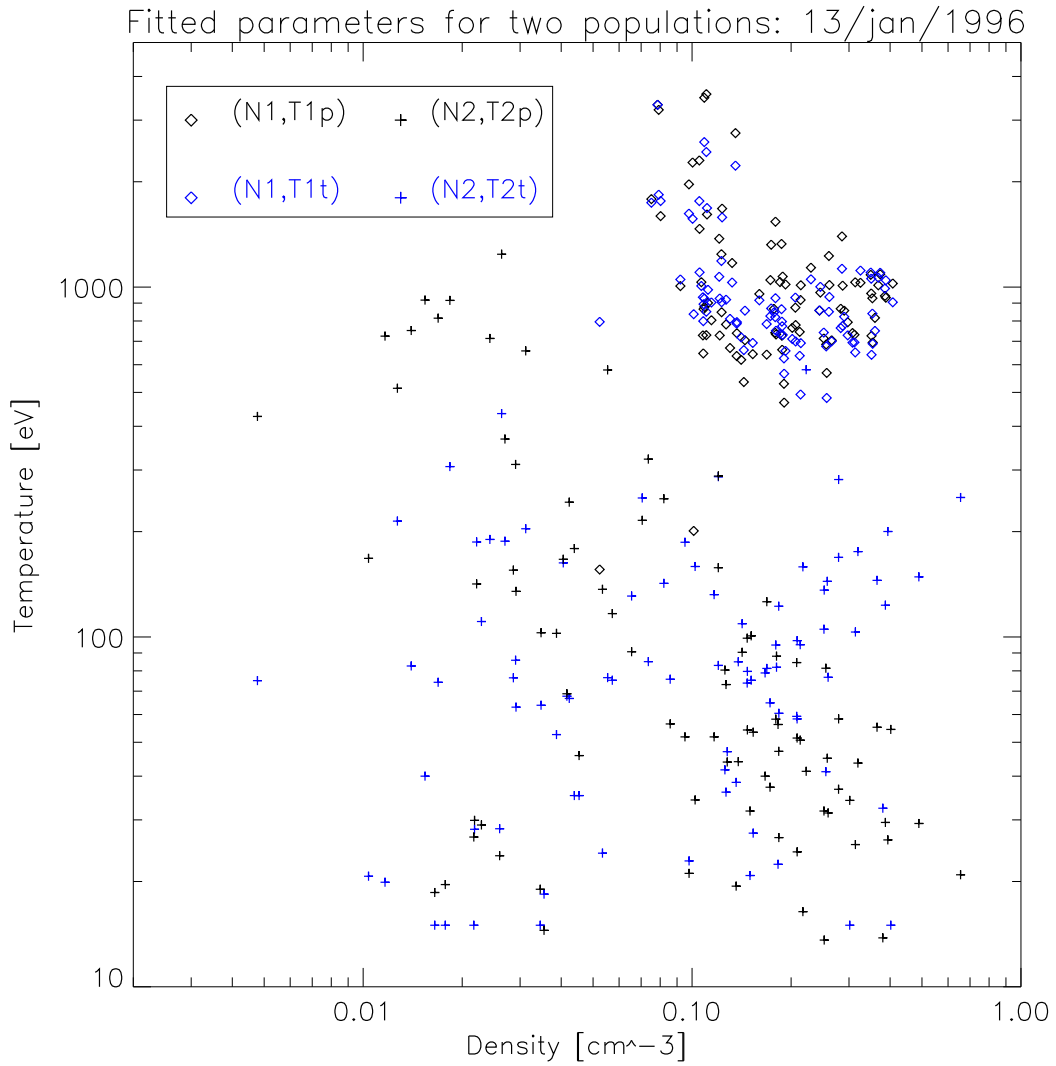


Figure 5.13: Temperature vs. density plot for the fitting model. Two populations are marked (crosses and diamonds) and two temperatures (parallel, T_p and perpendicular, T_t - black and blue). Despite the high variability of the second, “colder” component, two populations are well separated.

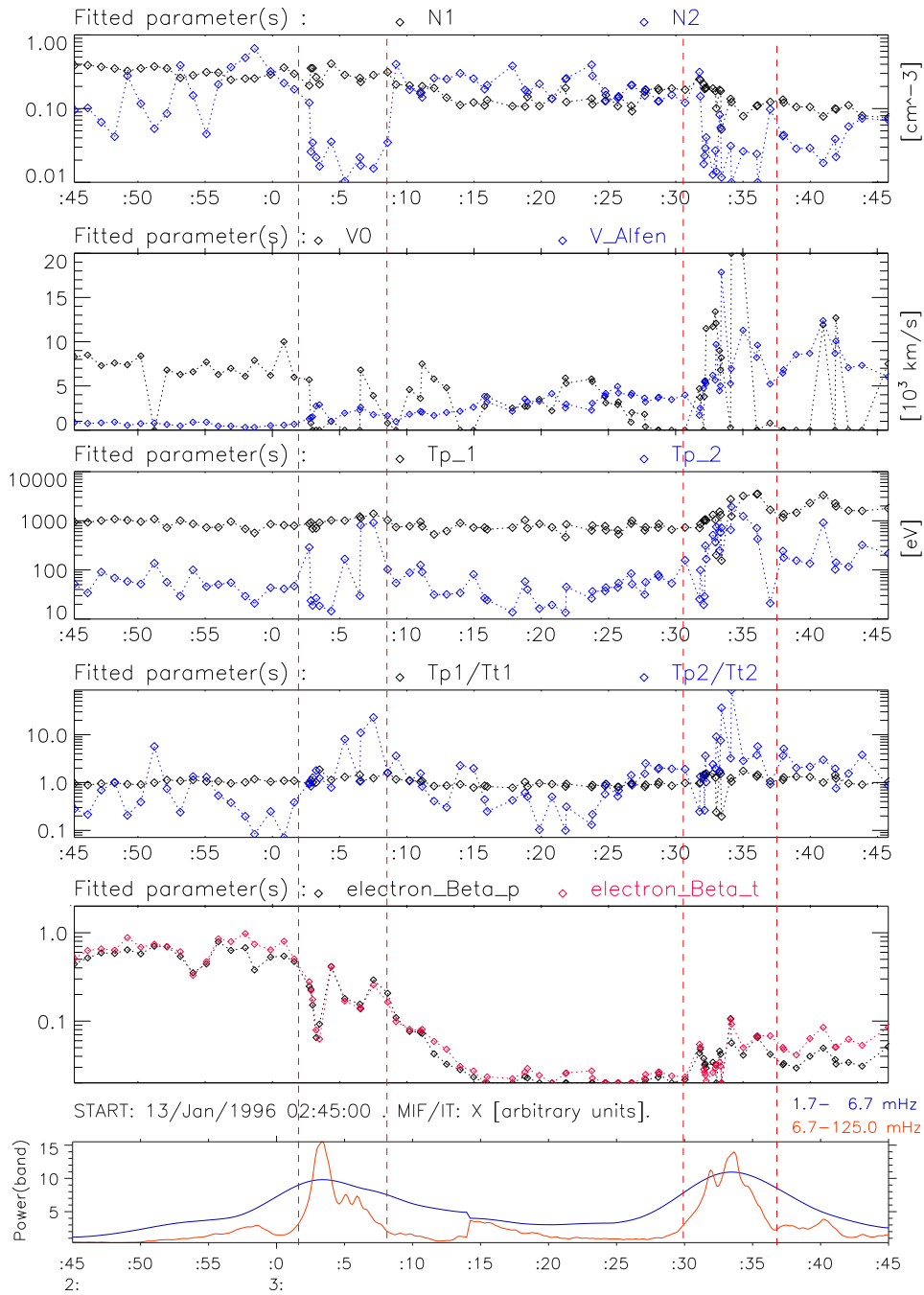


Figure 5.14: Two electron populations on 13 January 1996, represented by the fitted parameters; (from top) densities, N ; streaming (V_0) - and Alfvén velocity (assuming proton density equals to electron density); parallel temperatures, T_p ; anisotropy of temperature (parallel to perpendicular, T_p/T_t); electron beta parallel (p) and perpendicular (t). (bottom) intensity of magnetic pulsations.

so, due to the simultaneous significant density decrease (according to the results of previous sections) and rather low energies occupied by this population.

- iv Another benefit from the modeling approach is the confirmation of the low frequency, Pc5-like pulsations found in the density- and the temperature records of the colder component. The density of ~ 80 eV, parallel streaming population can be even larger than that of the “main” (hotter) population. These oscillations are present both in the high beta (before 03:00 UT) and low beta (around 03:20 UT) regions.
- v Parameters of the main population (N_1 , T_{p1} , T_{t1}) remain constant or slowly change. The isotropy of the “main population” does not change much even after the injections.

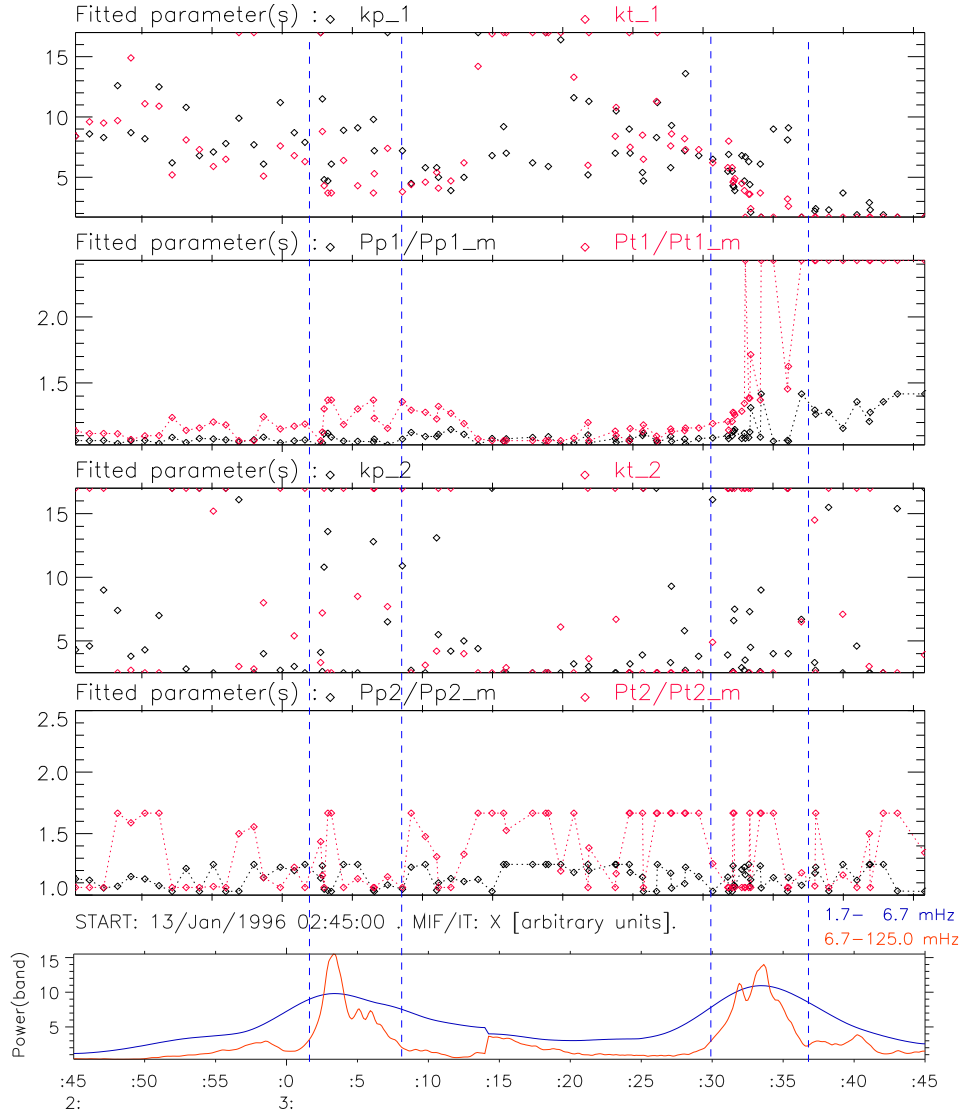


Figure 5.15: Fitted parameters for 13 January 1996 as a function of time; (Top to bottom) Kappa indices in the parallel / perpendicular directions (kp / kt) for the main population; ratio of the actual-to-maxwellian pressure for the main population (parallel and perpendicular); kappa indices for the second population (as above); pressure ratio of the actual-to-maxwellian case for the second population. Dashed lines mark the periods of enhanced $\delta \vec{B}$.

Further details following from the modeling are seen in Figure 5.15, where the spectral indices (κ and λ , called kp and kt on the plot) are shown for both components. The development of the higher energy tail of distribution function results in the increased pressure over the maxwellian values (compare e.g. Treumann 1999b, [198]). The ratio between the actual- and the maxwellian pressure, following from the fitted parameters is then plotted. It has to be noted, that the low and the upper level limit has been put for the values of spectral indices. This results in the sharp cut of the plotted values. After about 03:35 UT the temperature becomes very high and both the temperature and the “kappa” are sometimes underestimated.

There is no clear difference between the parallel and perpendicular spectral indices, κ and λ and their overall high variability is more important. For the main population, it correlates with the intensity of magnetic fluctuations, best seen as the changes of the lower limit of both indices. No regular changes are observed for the indices of the second population, and so in its pressure. As to the pressure of the main component, it mostly differs from the maxwellian at- and around times of increased δB . The strong systematic dominance of perpendicular pressure, after 03:37 UT may partially follow from the form of the assumed model fitting function and the high temperature of the main population. Good quality of the fit for most of the time (see the previous section), allows to think however that the values shown represent properly the non-maxwellian character of electron distribution function near the disturbed times.

Even more clear effect for the main population is shown in Figure 5.16, for the event of 16 January. There are the temperature, the parallel kappa index, the streaming velocity and the power of magnetic fluctuations plotted. While the temperature T1 of the main population is nearly constant, κ decreases (the high energy tail of distribution develops) with the wave enhancements *and* in the injected plasma after the dipolarization (compare Figure 4.34). Also in this case the energization of the electrons does not go through the temperature increase, but by developing the high energy tail of distribution (decreasing κ).

Results presented in this section show that the proposed modeling approach to reduce and analyze the data is very effective. It allows to better describe the observed features and to address the relevant physical processes in a better way. It has, however, the severe constraints due to the assumed type of modeling function and due to the difficulties in the automatic treatment of the large amount of data (see A.1). It could then be applied only in the limited extent. The first limitation (the modeling function) can be re-adapted to better represent the observed plasma properties. The second, however, is intimately related to the first one. The task of fully automatic nonlinear fitting is in this case close to the problem of the automatic pattern recognition. Related to the domain of the artificial intelligence, the development of a better tool requires additional study out of scope of the present work.

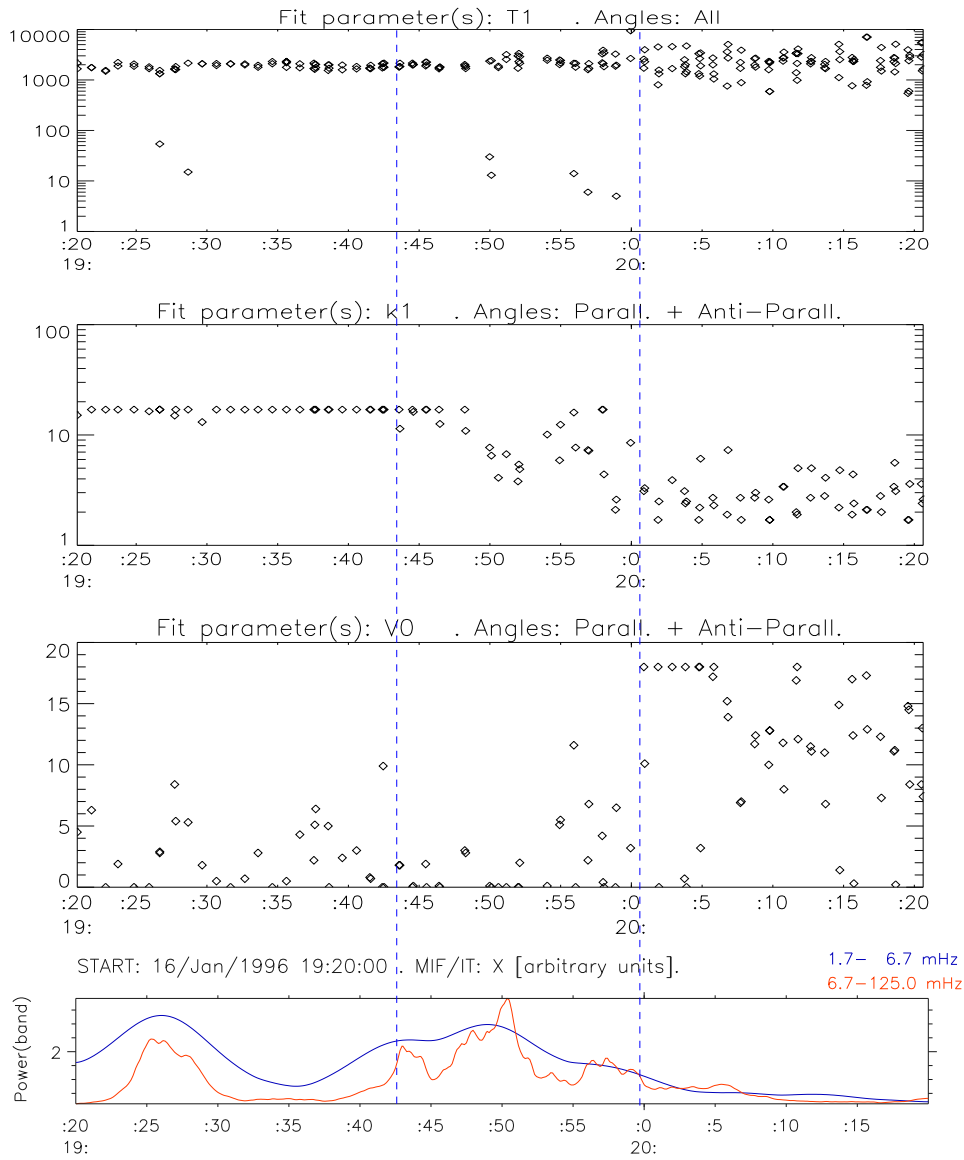


Figure 5.16: Selected fitted parameters as a function of time for the 16 January 1996: (from top) parallel and perpendicular temperature of the main population; parallel kappa index for the main population; streaming velocity of the second population; (bottom) intensity of magnetic pulsations.

5.4 Summary of observations

The results of the analysis from this chapter are summarized below.

Low energy electrons

It has been shown, that the plasma sheet electrons can be well described (for the selected “disturbed” events) as the mixture of two populations. Parallel electron fluxes at $\sim 0.1 - 1.0$ keV, observed here and reported sometimes in the near-geostationary plasma sheet before the substorm onset (e.g. Klumpar et al. 1988, [89]; Roux et al. 1991, [160]) can be regarded in terms of the additional electron population with the streaming velocities mainly of a few (and below about 15) times 10^3 km/s and the temperatures around 100 eV. It can be more dense during the growth phase of the substorm (as for the events of 13 January) and less easily observed for the weaker, localized disturbances (25 and 28 December). In the former case, it appears several minutes before the magnetic “bursts” (related to the current disruption). The colder population disappears quickly with the onset of local magnetic fluctuations in the Pi2 - Pc3 range and can reappear only after the magnetic burst, usually with the different characteristics (density, temperatures, streaming velocity). It is shown here, that this population is observed at distances below $\sim 11 R_E$ in the pre-midnight MLT sector during the substorm growth phase and in the later expansion phase, but *not* at the onset.

The occurrence and the characteristics of these electrons make them the potential magnetospheric counterpart of the SupraThermal Electron Bursts (STEB), observed at low altitudes near the boundaries of auroral oval and the acceleration region (e.g. Meng et al. 1978, [120]; Lotko et al., 1998, [103]; Miyake et al. 2001, [124]; Ivchenko et al. 2002, [71]). Mozer and Hull 2001, [126] in the study of electric fields from POLAR mentioned the similar counter-streaming electrons (their Plate 3) encountered often on the auroral field lines at altitudes up to 4 - 6 R_E but this feature was out of scope of their work.

“Balanced” currents and energy fluxes

Parallel particle- and energy fluxes carried by the electrons are obtained from the particle data. Except for the δB episodes (i.e. fluctuations in Pi2 - Pc3), the local *net* parallel currents carried by the electrons are up to about 15 - 30 nA/m² and the *net* energy flux is generally below 40 - 80 $\mu W/m^2$ (see Table 5.1). These values can easily be supported by the small differences in the parallel- and anti-parallel streaming, colder components. E.g. the average difference between the parallel/anti-parallel flux density of $5 \cdot 10^4$ [particles/(cm² s)] over the energy range between 0.2 and 0.7 keV would result in the net current of 40 nA/m² (see e.g. Figure 5.8). Increases of the field-aligned current and of the energy flux are observed around the δB events. The transient energy fluxes are slightly larger (1.6 to 2.5 times) for the pseudo-breakup-, and significantly larger for the substorm (5 and 30 times respectively, for the weak- and the intensive substorm).

These values are high, when compared to the “classical” reported values in the magnetosphere (note however, that no ion flux- or magnetic field- based estimates of the total electric current were done here) E.g. Frank et al. 1981, [51], reported the field aligned currents of about 3 to 13 nA/m² in the thin layers near the plasma sheet boundary at the distance $X_{GSM} \sim -20R_E$. Lui et al. 1992, [105] observed the cross tail current of 27 - 80 nA/m² in the near plasma sheet just before the disruption. Recently Wygant et al. 2002, [207], in the study related to the Alfvén waves, reported the peak of the earthward electron energy flux of 0.7 mW/m² observed in the PSBL below 6 R_E . In the case study of conjugated low altitude- and magnetospheric observations, Vaivads et al. 2003, [200], reported the in situ energy flux observed on Cluster up to 50 $\mu W/m^2$ on the quiet-time auroral field lines in the middle distant tail. The magnetospheric end in the two above works was located at the boundary of the plasma sheet (contrary to the near-Earth plasma

sheet observations shown here). The observations from the low altitudes, e.g. the case study from Freya satellite of Knudsen et al. 1998 ([91]) showed the particle flux of $0.1 - 1.0 \mu A/m^2$ carried mainly by the STEB electrons (near $0.5 keV$). Field-aligned current study from the Akebono satellite by Miyake et al. 2001, [124] provided the current densities in the lower part of the auroral acceleration region of -3 to $+1 \mu A/m^2$ and the downgoing electrons of $0.1 - 1.0 keV$ energy near the flanks of the acceleration region. Lotko et al. observed on the FAST satellite, the downgoing electron energy flux up to $1.6 mW/m^2$ ($7.2 mW/m^2$ projected to ionosphere over the quiet auroral oval), related to the field line resonance at $\sim 1.3 mHz$. Chaston et al. 2002, [23] reported the Alfvén wave accelerated electrons, also on FAST, with the maximum energy flux (mapped down) of about $5 mW/m^2$. On yet lower altitudes, above the Westward Traveling Surge (WTS) the structured region of precipitating electrons is well known (see e.g. the classical work of Meng et al. 1978 [120]): while the energy fluxes in the main body of WTS reach $10 mW/m^2$, with the maximum flux at energies of a few tens of keV, the surge front on the poleward side is characterized by the different electron spectra- the flux maximizes at a few hundreds eV yielding the energy fluxes up to tens (below 100) mW/m^2 .

The parallel fluxes observed here when mapped from the magnetosphere down to the ionosphere and assuming no parallel potential, should be multiplied by the “mirror ratio” B_{iono}/B_{mag} (or the ratio of the flux tube cross sections, roughly between 1000 and 3000 for the presented cases). The “undisturbed” fluxes mapped down would be comparable to the active WTS values, while the “transient” fluxes would yield slightly unrealistic values of up to $1 - 2 W/m^2$. This evidence strong energization processes going on in the locally and not only in the low altitude “accelerator” (below $\sim 3 - 3.5 R_E$) as proposed by the classical picture of auroral acceleration (see Section 1.3). This also suggest that this energization has to be very localized both in space and in time, as follows from the comparison with the typical energies released in the active auroral region. Similar conclusion was also put in, e.g., the recent wave- oriented study from POLAR at altitudes $4 - 6 R_E$ (Wygant et al. 2002, referenced above). Alternatively, large observed flux values can be associated with the electrons of pitch-angles mostly out of the loss cone, but below the angular resolution of the instrument. In such case fluxes mapped to the ionosphere would be significantly lower. This issue remains unresolved with the data available.

Transient fluxes

Clear effect was observed of the downgoing impulse of the electron energy flux, appearing shortly after the onset of δB (the Pi2 - Pc3 fluctuations), This feature occurs *in the absence* of colder electrons, and lasts 3 to 5 minutes, on the decreasing slope of the power peak in the case of the strong events. The particle fluxes do not exhibit such asymmetry, being strong also upward and appearing earlier. Both the particle- and the energy transient fluxes can be very strong in the case of a substorm, exceeding even more than 10 times the preceding, Pc5- related fluxes (above $0.5 - 1.0 mW/m^2$ in the field of view of a single detector window, $\sim 6 \times 22.5$ deg).

This features seem to correspond to the observations of the enhanced parallel electron fluxes of short duration of a few keV , inside the geostationary region by Johnstone et al. 1994 ([80]) and Perraut et al. 2000 b ([144]). No detailed relation to the substorm onset was shown in the first work, and no details of electron distributions were given in the second work, so it is difficult to precisely compare these observations to those reported here or to distinguish them from the events of the decreasing low energy fluxes reported by Klumpar et al. 1988, [89] and Roux et al. 1991, [160]. More recent observations of Wygant et al, 2002, [207], of strong, earthward directed energy flux carried by the electrons at $\sim 1 - 2 keV$ look similar, though were observed in slightly different place (PSBL, $4 - 6 R_E$).

Details of the distribution function for the “transient” events show, that electrons undergo the change as a whole, single population: no cold component could be found (within the time- and the field of view resolution of the instrument). The proposed explanation of these features (see the

following chapter) is directly related to the “convection surge” (e.g. Mauk 1989, [119]; Delcourt 2002, [37]).

Low- and high frequency oscillations

Parallel fluxes, both of energy and of particles, has been found oscillating in the Pc5 frequency range (about 3 to 5 minutes). They are seen both *before*- and *after* the onset of the sub-storm/pseudobreakup and are rather weak, best seen as the energy- integrated effect. The colder population, if present, is involved in these oscillations. Transient parallel fluxes seem to be “inserted” into the “train” of Pc5 oscillations, as a “disturbance” with the different phase and larger amplitude.

The similar (Pc5) oscillations are also observed in the magnetic field, with the amplitudes slightly larger after- then before the injection. The anticorrelation between the flux- and the magnetic field intensity was sometimes observed (e.g. for 13 January, not shown), which is the sign of the slow magnetosonic mode being involved, but in general the effect was not clear. There were changing differences of the amplitudes and of the phase, due probably to both the dependence on *total* current (including the ions, not analyzed here) and to the changing wave mode. With the rather low quality of the magnetic data, and no ion data available, further analysis of these features was not possible.

Intensity of the magnetic bursts (Pi2 - Pc3) seemed to be modulated by the Pc5 oscillations. The individual peaks last no longer than 4 - 5 minutes and the power of the bursts exceeds that of the lower frequency oscillations near the peaks of the transient flux (see blue and red curves at the bottom of Figures 5.1 to 5.4). This can be the signature of a new wave mode being excited and probably of the developing turbulence.

Pc5 oscillations are typically observed in the magnetic field data in the auroral zone at low altitudes and on the ground, at various levels of activity. They are usually attributed to the field line resonances (FLR) (e.g. Samson et al. 1992, [164] and references therein). Lotko et al. 1998, [103] (see also references therein) modeled the wave data and the suprathermal electrons observed on FAST (at low altitudes) with the dispersive FLR. Another mechanism proposed is based on the post-injection-, westward drifting energetic protons. Ivchenko et al. 2002 ([71]) proposed it for the Pc5 oscillations associated with the field-aligned current structures in the evening auroral oval during the recovery phase, also at low altitudes. For the geostationary event of Roux et al. 1991, [160], Holter et al. 1995, [61], found 300 sec. oscillations (together with the shorter, of 45 and 65 sec.) and attributed them to the slow magnetosonic- and the shear Alfvén waves flowing in the near- Earth current sheet. They observed the wave mode coupling in the curved magnetic field geometry, which explained temporary visible slow magnetosonic mode. Elphinstone in turn related the Pc5 oscillations to the azimuthally spaced auroral forms, suggesting their connection to the substorm growth and expansion.

The Pc3 - Pc1 range waves, below and around the proton cyclotron frequency ($f > \sim 0.1 f_{CH}$) are observed routinely during the cross tail current disruptions. They can be attributed to the multiple possible wave modes. Usually the cross-field current instabilities (e.g. Lui 2004 and references therein) or the current driven Alfvén waves (e.g. Perraut et al. 2000 a, [143]) are recalled. The δB observed here are probably of the same class.

To conclude, both the lower (Pc5) and the higher frequency (Pi2-Pc3) waves observed here fit well into the set of other observations, providing simultaneously new results. Unfortunately, the lack of the electric field and the low sampling rate of the magnetic field make the more detailed investigations impossible.

Waves and electrons

In this work, the low-energy magnetospheric electrons involved in the Pc5- like oscillations before- and after the substorm/pseudobreakup onset has been found. The similar electrons (STEB) were also observed at lower altitudes above the auroral discrete oval in the Pc5 wave structures (see e.g. Lotko et al. 1998, [103]; Ivchenko et al. 2002, [71]). The origin of the suprathermal electrons observed at low altitudes and the details of their acceleration leave, however, some open questions (see, e.g., Lotko 1998, [103]; Miyake 2001, [124]).

Quick disappearance of the low- energy electron population with the δB episodes (Pi2 - Pc3 waves) was also observed here, suggesting some kind of the wave-particle interactions. Increased wave power and its redistribution towards the higher frequencies (blue and red curves at the bottom of Figures 5.1 - 5.4) would suggest the development of an instability, influencing the colder population. Domination of Pi2 - Pc3 over the Pc5 however, is of duration shorter than the time when the low- energy fluxes are decreased or absent. Transient energy fluxes related to plasma injections, are also of shorter duration. This suggests that the two features (the injection-related transient fluxes and decrease of the low- energy electron flux) are not the same physical process, though are probably related. The possible interpretation, based on the mechanism of the turbulent diffusion proposed by Perraut et al. 200 a, [143] is presented in the following chapter.

Another new finding concerns the higher-frequency wave effect on the hotter population. It has been shown in two cases, that this component undergoes the turbulent energization. The temperature changes are not dramatic and the significant parallel anisotropy does not necessary appears on the hot population. Instead the enhanced non- maxwellian tails develops since the onset of the high frequency magnetic burst and the injection. This evidence the usefulness of the non-fluid and non-maxwellian description of plasma energization near the onset. This specific results has been possible due to the detailed analysis and modeling of the observed electron spectra and their changes.

Chapter 6

Discussion and summary.

This chapter contains the synthesis and the interpretation of the principal observed features (Section 6.1) as well as the ensuing discussion in the context of auroral particle acceleration (Section 6.2) and of substorm development (more precisely, the near-Earth current disruption class of models, introduced in Section 6.3). Finally, the results of the whole work are summarized in Section 6.4.

6.1 Interpretation of observed electron phenomena

The large scale aspects of the selected substorm- and pseudobreakup injection events were analyzed in Chapter 4. For the events accompanied by the intense magnetic fluctuation (the signatures of the current disruption), the details of the related microscopic electron distribution were investigated in the previous chapter. This chapter allows to address the question about the mechanisms responsible for the observed features. The related issues concern the eventual role of the low energy electrons (i.e. the fluxes of a few 100 eV) in the near-Earth plasma sheet in relation to the substorm development and the connection of the this region to the low altitude auroral zone. The features observed in the electron fluxes can be understood by recalling the concepts of the ballooning- or interchange mode instability in the near-Earth plasma sheet and of the acceleration in the high- altitude (magnetospheric) segment of the auroral field lines.

Low energy electron fluxes

This work demonstrates that the observed low energy electron fluxes can be viewed as to be supported by the separate, cold and counter-streaming population, and *not* as part of the single, hot population. Such separation shows that the processes which would thermalize the two populations are not significant on the considered time/space scales. In particular it has been the colder population (and *not* the hotter one) shown to participate in the low frequency, Pc5 oscillations. The drift speed of the colder population before the onset of δB is close to its thermal speed, and the opposite streams are only slightly “imbalanced”, resulting in the weak net parallel fluxes. The embedding hot magnetospheric electrons provide the background stabilization against the two stream instability.

The existence of the low energy electrons can be related to the shielding electrostatic potential, developing in the near-Earth plasma sheet due to the quasi-stationary external forcing, as described by LeContel et al. 2000b, [32]; (see also the introductory review in Sections 1.2 and 1.4.4 and the references therein). The solar wind influence during the substorm growth phase is the typical forcing of that kind. The important aspect of the shielding is its non-local character- the currents and large scale potential develop due to the nonlocal, bounce-averaged response of the medium. The parallel potential difference that develops (for the finite electron-to-ion tem-

perature ratio), influences the low energy electrons and induces the parallel currents. For the typical conditions of the growth phase, the potential difference was estimated to be about 100 eV (LeContel et al. 2000b, [32]), so it will be the low energy electrons, and *not* the hot population which will be the most influenced.

Perraut 2000a and 2000b, [143] and [144] presented the mechanism leading to disruption of the parallel current due to the turbulent diffusion of the electrons in the Current Driven Alfvén Wave (CDAW) - field (see also LeContel 2001, [33]). Parallel streaming electrons and the relative drift between the electrons and the ions were necessary to carry the current and to support the development of the instability. This mechanism was able to significantly accelerate the low-energy electrons in a short time and break down the parallel current, allowing the ballooning mode instability to grow (see Section 1.4.4 and the following section).

The auroral current system providing the magnetosphere-ionosphere coupling is closely related to the above shielding and to the electron acceleration. I demonstrate below that the cold population can significantly influence the current-voltage relationship for the low intensity parallel currents in the magnetospheric segment of the “auroral circuit”. With the cold population locally “disappeared”, the current system has to reconfigure itself. Depending on the strength of disturbance and the global configuration, this can lead eventually to the substorm onset (e.g. Perraut et al. 2000a, [143]; LeContel 2001, [33]; see also Section 1.4.4).

I did not discuss the origin of the cold electron population. The information currently available cannot support such discussion. The electrons of energies of few tens to ~ 100 eV are not uncommon in the flank borders of the equatorial plasma sheet (e.g. Popielawska et al. 1993, [148]; Fujimoto et al., 1997, [57]; Sauvaud et al. 1997, [170]). Another possible source to be considered is the auroral ionosphere, where the supra-thermal electrons forming the bursts (STEB) are observed (see the references in Section 5.4). The observations of the cold magnetospheric population presented here share the properties of the two sources mentioned.

Transient electron fluxes

The intense, parallel fluxes observed during the δB episodes occur *in the absence* of the low energy counter-streaming electrons. These fluxes correspond to the locally observed current disruption, dipolarization and the accompanying hot plasma injections.

The duration of transient fluxes, 3 to 5 minutes, corresponds to the bounce time of the typical plasma sheet ions between the magnetic mirror points (compare Table 1.1). These time-scales are very close to those of the “convection surge” mechanism and the related bounce-phase bunching of ions (Mauk 1989, [119]; Delcourt et al. 1990, [35], Delcourt 2002, [37]) The reason for the convection surge is the fast dipolarization during the substorm expansion phase, resulting in the temporary ion demagnetization- and trapping in the equatorial minimum of the magnetic field. This concerns, in particular, the $\sim 1 - 30$ keV, and hotter plasma sheet ions. The consequences of this process are the violation of the second adiabatic invariant of ions, the acceleration (related also to the violation of the first invariant) and the transient parallel electric field, accelerating the ions off the equator and the electrons- equatorward. The simulations demonstrate (Delcourt 2002, [37]) that the electric field disturbance can reach the low-altitude auroral zone in (roughly) 1 - 2 minutes.

Delcourt 2002 [37] suggested that the fast electron beams can be generated at the substorm onset by this electric field. The electrons can also be accelerated by the Alfvén waves (see below). Such beams (i.e. the separate “bumps” in the distribution function) however, are not seen in the events presented here, contrary to the parallel anisotropy during the δB episodes. This can result from the relatively low time resolution of the instrument- the full energy spectrum is scanned during almost 4 seconds (simultaneously over all angles- see Subsection 2.1.1), in the time comparable to the bounce half-period of electron of a few keV (compare Table 1.1) or because the beams are very quickly destroyed, e.g. by the Landau damping.

The gradient effect accompanying the transient fluxes says that they can be also related to the large scale structure passing over the satellite (the injection front). The possible reason of detecting the transient earthward energy flux is the large scale advection of the hotter plasma. In this case the increase in thermal energy of the freshly convected plasma should be high enough to overcome the energy flux of the equatorward streaming particles mirrored at low altitudes. At the same time, the parallel current, carried by the electrons streaming either earthward or equatorward, can develop. It is observed here, as follows from the simulations of Delcourt 2002, [37].

The intense transient energy flux is observed for the substorm cases (13/January/1996 and 16/January/1996). For the pseudobreakups, such strong parallel fluxes are not observed neither in energy nor in particles, though the transient character can be found during the event of 28/December/1995. This behavior should be expected, as no intense plasma injections occur during the pseudobreakups. This further supports the proposed explanation.

Waves

Oscillations in the Pc5 range are found in the magnetic field, as well as in the parallel electron fluxes. The amplitude of flux oscillations grow before the onset of pseudobreakup/ substorm to a limited degree (compare e.g. Figures 5.2 and 5.3). No clear, simple correlation was found between the particle- and the magnetic data, but there were signatures attributed to the slow magnetosonic mode (e.g. before $\sim 03:00$ UT, 13 January 1996, when the magnetic field strength and the electron density were in anti-phase; not shown). The oscillations develop probably as the field line resonances (e.g. Samson 1996, [164]; Lotko et al. 1998, [103] and references therein) or as the drift ballooning wave (see e.g. Holter et al. 1995, [61]; Erickson 2000, [44]; Cheng 2004, [27] and references therein).

From the data presented in this work, it is difficult to state for sure if the parallel currents are involved in the oscillations, because *only* the electron data were available. The increased amplitude of magnetic oscillations supports this point of view, especially for shorter wave periods in the Pi2-Pc3 range (much below the ion bounce period): they can still be carried by the bounce-integrated response of electrons. The higher frequency waves (Pi2 - Pc3) are in turn modulated by the Pc5 oscillations: with the periods comparable to the ion bounce time, Pc5 can reflect the total (ion and electron) parallel current effects. These facts are important for the understanding the role played by the waves.

Perraut 2000a, ([143] and 2000b [144]) proposed the turbulence of Current Driven Alfvén Waves (CDAW) to disrupt the parallel current. These electromagnetic waves, acting in the Pc3-Pc1 frequency range, result from the coupling between the Shear Alfvén Waves (SAW) and the Fast Magnetosonic waves, due to relative drift between electrons and ions (hence- the current). These waves remain unstable over the broad range of parameters and are driven by the electron-ion relative drift speed. They are able to significantly accelerate the electrons in the short time through the turbulent diffusion. In particular, for the sufficiently high drift speed and the wave amplitude, the energy gain of ~ 1 keV in 2 seconds was possible for the electrons initially of a few hundreds eV. This is the time much shorter than bounce period of electrons of the colder population, and even than for the few keV electrons of the principal magnetospheric population.

The observed modulation of amplitudes of Pi2-Pc3 waves can be related to the filamentations of parallel current and/or to the ballooning-mode drift waves in the neutral sheet. The increasing parallel shielding current, related to the low frequency Pc5 waves and forced by the disturbances in the neutral sheet can destabilize the current-driven waves. These waves can then disrupt the parallel current, allowing e.g. the ballooning-mode instability to grow. The final effect will be a pseudobreakup or a substorm (see Section 1.4.4 and the following section). The CDAW turbulence is not the only mechanism being able to influence the parallel streaming electrons, but the one directly related to the electron features observed here.

6.2 Consequences for auroral acceleration

There exist two main “ways of thinking” of the nature of the auroral particle acceleration. The first, model of a quasi-stationary-, large scale electrostatic potential structure was proposed by Knight and further modified by others (see the review in Section 1.3). It is also supported by several low altitude observations and agrees with the recent observations at higher altitudes (e.g. Kletzing and Scudder 1999, [87]; Mozer and Hull, 2001, [126]; Vaivads et al. 2003, [200]). Alternatively, the acceleration by the waves is recalled. During the last few years evidenced was found in support the importance of the Alfvén waves in generation of the parallel electric fields. Their interaction with the electrons is supported by the observations within- and below the auroral acceleration region (below $\sim 3 - 3.5 R_E$; see Section 1.3 and references therein). Recent observations by Wygant et al. 2002, [207] evidenced such acceleration also at higher altitudes (below $\sim 4 - 6 R_E$) in the PSBL.

What remains less explored is the possible extension of the acceleration region at higher altitudes and the mechanisms influencing the electrons there. As the byproduct of studies of the Alfvén waves and parallel potentials, Mozer and Hull 2001, [126] and Wygant et al. 2002, [207] reported the streaming electrons of energies below about 1 keV observed at altitudes up to $4 R_E$, and $6 R_E$ respectively but the origin of this component and its meaning were not considered.

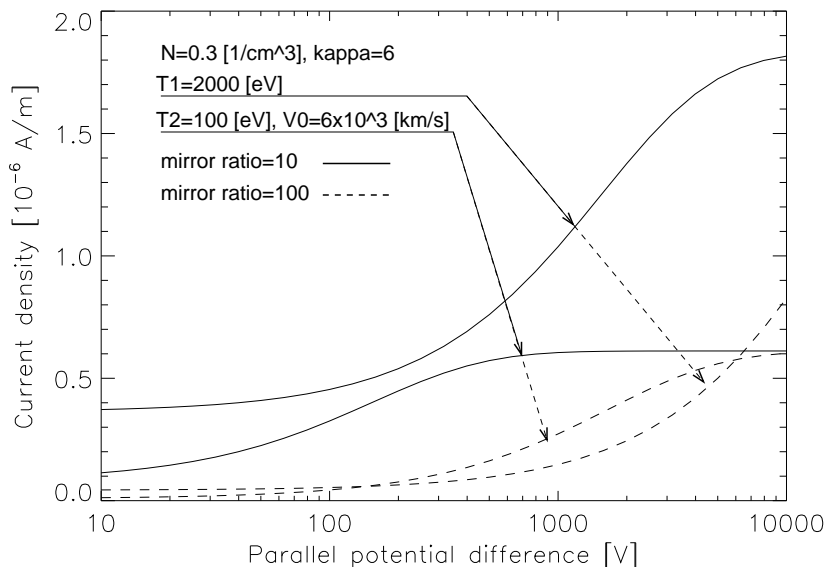


Figure 6.1: Large scale, parallel current-voltage relation for the two component electron magnetospheric source (simplified).

When present, the low energy electrons would change the parallel conductivity and thus influence the magnetospheric- ionospheric coupling. To verify this, the calculation of the current-voltage relationship analogue to the Knight relation (Equation 1.27) was performed. It was based on the model distribution function from the previous chapter (see Appendix A.1) for the set of the representative plasma parameters. The results of such calculations are shown in Figure 6.1, and the details are to be found in Appendix A.2. The current- voltage relationship was obtained for two components (hot and cold) separately, assuming in order to simplify that the power indices are the same and isotropic, the density of both components is equal and the temperatures are isotropic. The values of the parameters are shown in the Figure. Two pairs of curves are plotted- for the mirror ratio ζ equal 10 and 100 respectively ($\zeta = B/B_M$, where B and B_M are the magnetic field values in the observation point and in the mirror point, see Equation 1.25).

The choice of the rather uncommon low mirror ratios is motivated by the special interest in the upper segment of the field lines. For the observed values of \vec{B} and locations, the mirror ratios of 10 (of 100) will correspond roughly to the mirroring altitudes between 4.0 and 4.5 R_E (between 1.5 and 2.5 R_E). In other words, the interest is in the situation where the electrons reach either the upper part of the auroral acceleration region (below 3 – 3.5 R_E) or the altitudes above it, where the local Alfvén velocity is high enough to allow the eventual Alfvén waves to further accelerate the magnetospheric electrons. The pitch angle resolved by the instrument is at best one half of its larger angular window (roughly $1/2 \cdot 22.5$ deg) so no atmospheric loss cone could be seen. Assuming all the particles detected as the “parallel streaming” form actually the loss cone, they would have $\zeta = \text{Sin}^2(11.25 \text{ deg})$ i.e. mirror roughly above $\zeta = 26.2$ for the pitch angle of 11.25 deg ($\zeta = 10.4$ for 18 deg).

Plotted curves for the lower mirror ratio ($\zeta = 10$, solid curve) illustrate the essential role of colder electrons for the weak parallel current (or potential drop). Hot magnetospheric population cannot react for the potential energy much below its thermal energy, and below some 200 eV is supporting only the thermal current. At the same time, the streaming cold population is much easily driven, providing the nearly linear current response down to the potential about 10 V. Above some 300 V, the response gets saturated, but it is already within the linear regime of the hot population. The summary result of the coexisting colder and hotter populations is to provide the “more linear” current- voltage response over almost one more decade. The similar effect holds also for $\zeta = 100$ (lower altitudes- dashed curves) with the larger parallel potential necessary to compensate the enhanced mirror force. These examples do not fulfill the whole spectrum of the observed parameters and the more systematic study would be useful, but the general trend is shown. The calculations were also done for the other sample sets of parameters, demonstrating the general influence of changing temperatures, spectral indices, drift velocity and anisotropy in accord with other calculations (compare, e.g., Dors and Kletzing 1999, [39]; Janhunen and Olson 1998, [76]; Böstrom 2003, [18]).

The model of the “O-shaped” potential structure of the acceleration region (Janhunen and Olsson, 2000, [77]) requires the waves to accelerate the magnetospheric electrons in the upper part of the structure (at $\sim 4R_E$). It does not definitively states the place where the “pre-acceleration” by waves do occur or the exact wave mode, only pointing out the phase velocity close to parallel thermal speed of electrons. Such can be the role of waves in the model of Perraut et al. 2000a and 200b, [143] and [144]. of the parallel electron diffusion induced by the CDAW. This could explain the drop down of the cold population when the waves (Pc3 and higher) start to grow. The low frequency (Pc5) waves can be in turn described in terms of the quasi-static current-voltage relationship. The presented observations can thus further enrich and support the model of the O-shaped auroral potential structure. Cold electrons reflect between the mirror point above some 3 – 4 R_E , until they are accelerated by the higher frequency (Pc3 and above) waves or by the quasi-static parallel potential (Pc5 waves). If such “pre-acceleration” is strong enough, they can reach in the “accelerator segment” of the auroral circuit at lower altitudes. The mechanisms of the parallel current disruption by the Pc5 waves and by the Pc3 (and possibly higher frequency) waves are then in principle similar, when considering the low-energy electrons and the above mentioned O-shaped accelerating potential. Figure 6.2 illustrates acceleration of the electrons in this case. Acceleration by the CDAW and/or the quasi-static potential in the magnetospheric segment of the field lines (1) follows from the observations presented in this work.

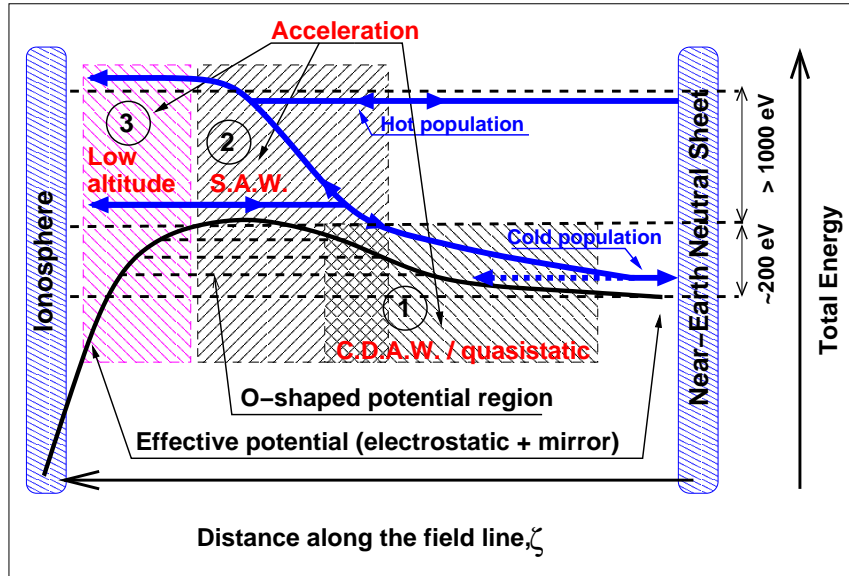


Figure 6.2: Sketch illustrating parallel acceleration of electrons. Three regions are marked: 1. magnetospheric segment with the CDAW or quasi-static, relatively weak acceleration; 2. region of higher Alfvén velocity closer to the Earth, where the Shear Alfvén Waves (SAW) can effectively accelerate the electrons (see Perraut et al. 2000b, [144]); 3. The downward auroral acceleration region. The O-shaped potential structure exists along the field line, with the barrier in regions 1 and 2. The low-energy, parallel streaming electrons mirror at the high-altitude potential barrier until they are “pre-accelerated” enough to reach the accelerator region below. The high-energy electrons can reach low-altitude accelerator, if they are enough field-aligned.

6.3 Consequences for substorm onset

The mechanisms and the conditions triggering the substorm were extensively analyzed and discussed several times (see Section 1.4.4 for the references).

Regarding the presented results, one finds that for each of the “positive” event chosen in Table 4.2 Chapter 4, (see also Figure 5.5 for the detailed views) the time sequence of the locally observed features is similar:

- i Pc5 waves appear; the low- energy electrons are involved.
- ii Pi2 - Pc3 waves start to grow; low energy component quickly disappear.
- iii Pi2 - Pc3 further intensify, above the level of Pc5 oscillations.
- iv Injection and dipolarization take place; transient, earthward energy fluxes appear (more or less intense); transient parallel flux of electrons appear (possibly the parallel electric current).
- v Pi2 - Pc3 fade and subsequently disappear.
- vi Eventually the low- energy component reappears (with the different set of parameters).

This sequence is only qualitative and does not include all important information, but can serve as a reference.

Model of current disruption

The observations can be interpreted within the framework of the near geostationary onset (NGO) model of a substorm. More specifically the nonlocal, bounce-averaged response of the near-Earth plasma sheet is recalled (LeContel 2000a, [31] and 2000b, [32]) and the drift ballooning waves (Roux 1991, [160]; Holter 1995, [61]; also Cheng 2004, [27] and references therein) and/or the field line resonances (e.g. Samson 1992, [164]; Lotko 1998, [103]; see also and references). It follows, that the Pc5 oscillations observed in the electron data can be attributed to the drift waves, that propagate in the azimuthal direction in the transient region between the “tail-like” and the “dipole-like” configuration of the magnetic field (near $\sim 10 R_E$). The waves, observed also in magnetic field, include the interchanging regions of earthward- and equatorward field-aligned currents (see Figure 1.11).

If restricted to the neighborhood of the cross-tail current sheet, this is the mechanism of the drift ballooning waves, and the frequencies higher than Pc5 (e.g. Holter et al. 1995, [61]) would only apply. It has to be pointed however, that the restriction to this specific mode or region (so the frequency range) is not necessary and perhaps not well motivated. Considering the current sheet only, would result in “filtering” the relatively high frequencies and considering only the particles trapped in the equatorial region (see e.g. Holter 1995, [61]). There are several wave mode proposed to play a role, and the detailed analysis require accounting for the nonlocal, bounce averaged response of plasma, specific for the region considered (e.g., LeContel et al. 2001, [33]; and recent reviews of Lui 2004, [110] and Cheng 2004, [27]). The proper discrimination among the different instability modes would principally require the numerical simulation and is out of scope of this work.

The field-aligned fluxes of low-energy electrons are involved in the Pc5 oscillations. There seems to be the saturation level, above which the waves cannot grow and the transient, stronger fluxes appear (roughly, below $10 nA/m^2$, see Figure 5.3 and Table 5.1). It means that such field-aligned currents can support the shielding up to a limited extent. In the framework of the NGO model, the increasing amplitude of the drift waves in the neutral sheet (e.g., the ballooning-mode) requires the increasing intensity of the field-aligned current to be stabilized. The low-energy electrons would follow such driving, until they are accelerated enough to cross the potential barrier at middle altitudes, become downward accelerated and lost from the system. As seen in the typical time sequence of events, (i) - (iii) above, the higher frequency waves are also observed (e.g., these can be CDAW as proposed by Perraut 2000a, [143] or LeContel et al. 2001, [33]). The excited waves (CDAW) further destabilize the field aligned current through the very effective acceleration of low-energy electrons. These two mechanisms act to destroy the shielding current.

Disruption of the parallel shielding current in turn destabilizes the drift waves in neutral sheen. The locally increased electric field can cancel the cross-tail electric field (see Figure 1.11) and the localized injection and dipolarization will occur. What then happens depends on the large scale configuration and the energy flow, resulting in the pseudobreakup or the substorm expansion onset. This “coupled” mechanism of the field-aligned- and the cross-tail current disruption *is similar* to the “ballooning- mode instability” model for the substorm development (e.g. Perraut-2000b, [144]; Erickson, 2000, [44]; also Cheng 2004, [27]). It is shown here, that the model can be extended to include the lower frequency waves becoming unstable. For the slower Pc5 oscillations, the particle bouncing at larger distances from the equator is important and the lower frequency, quasi-static mechanism of electron acceleration from the previous section could be included.

The new elements that appeared here, are: (i) The detailed analysis of electron properties near the injection and the current disruption. Demonstrated in particular was the origin of low energy electron fluxes and the electron input to the Pc5 waves before- and after the onset of substorm/pseudobreakup. (ii) The role of the cold population for the current-voltage relationships in the upper segment of the auroral field line.

Currents and supra-thermal electrons

The results of this work suggest connection between the supra-thermal electrons at lower altitudes and the low-energy electron population observed on Interball. The calculated (in the previous section) example of current-voltage relationship allows us to understand what happens, when the parallel current increases above certain level. As the response of the colder component for the forcing from the drift waves saturates, the parallel current can still grow (due to increasing response of the hot component), at the price of the increased parallel potential difference (see e.g. Böstrom 2003, [18] and 2004, [19]). This will further accelerate the cold component, forcing it to mirror at the successively lower altitudes. This is sketched in Figure 6.2 and described above. Note that the parallel potential difference is not strong (initially ~ 100 eV) and that the colder population extends in pitch angles out of the (very narrow at this point) atmospheric loss cone. Recalling these two facts one can see, that the effect of acceleration of colder component on the current will not be very important, *until* the electrons reach the top of the accelerator segment (near region 3 in Figure 6.2, below some $3R_E$). They will be then accelerated downward and lost due to precipitation, so they can no longer support the shielding current. The lack of easily driven current carriers can further increase the parallel electric field and accelerate the electrons which would cancel the shielding current.

The parallel acceleration of already anisotropic, colder component can be the mechanism responsible for the supra-thermal electrons (STEB) observed at lower altitudes. The above “quasi-static” loss of the cold magnetospheric population can accompany the Pc5 oscillations during the growth- and the recovery phase. Such effect was observed at low altitudes by Ivchenko et al. 2002, [71] and detected in connection with the field line resonances at the comparable frequencies by Lotko et al. 1998, [103]. In the similar way, “bursty” acceleration of the same component by CDAW just before the current disruption and injection can be responsible for the specific, STEB-like electron spectra and energy fluxes observed in the front of the Westward Traveling Surge (e.g. Meng et al. 1978, [120]; Miyake et al. 2001, [124]). The presented details of electron distribution function and the location of the satellite (in the pre-midnight MLT sector, close to the developing active events) suggest such scenario. It should be however investigated more carefully to allow for the final, quantitative conclusions.

Beginning of expansion phase

The observations of intense electric fields and Poynting energy fluxes were reported in last few years near the substorm onset in different regions of the magnetosphere. E.g. Erickson et al. 2000, [44] analyzed the fine structure of fields from the large amount of observations inside the geostationary region (by CRRES satellite). They identified so called “local explosive onset” phase (LEXO) associated with the intense Poynting flux oriented towards the Earth. It was preceded by the “Trigger Waves” in equatorial plane- the drift waves strong enough to locally divert the electric field (see Figure 1.11). Other observations also support the possibility of the Alfvén wave acceleration of electrons near the onset (e.g. Mozer and Hull 2001, [126]; Lotko et al. 1998, [103]). The conclusion from these observations is that the strong Poynting fluxes can transfer significant part of their energy to precipitating electrons in the upper part of the auroral accelerator segment or above.

The observed transient energy fluxes carried by the electrons seems to be the analogue of the LEXO event of Erickson et al. Though the Poynting flux cannot be obtained here, the analogy is suggested by the accompanying magnetic bursts of comparable frequencies, that occur in the similar situation. The duration of the above LEXO events was typically near 1 minute and the average power density was up to 0.23 mW/m², with the maximum of 1.3 mW/m² (see their Tables 3 and 5). These values provide a reasonable comparison for the Interball substorm-related values (see Table 5.1). Furthermore, the time sequence and the frequency range suggest,

that the trigger waves correspond to the beginning of the δB episodes on Interball, even though the duration of the trigger waves on CRRES *before* the LEXO is longer. Possible differences of the frequencies, amplitudes and duration can result from different location of spacecrafts or the different geophysical conditions.

The above considerations allow to sketch the simple scenario of the beginning of substorm expansion phase or of pseudobreakup, based on observations in the near-Earth plasma sheet. Interball observations at the onset show the earthward impulsive acceleration of the electrons. It follows the signatures of parallel and of cross-tail current disruption, which shows that it is not the cause, but the effect of the current disruption. In particular, it explains the anti-coincidence of the transient electron fluxes with the low-energy population involved into Pc5- related parallel fluxes. The above consequence is in agreement with the NGO model of substorm initiation, and more specifically with the ballooning-mode instability triggering the onset. The convection surge mechanism mentioned above and resulting from the rapid dipolarization of magnetic field, is responsible for the observed transient parallel fluxes of electrons, Related to trapping of ions in the equatorial region during the dipolarization, this mechanism also explain the duration of transient fluxes (of the order of ion bounce time, compare Table 1.1).

It is important to note, that the nonlocal, bounce-phase integrated effects are of importance in this case. Proper description of such effects should explain the evidence of lower frequency (Pc5) waves observed before- and after the increased, transient electron fluxes and Pi2-Pc3 magnetic fluctuations. The details of the above features still require more careful investigation. In particular the ion data and the magnetic field data of better quality and resolution would help to further analyze the wave mode involved. It was not possible nor available when I was working upon the thesis.

6.4 Summary

The purpose of this work was to explain the features observed in the low energy electron fluxes ($\sim 100\text{ eV} - 2\text{ keV}$) at the time of injection and current disruption events in the near-Earth plasma sheet.

The observations from the Interball Tail have been used towards this aim, as the main source of information. The analysis of the geomagnetic substorm-related features was the essential part of this work. The relevant, supporting data from multiple ground stations and satellites were also selected and analyzed as a part of the study. Having selected and analyzed four month worth of data (from October 1995 to January 1996) it was possible to identify the common large scale characteristics of the chosen events. The macroscopic properties of the electron component of plasma as well as the properties of distribution functions were analyzed. To better account for the observed microscopic properties, the approach of (nonlinear) fitting of the model function to the observed distributions was applied in two cases.

The principal results of this work can be summarized as follows

- i The observed features in the low-energy, field-aligned electron fluxes can be attributed to the separate population of electrons, colder than the typical plasma sheet electrons (below $\sim 200\text{ eV}$) and counter-streaming. The parameter range and the occurrence make these electrons a potential magnetospheric counterpart of the SupraThermal Electron Bursts (STEB) observed often below the acceleration region ($\sim 1 - 3 R_E$) in the auroral zone.
- ii Low frequency, Pc5 range oscillations were found in the parallel electron flux during the growth phase and since the late expansion phase. Colder population disappears with the the Pi2 - Pc3 magnetic fluctuations. After that, transient and stronger (in the case of a substorm) parallel energy flux appeared, directed earthward. Similar Pc5 oscillations have been found in the magnetic field. The observations of the Pc5 with the low energy electron

population involved in the plasma sheet is the new result, important for the considerations on the auroral particle acceleration.

- iii It has been shown, that the low-energy, streaming electrons are able to modify to some extent the (quasi-static) current-voltage relationships in the magnetospheric segment of the auroral circuit (at altitudes above $\sim 3 - 3.5 R_E$). This provides the quasi-static analogue of the field-aligned current disruption mechanism by the current driven Alfvén waves (by Perraut et al. 2000a, [143]). Though not significant when compared to the strong accelerating potential at low altitudes, this effect may be important in the magnetosphere for the long period oscillations and for the acceleration of the STEB electrons observed at low altitudes at the auroral oval boundaries (e.g. Lotko et al. 1998, [103]; Ivchenko et al. 2002, [71]).
- iv The presented observations are of importance for modeling of substorm development. First of all, the reported magnetospheric features correspond closely to the substorm onset observed on the ground in the same local time sector. Second, transient earthward energy flux of duration 3 to 5 minutes, carried by $\sim keV$ electrons coincides with the enhanced magnetic turbulence in the Pi2 - Pc3 frequency range, the signature of current disruption. Transient fluxes correspond to the effect of convection surge, occurring after the dipolarization. Finally, the disappearance of low energy electron fluxes, which carry the Pc5 oscillations, seems to be responsible for the local destabilization of the parallel current system. This can in turn locally disrupt the cross-tail current, which can lead to the substorm onset. The observed sequence of changes in electron fluxes and magnetic oscillations is therefore similar to switching on the substorm onset by the ballooning mode instability (Roux et al. 1991, [160]; Erickson et al. 2000, [44]), though the observed pre-onset Pc5 oscillations are rather related to field line resonances (also observed for one of above cases by Holter et al. 1995, [61]).
- v Another new result is the evidence, that the energy is transferred from the intensive ULF fluctuations to the magnetospheric (hotter) electron population by turbulent acceleration rather than by heating, at least for the observed substorm events. The temperature after the injection does not change dramatically, Contrary, the high energy, non-maxwellian tail of the distribution function develops during the enhanced Pi2 - Pc3 magnetic fluctuations. This kind of effects is a particle signature of the turbulent processes, which are observed simultaneously in the magnetic data. It further confirms the influence of the low frequency turbulence on electron acceleration along the auroral magnetic field lines.

In conclusion, the results of this work evidence the importance of the low energy ($\sim 100 eV$) electrons in the dynamics of the near- Earth magnetosphere near the substorm.

Appendix

A.1 Modeling the electron distribution function

A.1.1 The distribution function

As the basic model function, the anisotropic “kappa” (or the “generalized Lorentzian”) will be used in a slightly different form than usually met in literature. Expressed as the function of velocities, it have the form:

$$f(v_{\parallel}, v_{\perp}) = A \frac{1}{\left(1 + \frac{v_{\parallel}^2}{\kappa\omega_{\parallel}^2}\right)^{\kappa+1}} \frac{1}{\left(1 + \frac{v_{\perp}^2}{\lambda\omega_{\perp}^2}\right)^{\lambda+1}} \quad (\text{A-1})$$

with the normalizing coefficient:

$$A = \frac{1}{\pi^{3/2}} \frac{N}{\omega_{\parallel}\omega_{\perp}^2} \frac{\Gamma(\kappa + 1)}{\Gamma(\kappa + 1/2)\kappa^{1/2}} \quad (\text{A-2})$$

where the ω_{\parallel} and ω_{\perp} are the “characteristic” velocities- and κ , λ are the spectral indices- for the parallel- and the perpendicular directions, respectively and Γ is the Euler’s Gamma function. The above “factorized bi-lorentzian” (as I let myself call it) introduced by the Equation A-1 differs from the similar definition of the “product bi-lorentzian” of Summers and Thorne ([192]) in that it has two independent spectral indices and, as a consequence, the normalization factor A changes too (In particular, it is independent on λ). Note also, that the “characteristic” velocities *are not* simply the “thermal” velocities of the distribution (see the fundamental considerations on the kinetic- theory background of the kappa distributions and their thermodynamic consequences of Treumann 1999a, [197] and Treumann 1999b, [198], and the slightly different approach from the statistical point of view of Milovanov and Zelenyi 2000, [122]).

With the real data analysis, the use of the particle flux is often preferred. Expressed by energy and pitch angle and taking into account the parallel streaming of the particles, it is :

$$j(E, \tau) = C E \frac{1}{\left(1 + \frac{E\tau + E_0 - 2\sigma\sqrt{E\tau E_0}}{\kappa T_{\parallel}}\right)^{\kappa+1}} \frac{1}{\left(1 + \frac{E(1-\tau)}{\lambda T_{\perp}}\right)^{\lambda+1}} \quad (\text{A-3})$$

where:

$$C = \frac{2}{m^2} \left(\frac{m}{2\pi}\right)^{3/2} \frac{N}{T_{\parallel}^{1/2}T_{\perp}} \frac{\Gamma(\kappa_{\parallel} + 1)}{\Gamma(\kappa + 1/2)\kappa^{1/2}} \quad (\text{A-4})$$

is the normalizing constant, T_{\perp} and T_{\parallel} are the temperatures,

$$\tau = \cos\Theta^2$$

Θ being the pitch angle, and

$$E_0 = m_e V_0^2 / 2$$

is the kinetic energy of the (parallel) drift, V_0 . Finally, σ is the sign of the drift velocity (+1 or -1). Note that the E_0 is *not* the parallel electrostatic energy.

A.1.2 Assumptions

Based on the observed features, the modeling approach is applied to the flux of particles. The model function is composed of two above anisotropic kappas, depending on two different set of parameters, each describing two electron populations. The parameters to fit are: temperatures (parallel and perpendicular), density, power indices (parallel and perpendicular) and parallel streaming velocity for the second (colder) component. (Note, that the special form of the kappa function has been used and that parameters T are the “true” temperatures in the thermodynamic sense). The general form of the fitting function is proposed to be:

$$j(E, \tau) = j1(\mathbf{P1}; E, \tau) + j2(\mathbf{P1}; E, \tau) + j_{photo} \quad (\text{A-5})$$

where $\mathbf{P1} = \{N_1, T_{\perp 1}, T_{\parallel 1}, \kappa_1, \lambda_1\}$ and $\mathbf{P2} = \{N_2, T_{\perp 2}, T_{\parallel 2}, \kappa_2, \lambda_2, V_0\}$ are the sets of parameters—the density, the temperatures (parallel and perpendicular) and the power indices (parallel and perpendicular) for both components and the drift velocity. $j1$ and $j2$ are the bi-lorentzians of the form of A-3, but in $j1$ the drift is set to zero. j_{photo} is the power law function to model the “photo-electron” part of distribution at lowest energies. This component in general covers the lowermost dozens of eV, and is not discussed here. The “main” component is the hotter one and not streaming, typical for the plasma sheet. When only single population is present, the density of secondary component will be set to a small value. These assumptions are important for the initial guess of parameters of the fit.

It has to be stressed, that the fitting function depends nonlinearly on parameters. This is very different to a linear fitting and may result in the computational difficulties of the fundamental nature. This is because of the strong dependence of the on the initial guess. This was the case here and because of this further constraints had to be applied.

The model assumes the specific (monotonic) kind of angular dependence and hence is of the limited use. In particular, the “loss-cone” or the “horse-shoe” distribution, observed at low altitudes in the auroral zone does not fit into this class. In particular, the well known “partial shell” distribution type is met at the lower altitudes on the auroral field lines (e.g. Ergun et al. 1998, [43]; Strangeway et al. 2001, [191]). The atmospheric loss cone is below the angular resolution of the instrument but the effects of the concurrent Fermi- and betatron acceleration could play a role. The main interest here is in the field- aligned effects and in the “bulk” differences between the transverse- and the parallel direction. The *weak* “butterfly- like” angular distributions were sometimes found after the episode of magnetic fluctuations. Following Smets et al. 1999, [186] and Sergeev et al. 2001, [181], one should not to expect such effect for the spacecraft localized as the Interball. Neglecting these effect in the modeling does not significantly influence the results and the conclusions, while simplifying the approach.

In the consequence, the model can be seen as a reasonable tool , regarding the specific aim and the data set to be analyzed.

A.1.3 Method and its quality

The above model was used in the data reduction and representation for the events of 13 January 1996 and (partially) of 16 January 1996.

The necessary comments on the details are as follows:

- i The sum of two anisotropic, 3D functions was always applied (Equation 5.1) to follow the observations. When only one population was present in the data, it often led to the artificial results.
- ii The fitting function is completed by adding the power law component approximating the photoelectrons in the lowest part of the spectrum (generally below $\sim 100\text{eV}$).
- iii Because of the specific of the nonlinear fitting (see above), the implementation of a fully automatic routine appeared to be out of reach for the purposes of this work.
- iv The required manual setting of the initial guess was too much time consuming to be applied to all the events and only two events were partially analyzed.
- v The numerical scheme of Levenberg-Marquardt type was applied (see e.g. Numerical Recipes, Press et al., [150]).

The example of modeling are shown in Figures 5.10 - 5.12 in Section 5.3. Figure 5.13 in turn illustrates that two populations are well separated by the method, even if the parameters are highly variable. This shows that the model can provide the acceptable results. The advantages of this method are as follows:

- the secondary population is well reproduced (in the top row of the first figure and at the bottom of two remaining figures). This detail were missed in the preceding analysis of the moments.
- the non-maxwellian distributions, the high temperature spectra partially out of the detector's energy range and the photoelectrons in the low-energy part of spectrum are also well described and taken into account. These effects could significantly obscure the properties of plasma if using only the moments of the distribution function.

A.2 Current-Voltage relationship

Taking the distribution function of the single component in the form of Equation A-1 (eventually with the parallel drift set to zero) leaves too much free parameters to be investigated and is not considered in this work. The examples of the general dependence of the current voltage relationships on various selected distribution functions can be found e.g. in Böstrom 2003, [18]. The results of fitting the observed distributions (Section 5.3) show no significant difference between the parallel and perpendicular spectral indices for both cold and hot population. Temperature anisotropy of the colder population can certainly play a role, but this would interfere with the effect due to the parallel streaming. Moreover, hot population is mainly isotropic, except for the transient flux episodes, which are non-stationary, while the current- voltage relationships are by definition applicable to the stationary case, In consequence, I assumed κ equal to λ and the isotropic temperatures.

Following the usual procedure (Knight 1978, [90]; see also see Section 1.3), the starting point is Equation 1.26 including only the magnetospheric electrons moving downward. The components α contribute independently, so the cold- and the hot populations can be considered separately. The appropriate region of the phase space, A_α is choosed assuming the monotonic dependence of the potential on the magnetic field strength. This very strong assumption allows however to neglect the consideration of the local charge neutrality allowing for the direct integration. The result should be regarded as the lower limit for the potential difference to support the given value of the file-aligned current (see Chiu and Schultz 1978, [28]; Khazanov et al 1998, [85]; Böstrom 2003 and 2004, [18] and [19]).

To obtain the desired formula, one can take the distribution function depending on the parallel- and perpendicular kinetic energies, W_{\parallel} , W_{\perp} , and consider only the downgoing particles, $v_{\parallel} > 0$. Assuming the gyrotropy and the conserved magnetic moment μ , one obtains:

$$j(\Delta\Phi) = 2\pi \int_0^{\infty} \int_0^{\infty} f(W_{\parallel}, W_{\perp}) dW_{\parallel} dW_{\perp} \quad (\text{A-6})$$

where W_{\parallel} and W_{\perp} are related to the parallel potential difference $\Delta\Phi = q_e \Pi$ through the conservation equations 1.19 and 1.20 (conserving the same notation). Taking the isotropic temperature T (that will normalize W_{\parallel} and W_{\perp}), imposing $\lambda = \kappa$, one gets the expression relating the current and the voltage in the form:

$$j(\phi) = C \int_0^{\infty} \frac{1}{[1 + x + x_0 - 2\sqrt{(x x_0)}]^{\kappa+1}} \cdot \left\{ 1 - \frac{1}{[1 + (\pi + x)/(\zeta - 1)]^{\kappa}} \right\} dx \quad (\text{A-7})$$

where $x = E/T$, $x_0 = E_0/T$ and $\phi = q_e \Delta\Phi/T$ are respectively the kinetic energy of the particle, of the the average drift and the electrostatic potential energy, each normalized to the thermal energy. Parameter ζ is the mirror ratio and the normalization constant

$$C = \frac{N\Gamma(\kappa + 1)}{\Gamma(\kappa + 1/2)\sqrt{\kappa} T^{3/2}} \quad (\text{A-8})$$

This formula do not further simplifies, due to the square root term, and has to be integrated numerically. The calculations of this formula were performed using the internal routines of the “Mathematica” computer program and the results obtained for the specific set of parameters are plotted in Figure 6.1.

The effect of anisotropic temperature was also checked (taking the ratio T_{\parallel}/T_{\perp} equal to 2 and 1/2 for both populations, not shown). The calculations were in this situation more time consuming and the final effect was qualitatively in accord with the results shown e.g. by Böstrom 2003, [18]. The systematic investigation of such effects is currently out of scope of this work, but is planned to be published elsewhere.

Bibliography

- [1] Aikio, A. T., V. A. Sergeev, M. A. Shukhtina, L. I. Vagina, V. Angelopoulos, G. D. Reeves, Characteristics of pseudobreakups and substorms observed in the ionosphere, at geosynchronous orbit and in the midtail, *J. Geophys. Res.*, *104*, 12263, 1999.
- [2] Akasofu, S.-I., S. Chapman, The development of the main phase of magnetic storms, *J. Geophys. Res.*, *68*, 125, 1963.
- [3] Akasofu, S.-I., The development of the auroral substorm, *Planet. Space Sci.*, *12/4*, 273, 1968.
- [4] Akasofu, S.-I., What is a magnetospheric substorm, in *Proceedings of the A.G.U. Chapman Conference "Magnetospheric substorms and related plasma phenomena"*, Los Alamos Scientific Laboratory, 1978, Astrophysics and Space Science Library Vol. 78, D. Reidel Publishing Company, 447, 1980.
- [5] Andersson, L., N. Ivchenko, J. Clemmons, A.A. Namgaladze, B. Gustavsson, J.E. Wahlund, L. Eliasson, and R.Y. Yurik, Electron signatures and Alfvén waves, *J. Geophys. Res.*, *107*(A9), doi:10.1029/2001JA900096, 2002.
- [6] Angelopoulos, V., C. Kennel, C. F. Coroniti, F. V. Pellat, M. G. Kivelson et al., Statistical Characteristics of Bursty Bulk Flow Events, *J. Geophys. Res.*, *99*, 21257, 1994.
- [7] Axford, W.I., Viscous interaction between the solar wind and Earth's magnetopause, *Planet. Space Sci.*, *12*, 45, 1964.
- [8] Baker, D. N., T. J. Pulkkinen, V. Angelopoulos, W. Baumjohann, R. L. McPherron, Neutral line model of substorms: Past results and recent view, *J. Geophys. Res.*, *101*, 12975, 1996.
- [9] Baumjohann, P. Stauning et al., Spatial and temporal characteristics of impulsive structure of magnetospheric substorm, *J. Geophys. Res.*, *60*, 186, 1986.
- [10] Belian, R. D., D. N. Baker, E. W. Hones, P. R. Highbie, High-energy proton drift echoes: Multiple peak structure, *J. Geophys. Res.*, *89*, 9101, 1984.
- [11] Birmingham, T. J., The effects of pressure anisotropy on Birkeland currents in dipole and stretched magnetospheres *J. Geophys. Res.*, *97*, 3919, 1992.
- [12] Birn, J., M. Hesse, Details of current disruption and diversion in simulations of magnetotail dynamics, *J. Geophys. Res.*, *101*, 15345, 1996.
- [13] Birn, J., M. F. Thomsen, J. E. Borovsky, G. D. Reeves, D. J. McComas et al., Substorm electron injections: Geosynchronous observations and test particle simulations, *J. Geophys. Res.*, *103*, 9235, 1998.
- [14] Birn, J., M. Hesse, G. Haerendel, W. Baumjohann, K. Shiokawa, Flow braking and the substorm current wedge, *J. Geophys. Res.*, *104*, 19895, 1999.

- [15] Blecki, J., B. Nikutowski, P. Koperski, B. Popielawska, K. Kossacki, S.A. Romanov, S.P. Savin, "ELF plasma waves in hot and cold plasma fluxes observed by prognoz-8 in the magnetospheric tail", *Annales Geophysicae*, 12, 1006, 1994.
- [16] Blecki, J., D. G. Sibeck (editors), Acceleration and heating in the magnetosphere, *Proceedings of the COSPAR Colloquium on Acceleration and Heating in the Magnetosphere, held in Konstancin Jeziorna, Poland, 5-10 February, 2001*, *Adv. Space Res.*, 30/7, 2002.
- [17] Borovsky, J. E., Auroral arc thickness as predicted by various theories, *J. Geophys. Res.*, 98, 6101, 1993.
- [18] Böstrom, R., Kinetic and space charge control of current flow and voltage drops along the magnetic flux tubes: Kinetic effects, *J. Geophys. Res.*, 108, 8004, 2003.
- [19] Böstrom, R., Kinetic and space charge control of current flow and voltage drops along the magnetic flux tubes: Space charge effects, *J. Geophys. Res.*, 109, 208, 2004.
- [20] Büchner, J., L. M. Zelenyi, Regular and chaotic charged particle motion in magnetotaillike field reversals, 1, Basic theory of trapped motion, *J. Geophys. Res.*, 94, 11821, 1989.
- [21] Cattell, C., J. Dombeck, A. Keiling, J. Wygant, R. Bergmann et al., Comparison of solitary waves and wave packets observed at plasma sheet boundary to results from the auroral zone, *Phys. Chem. Earth*, 26/1-3, 97, 2001.
- [22] Chapman, S., N. Watkins, Avalanching and self-organized criticality, a paradigm for geomagnetic activity?, *Space Sci. Rev.* 95/1-2, 293, 2001.
- [23] Chaston, C. C., J. W. Bonnell, L. M. Peticolas, C. W. Carlson, J. P. McFadden, Driven Alfvén waves and electron acceleration: A FAST case study, *Geophys. Res. Lett.*, 29, doi:10.1029/2001GL013842, 2002.
- [24] Chen, J., Nonlinear dynamics of charged particles in the magnetotail, *J. Geophys. Res.*, 97, 15011, 1992.
- [25] Chen, J., P. J. Palmadesso, Chaos and nonlinear dynamics of single-particle orbits in magnetotaillike magnetic field, *J. Geophys. Res.*, 91, 1499, 1986.
- [26] Cheng, C. Z., A. T. Y. Lui, Kinetic ballooning instability for substorms onset and current disruption observed by AMPTE/CCE *Geophys. Res. Lett.*, 25, 4091, 1998.
- [27] Cheng, C., Z., Physics of substorm growth phase, onset and dipolarization, *Space Sci. Rev.* 113, 207, 2004.
- [28] Chiu, Y. T., M. Schultz, Self-consistent particle and parallel electrostatic field distributions in the magnetospheric- ionospheric auroral region, *J. Geophys. Res.*, 83, 629, 1978.
- [29] Christon, S. P., D. J. Williams, D. G. Mitchell, L. A. Frank, C. Y. Huang, Spectral characteristics of plasma sheet ion and electron populations during undisturbed geomagnetic conditions, *J. Geophys. Res.*, 94, 13409, 1989.
- [30] Christon, S. P., D. J. Williams, G. Mitchell, C. Y. Huang, L. L. Frank, Spectral characteristics of plasma sheet ion and electron populations during disturbed geomagnetic conditions *J. Geophys. Res.*, 96, 1, 1991.
- [31] LeContel, O., R. Pellat, A. Roux, Self-consistent quasi- static radial transport during the substorm growth phase *J. Geophys. Res.*, 106, 10929, 2000.

- [32] LeContel, O., R. Pellat, A. Roux, Self-consistent quasi- static parallel electric field associated with substorm growth phase, *J. Geophys. Res.*, *106*, 10817, 2000.
- [33] LeContel, O., A. Roux, S. Perraut, R. Pellat, O. Holter et al., Possible control of plasma transport in the near- Earth plasma sheet via current-driven Alfvén waves ($f \approx f_{H+}$), *J. Geophys. Res.*, *106*, 10817, 2001.
- [34] Chun, F. K., C. T. Russell, Field-aligned currents in the inner magnetosphere: Control by geomagnetic activity, *J. Geophys. Res.*, *102*, 2261, 1997.
- [35] Delcourt, D. C., J.-A. Sauvaud, A. Pedersen, Dynamics of single-particle orbits during substorm expansion phase, *J. Geophys. Res.*, *95*, 20853, 1990.
- [36] Delcourt, D. C., J.-A. Sauvaud, R. F. Martin, T. E. Moore, On the nonadiabatic precipitation of ions from the near-Earth plasma sheet, *J. Geophys. Res.*, *101*, 17409, 1996.
- [37] Delcourt, D. C., Particle acceleration by inductive electric fields in the inner magnetosphere, *J. Atm, Sol.- Terr. Phys.*, *64*, 551, 2002.
- [38] Dendy, R. O., B. M. Harvey, M. O'Brien, Fokker-Planck modeling of auroral wave-particle acceleration, *J. Geophys. Res.*, *100*, 21973, 1995.
- [39] Dors, E. E., C. A. Kletzing, Effects of suprathermal tails on auroral electrodynamics, *J. Geophys. Res.*, *104*, 6783, 1999.
- [40] Dungey, J. W., Interplanetary magnetic field and the auroral zones, , *Phys. Rev. Lett.*, *6*, 47, 1961.
- [41] Ebihara, Y., M. Ejiri, Numerical simulation of the ring current: Review, *Space Sci. Rev.*, *105/1-2*, 377, 2003.
- [42] Elphinstone, R. D., D. J. Hearn, L. L. Cogger, J. S. Murphree, H. Singer et al., Observations in the vicinity of substorm onset: implication for the substorm processes, *J. Geophys. Res.*, *100*, 7937, 1995.
- [43] Ergun, R. E., C. W. Carlson, J. P. McFadden, F. S. Mozer, G. T. Delory et al., FAST satellite observations of large-amplitude solitary structures, *Geophys. Res. Lett.*, *25*, 2041, 1998.
- [44] Erickson, G. M., N. C. Maynard, W. J. Burke, G. R. Wilson, M. A. Heinmann, Electromagnetics of substorm onsets in the near-geosynchronous plasma sheet, *J. Geophys. Res.*, *105*, 25265, 2000.
- [45] McFadden, J. P., C. W. Carlsson, R. E. Ergun, Microstructure of the auroral acceleration region as observed by FAST, *J. Geophys. Res.*, *104*, 14453, 1999.
- [46] Fairfield, D. H., R. P. Lepping, E. W. Hones, Jr., S. J. Blame, and J. R. Asbridge, Simultaneous measurements of magnetotail dynamics by IMP spacecraft, *J. Geophys. Res.*, *86*, 1396, 1981.
- [47] Fairfield, D. H., T. Mukai, M. Brittnacher, G. D. Reeves, S. Kokubun et al., Earthward Flow Bursts in the Inner Magnetotail and Their Relation to Auroral Brightenings, AKR Intensifications, Geosynchronous Particle Injections and Magnetic Activity, *J. Geophys. Res.*, *104*, 355, 1999.

- [48] Feraudy, de, H., J. Hanasz, R. Schreiber, G. Parks, M. Brittnacher et al., AKR bursts and substorm field line excitation, *Phys. Chem. Earth*, 26/1-3, 151, 2001.
- [49] Fok, M.-C., T. E. Moore, D. C. Delcourt, Modeling of inner plasma sheet and ring current during substorms, *J. Geophys. Res.*, 104, 14557, 1999.
- [50] Frank, L. A., K. L. Ackerson, Observations of charged particles precipitations in the auroral zone, *J. Geophys. Res.*, 76, 3612, 1971.
- [51] Frank, L. A., R. L. McPherron, R. J. DeCoster, B. G. Burek, K. L. Ackerson et al., Field-Aligned currents in the Earth's magnetotail, *J. Geophys. Res.*, 86, 687, 1981.
- [52] Frank, L. A., W. R. Paterson, J. B. Sigwarth, S. Kokubun, Observations of magnetic field dipolarization during auroral substorm onset, *J. Geophys. Res.*, 105, 15897, 2000.
- [53] Frank, L. A., W. R. Paterson, J. B. Sigwarth, T. Mukai, Observations of plasma sheet dynamics earthward of the onset with the Geotail spacecraft, *J. Geophys. Res.*, 106, 18823, 2001.
- [54] Friedel, R. H. W., A. Korth, G. Kremser, Substorm onsets observed by CRRES: Determination of energetic particle source regions *J. Geophys. Res.*, 101, 13137, 1996.
- [55] Friedel, R. H. W., H. Korth, M. G. Henderson, M. F. Thomsen, J. D. Scudder, Plasma sheet access to the inner magnetosphere, *J. Geophys. Res.*, 106, 5845, 2001.
- [56] Friedrich, E., J. C. Samson, I. Voronkov, G. Rostoker, Dynamics of the substorm expansive phase, *J. Geophys. Res.*, 106, 13145, 2001.
- [57] Fujimoto, M., T. Sugiyama, T. Mukai, T. Tamamoto, Y. Saito et al., Highly collimated electron beams in the dawn-flank of the magnetotail, *Phys. Chem. Earth*, 22, 645, 1997.
- [58] Gonzales, W. D., J. A. Joselyn, Y. Kamide, H. W. Kroehl, G. Rostoker, et al., What is a geomagnetic storm?, *J. Geophys. Res.*, 99, 5771, 1994.
- [59] Haerendel, G., Buchert, S., La Hoz, C., Raaf, B., Rieger, E., On proper motion of auroral arcs, *J. Geophys. Res.*, 98, 6087, 1993.
- [60] Hasegawa, A., K. Mima, M. Duong-van, Plasma distribution function in a suprathermal radiationfield, *Phys. Rev. Lett.*, 54, 2608, 1985.
- [61] Holter, O., C. Altman, A. Roux, S. Perraut, A. Pedersen et al., Characterization of low frequency oscillations at substorm breakup, *J. Geophys. Res.*, 100, 19109, 1995.
- [62] Hones Jr., E. W., Plasma flow in the plasma sheet and its relation to substorms, *Radio Sci.*, 8, 979, 1973.
- [63] Hones Jr., E. W., Plasma flow in the magnetotail and its implications for substorm theories, in *Dynamics of the magnetosphere*, S. I. Akasofu (editor), D. Reidel Publ. Co., Dordrecht, Holland, 545, 1980.
- [64] Hones, E. W., Jr., D. N. Baker, S. J. Bame W. C. Feldman, J. T. Gosling et al., Structure of the magnetotail at 220 Re *Geophys. Res. Lett.*, 11, 5, 1984.
- [65] Hoshino, M., K. Hirade, T. Mukai, Strong electron heating and non-maxwellian behaviour in magnetic reconnection, *Earth Planet. Space*, 53, 627, 2001.

- [66] Horton, W., H. V. Wong, J. W. Van Dam, Substorm trigger conditions, *J. Geophys. Res.*, *104*, 22745, 1999.
- [67] Hull, A. J., J. W. Bonnell, F. S. Mozer, J. D. Scudder, A statistical study of large-amplitude parallel electric fields in the upward current region of the auroral acceleration region, *J. Geophys. Res.*, *108*, doi:10.1029/2001JA007540, 2003.
- [68] Ieda, A., S. Machida, T. Mukai, Y. Saito, T. Yamamoto et al., Statistical analysis of the plasmoid evolution with Geotail observations, *J. Geophys. Res.*, *103*, 4453, 1998.
- [69] Ijima, T., T. A. Potemra, Large-scale characteristics of field-aligned currents associated with substorms, *J. Geophys. Res.*, *83*, 599, 1978.
- [70] McIlwain, C. E., Direct measurements of particles producing visible auroras, *J. Geophys. Res.*, *65*, 2727, 1960.
- [71] Ivchenko, N., Alfvén Waves and Spatio-Temporal Structuring in the Auroral Ionosphere, *PhD Thesis, Alfvén Laboratory, Royal Institute of Technology, Stockholm*, 2002.
- [72] Ivchenko, N., P. Eglitis, M. Berthomier, L. Peticolas, A. Kullen et al., Electron signatures and Alfvén waves, *in preparation: <http://www.plasma.kth.se/~ivchenko/pc5.ps>*, 2002.
- [73] Iyemori, T., and D. R. K. Rao, Decay of the Dst field of geomagnetic disturbances after substorm onset and its implication to storm-substorm relation, *Ann. Geophysicae*, *14*, 608, 1996.
- [74] Jacquy, C., J.-A. Sauvaud, J. Dandouras, Location and propagation of the magnetotail current disruption during substorm expansion: analysis and simulation of an ISEE multi-onset event, *Geophys. Res. Lett.*, *18*, 389, 1991.
- [75] Jacquy, C., J.-A. Sauvaud, J. Dandouras, A. Korth, Tailward propagating cross-tail current disruption and dynamics of near-earth tail: a multipoint measurement analysis, *Geophys. Res. Lett.*, *20*, 983, 1993.
- [76] Janhunen, P., A. Olsson, The current-voltage relationship revisited: exact and approximate formulas with almost general validity for hot magnetospheric electrons for bi-Maxwellian and kappa distributions, *Annales Geophys.*, *16*, 292, 1998.
- [77] Janhunen, P., A. Olsson, New model of auroral acceleration: O-shaped potential structure cooperating with waves, *Annales Geophys.*, *18*, 526, 2000.
- [78] Johnstone, A. D., J. D. Winningham, Satellite observations of suprathermal electron bursts, *J. Geophys. Res.*, *87*, 2321, 1998.
- [79] Johnstone, A. D., D. M. Walton, R. Liu, D. A. Hardy, Pitch angle diffusion of low-energy electrons by whistler mode waves, *J. Geophys. Res.*, *98*, 5959, 1993.
- [80] Johnstone, A. D., N. J. Flowers, R. Liu, Observations in the equatorial region of field-aligned electron and ion distributions in the energy range 100 eV to 5 keV associated with substorm onsets, in *Proceedings of the Second International Conference on Substorms (ICS2): University of Alaska, Fairbanks, 1994*, 321, 1994.
- [81] Kamide, Y., W. Baumjohann, *Magnetosphere-Ionosphere Coupling*, Springer-Verlag, 1993.
- [82] Kaufmann, R. L., Substorm currents: growth phase and onset, *J. Geophys. Res.*, *92*, 7472, 1987.

- [83] Kennel, C. F., H. E. Petschek, Limit on stably trapped particle fluxes, *J. Geophys. Res.*, *71*, 1, 1966.
- [84] Kepko, L., M. G. Kivelson, Flow bursts, braking and Pi2 pulsations, *J. Geophys. Res.*, *106*, 1903, 2001.
- [85] Khazanov, G. V., M. W. Liemohn, E. N. Krivorutsky, T. E. Moore, Generalized kinetic description of a plasma in an arbitrary field-aligned energy structure *J. Geophys. Res.*, *103*, 6871, 1998.
- [86] Kivelson, M. G., C. T. Russell (editors), *Introduction to SPACE PHYSICS*, Cambridge University Press, 1995.
- [87] Kletzing, C. A., J. D. Scudder, Auroral-plasma sheet electron anisotropy, *Geophys. Res. Lett.*, *26*, 971, 1999.
- [88] Kletzing, C. A., S. Hu, Alfvén Wave Generated Electron Time Dispersion, *Geophys. Res. Lett.*, *28*, 693, 2001.
- [89] Klumpar, D. M., J. M. Quinn, E. G. Shelley, Counter-streaming electrons at the geomagnetic equator near 9 R_E , *Geophys. Res. Lett.*, *15*, 1295, 1988.
- [90] Knight, S., Parallel electric fields, *Planet. Space Sci.*, *21*, 741, 1973.
- [91] Knudsen, D. J., J.H. Clemmons, J.-E. Wahlund, Correlation between core ion energization, suprathermal electron bursts, and broadband ELF plasma waves, *J. Geophys. Res.*, *103*, 4171, 1998.
- [92] Klimov, S.I., S. Romanov, E. Amata, J. Blecki, J. Büchner et al., ASPI experiment: measurements of fields and waves onboard of the INTERBALL-TAIL mission, in *INTERBALL Mission and Payload*, CNES-IKI-RSA, pp. 120-152, Toulouse, 1995.
- [93] Klimov, S. I., S. Romanov, E. Amata, J. Blecki, J. Büchner et al., ASPI experiment: measurements of fields and waves onboard of the INTERBALL-1 spacecraft, *Annales Geophysicae*, *15(5)*, 514, 1997.
- [94] Koperski, P., B. Popielawska, "Observations of cold electrons and strong low-frequency electric field fluctuations close to the neutral sheet at R=8 R_E ", *Proceedings of 1-st International Conference on Substorms*, ESA SP-335, Nodvijk, Holland, 369-364, 1992.
- [95] Koperski, P., J.-A. Sauvaud, S. Romanov, The electron mixing and acceleration signatures as seen near the cusp and on the flank, *Adv. Space Res.*, *30/7*, 1731, 2002.
- [96] Korth, H., F. Thomsen, J. E. Borovsky, D. J. McComas, Plasma Sheet access to geosynchronous orbit, *J. Geophys. Res.*, *104*, 25047, 1999.
- [97] Lepping, R. P., M. Acuna, R. Burlaga, W. Farrell, J. Slavin et al., The WIND magnetic field investigation, *Space Sci. Rev.* *71*, 207, 1995.
- [98] Lin, R. P., et al., A Three-dimensional Plasma and Energetic Particle Investigation for the Wind Spacecraft, in *Global Geospace Mission*, C. T. Russell (editor), Kluwer Acad. Publ., Dordrecht, Holland, 125, 1995.
- [99] Liou, K., C.-I. Meng, A. T. Y. Lui, P. T. Newell, M. Brittnacher, G. Parks, G. D. Reeves, R. R. Anderson, K. Yumoto, On relative timing in substorm onset signatures, *J. Geophys. Res.*, *104*, 22807, 1999.

- [100] Liou, K., C.-I. Meng, P. T. Newell, K. Takahashi, S.-I. Ohtani, A. T. Y. Lui, Evaluation of low-latitude Pi2 pulsations as indicators of substorm onset using Polar ultraviolet imagery *J. Geophys. Res.*, *105*, 2495, 2000.
- [101] Liou, K., C.-I. Meng, P. T. Newell, A. T. Y. Lui, G. D. Reeves, R. D. Belian, Particle injections with auroral expansions, *J. Geophys. Res.*, *106*, 5873, 2001.
- [102] Lopez, R. E., A. T. Y. Lui, A multisatellite case study of the expansion of a substorm current wedge in the near-Earth magnetotail, *J. Geophys. Res.*, *95*, 8009, 1990.
- [103] Lotko, W., A. V. Streltsov, C. W. Carlson, Discrete auroral arc, electrostatic shock and suprathermal electrons powered by dispersive, anomalously resistive field line resonances, *Geophys. Res. Lett.*, *25*, 4449, 1998.
- [104] Lui, A. T. Y., A. Mankofsky, C.-L. C. K. Papadopoulos, C. S. Wu, A current disruption mechanism in the neutral sheet: a possible trigger for substorm expansions, *Geophys. Res. Lett.*, *17*, 745, 1990.
- [105] Lui, A. T. Y. , R. E. Lopez, B. J. Anderson, K. Takahashi, L. J. Zanetti et al., Current disruption in the near-Earth neutral sheet region, *J. Geophys. Res.*, *97*, 1461, 1992.
- [106] Lui, A. T. Y., Current disruption in the earth's magnetosphere: Observations and models, *J. Geophys. Res.*, *101*, 13067, 1996.
- [107] Lui, A. T. Y., K. Liou, M. Nose, S. Ohtani, D. J. Williams et al., Near-Earth Dipolarization: Evidence for a Non-MHD Processes, *Geophys. Res. Lett.*, *26*, 2905, 1999.
- [108] Lui, A. T. Y., A multiscale model of substorms, *Space Sci. Rev.*, *95/1-2*, 325, 2001.
- [109] Lui, A. T. Y., Current controversies in magnetospheric physics, *Rev. Geophys.*, *39/4*, 535, 2001.
- [110] Lui, A. T. Y., Potential plasma instabilities for substorm expansion onsets, *Space Sci. Rev.* *113*, 127, 2004.
- [111] Lundin, R., I. Sandahl, Some characteristics of the parallel electric field acceleration of electrons over discreteauroral arcs as observed from two rocket flights, in *Symposium on European Rocket Research*, vol.135 of *Eur. Space Agency Spec. Publ.*, *135*, 125, 1978.
- [112] Lundin, R., L. Eliasson, Auroral energization processes, *Annales Geophys.*, *9*, 202, 1991.
- [113] Lyons, L. R., Generation of large-scale regions of auroral currents, electric potentials, and precipitation by the divergence of the convection electric field, *J. Geophys. Res.*, *85*, 17, 1980.
- [114] Lysak, R. L., Electrodynamic coupling of the magnetosphere and ionosphere, *Space Sci. Rev.*, *52/1+2*, 33, 1990.
- [115] Machida, S., Y. Miyashita, A. Ieda, A. Nishida, T. Mukai et al., GEOTAIL observations of flow velocity and north-south magnetic field variations in the near and mid-distant tail associated with substorm onsets, *Geophys. Res. Lett.*, *26*, 635, 1999.
- [116] Maksimovic, M., V. Pierrard, J. Lemaire, A kinetic model of the solar wind with Kappa distributions in the corona, *Astron. Astrophys.*, *324*, 725 1997.
- [117] Marklund, G. T., T. Karlsson, Characteristics of the auroral particle acceleration in the upward and downward current regions, *Phys. Chem. Earth*, *26/1-3*, 81, 2001.

- [118] Martin, R. F. Jr., T. W. Speiser, a predicted energetic ion signature of a neutral line in the geomagnetic tail, *J. Geophys. Res.*, *93*, 11521, 1988.
- [119] Mauk, B. H., Generation of macroscopic magnetic field-aligned electric fields by the convection surge ion acceleration mechanism, *J. Geophys. Res.*, *94*, 8911, 1989.
- [120] Meng, C.-I., A. L. Snyder Jr., H. W. Kroehl, Observations of auroral westward travelling surges and electron precipitations, *J. Geophys. Res.*, *83*, 575, 1978.
- [121] Miller, J. A., J. Steinacker, Stochastic gyroresonant electron acceleration in a low-beta plasma. II. Implications of thermal effects in a solar flare plasma, *Astrophys. J.* *399*, 284, 1992.
- [122] Milovanov, A. V., L. M. Zelenyi, Functional background of the Tsallis entropy: “coarse-grained” systems and “kappa” distribution functions, *Nonlin. Processes in Geophys.*, *7*, 211, 2000.
- [123] Miyashita, Y., S. Machida, T. Mukai, Y. Saito, K. Tsuruda et al., A statistical study of variations in the near and mid-distant magnetotail associated with substorm onsets: GEOTAIL observations *J. Geophys. Res.*, *105*, 15913, 2000.
- [124] Miyake, W., R. Yoshioka, A. Matsuoka, T. Mukai, T. Nagatsuma, Low-frequency electric field fluctuations and field-aligned electron beams around the edge of an auroral acceleration region, *Annales Geophys.*, *19*, 389, 2001.
- [125] Mozer, F. S., C. A. Cattell, M. K. Hudson, R. L. Lysak, M. Temerin, et al. Satellite measurements and theories of auroral particle acceleration, *Space Sci. Rev.*, *27*, 155, 1980.
- [126] Mozer, F. S., A. Hull, Origin and geometry of upward parallel electric fields in the auroral acceleration region, *J. Geophys. Res.*, *106*, 5763, 2001.
- [127] Nagai, T., T. Mukai, T. Yamamoto, A. Nishida, S. Kokubun, et al., Plasma sheet pressure changes during the substorm growth phase, *Geophys. Res. Lett.*, *24*, 963, 1997.
- [128] Nagai, T., M. Fujimoto, Y. Saito, S. Machida, T. Terasawa, et al., Structure and dynamics of magnetic reconnection for substorm onsets with Geotail observations, *J. Geophys. Res.*, *103*, 4419, 1998.
- [129] Nakamura, R., W. Baumjohann, M. Brittnacher, V. A. Sergeev, M. Kuybyshkin et al., Flow bursts and auroral activations: Onset timing and foot point location, *J. Geophys. Res.*, *106*, 10777, 2001.
- [130] Nakamura, R., W. Baumjohann, R. Schodel, M. Brittnacher, V. A. Sergeev et al., Earthward flow bursts, auroral streamers, and small expansions *J. Geophys. Res.*, *106*, 10791, 2001.
- [131] Nishikawa, K. I., Global particle simulation study of substorm onset and particle acceleration, *Space Sci. Rev.*, *95*, 361, 2001.
- [132] Oguti, T., Rotational deformations and related drift motions of auroral arcs, *J. Geophys. Res.*, *79*, 3861, 1974.
- [133] Ohtani, S., S. Kokubun, C. T. Russell, Radial expansion of the tail current disruption during substorm: A new approach to the substorm onset region, *J. Geophys. Res.*, *97*, 3129, 1992.
- [134] Ohtani, S., Substorm trigger processes in the magnetotail: recent observations and outstanding issues, *Space Sci. Rev.*, *95/1-2*, 347, 2001.

- [135] Ohtani, S., R. Yamaguchi, H. Kawano, F. Creutzberg, J.B. Sigwarth et al., Does the braking of the fast plasma flow trigger a substorm?: A study of the August 14, 1996, event, *Geophys. Res. Lett.*, *29*, doi:10.1029/2001GL013785, 2002.
- [136] Olbert, S., Summary of experimental results from M.I.T. detector on IMP-1, in *Physics of Magnetosphere*, R. L. Carlovillano (editor), D. Reidel, Norwell, Mass., 1968.
- [137] Olsson, J., Pi2 pulsations and substorm onsets: A review *J. Geophys. Res.*, *104*, 17,499, 1999.
- [138] Onsager, T. G., M. F. Thomsen, J. T. Gosling, S. J. Bame, Electron distribution in the plasma sheet boundary layer: Time-of-flight effects, *Geophys. Res. Lett.*, *17*, 1837, 1990.
- [139] Opgenoorth, H. J., and R. J. Pellinen, The reaction of the global convection electrojetsto the onset and expansion of the substorm current wedge, in *Substorms-4*, Eds. S. Kokubun and Y. Kamide, Co-publication: Terra Scientific Publishing Company (Tokyo)/Kluwer Academic Publishers (Dordrecht) 663, 1998.
- [140] Parks, G., L. J. Chen, M. McCarthy, D. Larson, R. P. Lin et al., Reply, *Geophys. Res. Lett.*, *26*, 2639, 1999.
- [141] Pierrard, V., New model of magnetospheric current-voltage relationship, *J. Geophys. Res.*, *101*, 2669, 1996.
- [142] Perraut, S., A. Morane, A. Roux, A. Pedersen, R. Schmidt et al., Characterization of small scale turbulence observed at substorm onsets: relationships with parallel acceleration of particles, *Adv. Space Res.*, *13/4*, (4)217, 1993.
- [143] Perraut, S., O. LeContel, A. Roux, A. Pedersen Current-driven electromagnetic ion cyclotron instability at substorm onset, *J. Geophys. Res.*, *105*, 21097, 2000.
- [144] Perraut, S., O. LeContel, A. Roux, R. Pellat, A. Korth et al., Disruption of parallel current at substorm breakup, *Geophys. Res. Lett.*, *27*, 4041, 2000.
- [145] Petrukovich, A. A., V. A. Sergeev, L. M. Zelenyi, T. Mukai, T. Yamamoto, S. Kokubun, K. Shiokawa, C. S. Deehr, E. Y. Budnik, J. Büchner, A. O. Fedorov, V. P. Grigorieva, T. J. Hughes, N. F. Pissarenko, S. A. Romanov, I. Sandahl, Two spacecraft observations of a reconnection pulse during an auroral breakup, *J. Geophys. Res.*, *103*, 47, 1998.
- [146] McPherron, R. L., Substorm related changes in the geomagnetic tail: The growth phase, *Planet. Space Sci.*, *20*, 1521, 1972.
- [147] McPherron, R. L., D. N. Baker, L. F. Bargatze, C. R. Clauer, R. E. Holzer, IMF control of geomagnetic activity, *Adv. Space Res.*, *8(9)*, 71, 1988.
- [148] Popielawska, B., P. Koperski, D. Zwolakowska, R. Lundin, A. V. Zakharov, On the low energy electrons in the magnetotail *Adv. Space Res.*, *13/4*, (4)53, 1993.
- [149] Popov, G. V., V. I. Degtjarev, S. S. Sheshukov, A. D. Johnstone, Influence of geostationary spacecraft charging on measurements of low energy (0.05 - 20 KeV) electron spectra, *Adv. Space Res.*, *20/3*, 449, 1997.
- [150] Press, W. H., S. A. Teukolsky, W. T. Wetterling, B. P. Flannery *Numerical Recipes in Fortran 77: the art of scientific computing*, Second Edition, 2001.

- [151] Pritchett, P. L., F. V. Coroniti, Localized convection flows and field-aligned current generation in a kinetic model of near-Earth plasma sheet, *Geophys. Res. Lett.*, *27*, 3161, 2000.
- [152] Pulkkinen, T. I., D. N. Baker, R. J. Pellinen, J. Büchner, H. E. J. Koskinen et al., Particle scattering and current sheet stability in the geomagnetic tail during the substorm growth phase *J. Geophys. Res.*, *97*, 19283, 1992.
- [153] Reeves, G. D., R. D. Belian, and T. A. Fritz, Numerical tracing of energetic particle drifts in a model magnetosphere, *J. Geophys. Res.*, *96*, 13,997, 1991.
- [154] Reeves G. D., G. Kettmann, T. A. Fritz and R. D. Belian, Further investigation of the CDAW 7 substorm using geosynchronous Particle Data: multiple injections and their implications, *J. Geophys. Res.*, *97*, 6417, 1992.
- [155] Reeves, G. D., New perspectives on substorm injections, *Proceedings of the Fourth International Conference on Substorms, ICS-4, Hamanako, Japan, March 1998*, 1998.
- [156] Ronmark, K., Auroral current voltage relation, *J. Geophys. Res.*, *107*(A12), doi:10.1029/2002JA009294, 2002.
- [157] Rostoker, G., S.-I. Akasofu, J. C. Foster, R. A. Greenwald, Y. Kamide, et al., Magnetospheric substorms-definition and signatures, *J. Geophys. Res.*, *85*, 1663-1668, 1980.
- [158] Rostoker, G., On the place of the pseudo-breakup in a magnetospheric substorm, *Geophys. Res. Lett.*, *25*, 217, 1998.
- [159] Rostoker, G., Identification of substorm expansive phase onset *J. Geophys. Res.*, *107*(A7), doi:10.1029/2001JA003504, 2002.
- [160] Roux, A., S. Perraut, P. Robert, A. Morane, A. Pedersen et al. Plasma instability related to the westward travelling surge, *J. Geophys. Res.*, *96*, 17697, 1991.
- [161] Safrankova, J., Z. Nemecek (editors), Papers of the *NATO Advanced Research Workshop "Coordinated Studies of the Solar Wind-Magnetosphere-Ionosphere Interaction: INTERBALL Observations"*, *Czech. J. Phys.*, *49*, 1999.
- [162] Sato, T., T. Ijima, Primary sources of large-scale Birkeland currents *Space Sci. Rev.*, *24*, 347, 1979.
- [163] Safargaleev, V. V., A. E. Kozlovsky, S. V. Osipenko, V. R. Tagirov, Azimuthal expansion of high-latitude auroral arcs *Annales Geophys.*, *21*, 1793, 2003.
- [164] Samson, J. C., D. D. Wallis, T. J. Hughes, F. Creutzberg, J. M. Ruohoniemi et al., Substorm Intensifications and Field Line Resonances in the Nightside Magnetosphere, *J. Geophys. Res.*, *97*, 8495, 1992.
- [165] Sauvaud, J.-A., J. R. Winckler, Dynamics of plasma, energetic particles, and field near synchronous orbit in the nighttime sector during magnetospheric substorms, *J. Geophys. Res.*, *85*, 2043, 1980.
- [166] Sauvaud, J.-A., A. Saint-Marc, I. Dandouras, H. Reme, A. Korth et al., A Multisatellite study of the plasma sheet dynamics at substorm onset, *Geophys. Res. Lett.*, *11*, 500, 1984.
- [167] Sauvaud, J.-A., J. P. Treilhou, A. Saint-Marc, J. Dandouras, H. Reme, Large scale response of the magnetosphere to a southward turning of the interplanetary magnetic field, *J. Geophys. Res.*, *92*, 2365, 1987.

- [168] Sauvaud, J.-A., H. Barthe, C. Aoustin, J. J. Thocaven, J. Rouzaud, J. Bouyssou, M. Casignol, P. Souleille, J. M. Bosqued, T. Beutier, J. Crasnier, J. Dandouras, C. Jacquey, H. Reme, The electron experiment: a top-hat spectrometer for the tail probe, in *INTERBALL Mission and Payload*, CNES-IKI-RSA, pp. 120-152, Toulouse, 1995.
- [169] Sauvaud, J.-A., C. Jacquey, T. Beutier, C. Owen, R. P. Lepping, C. T. Russell, R. J. Belian, Large scale dynamics of the magnetospheric tail induced by substorms: a multisatellite study, *J. Geomag. Geoelectr.*, *48*, 675, 1996.
- [170] Sauvaud, J.-A., P. Koperski, T. Beutier, H. Barthe, C. Aoustin, J.J. Thocaven, J. Rouzaud, E. Penou, O. Vaisberg, N. Borodkova, The INTERBALL-Tail ELECTRON experiment: initial results on the low-latitude boundary layer of the dawn magnetosphere, *Annales Geophysicae*, *15(5)*, 587, 1997.
- [171] Sauvaud, J.-A., D. Popescu, D. C. Delcourt, G. K. Parks, M. Brittnacher et al., Sporadic plasma sheet ion injections into the high altitude auroral bulge: satellite observations, *J. Geophys. Res.*, *104*, 28565, 1999.
- [172] Schlickeiser, R., γ -ray evidence for galactic in-situ electron acceleration *Astron. Astrophys.*, *319*, L5, 1997.
- [173] Schriver, D., M. Ashour-Abdalla, R. L. Richard, On the origin of the ion-electron temperature difference in the plasma sheet, *J. Geophys. Res.*, *103*, 14879, 1998.
- [174] Sergeev, V. A., E. M. Sazhina, N. A. Tsyganenko, J. A. Lundblad, F. Soras, Pitch angle scattering of energetic protons in the magnetotail current sheet as the dominant source of their anisotropy: precipitation into the nightside magnetosphere *Planet. Space Sci.*, *31*, 1147, 1983.
- [175] Sergeev, V. A., R. J. Pellinen, T. Bosinger, W. Baumjohann, P. Stauning et al., Spatial and temporal characteristics of impulsive structure of magnetospheric substorm, *J. Geophys. Res.*, *60*, 186, 1986.
- [176] Bosinger, T., R. D. Belian, G. D. Reeves, T. E. Cayton, Drifting holes in the energetic electron flux at geosynchronous orbit Following Substorm onset *J. Geophys. Res.*, *97*, 6541, 1992.
- [177] Sergeev, V. A., T. I. Pulkkinen, R. J. Pellinen, Coupled mode scenario for the magnetospheric dynamics, *J. Geophys. Res.*, *101*, 13047, 1996.
- [178] Sergeev, V. A., M. A. Shukhtina, R. Rasinkangas, A. Korth, G.D. Reeves, H. J. Singer, M. F. Thomsen, L. I. Vagina, Event study of deep energetic particle injections during substorm, *J. Geophys. Res.*, *103*, 9217, 1998.
- [179] Sergeev, V. A., K. Liou, C.-I. Meng, P. T. Newell, M. Brittnacher, G. Parks, G. D. Reeves, Development of auroral streamers in association with localized impulsive injections to the inner magnetotail, *Geophys. Res. Lett.*, *26*, 417, 1999.
- [180] Sergeev, V. A., J.-A. Sauvaud, D. Popescu, R. A. Kovrazhkin, K. Liou, P. T. Newell, M. Brittnacher, G. Parks, R. Nakamura, T. Mukai, G. D. Reeves, Multiple-spacecraft observations of a narrow transient plasma jet in the Earth's plasma sheet, *Geophys. Res. Lett.*, *27*, 851, 2000.
- [181] Sergeev, V. A., W. Baumjohann, K. Shiokawa, Bi-directional electron distributions associated with near-tail flux transport, *Geophys. Res. Lett.*, *28*, 3813, 2001.

- [182] Shiokawa, K., W. Baumjohann, G. Haerendel, Braking of high-speed flows in the near-Earth tail, *Geophys. Res. Lett.*, *24*, 1179, 1997.
- [183] Shiokawa, K., W. Baumjohann, G. Haerendel, H. Fukunishi, High- and low-altitude observations of adiabatic parameters associated with auroral electron acceleration, *J. Geophys. Res.*, *105*, 2541, 2000.
- [184] Smets, R., D. Delcourt, D. Fontaine, R. F. Martin Jr., Structure of electron and ion distribution functions near reconnection line *J. Geophys. Res.*, *101*, 24837, 1996.
- [185] Smets, R., D. Delcourt, D. Fontaine, Ion and electron distribution functions in the distant magnetotail: Modeling of Geotail observations, *J. Geophys. Res.*, *103*, 2407, 1998.
- [186] Smets, R., D. Delcourt, J.-A. Sauvaud, P. Koperski, Electron pitch angle distributions following the dipolarization phase of a substorm, *J. Geophys. Res.*, *104*, 14571, 1999.
- [187] Song, Y., R. L. Lysak, The physics of the auroral dynamo regions and auroral particle precipitations *Phys. Chem. Earth*, *26/1-3*, 33, 2001.
- [188] Southwood, D. J., M. G. Kivelson, An approximate description of field-aligned currents in a planetary magnetic field, *J. Geophys. Res.*, *96*, 67, 1991.
- [189] Speiser, T. W., Particle trajectory in model current sheets, 1, Analytical solutions, *J. Geophys. Res.*, *70*, 4219, 1965.
- [190] Stasiewicz, K., A global model of gyroviscous field line merging at the magnetopause, *J. Geophys. Res.*, *96*, 77, 1991.
- [191] Strangeway, R. J., R. E. Ergun, C. W. Carlson, J. P. McFadden, G. T. Delory et al., Accelerated electrons as the source of Auroral kilometric radiation *Phys. Chem. Earth*, *26/1-3*, 145, 2001.
- [192] Summers, d., R. M. Thorne, The modified plasma dispersion function, *Phys. Fluids B* **3**, 1835, 1991.
- [193] Summers, D., Ma C.-Y., Rapid acceleration of electrons in the magnetosphere by fast-mode MHD waves *J. Geophys. Res.*, *105*, 15887, 2000.
- [194] Takahashi, K., L. J. Zanetti, R. E. Lopez, R. W. McEntire, T. A. Potemra et al., Disruption of the magnetotail current sheet observed by AMPTE/CCE, *Geophys. Res. Lett.*, *14*, 1019, 1987.
- [195] Temerin, M., K. Cerny, W. Lotko, F. S. Mozer, Observations of double layers and solitary waves on auroral zone field lines, *Phys. Rev. Lett.*, *48*, 1175, 1982.
- [196] Thomsen, M. F., J. Birn, J. E. Borovsky, K. Morzinski, D. J. McComas, G. B. Reeves, Two-satellite observations of substorm injections at geosynchronous orbit, *J. Geophys. Res.*, *106*, 8405, 2001.
- [197] Treumann, R. A., Kinetic theoretical foundations of Lorentzian statistical mechanics, *Physica Scripta*, *59*, 19, 1999.
- [198] Treumann, R. A., Generalized-Lorentzian thermodynamics, *Physica Scripta*, *59*, 204, 1999.
- [199] Uozumi, T., K. Yumoto, H. Kawano, A. Yoshikawa, J. V. Olsson, S. I. Solovyev, E. F. Vershinin, Characteristics of energy transfer of Pi2 magnetic pulsations: Latitudinal dependence *Geophys. Res. Lett.*, *27*, 1619, 2000.

- [200] Vaivads, A., M. Andr e, S. Buchert, A. I. Ericksson, A. Olsson et al, What high altitude observations tell us about the auroral acceleration: A cluster/DMSP conjunction, *Geophys. Res. Lett.*, *30*, 1106, 2003.
- [201] Vasyliunas, V. M., A survey of low-energy electrons in the evening sector of the magnetosphere with OGO 1 and OGO 3, *J. Geophys. Res.*, *73*, 2839, 1968.
- [202] Vasyliunas, V. M., Mathematical model of magnetospheric convection and its coupling to the ionosphere, in *Particles and fields in the Magnetosphere*, B. McCormack (editor), D. Reidel Publ. Co., Dordrecht, Holland, 29, 1970.
- [203] Vasyliunas, V. M., Fundamentals of current disruption, in *Magnetospheric Physics*, T. A. Potemra (eds.), AGU Monograph, 28, 63, 1984.
- [204] Vogt, J., Alfvén wave coupling in the auroral current circuit *Surveys in Geophysics*, *23/4*, 335, 2002.
- [205] Walker, R. J., R. L. Richard, M. Ashour-Abdalla, The entry of solar wind ions into the magnetosphere, in *Physics of the Magnetopause*, P. Song, B. U. Ö. Sonnerup and M. Thomsen (editors), AGU Geophys. Monogr., Vol. 20, 311, 1995.
- [206] Wright, A. N., W. Allan, P. A. Damiano, Alfvén wave dissipation via electron energization *Geophys. Res. Lett.*, *30*, doi:10.29/2003GL017605, 2003.
- [207] Wygant, J. R., A. Keiling, C. A. Cattell, . L. Lysak, M. Temerin et al., Evidence for kinetic Alfvén waves and parallel electron energization at 4-6 R_E altitudes in the plasma sheet boundary layer, *J. Geophys. Res.*, *107*(A8), doi:10.1029/2001JA900113, 2002.
- [208] Yahnin, A., M. V. Malkov, V. A. Sergeev, R. J. Pellinen, O. Aulamo et al., *J. Geophys. Res.*, *99*, 4039-4051, 1994.
- [209] Yermolaev, Yu. I., A. O. Fedorov, O. L. Vaisberg, V. M. Balebanov, Yu. A. Obod, R. Jimenez, J. Fleites, L. Llera, A. N. Omelchenko, Ion distribution dynamics near the Earth's bow shock: first measurements with the 2D ion energy spectrometer CORALL on the INTERBALL/Tail-probe satellite, *Annales Geophysicae*, *15*(5), 533, 1997.
- [210] Zmuda, A. J., J. H. Martin, F. T. Heuring, Transverse magnetic disturbances at 1100 kilometers in the auroral region, *J. Geophys. Res.*, *71*, 5033, 1966.

Acknowledgments

I wish to extend my warmest thanks to everyone who has in any way helped me with preparing and finishing this work and encouraged me along the way.

I want to thank, first of all, Dr. Jean-André Sauvaud from C.E.S.R., Toulouse, France, for providing me with opportunity to learn from him, and for offering me an access to the Interball ELECTRON data. My thesis adviser, Dr. Barbara Popielawska, for her helpful comments and big patience, when I was extending my deadline. I have held helpful discussions on the magnetospheric physics with Christian Jacquey from C.E.S.R., Toulouse and with Ela Wodnicka, SRC Warszawa. I am also very thankful to the whole group working, under guidance of J.-A. Sauvaud, on the ELECTRON experiment. Thanks also for the data processing to J. Durand (CNES, Toulouse) and E. Penou (C.E.S.R.). Dr. S. Romanov (SRI, Moscow, Russia) for the magnetic data- without the MIF-M instrument I would certainly have nothing to do. Dr. Józef Juchniewicz, Space Research Center, Warszawa for various kinds of support and Dr. Lech Kruś, System Research Institute PAS and Hewlett-Packard Education group in Warszawa for the opportunities to find the additional source of finances.

This work would not even start without the geophysical data I was using to support the observations from Interball. The list of the institutes and of the individuals I wish to acknowledge is put below.

The list of individuals, that I wish to acknowledge is very long; I keep it in my heart and in memory, often accompanied with love. Of course, colleagues from the laboratories in Toulouse and in Warszawa, but also friends, who come from backgrounds other than physics: Majka Shephard has helped me with some English (but still all the errors being my fault), Piotr Malec, Anka Salwa, Ula Styczek, have offered me their time and friendship and with Krysia Hulewicz we have talking a lot on energy. There are two special ladies I want to thank, keeping them in my memory and in my heart: Ula Orłowska and Marta Wachowicz. I also thank my Mother and my Brother for everything. I wish also to thank His Holiness XIV Dalai Lama of Tibet for the sense of support when I was working upon my thesis, and to wish Him all the best. Similarly, I keep warm thoughts for Pope John Paul II for the lessons He gave us in His last days.

Finally, I want to acknowledge: *Prof G. Parks* for the data from WIND; *Los Alamos National Laboratory* (Dr. R. Belian) for the SOPA instrument data; Dr. Partick Newell at *JHU APL* for the usefull comments on the DMSP data. *Canadian Space Agency* for the magnetic and the optical data from CANOPUS chain of observatories (especially Dr. Fokke Creutzberg for the usefull and encouraging comments); *Danish Meteorological Institute* (in particular Dr. J. Watermann) and *Space Physics Research Laboratory at the University of Michigan* (Dr. R. Clauer) for the magnetic data from Greenland; *Prof. K. Yumoto from STEL, Nagoya, Japan*, for the magnetic data from MM210 magnetometer chain; *National Institute for Polar Research, Japan* (Dr. Akira Kadokura) for the magnetic data from Iceland and Syowa station; Dr. J.J.Schott from *EOST, Univ. de Strasbourg, France*, for the magnetic data from Port Aux Francais; the institutes who maintain the *IMAGE network* for the magnetic data; *SAMNET, the PPARC facility deployed by the University of York UK* for the magnetic data. I also would like to thank everyone providing the Internet global data services, in particular World Data Centers, NSSDC, SPIDR.

Podsumowanie wyników

Celem tej pracy było wyjaśnienie efektów obserwowanych w strumieniach nisko-energetycznych elektronów (od $\sim 100 eV$ do $\sim 2 keV$), w czasie poprzedzającym i podczas zdarzeń typu: iniekcja gorętszej plazmy i rozerwanie prądu, w bliskiej warstwie plazmowej magnetosfery ziemskiej.

W tym celu, jako podstawowe źródło danych wykorzystano obserwacje satelity Interball Tail. Analiza zjawisk geofizycznych związanych z subburzami magnetycznymi była częścią pracy o zasadniczym znaczeniu. Dotyczyła ona selekcji i interpretacji obserwacji z wielu stacji naziemnych oraz pochodzących z innych satelitów. Po analizie i wyborze przypadków z czterech miesięcy (od Października 1995 do Stycznia 1996) możliwe było zidentyfikowanie typowych, wielkoskalowych cech wybranej klasy zdarzeń.

Badano makroskopowe własności elektronowego składnika plazmy jak też mikroskopowe cechy jego funkcji rozkładu. Aby lepiej uwzględnić te własności, zastosowano między innymi podejście polegające na (nieliniowym) dopasowaniu modelowych funkcji do obserwowanych rozkładów mikroskopowych.

Główne wyniki tej pracy mogą być podsumowane następująco

- i Efekty obserwowane w podłużnych strumieniach nisko-energetycznych elektronów można przypisać dodatkowej populacji elektronów, chłodniejszej niż typowa dla warstwy plazmowej (temperatura poniżej $\sim 200 eV$) i uformowanej w przeciwbieżne wiązki wzdłuż pola magnetycznego. Zakres parametrów i występowanie czynią te elektrony potencjalnym magnetosferycznym odpowiednikiem dla “Rozbłysków Nadtermicznych Elektronów” (*ang. SupraThermal Electron Burst*, STEB) obserwowanych często poniżej rejonu przyspieszenia w strefie zorzowej (na wysokościach $\sim 1 - 3$ promieni ziemskich).
- ii Zaobserwowano oscylacje niskich częstotści typu Pc5 występujące w podłużnym strumieniu elektronów w czasie fazy wzrostu i począwszy od późnej fazy ekspansji subburzy. Chłodna populacja zanikała wraz z rozwojem fluktuacji pola magnetycznego w zakresie pulsacji Pi2 - Pc3. Następnie pojawiał się przejściowy i silniejszy (w przypadku subburzy), podłużny strumień energii kinetycznej skierowany do Ziemi. Oscylacje w zakresie Pc5 znaleziono również w danych magnetycznych. Identyfikacja oscylacji typu Pc5 w których uczestniczy populacja niskoenergetycznych elektronów w warstwie plazmowej jest nowym wynikiem, ważnym przy rozpatrywaniu przyspieszenia cząstek wzdłuż zorzowych linii pola magnetycznego.
- iii Pokazano, że nisko energetyczne elektrony poruszające się wzdłuż pola \vec{B} są w stanie modyfikować w pewnym zakresie (quasistatyczne) relacje prądowo-napięciowe w magnetosferycznym segmencie zorzowego obwodu prądowego (na wysokościach powyżej około 3 – 3.5 promieni ziemskich). Jest to quasistatyczny odpowiednik mechanizmu rozerwania prądu podłużnego poprzez fale Alfvéna generowane prądowo (zaproponowanego przez Perraut i in. 2000a, [143]). Mimo że mało znaczący w porównaniu z silnym przyspieszającym potencjałem na niskich wysokościach, efekt ten może być istotny w magnetosferze dla oscylacji o dużym okresie oraz dla generacji nadtermicznych elektronów (STEB) obserwowanych na niskich wysokościach na skrajach owalu zorzowego (np. Lotko i in. 1998, [103]; Ivchenko i in. 2002, [71], [72]).

iv Przedstawione obserwacje są ważne dla modelowania rozwoju subburz. Przede wszystkim, zidentyfikowane zjawiska magnetosferyczne odpowiadają bezpośrednio chwilom rozpoczęcia subburz, widzianych na Ziemi w tym samym sektorze czasu lokalnego. Po drugie, trwające przez 3 do 5 minut przejściowe strumienie energii, niesionej w kierunku Ziemi przez elektrony o energiach powyżej $\sim 1 \text{ keV}$, towarzyszą wzmożonej turbulencji pola magnetycznego w zakresie częstości Pi2 - Pc3, będącej oznaką rozerwania warstwy prądowej i/lub prądu podłużnego. Przejściowe strumienie odpowiadają zjawisku konwekcyjnego napływu gorącej plazmy (*ang. Convection Surge*), towarzyszącemu dipolaryzacji pola magnetycznego. Wreszcie, zanikanie nisko-energetycznych strumieni elektronów, podtrzymujących oscylacje Pc5, wydaje się odpowiadać za lokalną destabilizację systemu prądów. Może to spowodować rozerwanie prądu poprzecznego w ogonie magnetosfery, prowadząc do rozpoczęcia subburzy. Obserwowana sekwencja zmian podłużnego strumienia elektronów i fluktuacji magnetycznych jest więc podobna do rozpoczęcia subburzy wskutek niestabilności modu typu “ballooning” (Roux i in. 1991, [160]; Erickson i in. 2000, [44]), mimo że obserwowane tu oscylacje Pc5 są powolniejsze i raczej związane z rezonansami linii pola magnetycznego (*ang. Field Line Resonances*; również obserwowanymi dla jednego ze wspomnianych przypadków - Holter i in. 1995). Oznacza to konieczność dokładniejszego uwzględnienia własności elektronów w modelowaniu rozwoju subburz.

v Innym nowym wynikiem jest wykazanie, że energia intensywnych fluktuacji niskich częstości (ULF) jest przekazywana do magnetosferycznej (gorętszej) populacji elektronów głównie poprzez turbulentne przyśpieszanie a nie poprzez grzanie, przynajmniej w przypadku zaobserwowanych subburz. Temperatura po iniekcji nie zmieniła się drastycznie. W przeciwieństwie do tego, wraz ze wzmożonymi fluktuacjami magnetycznymi typu Pi2 - Pc3, rozwijał się niemaxwellowski “ogon” w wysokoenergetycznej części funkcji rozkładu. Tego typu efekt jest “cząsteczkową” oznaką zachodzących procesów turbulencyjnych, widocznych w polu magnetycznym i jest dalszym potwierdzeniem wpływu turbulencji niskich częstości na przyśpieszanie elektronów wzdłuż zorzowych linii pola magnetycznego.

Podsumowując, wyniki tej pracy wykazują że elektrony o niskich energiach (od $\sim 100 \text{ eV}$ do kilku keV) pełnią ważną rolę w dynamice bliskiej magnetosfery ziemskiej podczas subburz.